ANL/RERTR/TM-12/49

Review of the Oak Ridge National Laboratory (ORNL) Neutronic Calculations Regarding the Conversion of the High Flux Isotope Reactor (HFIR) to the Use of Low Enriched Uranium (LEU) Fuel

Nuclear Engineering Division

About Argonne National Laboratory

Argonne is a U.S. Department of Energy laboratory managed by UChicago Argonne, LLC under contract DE-AC02-06CH11357. The Laboratory's main facility is outside Chicago, at 9700 South Cass Avenue, Argonne, Illinois 60439. For information about Argonne and its pioneering science and technology programs, see www.anl.gov.

Availability of This Report

This report is available, at no cost, at http://www.osti.gov/bridge. It is also available on paper to the U.S. Department of Energy and its contractors, for a processing fee, from:

U.S. Department of Energy
Office of Scientific and Technical Information
P.O. Box 62
Oak Ridge, TN 37831-0062
phone (865) 576-8401
fax (865) 576-5728
reports@adonis.osti.gov

Disclaimer

This report was prepared as an account of work sponsored by an agency of the United States Government. Neither the United States Government nor any agency thereof, nor UChicago Argonne, LLC, nor any of their employees or officers, makes any warranty, express or implied, or assumes any legal liability or responsibility for the accuracy, completeness, or usefulness of any information, apparatus, product, or process disclosed, or represents that its use would not infringe privately owned rights. Reference herein to any specific commercial product, process, or service by trade name, trademark, manufacturer, or otherwise, does not necessarily constitute or imply its endorsement, recommendation, or favoring by the United States Government or any agency thereof. The views and opinions of document authors expressed herein do not necessarily state or reflect those of the United States Government or any agency thereof, Argonne National Laboratory, or UChicago Argonne, LLC.

ANL/RERTR/TM-12/49

Review of the Oak Ridge National Laboratory (ORNL) Neutronic Calculations Regarding the Conversion of the High Flux Isotope Reactor (HFIR) to the Use of Low Enriched Uranium (LEU) Fuel

prepared by
A. Bergeron
Nuclear Engineering Division, Argonne National Laboratory

July 31, 2012

[This page intentionally blank]

Acknowledgements

Argonne National Laboratory's work was supported by the Global Threat Reduction Initiative (GTRI), Reduced Enrichment for Research and Test Reactors (RERTR) Program of the National Nuclear Security Administration (NNSA) and the U.S. Department of Energy (U.S. DOE) under Prime Contract No. DE-AC02-06CH11357 between the U.S. Department of Energy and UChicago Argonne, LLC. This work could not have been possible without the close collaboration of the Oak Ridge National Laboratory (ORNL) staff. The author would like to acknowledge, in particular, the efforts of Germina Ilas, David Renfro, David Chandler, David Cook and James Freels. Their knowledge, availability, and responsiveness have been very much appreciated. The author would also to thank his Argonne colleagues for their ideas, comments and criticisms that helped improve, without any doubt, the quality of this work: James Sienicki, Benoit Dionne, Erik Wilson and John Stevens.

Abstract

In awareness of the risk caused by the proliferation of nuclear materials, the international community initiated in 1978 the Reduced Enrichment for Research and Test Reactors (RERTR) Program [Ref. 1]. The goal of the RERTR program is to seek solutions to convert the reactors using High Enriched Uranium (HEU) fuel (^{235}U/U ≥ 20 wt. %) to the use of Low Enriched Uranium (LEU) Fuel (^{235}U/U < 20 wt. %). Among the 200 reactors worldwide currently in the scope of the program, about 70 have been converted or shut down prior to conversion. In the U.S., six high reactors remain to be converted [Ref. 2].

One of the U.S. reactors is the High Flux Isotope Reactor (HFIR) located at Oak Ridge National Laboratory (ORNL). This multipurpose reactor is mainly used for neutron scattering experiments and isotope production. It has two fuel elements made of involute-shaped fuel plates [Ref. 3].

The ORNL Research Reactor Division (RRD) has prepared during FY2011 two series of calculations, one neutronic and one thermal-hydraulic (TH), in support of the conversion activities for HFIR. The neutronic calculations cover mainly the evaluation of the matrix of performance (cycle length and flux), the distribution of power in the fuel elements, kinetics parameters and reactivity coefficients [Ref. 4].

As defined by the RRD procedures, the calculations have to be reviewed. Per internal decision, the RRD proposed an external reviewer, Argonne National Laboratory (ANL). The results of the Argonne neutronic review are presented in this report. The results of the TH review are presented in a separate report.

The main conclusion of the ORNL reactor physics analyses is that the proposed reference HFIR LEU core (using the so-called monolithic UMo fuel [Ref. 5]) could maintain the current level of performance (obtained with a HEU core at 85MW) if it is operated at 100MW. However, to operate within the same safety limits as the current HEU core, the thermal hydraulic analyses show that the peaking of the power distribution occurring at the bottom of the fuel plates has to be reduced.

The RRD has found a potential solution by reducing the fuel thickness at the bottom of the fuel plate. This would require addition of an axial grading to the already radially-graded fuel. Thus, the review has been focused on independently recalculating all of the ORNL calculations and making an as fair as possible comparison between the current 85MW HEU core and the reference 100MW LEU core design.

ORNL and ANL have used the same computational tools to perform the work. The codes MCNP [Ref. 6] and ORIGEN [Ref. 7] have been used to perform the steady state and depletion calculations, respectively. The communication between the two codes has been carried out by the code VESTA [Ref. 8].

Even though the code MCNP is able to handle complex geometries, it cannot model the involute shape. Nonetheless, ANL has developed an innovative methodology to model the involute shape with MCNP with an approximation that can be made as accurate as desired. Thus, ANL has been able to perform the calculations using an explicit (or discrete) description of the fuel elements.

The current modeling used by ORNL consists in homogenizing the different fuel element components (cladding, fuel, coolant…). Although this method is easier to implement, it may also affect the reactor physics which may have an impact on the calculated results.

Even though some differences in the physics parameters (flux for instance) have been detected between the HEU explicit (ANL) and homogenized (ORNL) models, they are small enough to not significantly impact the performance parameters. However, this is not the case for the LEU core where the differences in the physics parameters lead to significant differences in the performance parameters, especially the cycle length (found to be considerably longer in the explicit model). Nonetheless, the others parameters calculated by ANL (power distribution, kinetics parameters…) are in good agreement with those calculated by ORNL.

Some inconsistencies have been detected in the original ORNL inputs that have been corrected in the reference ones used by ANL for the review and, therefore, the cycle length difference between the LEU homogenized and explicit models has been amplified.

Consequently, the ANL comparison of the HFIR HEU and LEU cores has given different results than the ORNL results. The ORNL matrix of performance for the 100MW LEU reference design shows that the reactor cycle length would be as long and the flux as high as the current 85MW HEU core. In contrast, the ANL matrix of performance shows that the 100MW LEU design would have a significantly longer cycle length (~33days) than the current 85MW HEU core (~25days).

In addition, it has been shown that, if the reactor is operated for 33days, the neutron fluence would be high enough to increase the overall reactor performance by a significant factor. If the reactor is forced to shut down after 25days, calculations show that the neutron flux would be high enough to maintain the performance of the neutron scattering experiments but losses are predicted to occur in several irradiation facilities.

Increasing the cycle length may not be possible for other reasons. For instance, a longer cycle length can increase the cumulative oxide layer thickness growth on the plate. The increase in the neutron fluence may affect the lifetime of the reactor vessel and, by reducing the time for maintenance, pose operational challenges. An assessment of these as well as other potential questions associated with a 33 day cycle length is needed. Since such an assessment has not been carried out, ANL cannot conclude that the ORNL reference LEU core should or could operate at 100MW.

The conclusions of the ANL review are different than those of the ORNL investigation mainly because the explicit and homogenized methodologies used to model the core are different. In this report, an attempt is made to justify and explain as clearly as possible why the ANL methodology is thought to be better suited for HFIR analyses. It is acknowledged that because the ANL and ORNL LEU models have not been benchmarked against experiments, it is possible that doubts could be raised concerning the ability of the models to correctly capture all of the physics behavior of the reactor.

Table of Contents

Acknowledgements **5**

Abstract **6**

Table of Figures **10**

List of Tables **15**

1 Introduction **17**

2 Brief Description of the HFIR Reactor **18**

2.1 The HFIR Reactor 18

2.2 The HEU Fuel Elements 22

2.3 Proposed LEU Fuel Elements 26

2.4 Experiment Facilities and Matrix of Performance 33

2.4.1 Neutron Activation Analysis (NAA) 33

2.4.2 Gamma Irradiation (GI) 34

2.4.3 Neutron Scattering Experiment (NSE) 34

2.4.4 In-core Irradiation Facilities (IIF) 34

3 Computational Methods **36**

3.1 Steady Sate Calculations – MCNP 36

3.2 Depletion Calculations - ORIGEN 36

3.3 Monte-Carlo-Depletion - VESTA 36

3.4 Nuclear Library 37

3.5 Critical Search 37

3.6 Generating MCNP Cards for Discrete Involute Modeling 37

4 Review of the ORNL RRD Neutronic Calculations **39**

4.1 Scope of the Study 39

4.2 Review of the ORNL MCNP Inputs, Methodologies and Assumptions 40

4.2.1 Region I – Central target (FTT) 41

4.2.2 Region II – Inner Fuel Element (IFE) 43

4.2.3 Region III – Outer Fuel Element (OFE) 49

4.2.4 Region IV – Inner Control Element (ICE) & Outer Control Element (OCE) 53

4.2.5 Region V – Irradiation Facilities & Removable Beryllium Reflector (RB) 55

4.2.6 Region VI – Beam tubes & Permanent Beryllium Reflector (PB) 56

4.3 Review of the ORNL RRD Neutronic Calculations 57

4.3.1 Reference Model Preparation 57

4.3.2 Cycle Length Prediction 65

4.3.3 Power Distribution 75

4.3.4 Neutron Flux 89
4.3.5 Other Calculations 106
5 Conclusions 115
References 116
Appendices 118
Table of Contents 118
Appendix A – Circle Involute 119
Appendix B – Methodology to Model Step-by-Step the Involute Shape with MCNP 121
B-1 Methodology 121
B-2 Generate a Mesh 121
B-3 Generate a Plate 123
B-4 Duplicate the Plate 124
B - References 124
Appendix C – Investigation of the Differences between Explicit and Homogenized Models .. 125
C-1 Introduction 125
C-2 Homogeneous vs. Heterogeneous 125
C-3 Predicted Cycle Length 127
C-4 Isotope Mass Evolution 130
C-5 Scalar Neutron Flux 132
C-6 Average Neutron Energy 134
C-7 Isotope Anti-reactivity 137
C-8 Pseudo k-effective 145
C-9 Conclusions 148
C - References 149
Appendix D – HEU and LEU Power Distributions of configuration l11 at BOC, day 1 and EOC 150

Table of Figures

Figure 2.1.1 – Aerial view of the HFIR site [Ref. 3]. 18
Figure 2.1.2 –Axial cross sectional view of the HFIR reactor [Ref. 3]. 20
Figure 2.1.3 – Plan view of the HFIR core assembly [Ref. 3]. 21
Figure 2.1.4 – Schematic representation of the position of the control elements during the cycle. 21
Figure 2.2.1 – View of a mockup of the inner and outer elements [Ref. 4]. 22
Figure 2.2.2 –Illustration of the HEU IFE and OFE fuel distributions [Ref. 9]. Not to scale. 23
Figure 2.2.3 – Thickness of the fuel and filler along the fuel plate width in both HEU IFE (left) and OFE fuel plates (right). 24
Figure 2.2.4 – Cross-section at scale 1:1 of the IFE fuel plates before bending. 24
Figure 2.2.5 – Cross-section at scale 1:1 of the OFE fuel plates before bending. 24
Figure 2.3.1 - Thickness of the fuel and filler along the fuel plate width in reference LEU IFE (solid lines). 27
Figure 2.3.2 - Thickness of the fuel and filler along the fuel plate width in reference LEU OFE (solid lines). 27
Figure 2.3.3 – Three-dimensional view of the LEU IFE fuel foil thickness at fuel plate bottom (last 4cm) before bending. View from the inner edge. 28
Figure 2.3.4 –Illustration of the LEU IFE plate cross section at elevations above 3cm from the bottom of the fuel. 28
Figure 2.3.5 – Illustration of the LEU IFE plate cross section at elevations between the bottom to +1cm above the bottom of the fuel. 28
Figure 2.3.6 – Three-dimensioanal view of the LEU OFE fuel foil bottom (last 4cm) before bending. View from the inner edge. 29
Figure 2.3.7 – Illustration of the LEU OFE plate cross section at elevations above 3cm above the bottom of the fuel. 29
Figure 2.3.8 – Illustration of the LEU OFE plate cross section at elevations between the bottom to +1cm above the bottom of the fuel. 29
Figure 2.4.1 – Top view of the in-core experiment facilities of HFIR. The size of the flux trap (represented by the hexagonal lattice surrounded by a dark gray disk at the center of the figure) is exaggerated. The fuel and control elements are not visible on this figure [Ref. 3]. 33
Figure 3.1 – Typical calculational scheme used for the review. 38
Figure 4.2.1.1 – MCNP screenshots of the FTT. The pictures on the left and right show a top view of the FTT as it is in *HFV4.0* and *leu2011*, respectively. 41
Figure 4.2.2.1 – MCNP screenshots of the IFE. The pictures on the left and right show a top view of the IFE as it is in *HFV4.0* and *leu2011*, respectively. 43
Figure 4.2.3.1 – MCNP screenshots of the OFE. The pictures on the left and right show a top view of the OFE as it is in *HFV4.0* and *leu2011*, respectively. 49
Figure 4.2.4.1 – MCNP screenshot of the control elements (top view). 53
Figure 4.2.5.1 - MCNP screenshot of the removable and semi-permanent reflector (top view). 55
Figure 4.2.6.1 – MCNP screenshot of region VI (top view). This region appears in color on the picture. 56
Figure 4.3.1.1.1 – MCNP screenshots of the HFIR fuel elements (half top view). The picture on the top left has been obtained with the ORNL homogenized model. The picture on the top right has been obtained for the ANL explicit model. The bottom picture is an enlargement of the area represented by the white rectangle on the top right picture. 60

Figure 4.3.1.1.2 – MCNP screenshots of the inner (left) and outer (right) cladding as modeled in both HEU and LEU ANL reference inputs (25 cells each). 61

Figure 4.3.1.1.3 – 3D view of the inner (left) and outer (right) LEU fuel and details of the bottom as modeled in the LEU reference inputs. The triangular base of the polyhedrons used to model the region doubly graded is clearly visible on the details pictures. 61

Figure 4.3.2.1.1 – Critical control elements positions obtained with *HFV4.0* and *HFV4.0-explicit* (at 85MW). Uncertainty max. < 100pcm/steady state calculation at 1-σ. 67

Figure 4.3.2.1.2 – k-effective values associated with the critical control element positions obtained with *HFV4.0* and *HFV4.0-explicit*. 67

Figure 4.3.2.1.3 – k-effective evolution obtained with ANL explicit model "Series *c400* – HEU" using the experimental critical position modified to reflect the conditions of the reactor at BOC 400. 68

Figure 4.3.2.1.4 – Critical control element positions obtained with ANL explicit model "Series *c400* – HEU" modified to reflect the conditions of the reactor at BOC 400 and comparison with experimental positions. Uncertainty max. < 100pcm/steady state calculation at 1-σ. 68

Figure 4.3.2.2.1 - Critical control element positions obtained with *leu2011* and *leu2011-explicit* (at 100MW). Uncertainty < 100pcm/steady state calculation at 1-σ. 70

Figure 4.3.2.2.2 – Evolution of the variation of reactivity between *leu2011*-explict and *leu2011* (blue curve). The corresponding discrepancy in control element positions is shown in green (scale on the right vertical axis). Uncertainty < 100pcm/steady state calculation at 1-σ. 70

Figure 4.3.2.2.3 – Illustration of the difference between a heterogeneous (left) and homogeneous (right) system. The probability of being captured at intermediate energy is higher in a homogeneous system because the probability to meet heavy nuclei is higher. 71

Figure 4.3.2.3.1 – Critical control element positions for the 4 ANL reference inputs. Uncertainty < 100pcm/steady state calculation at 1-σ. 74

Figure 4.3.3.2.1 – Evolution of the fraction of power deposited in both elements (top), OFE (middle) and IFE (bottom). 78

Figure 4.3.3.3.1 – Relative Power density in the HEU IFE fuel at BOC. HEU Series *c400* & *l11* compared with the reference distribution provided in the SAR Table 4.3.1. Uncertainty max. < 0.1 relative power density at 1-σ. 81

Figure 4.3.3.3.2 – Relative Power density in the HEU OFE fuel at BOC. HEU Series *c400* & *l11* compared with the reference distribution provided in the SAR Table 4.3.1. Uncertainty max. < 0.1 relative power density at 1-σ. 82

Figure 4.3.3.3.3 – Relative Power density in the HEU IFE fuel at EOC. HEU Series *c400* & *l11* compared with the reference distribution provided in the SAR Table 4.3.1. Uncertainty max. < 0.1 relative power density at 1-σ. 83

Figure 4.3.3.3.4 – Relative Power density in the HEU OFE fuel at EOC. HEU Series *c400* & *l11* compared with the reference distribution provided in the SAR Table 4.3.1. Uncertainty max. < 0.1 relative power density at 1-σ. 84

Figure 4.3.3.3.5 – Relative Power density in the LEU IFE fuel at BOC. LEU Series *c400* & *l11* compared with the reference distribution provided in ORNL [Ref. 4], Table 5. Uncertainty max. < 0.1 relative power density at 1-σ. 85

Figure 4.3.3.3.6 – Relative Power density in the LEU OFE fuel at BOC. LEU Series *c400* & *l11* compared with the reference distribution provided in ORNL [Ref. 4], Table 5. Uncertainty max. < 0.1 relative power density at 1-σ. 86

Figure 4.3.3.3.7 – Relative Power density in the LEU IFE fuel at EOC. LEU Series *c400* & *l11* compared with the reference distribution provided in ORNL [Ref. 4], Table 6. Uncertainty max. < 0.1 relative power density at 1-σ. 87

Figure 4.3.3.3.8 – Relative Power density in the LEU OFE fuel at EOC. LEU Series *c400* & *l11* compared with the reference distribution provided in ORNL [Ref. 4], Table 6. Uncertainty max. < 0.1 relative power density at 1-σ. 88

Figure 4.3.4.2.1 – Radial flux distribution at BOC calculated with the Series *l11* HEU and LEU cores. Top, middle and bottom graphs represent the thermal, epithermal and fast flux. A half-core view of the core is added to help the comprehension. Five regions are highlighted: Region 1 is the flux trap; Regions 2 and 3 are the IFE and OFE; Regions 4 and 5 are the removable and permanent reflector, respectively. Uncertainty max. < 1% at 1-σ. 91

Figure 4.3.4.2.2 – Radial flux distribution at day25 (EOC of the HEU core) calculated with the Series *l11* HEU and LEU cores. Top, middle and bottom graphs represent the thermal, epithermal and fast flux. A half-core view of the core is added to help the comprehension. Five regions are highlighted: Region 1 is the flux trap; Regions 2 and 3 are the IFE and OFE; Regions 4 and 5 are the removable and permanent reflector, respectively. Uncertainty max. < 1% at 1-σ. 92

Figure 4.3.4.2.3 – Variation of flux between the LEU and HEU cores at BOC (series *l11*). Top, middle and bottom graphs represent the thermal, epithermal and fast flux. A half-core view of the core is added to help the comprehension. Five regions are highlighted: Region 1 is the flux trap; Regions 2 and 3 are the IFE and OFE; Regions 4 and 5 are the removable and permanent reflector, respectively. Uncertainty max. < 2% at 1-σ. 93

Figure 4.3.4.2.4 – Variation of flux between the LEU and HEU core at day25 (EOC for HEU core). Top, middle and bottom graphs represent the thermal, epithermal and fast flux. A half-core view of the core is added to help the comprehension. Five regions are highlighted: Region 1 is the flux trap; Regions 2 and 3 are the IFE and OFE; Regions 4 and 5 are the removable and permanent reflector, respectively. Uncertainty max. < 2% at 1-σ. 94

Figure 4.3.4.2.5 – Thermal flux in the beam tubes at BOC (left) and EOC (right) obtained with Series *l11*. Uncertainty max. < 5% at 1-σ. 95

Figure 4.3.4.2.6 – Variation of thermal flux for LEU and HEU in the beam tubes at BOC (left) and EOC (right) obtained with Series *l11*. Uncertainty max < 9% at 1-σ. 96

Figure 4.3.4.4.1 – Comparison of performance for LEU/HEU for three different scenarios using the Series *c400* inputs. Uncertainty max. < 2% at 1-σ. 104

Figure 4.3.4.4.2 – Comparison of performance for LEU/HEU for three different scenarios using the Series *l11* inputs. Uncertainty max. < 2% at 1-σ. 105

Figure 4.3.5.1.1 – ω versus reactivity for Series *c400* HEU and LEU core at BOC (left) and EOC (right). 108

Figure 4.3.5.1.2 – ω versus reactivity for series *l11* HEU and LEU core at BOC (left) and EOC (right). 108

Figure 4.3.5.1.3 – Simulation of the response of the Series *c400* HEU and LEU cores to an insertion of reactivity of 1000pcm and SCRAM initiated 0.3s later. The top figure represents the evolution of the neutron population. The bottom figure represents the evolution of the reactivity. 108

Figure 4.3.5.2.1 – Differential worth of the control elements obtained with Series *c400* at BOC. The top, middle and bottom figure presents the results obtained for the ICE, OCE and ICE and OCE combined, respectively. Uncertainty max. < 5cents/inch at 1-σ. 111

Figure 4.3.5.2.2 – Differential worth of the control elements (ICE and OCE combined) obtained with Series *c400* at BOC and EOC. Uncertainty max. < 5cents/inch at 1-σ. 112

Figure 4.3.5.3.1 – k-effective variation versus the percentage of void introduced in the flux trap. Top and bottom graphs represent the results obtained at BOC and EOC, respectively. Uncertainty max. < 15pcm at 1-σ. 113

Figures - Appendix A

Figure A1 – Representation of a circle involute (red) generated around the blue circle of radius k. 119

Figures - Appendix B

Figure B1 – Portion of cylinder (black dashed line) included between two involute plates (light blue) that can be used to generate a mesh 122

Figure B2 – Mesh generated used for HFIR explicit models. The picture on the right is an enlargement of the left picture. 122

Figures - Appendix C

Figure C1 – Illustration of the difference between a heterogeneous (left) and homogeneous (right) system. The probability of being captured at intermediate energy is higher in a homogeneous system because the probability to meet heavy nuclei is higher. 126

Figure C2 – Predicted control element positions which maintain criticality in the reactor during irradiation at 85MW obtained with HEU explicit and homogenized models. 128

Figure C3 - Predicted control elements positions which maintain criticality in the reactor during irradiation at 100MW obtained with LEU explicit and homogenized models. 128

Figure C4 – Evolution of the reactivity difference, where a higher reactivity is modeled with the LEU explicit model vs. the homogeneous model over the course of depletion. 129

Figure C5 – Neutron scalar flux evolution in the IFE for homogenized and explicit models. Graph on the left is for the HEU configurations. Graph on the right is for the LEU configurations. 133

Figure C6 – Neutron scalar flux evolution in the OFE for homogenized and explicit models. Graph on the left is for the HEU configurations. Graph on the right is for the LEU configurations. 133

Figure C7 – ^{10}B (n,α) cross section versus energy in the range 1 to 35 eV. 135

Figure C8 – Average neutron energy evolution in the IFE for homogenized and explicit models. Graph on the left is for the HEU configurations. Graph on the right is for the LEU configurations. 136

Figure C9 – Average neutron energy evolution in the OFE for homogenized and explicit models. Graph on the left is for the HEU configurations. Graph on the right is for the LEU configurations. 136

Figure C10 – Variation of anti-reactivity between homogenized and explicit models in the IFE obtained for ^{135}Xe, ^{149}Sm and ^{10}B. Graph on the left is for the HEU configurations. Graph on the right is for the LEU configurations. 140

Figure C11 – Variation of anti-reactivity between homogenized and explicit modes in the IFE obtained for ^{234}U, ^{235}U, ^{236}U, ^{237}U and ^{238}U. Graph on the left is for the HEU configurations. Graph on the right is for the LEU configurations. 140

Figure C12 – Variation of anti-reactivity between homogenized and explicit models in the IFE obtained for ^{237}Np, ^{238}Np and ^{239}Np. Graph on the left is for the HEU configurations. Graph on the right is for the LEU configurations. 141

Figure C13 – Variation of anti-reactivity between homogenized and explicit models in the IFE obtained for ^{238}Pu, ^{239}Pu, ^{240}Pu, ^{241}Pu and ^{242}Pu. Graph on the left is for the HEU configurations. Graph on the right is for the LEU configurations. 141

Figure C14 – Variation of anti-reactivity between homogenized and explicit model in the OFE obtained for ^{135}Xe and ^{149}Sm. Graph on the left is for the HEU configurations. Graph on the right is for the LEU configurations. 142

Figure C15 – Variation of anti-reactivity between homogenized and explicit models in the OFE obtained for ^{234}U, ^{235}U, ^{236}U, ^{237}U and ^{238}U. Graph on the left is for the HEU configurations. Graph on the right is for the LEU configurations. 142

Figure C16 – Variation of anti-reactivity between homogenized and explicit models in the OFE obtained for ^{237}Np, ^{238}Np and ^{239}Np. Graph on the left is for the HEU configurations. Graph on the right is for the LEU configurations. 143

Figure C17 – Variation of anti-reactivity between homogenized and explicit models in the OFE obtained for ^{238}Pu, ^{239}Pu, ^{240}Pu, ^{241}Pu and ^{242}Pu. Graph on the left is for the HEU configurations. Graph on the right is for the LEU configurations. 143

Figure C18 – Evolution of the variation of reactivity between the LEU explicit and homogenized models obtained with MCNP calculations and pseudo k-effective calculations. 147

List of Tables

Table 2.2.1 – ANL reference composition of the HEU IFE fuel 25

Table 2.2.2 – ANL reference composition of the HEU IFE filler containing the burnable absorber 25

Table 2.2.3 – ANL reference composition of the HEU OFE fuel 25

Table 2.3.1 – ANL reference composition of the LEU IFE & OFE fuel [Ref. 4] 30

Table 2.3.2 – ANL reference composition of the LEU IFE filler containing the burnable absorber 30

Table 2.3.2 – ANL reference composition of the LEU zirconium layer [Ref. 4] 31

Table 2.3.4 – Summary of HEU and LEU core characteristics 32

Table 2.4.1 – Summary of the matrix of performance considered for the review 35

Table 4.2.1 – Differences between the two MCNP inputs provided by ORNL for the review 40

Table 4.2.2.1 – IFE radial mesh in the MCNP models *HFV4.0* and *leu2011* 40

Table 4.2.2 – Conditions of pressure and temperature of the light water considered in *HFV4.0* and *leu2011* MCNP inputs. The coolant density is deduced from the NIST database [Ref. 19] 42

Table 4.2.1.1 – List of materials present in *HFV4.0* Region I with an ambiguous density 44

Table 4.2.2.2 – IFE axial mesh in the MCNP models *HFV4.0* and *leu2011* 45

Table 4.2.2.3 – ^{235}U distribution in the HEU IFE and variation between ANL / *HFV4.0* 46

Table 4.2.2.4 – ^{10}B distribution in the HEU IFE and variation between ANL / *HFV4.0* 46

Table 4.2.2.5 – ^{235}U distribution in the LEU IFE and variation between ANL / *leu2011* 47

Table 4.2.2.6 – ^{10}B distribution in the LEU IFE and variation between ANL / *leu2011* 48

Table 4.2.3.1 – OFE Radial mesh in the MCNP models *HFV4.0* and *leu2011* 49

Table 4.2.3.2 – ^{235}U distribution in the HEU OFE and variation between ANL / *HFV4.0* 51

Table 4.2.3.3 – ^{235}U distribution in the LEU OFE and variation between ANL / *leu2011* 52

Table 4.2.4.1 – CE dimensions updated in both MCNP inputs 54

Table 4.2.4.2 – Reference absorbing materials masses and comparison with *HFV4.0* values 54

Table 4.3.1.1.1 – ANL reference radial mesh for depletion & power calculations 58

Table 4.3.1.1.2 – ANL reference axial mesh for depletion & power calculations 59

Table 4.3.1.2.1 – Summary of the different input modifications leading to the ANL reference inputs and their effects on the reactivity. Uncertainty < 12pcm at 1-σ. 63

Table 4.3.1.2.2 – Results of the criticality calculations carried out with the 4 ANL reference inputs (control element position 45.72cm withdrawn). Uncertainty < 12pcm at 1-σ. 64

Table 4.3.2.2.1 – Absorption rate of ^{238}U (expressed in 10^{12} absorption/s) obtained with the HEU and LEU homogeneous (RZ) and heterogeneous (explicit) models by locations and time in the cycle. 72

Table 4.3.2.3.1 – Calculated cycle length for ANL reference inputs. 74

Table 4.3.3.1.1 – Contribution to the power and methods to evaluate them 76

Table 4.3.3.2.1 – Detail of the different contributions to the IFE and OFE powers at different periods of time and for the 4 reference inputs. Uncertainty max. < 0.5% of the value at 1-σ 79

Table 4.3.4.1.1 – Number of neutrons created per second, τ, in the reactor. Uncertainty max. < 0.5% at 1-σ. 89

Table 4.3.4.3.1 – Neutron flux comparison ORNL / ANL. ANL uncertainty max < 0.5% at 1-σ 96

Table 4.3.4.3.2 – Neutron flux comparison HEU/LEU at BOC. ANL uncertainty max. < 0.5% at 1-σ 98

Table 4.3.4.3.3 – Neutron flux comparison HEU/LEU at EOC. ANL uncertainty max. < 0.5% at 1-σ 99

Table 4.3.4.4.1 – Matrix of performance for Series *c400* HEU & LEU cores. Uncertainty max. < 1% at 1-σ 101

Table 4.3.4.4.2 – Matrix of performance for series *l11*, HEU & LEU core. Uncertainty max. < 1% at 1-σ 102

Table 4.3.5.1.1 – Beta-effective values obtained with ANL reference inputs. Uncertainty max. < 7pcm at 1-σ 107
Table 4.3.5.1.2 – Beta-effective values obtained with ANL reference inputs. Uncertainty max. < 0.12×10^{-6}s at 1-σ 107
Table 4.3.5.4.1 – ORNL and ANL Series *c400* CVR values for a coolant void fraction of 10%. Uncertainty max. < 2pcm/%-void at 1-σ 114

Tables - Appendix C

Table C1 – Mass evolution of different isotopes present in the IFE fuel, filler and OFE for HEU and LEU configurations 131
Table C2 – Isotopes and reactions selected for the anti-reactivity calculations 139

Tables - Appendix D

Table D1 – HEU fuel at 85MW – configuration l11 – BOC – IFE – relative power density 150
Table D2 – HEU fuel at 85MW – configuration l11 – BOC – OFE – relative power density 151
Table D3 – HEU fuel at 85MW – configuration l11 – day 1 – IFE – relative power density 152
Table D4 – HEU fuel at 85MW – configuration l11 – day 1 – OFE – relative power density 153
Table D5 – HEU fuel at 85MW – configuration l11 – day 1 – IFE – relative power density 154
Table D6 – HEU fuel at 85MW – configuration l11 – day 1 – OFE – relative power density 155
Table D7 – LEU fuel at 100MW – configuration l11 – BOC – IFE – relative power density 156
Table D8 – LEU fuel at 100MW – configuration l11 – BOC – OFE – relative power density 157
Table D9 – LEU fuel at 100MW – configuration l11 – day 1 – IFE – relative power density 158
Table D10 – LEU fuel at 100MW – configuration l11 – day 1 – OFE – relative power density 159
Table D11 – LEU fuel at 100MW – configuration l11 – EOC – IFE – relative power density 160
Table D12 – LEU fuel at 100MW – configuration l11 – EOC – OFE – relative power density 161
Table D13 – HEU fuel at 85MW – configuration l11 – BOC – IFE – heat flux (W/cm^2) 162
Table D14 – HEU fuel at 85MW – configuration l11 – BOC – OFE – heat flux (W/cm^2) 163
Table D15 – HEU fuel at 85MW – configuration l11 – day 1 – IFE – heat flux (W/cm^2) 164
Table D16 – HEU fuel at 85MW – configuration l11 – day 1 – OFE – heat flux (W/cm^2) 165
Table D17 – HEU fuel at 85MW – configuration l11 – EOC – IFE – heat flux (W/cm^2) 166
Table D18 – HEU fuel at 85MW – configuration l11 – EOC – OFE – heat flux (W/cm^2) 167
Table D19 – LEU fuel at 100MW – configuration l11 – BOC – IFE – heat flux (W/cm^2) 168
Table D20 – LEU fuel at 100MW – configuration l11 – BOC – OFE – heat flux (W/cm^2) 169
Table D21 – LEU fuel at 100MW – configuration l11 – day 1 – IFE – heat flux (W/cm^2) 170
Table D22 – LEU fuel at 100MW – configuration l11 – day 1 – OFE – heat flux (W/cm^2) 171
Table D23 – LEU fuel at 100MW – configuration l11 – EOC – IFE – heat flux (W/cm^2) 172
Table D24 – LEU fuel at 100MW – configuration l11 – EOC – OFE – heat flux (W/cm^2) 173

1 Introduction

The present report describes the result of the ANL review of the neutronic calculations that have been produced during FY2011 by the Oak Ridge National Laboratory (ORNL) Research Reactor Division (RRD) in support of the conversion analyses for the High Flux Isotope Reactor (HFIR) reactor [Ref. 4]. The ORNL calculations cover mainly the evaluation of the matrix of performance (neutron flux and cycle length), the distribution of power, kinetics parameters and reactivity coefficients. The review has consisted in verifying the ORNL model inputs, independently performing all of the calculations and comparing the 85MW High Enriched Uranium (HEU) to the proposed reference 100MW Low Enriched Uranium (LEU) core designs. Unless otherwise specified, all of the physical units are expressed in the System International (SI).

The report is organized as follow:

- In Section 2, a description of HFIR is provided. It includes the general concept of the reactor, a detailed description of the HEU and the proposed reference LEU cores. A definition of the reactor matrix of performance and how to calculate it are also provided.

- The computational methods used for the review are described in Section 3.

- The results of the review are described in Section 4. This part of the report is divided in several subsections. After a brief recall of the scope of the work, the results of cross-checking the ORNL inputs cross-checking are presented. The effects of refinements or corrections on the reactor's physics will be discussed. The process of production of the ANL reference inputs will also be described. These reference inputs have been used to independently perform all of the ORNL calculations. The methodologies used and the results obtained from the calculations will then be described in the final subsection.

- The remaining part of the report includes the Conclusions and Appendices.

2 Brief Description of the HFIR Reactor

2.1 The HFIR Reactor

The High Flux Isotope Reactor (HFIR), located at Oak Ridge National Laboratory (ORNL), achieved first criticality August 25 1965. Even though the reactor fulfills a wide range of missions, it has been primarily designed for transplutonium isotope production [Ref. 9]. Following a 2-year long survey on flux trap reactors and their potential application for heavy isotope production [Ref. 10], the U.S. Atomic Energy Commission (forerunner to the U.S. DOE) decided to build HFIR in November 1958 [Ref. 11]. The first HFIR physics report was issued in 1960 [Ref. 12], immediately followed by the first critical experiments employing prototype HFIR fuel elements and control rods [Ref. 13]. The construction of the reactor was completed in 1964. Low-power operation was completed in January 1966 and full power (100MW thermal) was achieved in September 1966 [Ref. 9]. The reactor operated without any notable incident until November 1986 when it was discovered that, due to neutron-induced-radiation, the reactor vessel was being embrittled at a faster rate than expected. After a long shutdown and modification made to the operating pressure of the primary coolant, the reactor was re-started in April 1989 and reached its new full power, 85MW nuclear, in May 1990. HFIR underwent another long shutdown in 2006 in order to refurbish the facility. Significant upgrading of the neutron scattering experiment equipment was carried out during this period. The refurbishment was completed in 2007 [Ref. 14].

Today, HFIR continues to fulfill its two main missions: isotope production and neutron scattering experimentation. HFIR has approximately 600 users each year for both scattering and in-core research [Ref. 14]. An aerial view of the facility is given in Figure 2.1.1.

Figure 2.1.1 – Aerial view of the HFIR site [Ref. 3].

HFIR is a light water moderated and cooled, beryllium reflected, flux-trap type reactor. The reactor core assembly is contained in a pressure vessel located in a light water pool. The

external diameter of the vessel is about 244cm and its height is approximately 500cm. The reactor core is cylindrical, approximately 61cm high and has a diameter of 114cm. A cross-sectional view of the reactor and a plan view of the core assembly are given in Figures 2.1.2 and 2.1.3, respectively. At the center of the core, a hole of 12.7cm diameter forms the Flux Trap Target region (FTT). More details on the FTT are given in Section 2.4. The flux trap is surrounded by two concentric annular fuel elements. Each consists of sandwich-type fuel plate (fuel surrounded by cladding) curved as a circle involute. The involute shape allows the coolant gap between the plates to have a constant thickness. More details on the fuel elements are given in Sections 2.2 and 2.3.

Surrounding the fuel elements is an annular region containing the control elements (CEs). They consist of two 1cm-thick concentric cylinders. Light water circulates between the CEs in order to cool them. To compensate fuel burnup throughout the life of the core, the CEs are gradually, vertically and symmetrically withdrawn. The inner cylinder (ICE) is used for both shim control and regulation and is moved downward during the cycle. The outer cylinder (OCE) is made of four plates that can be moved independently to SCRAM the reactor at any time and are referred to the shim-safety plates. They are moved upward during the cycle. The typical position of the CEs at different times during the cycle is illustrated in Figure 2.1.4. To reduce axial variations in the power distributions, the control elements are divided into three axial sections. Each of them incorporates different materials which have different neutron absorbing characteristics. The so-called white material (lower section of the OCE, upper section of the ICE) is made of aluminum and has a low neutron absorbing power. The so-called gray material, present in the central section, is made of tantalum dispersed in aluminum and has a moderate neutron absorbing power. The so-called black material (upper section of the OCE, lower section of the ICE) is made of Eu_2O_3 dispersed in aluminum and is highly neutron absorbing. In addition, due to the high-cross-section of its daughter products, the efficiency of the black region tends to increase with time of irradiation [Ref. 15].

A 30cm-thick beryllium annular reflector surrounds the control element region. The damages caused by radiation are more important in the innermost part of the reflector. To avoid excessive changes, the reflector is divided in three regions. The inner part is made of four concentric cylinders axially separated by a thin gap to allow the water to cool them. The three first cylinders (~5cm-thick) are replaced every ~40 cycles and constitute the first part of the reflector and is called the Removable Beryllium reflector (RB). The fourth one (5cm-thick), second part of the reflector, is replaced every ~80 cycles and is called the Semi-permanent Beryllium reflector (SB). The last part and outermost section of the reflector (~20cm-thick), called the Permanent Beryllium Reflector (PB), is replaced every~135 cycles. The three regions of the reflector contain a significant number of experiment facilities such as the four beam tubes, the engineering facilities and the large and small vertical experiment facilities. More details on the experiment facilities are given in Section 2.4. The entire core is surrounded by light water in order to prevent significant radiation damage and heating in the pressure vessel. The water enters the pressure vessel through two ~41cm-diameter pipes located above the core (one of them is visible in Figure 2.1.2). The coolant passes downward through the core and exits through a ~46cm-diameter pipe located just below the core. The inlet flow rate is $1.01m^3/s$. Through the fuel elements, the flow rate is $0.82m^3/s$ and the coolant velocity is 15.5m/s. The rest of the flow cools down the other regions of the core: reflector, flux trap, control elements. The nominal inlet pressure is 3.33MPa. The core outlet pressure is 2.572MPa (pressure drop through the core is 0.758MPa). The inlet temperature is 322K and the outlet temperature is 342K [Ref. 15].

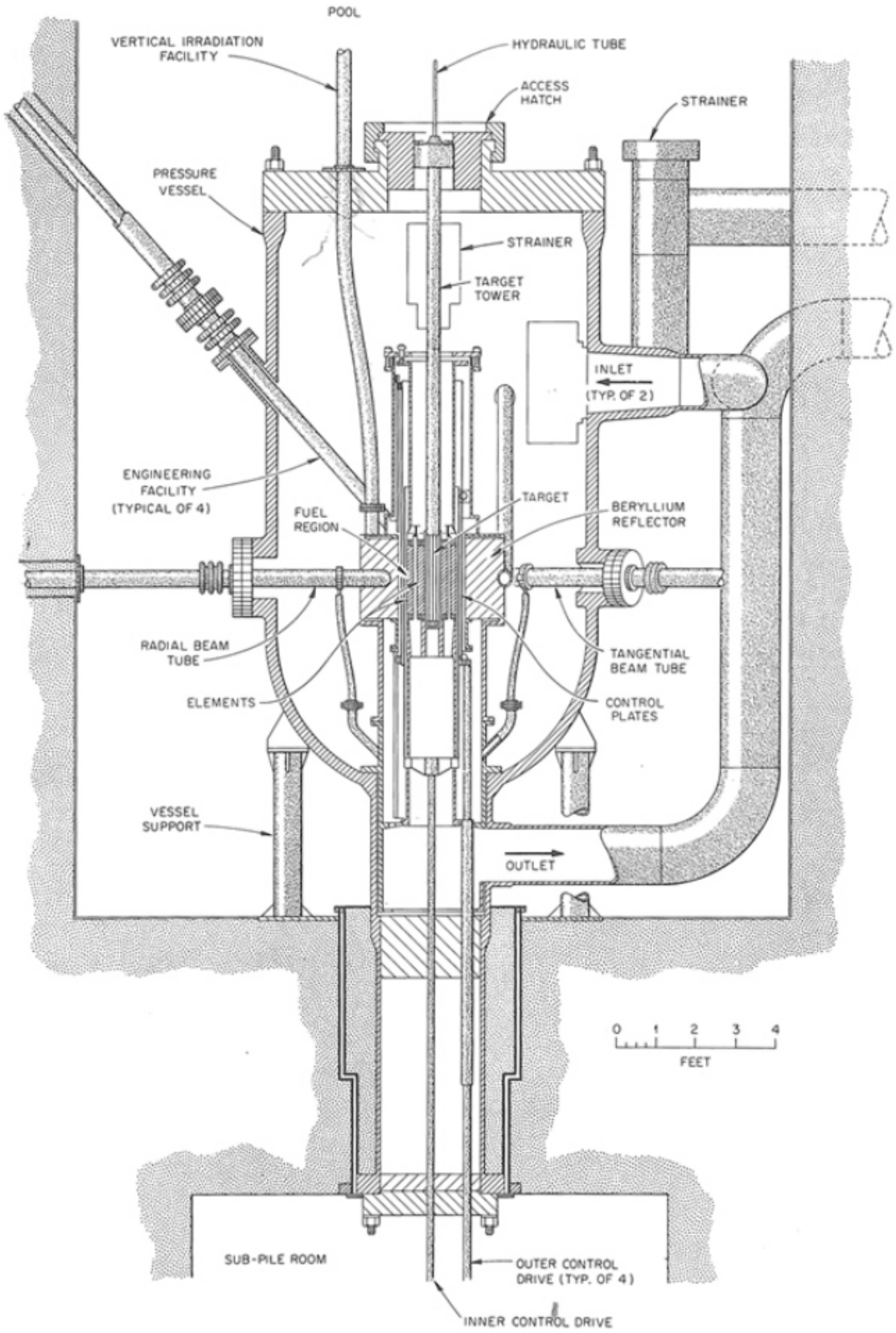

Figure 2.1.2 –Axial cross sectional view of the HFIR reactor [Ref. 3].

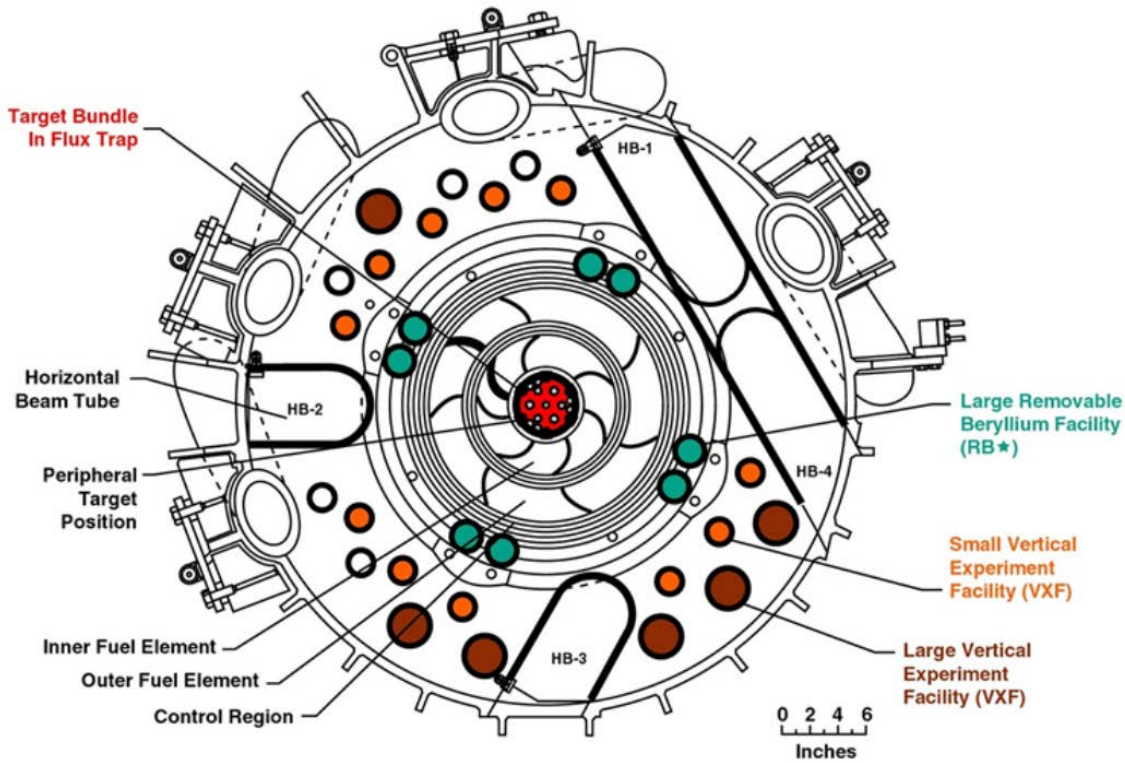

Figure 2.1.3 – Plan view of the HFIR core assembly [Ref. 3].

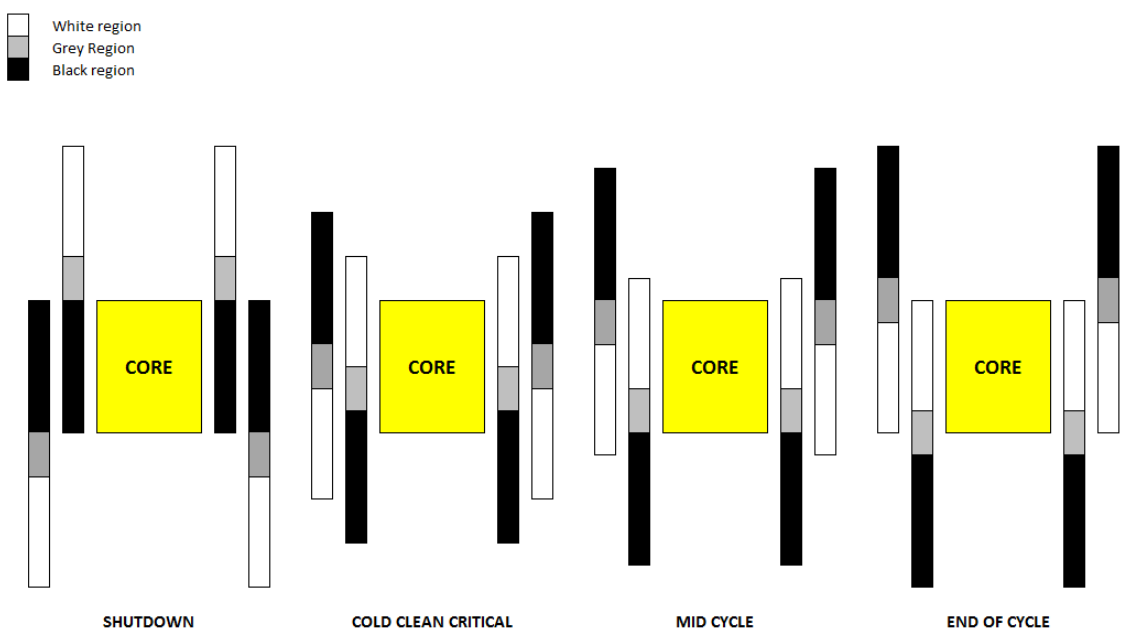

Figure 2.1.4 – Schematic representation of the position of the control elements during the cycle - Not to scale.

2.2 The HEU Fuel Elements

The HEU core is made of two concentric annular fuel elements separated by a 0.84cm-thick water gap. Both elements are made of sandwich-type fuel plates (two cladding plates surrounding a thin layer of fuel). A picture of a mockup of the fuel elements is given in Figure 2.2.1. The plate thickness is 0.127cm and the coolant gap between the plates is also 0.127cm-thick. The plates are 60.96cm high and the length of the fuel is 50.80cm. The width of the inner and outer plates is 9.21 and 8.10cm, respectively. The width of the inner and outer fuel along the involute arc length is 7.79 and 7.02cm, respectively. The cladding is made of 6061 aluminum alloy and its thickness is 0.0254cm. In order to keep a constant coolant gap thickness, the plates are curved as circle involutes. The inner fuel element (IFE) incorporates 171 plates whereas the outer fuel element (OFE) has 369 plates (total of 540 plates). Both inner and outer fuel plates are contained between two 0.635cm-thick cylindrical aluminum side-plates. The inner and outer radii of the IFE are 6.44 and 13.44cm, respectively. The inner and outer radii of the OFE are 14.27 and 21.77cm, respectively. In order to reduce the maximum-to-average power density ratio, the fuel is radially graded. The fuel grading is different in the inner and outer elements. Figure 2.2.2 shows a view of the fuel distribution in both elements and Figure 2.2.3 shows the fuel thickness variation along the plate's width in both elements.

The fuel is made of highly enriched U_3O_8 fuel ($^{235}U/U$ = 93 wt. %) dispersed in an aluminum matrix. The fuel density is different in the inner and outer elements. Both elements contain a total of 9.4kg of ^{235}U (2.6kg in the IFE and 6.8kg in the OFE). In addition, a burnable absorber, boron in the form of B_4C, is present in the inner fuel plates. In particular, 2.8g of ^{10}B are present in the whole IFE (0.0164g/plate). It is used to shift the power to the outer fuel element and reduce the core reactivity (~5000pcm) at Beginning of Life (BOL). The inner fuel, inner burnable filler and outer fuel reference compositions used for this review are given in Tables 2.2.1, 2.2.2 and 2.2.3, respectively. They have been obtained from several ORNL datasets. When available, impurities have been included.

To appreciate the relative dimensions of the fuel constituents, a cross-sectional view of the inner and outer fuel plates before bending is given at scale 1:1 in Figures 2.2.4 and 2.2.5, respectively. Finally, a summary of the different characteristics of the fuel elements is given in Section 2.3, Table 2.3.4.

Figure 2.2.1 – View of a mockup of the inner and outer elements [Ref. 4].

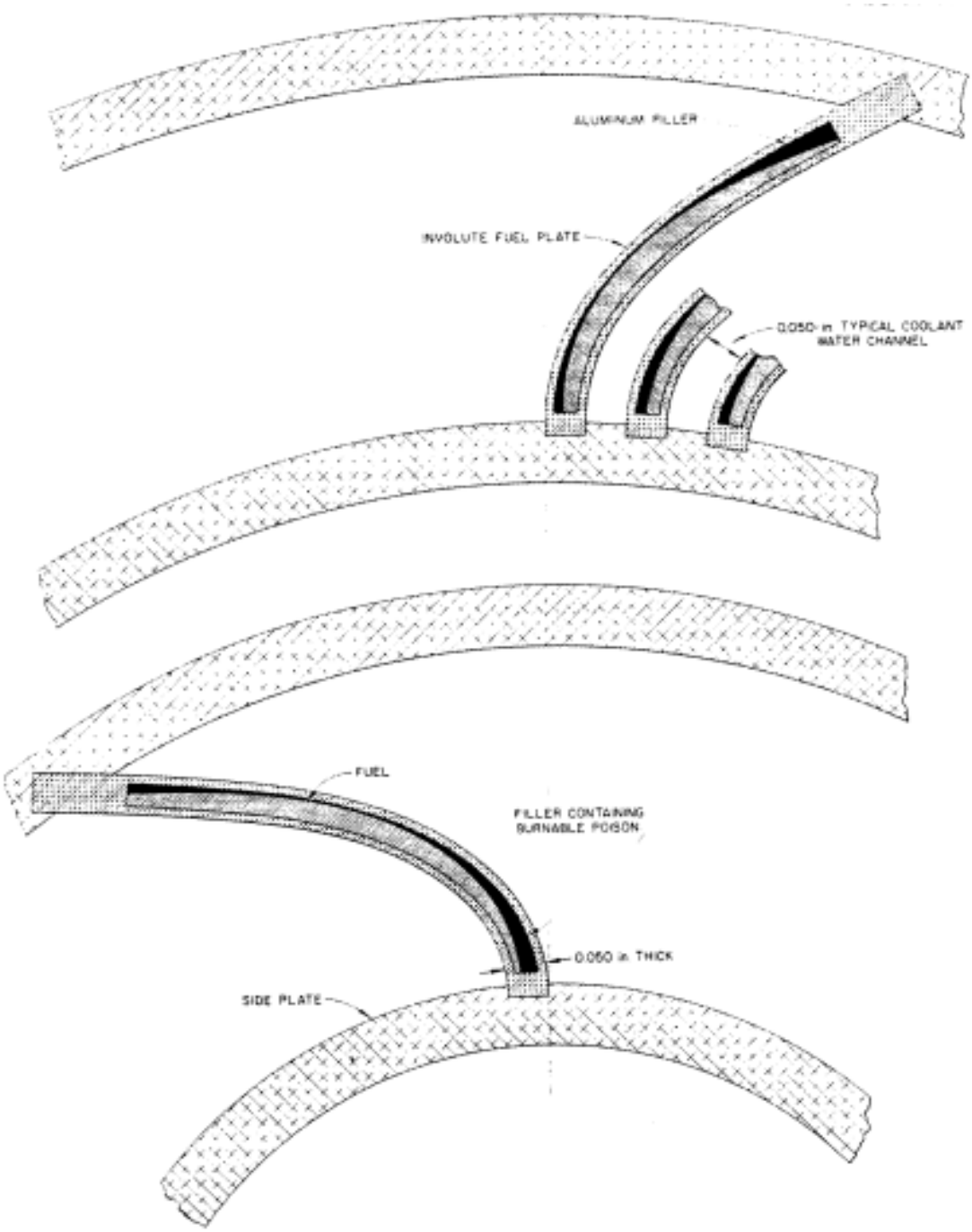

Figure 2.2.2 –Illustration of the HEU IFE and OFE fuel distributions [Ref. 9]. Not to scale.

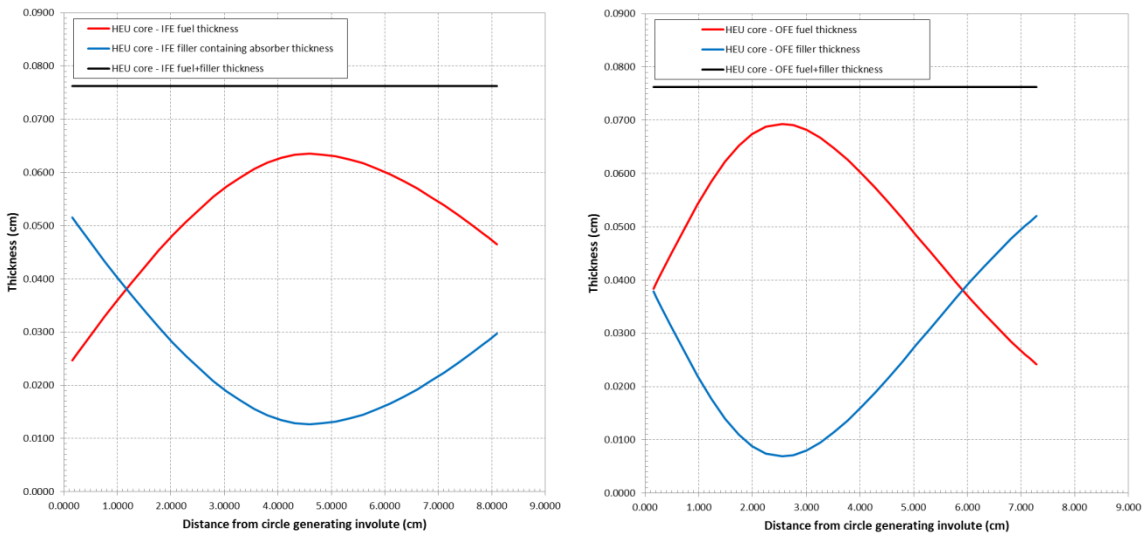

Figure 2.2.3 – Thickness of the fuel and filler along the fuel plate width in both HEU IFE (left) and OFE fuel plates (right).

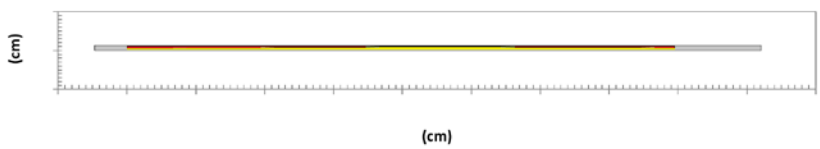

Figure 2.2.4 – Cross-section at scale 1:1 of the IFE fuel plates before bending. The cladding appears in gray, the fuel in yellow and the filler containing the B_4C is in red. If printed without pagination modification, given at scale 1:1.

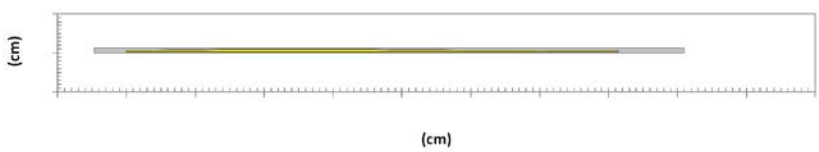

Figure 2.2.5 – Cross-section at scale 1:1 of the OFE fuel plates before bending. The cladding appears in gray and the fuel in yellow. If printed without pagination modification, given at scale 1:1.

Table 2.2.1 – ANL reference composition of the HEU IFE fuel

isotope	density (g/cc)	molar mass (g/mol)	atomic density (at/barn.cm)
^{16}O	1.4063E-01	1.5995E+01	5.2948E-03
^{234}U	7.7168E-03	2.3404E+02	1.9856E-05
^{235}U	7.2228E-01	2.3504E+02	1.8505E-03
^{236}U	3.1133E-03	2.3605E+02	7.9425E-06
^{238}U	4.2383E-02	2.3805E+02	1.0722E-04
^{27}Al	2.3181E+00	2.6982E+01	5.1737E-02
total =	3.2342E+00	-	5.9017E-02

Table 2.2.2 – ANL reference composition of the HEU IFE filler containing the burnable absorber

isotope	density (g/cc)	molar mass (g/mol)	atomic density (at/barn.cm)
^{10}B	1.7848E-03	1.0013E+01	1.0734E-04
^{11}B	7.8988E-03	1.1009E+01	4.3206E-04
^{12}C	2.6871E-03	1.2000E+01	1.3485E-04
^{27}Al	2.6577E+00	2.6982E+01	5.9318E-02
^{54}Fe	3.9110E-04	5.3940E+01	4.3664E-06
^{56}Fe	6.1395E-03	5.5935E+01	6.6099E-05
^{57}Fe	1.4179E-04	5.6935E+01	1.4997E-06
^{58}Fe	1.8869E-05	5.7933E+01	1.9614E-07
^{28}Si	6.1707E-03	2.7977E+01	1.3282E-04
^{29}Si	3.1347E-04	2.8976E+01	6.5147E-06
^{30}Si	2.0689E-04	2.9974E+01	4.1566E-06
^{63}Cu	3.2388E-03	6.2930E+01	3.0994E-05
^{65}Cu	1.4449E-03	6.4928E+01	1.3402E-05
^{55}Mn	6.6915E-04	5.4938E+01	7.3348E-06
total =	2.6888E+00	-	6.0260E-02

Table 2.2.3 – ANL reference composition of the HEU OFE fuel

isotope	density (g/cc)	molar mass (g/mol)	atomic density (at/barn.cm)
^{16}O	1.9128E-01	1.5995E+01	7.2017E-03
^{234}U	1.0496E-02	2.3404E+02	2.7006E-05
^{235}U	9.8238E-01	2.3504E+02	2.5169E-03
^{236}U	4.2344E-03	2.3605E+02	1.0803E-05
^{238}U	5.7648E-02	2.3805E+02	1.4583E-04
^{27}Al	2.2101E+00	2.6982E+01	4.9327E-02
total =	3.4561E+00	-	5.9229E-02

2.3 Proposed LEU Fuel Elements

The information regarding the proposed reference LEU core design is obtained from [Ref. 4] and [Ref. 16].

The LEU core described in this section is the one that has been assumed by ORNL for their calculations. For the review, ANL has also assumed it as a reference design. Except for the nature, shape of the fuel and mass of burnable absorber, all of the characteristics of the elements are similar to the HEU ones (e.g. number and dimensions of the plates, side-plate compositions and dimensions…).

The fuel is a low enriched (^{235}U/U = 19.75 wt. %) metal foil (so-called monolithic) of U-Mo alloy fuel (Mo/UMo = 10 wt. %). Its density is 17.02g/cc [Ref. 4]. A total of 25.27kg of ^{235}U are considered (6.39kg in the IFE, 18.88kg in the OFE). The corresponding uranium loading is 127.95kg which represents an increase of almost a factor 13 when compared to the HEU core. The fuel is identical in both elements and its composition is given in Table 2.3.1. To prevent the undesirable reaction between the fuel and the aluminum of the cladding, a very thin layer (0.00254cm) of zirconium is deposited on the front and back sides of the fuel. As for the HEU core, a burnable absorber, boron in the form of B_4C, is present in the inner fuel plates. In total 5.4g of ^{10}B are present in the whole IFE (0.0316g/plate). The IFE filler composition is given in Table 2.3.2. The zirconium layer composition is given in table 2.3.3.

The shape of the LEU fuel foil inside of the plate is significantly different from that of the HEU fuel. The design is the result of an iterative process that was intended to maximize the reactor performance while maintaining the current TH safety margins. The iterative process is discussed in detail in [Ref. 4].

As for the HEU plates, the LEU fuel is radially graded in order to reduce the maximum-to-average power density ratio. However, since the fuel is a metal foil, a smooth radial grading cannot be achieved and the fuel has sharp edges. The IFE and OFE fuel radial distributions are given in Figures 2.3.1 and 2.3.2, respectively. The HEU fuel distribution is also included on these figures for the comparison. The main conclusion of the ORNL reactor physics analyses is that the HFIR LEU core could maintain the current level of performance if it is operated at 100MW. However, to operate at the same safety limits as the HEU core, the thermal hydraulic analyses show that the peaking of the power distribution occurring at the bottom of the active zone of the fuel plates has to be reduced.

The ORNL reference LEU design solves the power peaking problem by reducing the fuel foil thickness at the bottom of the plate. This requires adding an axial grading to the already radially-graded fuel. As for the HEU plates, the length of the fuel zone is 50.8cm. From the top to 3cm above the bottom, the fuel is only radially graded. In addition to the radial grading, the fuel thickness is then smoothly axially reduced from 3cm above the bottom to 1cm above the bottom in such a way that the last centimeter of fuel is neither radially nor axially graded but flat with a very thin thickness (0.0075cm). A three-dimensional (3D) view of the shape of the bottom of the IFE fuel foil is provided in Figure 2.3.3. Cross-sections of the IFE plate before and after the axial grading are shown in Figures 2.3.4 and 2.3.5. The corresponding figures for the OFE plates are provided in Figures 2.3.6, 2.3.7 and 2.3.8. A summary of the characteristics of the HEU and LEU core is provided in Table 2.3.4.

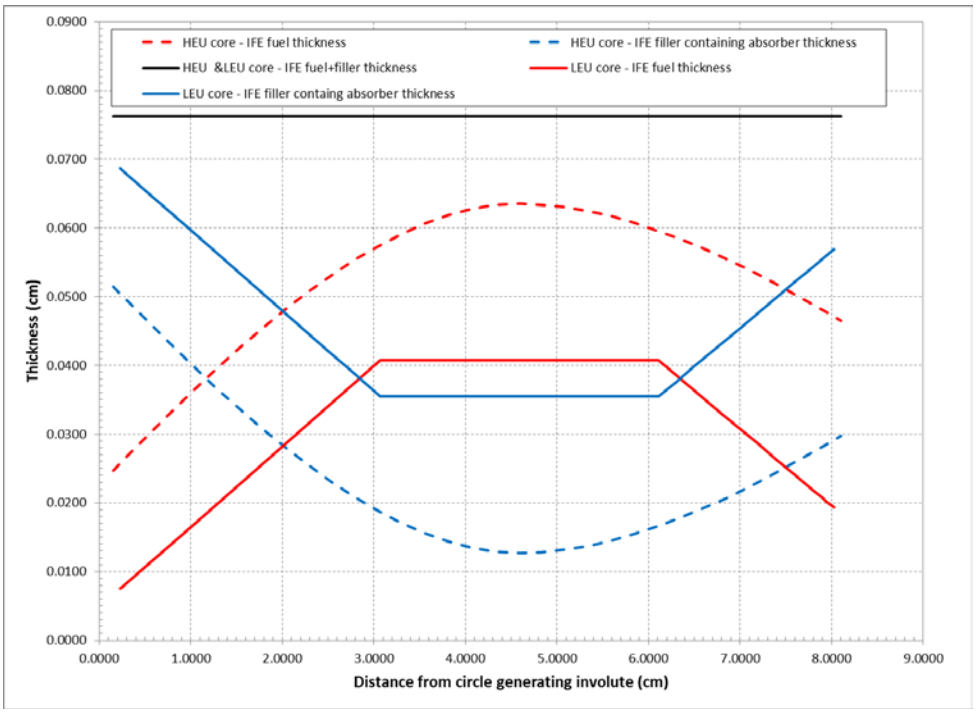

Figure 2.3.1 - Thickness of the fuel and filler along the fuel plate width in reference LEU IFE (solid lines). The HEU IFE fuel and filler distribution are recalled (dash line).

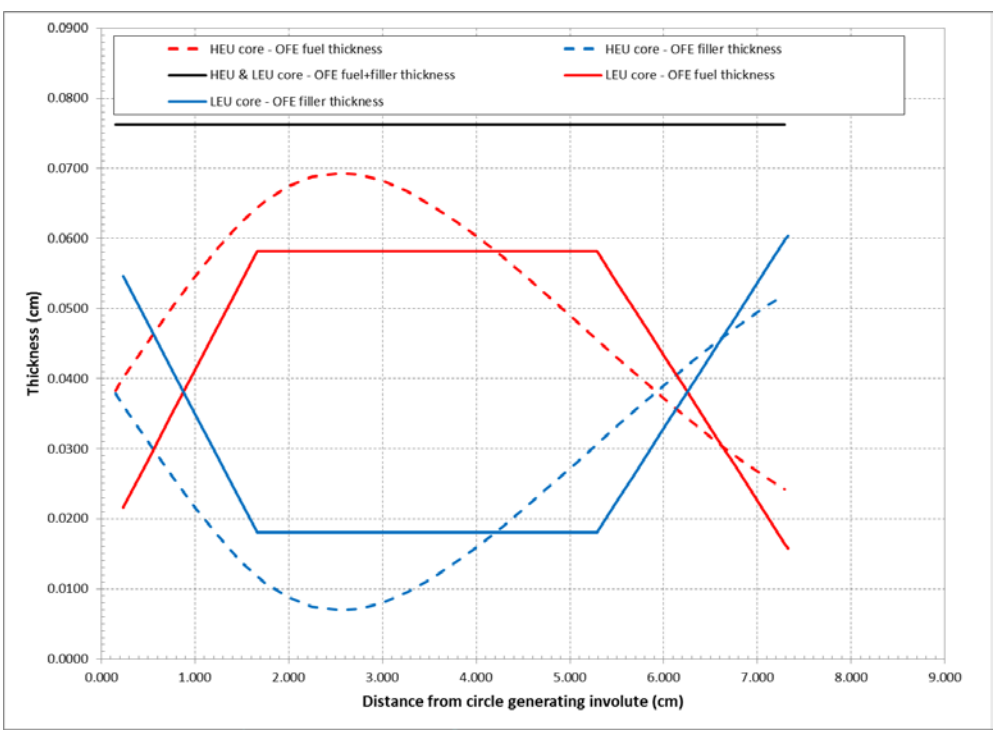

Figure 2.3.2 - Thickness of the fuel and filler along the fuel plate width in reference LEU OFE (solid lines). The HEU OFE fuel and filler distribution are recalled (dash line).

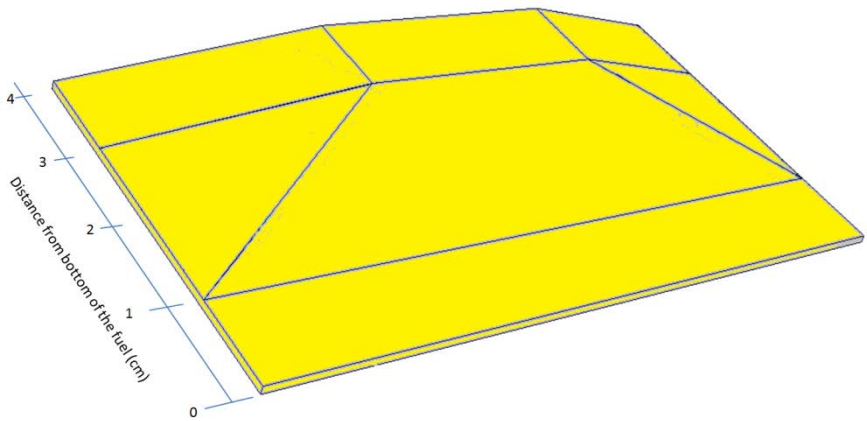

Figure 2.3.3 – Three-dimensional view of the LEU IFE fuel foil thickness at fuel plate bottom (last 4cm) before bending. View from the inner edge.

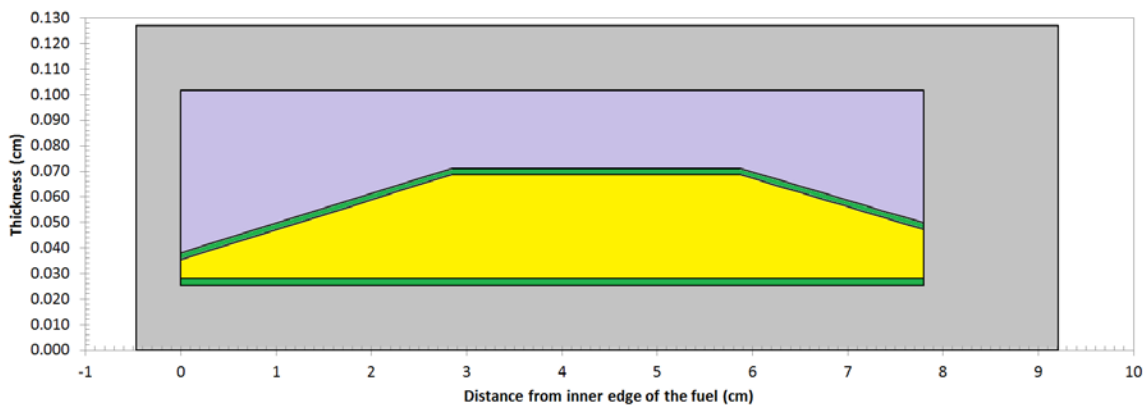

Figure 2.3.4 –Illustration of the LEU IFE plate cross section at elevations above 3cm from the bottom of the fuel. The cladding appears in gray, the zirconium layers in green, the fuel in yellow and the filler containing the burnable absorber is lavender.

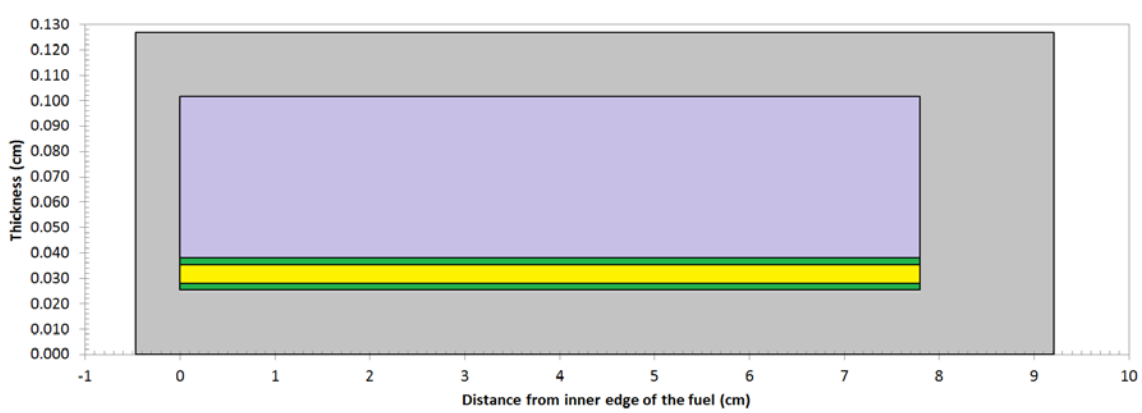

Figure 2.3.5 – Illustration of the LEU IFE plate cross section at elevations between the bottom to +1cm above the bottom of the fuel. The cladding appears in gray, the zirconium layers in green, the fuel in yellow and the filler containing the burnable absorber is lavender.

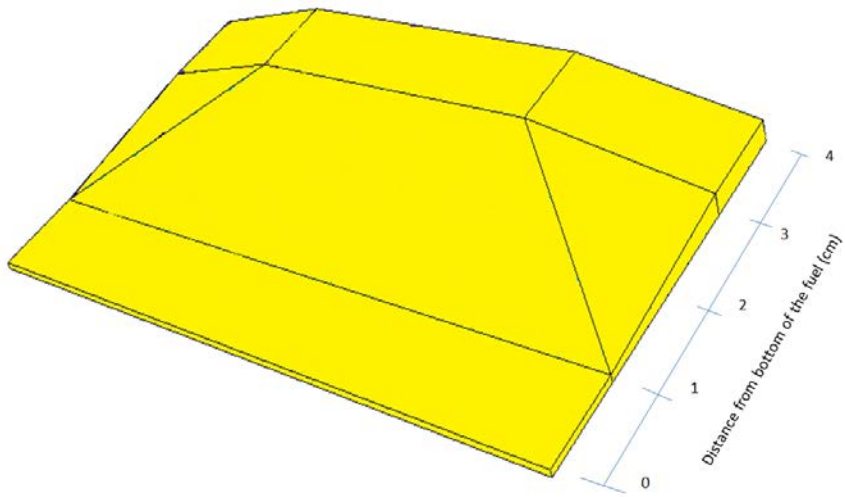

Figure 2.3.6 – Three-dimensioanal view of the LEU OFE fuel foil bottom (last 4cm) before bending. View from the inner edge.

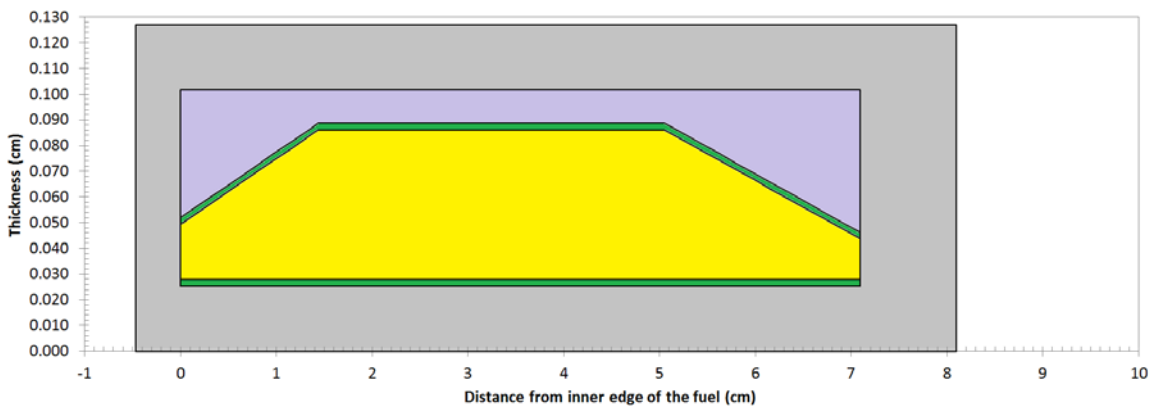

Figure 2.3.7 – Illustration of the LEU OFE plate cross section at elevations above 3cm above the bottom of the fuel. The cladding appears in gray, the zirconium layers in green, the fuel in yellow and the filler containing the burnable absorber is lavender.

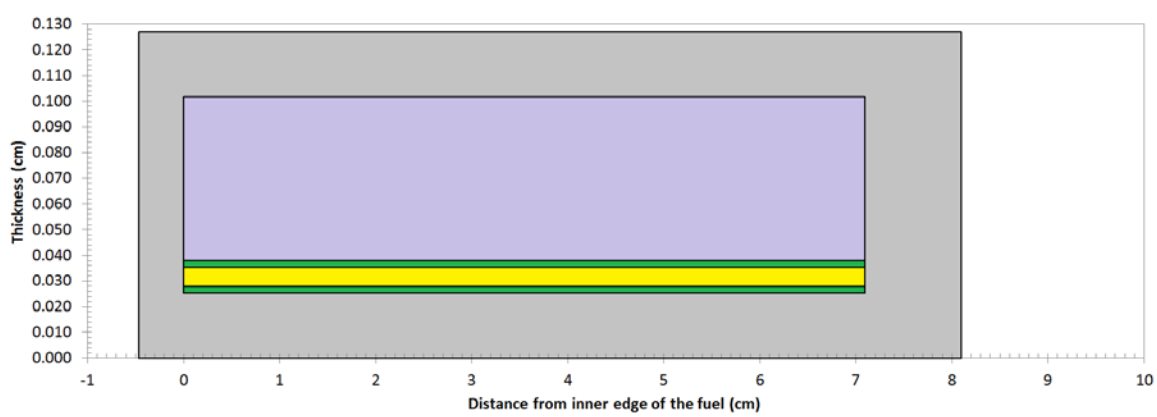

Figure 2.3.8 – Illustration of the LEU OFE plate cross section at elevations between the bottom to +1cm above the bottom of the fuel. The cladding appears in gray, the zirconium layers in green, the fuel in yellow and the filler is lavender.

Table 2.3.1 – ANL reference composition of the LEU IFE & OFE fuel [Ref. 4]

isotope	density (g/cc)	molar mass (g/mol)	atomic density (at/barn.cm)
^{234}U	2.5275E-02	2.3404E+02	6.5033E-05
^{235}U	3.0253E+00	2.3504E+02	7.7511E-03
^{236}U	1.3924E-01	2.3605E+02	3.5523E-04
^{238}U	1.2128E+01	2.3805E+02	3.0681E-02
^{92}Mo	2.4080E-01	9.1907E+01	1.5778E-03
^{94}Mo	1.5380E-01	9.3905E+01	9.8630E-04
^{95}Mo	2.6770E-01	9.4906E+01	1.6986E-03
^{96}Mo	2.8380E-01	9.5905E+01	1.7820E-03
^{97}Mo	1.6440E-01	9.6906E+01	1.0216E-03
^{98}Mo	4.2020E-01	9.7905E+01	2.5846E-03
^{100}Mo	1.7140E-01	9.9907E+01	1.0331E-03
total =	1.7020E+01	-	4.9536E-02

Table 2.3.2 – ANL reference composition of the LEU IFE filler containing the burnable absorber [Ref. 4]

isotope	density (g/cc)	molar mass (g/mol)	atomic density (at/barn.cm)
^{10}B	1.9957E-03	1.0013E+01	1.2003E-04
^{11}B	8.8322E-03	1.1009E+01	4.8312E-04
^{12}C	3.0047E-03	1.2000E+01	1.5078E-04
^{27}Al	2.6574E+00	2.6982E+01	5.9311E-02
^{54}Fe	3.9106E-04	5.3940E+01	4.3659E-06
^{56}Fe	6.1386E-03	5.5935E+01	6.6089E-05
^{57}Fe	1.4177E-04	5.6935E+01	1.4995E-06
^{58}Fe	1.8867E-05	5.7933E+01	1.9612E-07
^{28}Si	6.1701E-03	2.7977E+01	1.3281E-04
^{29}Si	3.1345E-04	2.8976E+01	6.5141E-06
^{30}Si	2.0687E-04	2.9974E+01	4.1562E-06
^{63}Cu	3.2385E-03	6.2930E+01	3.0991E-05
^{65}Cu	1.4448E-03	6.4928E+01	1.3401E-05
^{55}Mn	6.6902E-04	5.4938E+01	7.3335E-06
total =	2.6900E+00	-	6.0333E-02

Table 2.3.3 – ANL reference composition of the LEU zirconium layer [Ref. 4]

isotope	density (g/cc)	molar mass (g/mol)	atomic density (at/barn.cm)
^{90}Zr	3.2908E+00	8.9905E+01	2.2043E-02
^{91}Zr	7.2564E-01	9.0906E+01	4.8070E-03
^{92}Zr	1.1213E+00	9.1905E+01	7.3475E-03
^{94}Zr	1.1611E+00	9.3906E+01	7.4461E-03
^{96}Zr	1.9105E-01	9.5908E+01	1.1996E-03
total =	6.4900E+00	-	4.2843E-02

Table 2.3.4 – Summary of HEU and LEU core characteristics

core parameters	HEU		LEU	
Reactor Power, MW	85		100	
Plate length, cm	60.96		60.96	
Number of fuel elements	2		2	
Cladding type	Al-6061		Al-6061	
Fuel type	U_3O_8 - Al		UMo (10 wt. % Mo)	
Fuel form	mixed powder		"monolithic" foil	
Total ^{235}U loading, kg	9.400		25.27	
Total uranium loading, kg	10.11		127.95	
^{235}U enrichment (wt. %)	93.10		19.75	
fuel element parameters	**HEU**		**LEU**	
	IFE	**OFE**	**IFE**	**OFE**
Number of fuel plates	171	369	171	369
^{235}U loading, g	2,600	6,800	6,400	18,880
uranium loading, g	2,793	7,304	32,405	95,595
^{235}U mass per plate, g	15.20	18.43	37.43	51.22
uranium mass per plate, g	16.33	19.80	189.5	259.3
Fuel volume in one plate, cm^3	21.02	18.77	12.35	16.92
^{235}U density, g/cm^3	0.723	0.982	3.025	3.025
Uranium density, gU/cm^3	0.778	1.056	15.32	15.32
Fuel density, g/cm^3	3.310	3.762	17.02	17.02
^{10}B mass in element, g	2.800	None	5.400	None
burnable filler volume per plate, cm^3	9.175	None	15.85	None
^{10}B mass per plate, g	0.016	None	0.032	None
^{10}B density in burnable filler, mg/cm^3	1.785	None	1.992	None
Radius of circle generating involute, cm	6.9126	14.9170	6.9126	14.9170
Plate thickness, cm	0.1270	0.1270	0.1270	0.1270
Coolant channel thickness, cm	0.1270	0.1270	0.1270	0.1270
cladding thickness, cm	0.0254	0.0254	0.0254	0.0254
Fuel plate width, cm	8.1000	7.3000	8.1000	7.3000
Fuel height, cm	50.800	50.800	50.800	50.800
fuel width, cm	7.7900	7.0200	7.7960	7.0890
maximum fuel thickness, cm	0.0635	0.0693	0.0407	0.0582
minimum fuel thickness, cm	0.0247	0.0242	0.0075	0.0075

2.4 Experiment Facilities and Matrix of Performance

This section describes the different experiment facilities located in HFIR. They can be divided in four categories: Neutron Activation Analyses (NAA), Gamma Irradiation (GI), Neutron Scattering Experiment (NSE) and In-core Irradiation Facilities (IIF). A top view of the in-core experiment facilities is presented in Figure 2.4.1. The contribution of each of these experiment categories to the matrix of performance, summarized in Table 2.4.1, is also discussed.

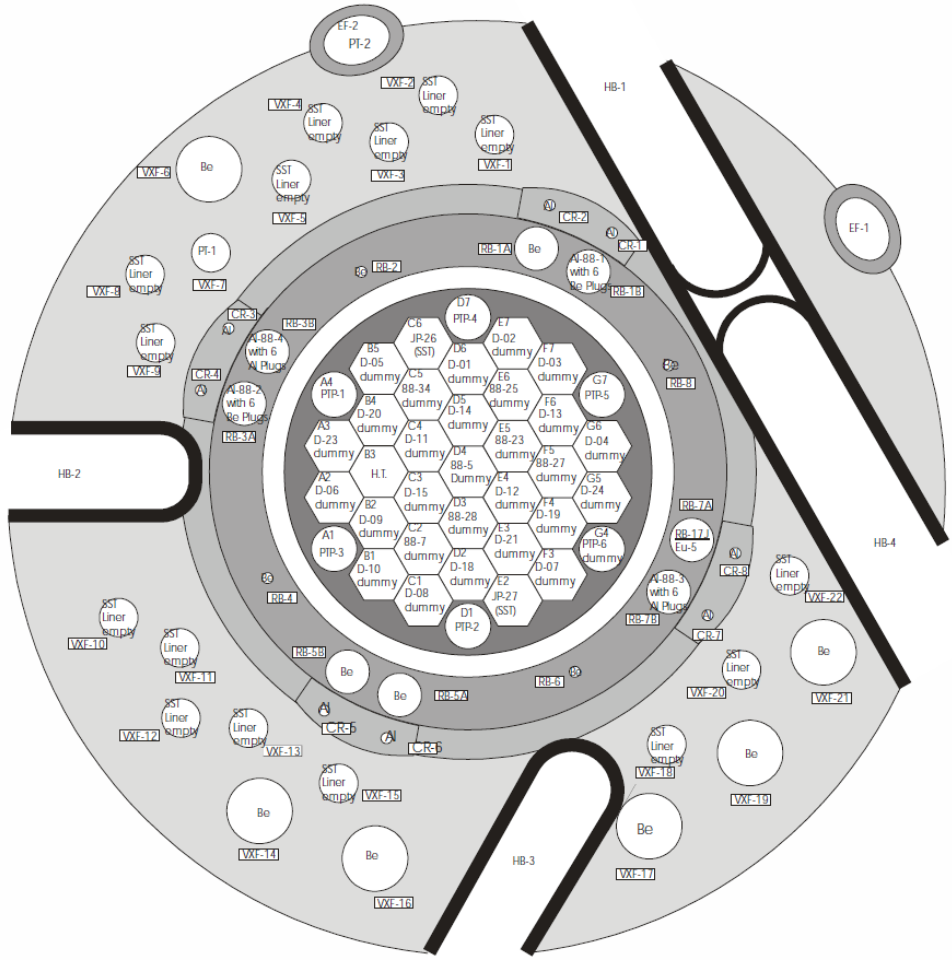

Figure 2.4.1 – Top view of the in-core experiment facilities of HFIR. The size of the flux trap (represented by the hexagonal lattice surrounded by a dark gray disk at the center of the figure) is exaggerated. The fuel and control elements are not visible on this figure [Ref. 3].

2.4.1 Neutron Activation Analysis (NAA)

The NAA consists of bombarding a sample with neutrons and the radioisotopes produced are analyzed to determine the sample composition. The NAA facilities at HFIR have a wide range of application, from nuclear non-proliferation to geology or even forensics. Two reactor-based NAA facilities (EF-1 and EF-2) are located at the outer periphery of the permanent reflector in the so-called slant engineering facilities (visible on Figure 2.4.1). Because material activation generally does not require an important neutron flux and a long time of irradiation, the performance of the NAA will not be affected by the conversion to LEU fuel. Consequently, NAA is not included in the scope of the study.

2.4.2 Gamma Irradiation (GI)

Materials can be irradiated from gamma radiations that come from the HFIR spent fuels. Located in a dedicated pool, the gamma irradiation chamber can accommodate samples up to 64cm-long and 8.26cm-diameter. Because the chamber is not located in the core and is not covered by the ORNL calculations, GI is not part of the matrix of performance.

2.4.3 Neutron Scattering Experiment (NSE)

Because they are electrically neutral and have a wavelength similar to the spacing between atoms, neutrons scattered in matter are very well fitted to understanding material properties at the atomic scale. HFIR has four horizontal beam tubes (HB-1 to HB-4) which supply neutrons to several neutron scattering instruments. Except for HB-4, all of them are thermal neutron beam tubes. A cold source (small vessel containing supercritical hydrogen at 17K) is located in the head of HB-4 to slow down the incoming thermal neutrons to produce a beam of cold neutrons (wavelength of 0.4 to 1.2nm). The four beam tubes are visible on Figure 2.4.1. A total of 11 instruments are associated with the 4 beam tubes (2 with HB-1, 3 with HB-2, 2 with HB-3 and 4 with HB-4). The magnitude of the thermal flux is considered the relevant parameter for the performance of the NSE. Because the magnitude of the thermal flux evolves during the cycle, an average value between Beginning of Cycle (BOC) and End of Cycle (EOC) is used.

2.4.4 In-core Irradiation Facilities (IIF)

A significant number of in-core irradiation facilities are present in HFIR, located from the flux trap to the permanent beryllium reflector. Thirty-one target positions + 6 peripherals are provided in the flux trap. This is in the flux trap that the flux is the strongest (~1-3x10^{15}n/cm^2/s). Except for the hydraulic tube (position B3 in Figure 2.4.1), the flux trap rods have been designed for transplutonium isotope production. The active length of the rods is identical to the length of the fuel (50.8cm) and their diameter is 0.635cm. The hydraulic tube is dedicated to production of short half-life medical isotopes that need to be irradiated for a shorter time than the normal cycle length. The system consists of capsules (called rabbits) that can shuffle between the core and the loading station. The typical size of the sample is 5.56cm-long and 0.648cm-diameter.

A total of 36 irradiation positions are located in the different regions of the reflector. They are distributed as follow:

- Eight large (4.6cm-diameter) and four small (1.27cm-diameter) irradiation positions, called large and small removable beryllium reflector facilities, respectively, are located in the removable beryllium reflector. They are noted as RB-1A to RB8 on Figure 2.4.1.
- Eight 1.27cm-diameter positions are present in the semi-permanent reflector and are called the control rod access plug facilities (noted as CR-1 to CR-8 on Figure 2.4.1).
- Finally, sixteen small (4.02cm-diameter) and six large (7.20cm-diameter) positions are located in the permanent reflector. They are called the small and large vertical experiment facilities (VXF-1 to 22 on Figure 2.4.1).

The production rate of a given isotope depends not only on the magnitude of the flux but also on the time of exposure to the flux. For all the irradiation facilities, the neutron fluence (neutron flux integrated over the time of irradiation) is then the relevant parameter. Due to the

symmetry of the radial distribution of the neutron flux, there is no need to evaluate the performance of each position individually. Instead, facilities can be grouped by their relative distance from the core center. Thus, the fluence will be evaluated in only 11 locations (later called rings). Each of them will tally the fluence of all irradiation positions located at a constant distance from the center of the core. Each type of target has its own optimum neutron energy. It is then preferable to look at the fluence at different energy levels: thermal, epithermal and fast. The list of the different irradiation positions and their associated rings is given in Table 2.4.1.

Table 2.4.1 – Summary of the matrix of performance considered for the review

Neutron activation	Distance from core center, cm	Metric of performance
EF-1 & 2	55	non-evaluated
Gamma Irradiation	**Distance from core center, cm**	**Metric of performance**
chambers	out of pile	non-evaluated
Neutron scattering	**Distance from core center, cm**	**Metric of performance**
HB-1	35	average thermal flux
HB-2	35	average thermal flux
HB-3	35	average thermal flux
HB-4	35	average thermal flux

In core Irradiation Ring	Position	Distance from core center, cm	Metric of performance
0	D4	0	thermal, epithermal, fast fluence
1	C4, D5, E5, E4, D3, C3	1.5	thermal, epithermal, fast fluence
2	C5, D6, E6, F6, F5, F4, E3, D2, C2, B2, B3, B4	3	thermal, epithermal, fast fluence
3	B5, C6, E7, F7, G6, G5, F3, E2, C1, B1, A2, A3	4.5	thermal, epithermal, fast fluence
4	A1, A4, D7, G7, G4, D1	5.5	thermal, epithermal, fast fluence
5	RB-2, 4, 6, 8	26.3	thermal, epithermal, fast fluence
6	RB-1A, 1B, 3A, 3B, 5A, 5B, 7A, 7B	27.2	thermal, epithermal, fast fluence
7	CR-1, 2, 3, 4, 5, 6, 7, 8	32	thermal, epithermal, fast fluence
8	VXF-1, 3, 5, 7, 9, 11, 13, 15, 18, 20, 22	38.6	thermal, epithermal, fast fluence
9	VXF-2, 4, 8, 10, 12	44.2	thermal, epithermal, fast fluence
10	VXF-6, 14, 16, 17, 19, 21	45.1	thermal, epithermal, fast fluence

3 Computational Methods

The ORNL reactor physics calculations cover the evaluation of the matrix of performance and several other important parameters. This type of calculation requires a detailed model of the whole reactor. The tools described below have been selected at ANL to perform the review. They are mostly identical to the ones used by ORNL. The typical computational scheme used at ANL is summarized in Figure 3.1.

3.1 Steady Sate Calculations – MCNP

The Monte Carlo N Particles (MCNP) computer code has been selected to perform the steady state calculations. This software package was developed by Los Alamos National Laboratory (LANL) [Ref. 6]. It is used primarily for the simulation of nuclear processes and particle interactions such as neutrons, photons and electrons. Its range of application is very large and covers, among other things, medical physics, fission and fusion reactor design, criticality and radiation protection. The MCNP code has a large base of users worldwide and has often been benchmarked against experiments. Its ability to model complex geometries in three-dimensions (3D) and calculate a wide variety of parameters (eigenvalues, neutron flux, spectrum…) make the code an excellent tool for the study of complex systems such as HFIR. However, MCNP is not able to model explicitly the involute shape. In late 2010, ANL developed a methodology to model an approximation of the involute almost as accurately as desired (see Section 3.5, Appendix B or [Ref. 17]). Except where indicated otherwise, Version 1.51 of MCNP has been used for the review.

3.2 Depletion Calculations - ORIGEN

ORIGEN is a versatile tool that has been designed for calculating the buildup, decay and processing of radioactive materials [Ref. 7]. It has been developed by ORNL. ORIGEN uses the matrix exponential method to solve a large system of coupled, linear differential equations. ORIGEN v2.2 has been used as the depletion module for the HFIR analyses but it has not been used directly. It has been coupled with MCNP5 via the code VESTA (see Section 3.3).

3.3 Monte-Carlo-Depletion - VESTA

To study the evolution of a complex reactor like HFIR requires having a detailed time-discretization of the cycle and, consequently, performing multi-step depletion calculations. In order to reduce the calculational time and the risk of error, a so-called Monte-Carlo Depletion code has been used to couple the steady state calculation (performed by MCNP) with the depletion module (performed by ORIGEN). Among the codes available (MCODE, MONTEBURNS…), the code VESTA, developed by the Institut de Radioprotection et de Sûreté Nucléaire (IRSN) has been selected mainly because it uses the Multigroup Binning Approach (MBA) [Ref. 18]. It has been shown that for coupled core-evolution calculations, a significant part of the computational time is due to the calculation of the reaction rates performed during the steady state calculation. The MBA method does not require the calculation of the reaction rates directly from the steady state calculation but only the calculation of the flux in a very fine-group structure which is far less time consuming. Pre-generated point-wise cross-sections are then weighted with the fine-group flux and collapsed in order to generate one group cross-sections. These cross-sections can then be used by the depletion module (ORIGEN).

3.4 Nuclear Library

The nuclear library used is ENDF/B7. The point-wise pre-generated cross-sections (43,000 groups) used by VESTA are also based on this library. ORIGEN uses its own fission yield and decay library. The one group cross-sections used by ORIGEN are obtained from the VESTA calculation.

3.5 Critical Search

Due to fission product buildup and fuel consumption, the reactivity of the core decreases over the time of irradiation. To maintain the reactor critical, control elements are gradually withdrawn in order to reduce their worth on the core reactivity. Once the control elements have reached their limit position (fully withdrawn), the cycle is over because criticality cannot be achieved any longer. Thus, calculation of the critical control element positions during the cycle can be used to estimate the cycle length of the core. ANL used a simple but robust method to calculate the critical position of the control elements. The problem that a critical search algorithm has to solve is to predict by how much the control elements have to be moved to achieve criticality. The ANL methodology is based on the evaluation of a very simple parameter which is the average worth of the control elements. It is calculated between two extreme points: control elements fully inserted and fully withdrawn. The variation of reactivity obtained between them is then divided by the distance between these two points. This calculation gives an average reactivity worth per unit distance. If, at the end of the steady state calculation, criticality is not achieved, the missing or excess reactivity is calculated and divided by the average worth of the control elements which provides a guess for the critical position. The process is repeated until criticality (plus or minus the uncertainties of the steady state calculation) is achieved. This method is simple, works with different systems, and can certainly be improved but has been judged efficient enough for the type of calculations carried out for this review.

3.6 Generating MCNP Cards for Discrete Involute Modeling

As stated in Section 3.1, despite the fact that MCNP can handle complex geometries, it cannot model the involute shape. Many possibilities exist to get around this difficulty: One can homogenize the fuel element (as ORNL does to model HFIR) or approximate the shape by using another geometric shape (cylinders were previously used to model the French High Flux Reactor, RHF). However, an approximate modeling of the fuel elements will always introduce a systemic bias on the physics of the model which needs to be assessed (via benchmarking for instance). In order to reduce the geometric bias to the lowest level possible, ANL has developed a methodology based on discretization of the involute [Ref. 17]. Once “sliced” in several parts, the pieces of the involute plate can be modeled by simple geometric objects such as polyhedrons. The magnitude of the geometric bias is thus directly correlated to the degree of discretization: The finer the discretization, the lower the bias. The details of the methodology are given in Appendix B.

Cell, geometric and data cards used in the MCNP inputs to model the discrete involute are generated externally, and at this date, in a simple spreadsheet. A more sophisticated tool aimed at generating these cards automatically will probably be designed in the near future.

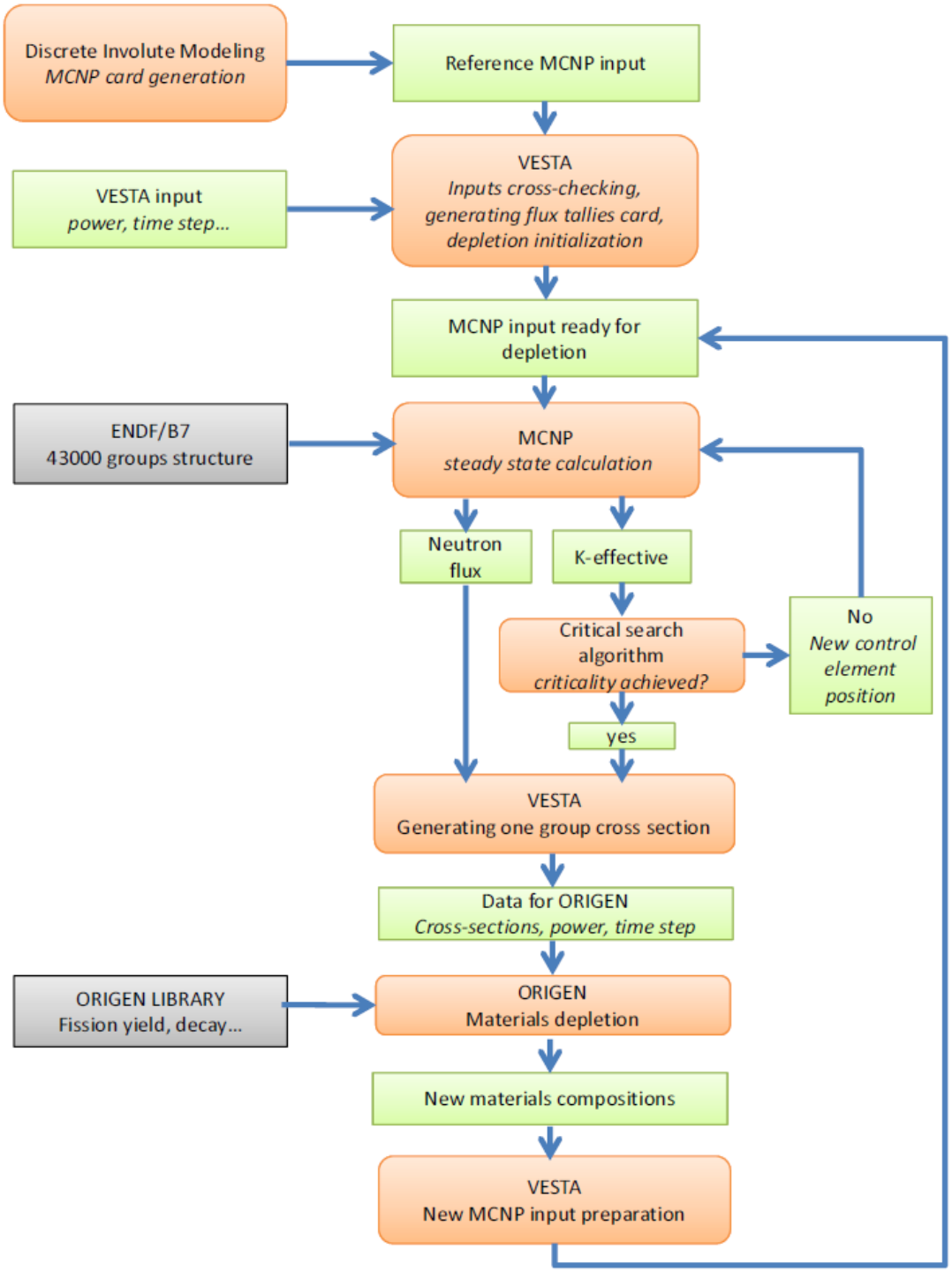

Figure 3.1 – Typical calculational scheme used for the review.

4 Review of the ORNL RRD Neutronic Calculations

4.1 Scope of the Study

The ORNL Research Reactor Division (RRD) has produced two series of calculations in the context of their activities supporting the conversion of HFIR from the use of HEU fuel to LEU fuel. The calculations have been carried out considering a reference LEU design of the core. One series is focused on the neutronic calculations whereas the other is focused on thermal-hydraulic calculations. Both are obviously complementary and the results obtained with the two series of calculations have been compiled in the Technical Memorandum report, ORNL/TM-2010/318 [Ref. 4]. HFIR is currently operating with a HEU core at 85MW thermal. The main conclusion of the ORNL work is that the proposed 100MW thermal LEU core should maintain the current performance and operate within the same safety limits. As defined by ORNL during FY2011, the request to ANL is to review the two series of RDD calculations. The present report covers the neutronic part only. The RRD neutronic calculations contain:

- Two reference MCNP models of HFIR (HEU and LEU core).
- Supporting documentation which includes a brief description of the MCNP inputs, justification of assumptions, types of calculations and methodologies [Ref. 16].
- All the calculation input and output files.

The ORNL calculations cover the evaluation of the matrix of performance (cycle length and flux), the distribution of power in the fuel elements, the kinetics parameters and the reactivity coefficients. Since the main conclusion of the ORNL work is that the LEU core would need to operate at 100MW to reach the performance of the HEU core at 85MW, the review has been mainly focused on establishing a comparison between the two cores.

In late 2010, a new methodology was developed at ANL to model with reasonable precision the geometry of the involute shape with the code MCNP [Ref. 17]. This methodology has been re-applied for the review to model the HFIR cores explicitly, and thus replace the classic homogeneous description of the fuel elements. These explicit models are believed to capture more accurately the physics of HFIR and its behavior. A description, step by step, of the production process of these discrete fuel elements models is given in Appendix B. All of the ORNL calculations have been repeated using the new explicit models. Nonetheless, since the base of the work is the ORNL MCNP models, it has been considered important to cross check the ORNL inputs. Thus, as a preliminary step to the review, the results of this input cross checking are compiled. For the HEU core, all the ORNL calculations have been carried out at 85MW whereas for the LEU core the power was set at 100MW. The scope of the review is not intended to go beyond the scope of the RRD calculation. This means that, for the review, the HEU and LEU cores are studied at the same power levels as considered by ORNL.

4.2 Review of the ORNL MCNP Inputs, Methodologies and Assumptions

This section presents the results of the MCNP input cross-checking. The MCNP input for HFIR describes the reactor in six different regions:

- Region I: Central Target or Flux Trap Target (FTT).
- Region II: Inner Fuel Element (IFE).
- Region III: Outer Fuel Element (OFE).
- Region IV: Inner Control Element (ICE) and Outer Control Element (OCE).
- Region V: Irradiation Facilities and Removable Beryllium Reflector (RB).
- Region VI: Beam tubes, Concrete Wall and Permanent Beryllium Reflector (PB).

Two MCNP inputs were provided by ORNL for the review. One, called *HFV4.0*, is a model of HFIR with a HEU core in the condition at the Beginning of Cycle (BOC) 400. The other one, called *leu2011*, is based on the *HFV4.0* model but it is a LEU core. Additional differences, listed in Table 4.2.1, exist between the two models. These differences have a significant effect on the core reactivity and prevent their use for direct comparison of the HEU and LEU cores.

Table 4.2.1 – Differences between the two MCNP inputs provided by ORNL for the review

	HFV4.0	*leu2011*
FTT composition	dummy targets	curium targets
ICE & OCE materials	fresh	depleted
RB experiment facilities	beryllium plugs	dummy targets

The reactor is cooled by light water. In the MCNP input, three conditions of pressure and temperature are considered as a reference by ORNL [Ref.15], depending upon whether the coolant is above, in or below the core. These conditions are summarized in Table 4.2.2 below. These conditions have been systematically checked in each region.

Table 4.2.2 – Conditions of pressure and temperature of the light water considered in *HFV4.0* and *leu2011* MCNP inputs. The coolant density is deduced from the NIST database [Ref. 19]

coolant location	pressure (Mpa)	temperature (K)	coolant density (g/cc)
above the core	3.930	322.15	0.98989
in the core	2.951	332.15	0.98495
below the core	2.572	342.15	0.97942

The following sub-sections will describe the input region by region and the different inconsistencies (if any) revealed by the cross-checking. The effect on the reactor physics of these inconsistencies is not discussed in this section but is discussed later when the preparation of the reference inputs is described (Section 4.3.1.2).

4.2.1 Region I – Central target (FTT)

The basket of the FTT region has 37 experimental sites. The basket has been designed for rods containing target materials (plutonium, curium…) for producing transplutonium isotopes. When production targets are not available, the experimental locations are occupied by aluminum rods called dummy targets. The rods are cooled down and moderated by light water flowing downward from above the core. The basket and its 37 experimental sites are explicitly modeled in the MCNP inputs. Figure 4.2.1.1 shows a top view of the *HFV4.0* and *leu2011* FTT. In *HFV4.0*, the FTT contains no production targets but dummy targets whereas in *leu2011*, the basket is filled out with curium targets.

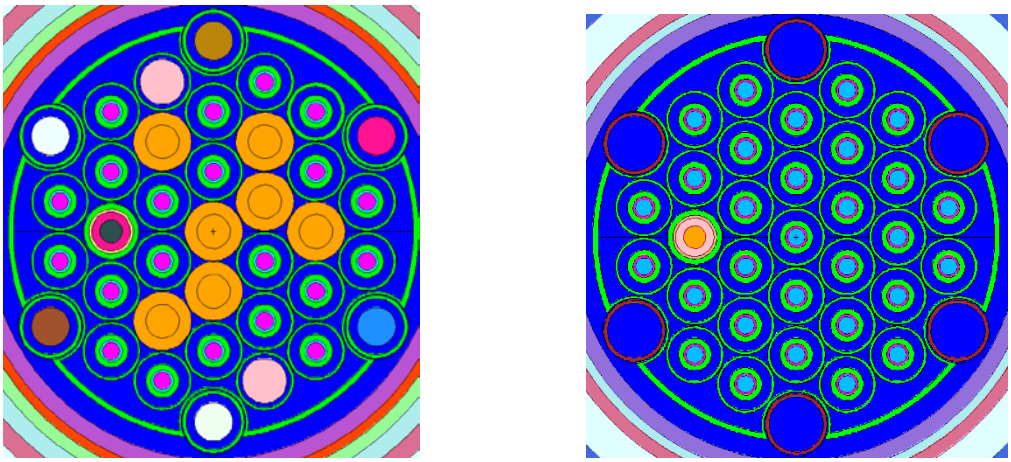

Figure 4.2.1.1 – MCNP screenshots of the FTT. The pictures on the left and right show a top view of the FTT as it is in *HFV4.0* and *leu2011*, respectively. On the pictures, the basket appears in green and the light water appears in blue.

Several inconsistencies have been detected in the material compositions of this region in both inputs. They are described below.

- Three materials are used to model the light water above, in and below the FTT (Materials m1, m2, m3, respectively). The conditions of pressure and temperature of the coolant are provided in Table 4.2.1. As a result, it appears that the densities used in MCNP are systematically 0.76% higher than what they should be.
- In the supporting documentation [Ref. 16], it is said that the curium target composition used in *leu2011* is given in Table C.1 of [Ref. 20] and also in Table A.3 of [Ref. 4]. However the isotope, ^{250}Cm, is present in *leu2011* but not in the aforementioned tables.
- In *HFV4.0*, there is a mismatch between the non-normalized material fraction in the data cards and the material density in the cell cards. The problematic materials are listed in Table 4.2.1.1.

Table 4.2.1.1 – List of materials present in *HFV4.0* Region I with an ambiguous density

material	Non-normalized density fraction in data card	material density in cell card (at/barn.cm)	variation data/cell card
m512	6.0324E-02	4.8210E-02	20.08%
m711	6.0324E-02	5.9374E-02	1.57%
m722	5.4866E-02	6.0000E-02	-9.36%
m723	6.0324E-02	5.9374E-02	1.57%
m726	6.0324E-02	5.9374E-02	1.57%
m732	5.4381E-02	6.0000E-02	-10.33%
m733	6.0324E-02	5.9374E-02	1.57%
m736	6.0324E-02	5.9374E-02	1.57%
m742	5.4201E-02	6.0000E-02	-10.70%
m743	6.0324E-02	5.9374E-02	1.57%
m746	6.0324E-02	5.9374E-02	1.57%
m751	6.0324E-02	5.9374E-02	1.57%
m752	5.4576E-02	6.0000E-02	-9.94%
m753	4.7497E-02	6.0000E-02	-26.32%
m756	6.0324E-02	5.9374E-02	1.57%
m766	6.0324E-02	5.9374E-02	1.57%
m767	4.7497E-02	6.0242E-02	-26.83%

4.2.2 Region II – Inner Fuel Element (IFE)

The IFE consists of 171 involute-shaped fuel plates. In both the HEU and proposed LEU core, the inner fuel plates contain ^{10}B as a burnable absorber. The ORNL MCNP inputs do not model explicitly the plates. Instead, the fuel elements are modeled by homogenizing the fuel, cladding, boron and water between the plates. To take into account the radial (and axial, if any) grading of the fuel, the homogenized fuel elements are subdivided in radial/axial regions in which the composition of the homogenized fuel changes.

A top view of the *HFV4.0* and *leu2011* IFE is given in Figure 4.2.2.1. In both *HFV4.0* and *leu2011,* the IFE is divided into 8 radial regions. However the radial mesh size, given in Table 4.2.2.1, is different between the two models. The fuel is axially divided into 7 regions in *HFV4.0* whereas it is divided into 19 regions in *leu2011*. The details of the axial divisions for both inputs is provided in Table 4.2.2.2

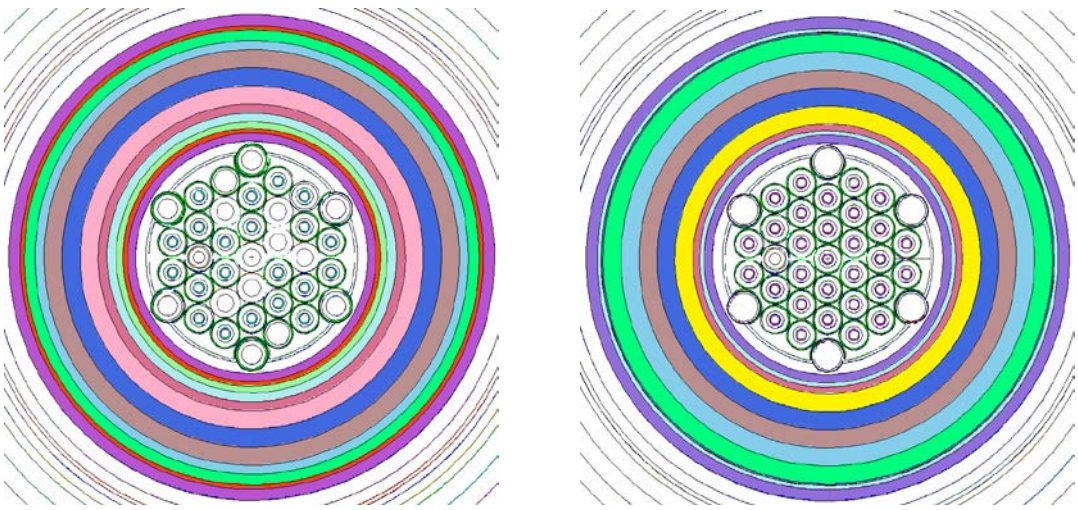

Figure 4.2.2.1 – MCNP screenshots of the IFE. The pictures on the left and right show a top view of the IFE as it is in *HFV4.0* and *leu2011*, respectively. The different colored rings represent the different fuel plate radial regions.

The composition of the homogenized materials has been checked. Some of them are identical in *leu2011* and *HFV4.0*. They represent the homogenization of the unfueled part of the plate (cladding) and the coolant. They will be later called coolant-clad materials. The few inconsistencies that have been detected in in both inputs for this region are described below.

- Three materials are used to model the coolant-clad materials whether they are above, at the same level or below the fuel (Materials m70, m200, m71). The conditions of pressure and temperature of the coolant are given in Table 4.2.2. In both inputs, the oxygen and hydrogen densities used in MCNP are, respectively, 0.76% and 1.28% which are higher than expected. The fact that the hydrogen difference is higher than the oxygen is explained by the fact that additional hydrogen has been introduced as a cladding impurity. It is not recommended since the light water thermal scattering S(α,β) depends on the hydrogen amount. Consequently, this excess of hydrogen creates an inconsistency with the S(α,β).

- In *HFV4.0*, the fuel and boron density distributions have been compared to the ones that can be extracted from the technical drawing of the inner fuel element [Ref. 21]. Variations in fuel and boron distribution are given in Tables 4.2.2.3 and 4.2.2.4 respectively. As one can see, variations are relatively small and do not exceed a few percent.
- In *leu2011*, the fuel and boron distributions in the IFE have been compared to the ones that can be extracted from the information on the reference LEU design provided in [Ref. 4]. Due to the axial grading of the fuel, 4 different regions are considered: The first one goes from the top of the fuel to 3cm above the bottom of the fuel (radial grading only). The second and third ones go from 3cm above the bottom of the fuel to 1cm above the bottom of the fuel. This is the region where the fuel is both axially and radially graded. This 2cm long region is split in two equally spaced parts. The last region goes from 1cm above the bottom of the fuel to the bottom of the fuel (no radial or axial grading). Variations in the ^{235}U distribution between the ANL calculations and *leu2011* for these 4 axial regions are given in Table 4.2.2.5. As one can see, the variations are very small (<0.2%) for most of the fuel materials with the notable exception of the materials in the Radial Layers 4 and 5 where the fuel is graded axially and radially (from +3 to +1cm above the bottom of the fuel). The origin of these discrepancies is not understood. Variations in the ^{10}B distribution between the ANL calculations and *leu2011* for the 4 axial regions are presented in Table 4.2.2.6. As previously, the variations are very small (<0.3%) for most of the materials but significant discrepancies are sometimes observed (-7 to +26%). The origin of these discrepancies is not understood.
- In *leu2011*, the cladding composition used for the homogenization of the fuel and coolant is different than the one used for the coolant-clad materials. However, the composition used for the coolant-clad materials in *leu2011* is the same than as used in *HFV4.0*. If it has been judged necessary to change the cladding composition from *HFV4.0* to *leu2011,* it has not been propagated everywhere.

Table 4.2.2.1 – IFE radial mesh in the MCNP models *HFV4.0* and *leu2011*

	outer radius (cm)		delta radius (cm)	
radial region #	***HFV4.0***	***leu2011***	***HFV4.0***	***leu2011***
1	7.50	7.50	0.36	0.36
2	8.00	8.50	0.50	1.00
3	8.50	9.50	0.50	1.00
4	9.50	10.5	1.00	1.00
5	10.5	11.5	1.00	1.00
6	11.5	12.5	1.00	1.00
7	12.0	12.59	0.50	0.09
8	12.6	12.6	0.60	0.01

Table 4.2.2.2 – IFE axial mesh in the MCNP models *HFV4.0* and *leu2011*

	top edge location from bottom of the fuel (cm)		delta height (cm)	
axial region #	***HFV4.0***	***leu2011***	***HFV4.0***	***leu2011***
1	50.8	50.8	6.4	0.5
2	44.4	50.3	8.0	0.5
3	36.4	49.8	8.0	1.0
4	28.4	48.8	6.0	1.0
5	22.4	47.8	8.0	1.4
6	14.4	46.4	8.0	4.2
7	6.4	42.2	6.4	4.2
8		38.0		8.4
9		29.6		3.2
10		26.4		2.0
11		24.4		3.2
12		21.2		8.4
13		12.8		4.2
14		8.6		4.2
15		4.4		1.4
16		3.0		1.0
17		2.0		1.0
18		1.0		0.5
19		0.5		0.5

Table 4.2.2.3 – ^{235}U distribution in the HEU IFE and variation between ANL / *HFV4.0*

radial region #	*HFV4.0* ^{235}U atomic density after homogenization (at/barn.cm)	ANL ^{235}U atomic density after homogenization (at/barn.cm)	variation ANL/*HFV4.0* (%)
1	2.0570E-04	2.0632E-04	0.2999%
2	2.5100E-04	2.5096E-04	-0.0175%
3	3.0310E-04	3.0421E-04	0.3653%
4	3.7650E-04	3.7869E-04	0.5823%
5	4.4800E-04	4.4621E-04	-0.4003%
6	4.5450E-04	4.5392E-04	-0.1278%
7	4.1710E-04	4.1778E-04	0.1623%
8	3.7180E-04	3.7135E-04	-0.1199%

Table 4.2.2.4 – ^{10}B distribution in the HEU IFE and variation between ANL / *HFV4.0*

radial region #	*HFV4.0* ^{10}B atomic density after homogenization (at/barn.cm)	ANL ^{10}B atomic density after homogenization (at/barn.cm)	variation ANL/*HFV4.0* (%)
1	2.0412E-05	2.0237E-05	-0.8564%
2	1.7751E-05	1.7649E-05	-0.5750%
3	1.4691E-05	1.4562E-05	-0.8795%
4	1.0380E-05	1.0243E-05	-1.3136%
5	6.1801E-06	6.3292E-06	2.4123%
6	5.7983E-06	5.8820E-06	1.4440%
7	7.9951E-06	7.9774E-06	-0.2204%
8	1.0656E-05	1.0669E-05	0.1220%

Table 4.2.2.5 – ^{235}U distribution in the LEU IFE and variation between ANL / *leu2011*

	radial region #	*leu2011* ^{235}U atomic density after homogenization (at/barn.cm)	ANL ^{235}U atomic density after homogenization (at/barn.cm)	variation ANL/*leu2011* (%)
From top to +3cm above bottom of the fuel	1	2.9689E-04	2.9685E-04	-0.0118%
	2	5.7138E-04	5.7123E-04	-0.0262%
	3	1.0101E-03	1.0098E-03	-0.0287%
	4	1.2424E-03	1.2420E-03	-0.0322%
	5	1.2424E-03	1.2420E-03	-0.0322%
	6	9.4664E-04	9.4639E-04	-0.0259%
	7	6.2302E-04	6.2298E-04	-0.0070%
	8	5.9209E-04	5.9206E-04	-0.0049%
From +3cm to +2cm above bottom of the fuel	1	2.9689E-04	2.9689E-04	-0.0004%
	2	5.7132E-04	5.7116E-04	-0.0288%
	3	9.1806E-04	9.1798E-04	-0.0090%
	4	1.1607E-03	9.8856E-04	-14.831%
	5	1.1607E-03	9.8897E-04	-14.795%
	6	8.2654E-04	8.2617E-04	-0.0444%
	7	5.3299E-04	5.3294E-04	-0.0086%
	8	5.0207E-04	5.0119E-04	-0.1762%
From +2cm to +1cm above bottom of the fuel	1	2.9081E-04	2.9082E-04	0.0040%
	2	4.4168E-04	4.4167E-04	-0.0030%
	3	4.8227E-04	4.8234E-04	0.0148%
	4	5.3949E-04	4.8220E-04	-10.619%
	5	5.3949E-04	4.8234E-04	-10.593%
	6	4.6625E-04	4.6618E-04	-0.0159%
	7	3.5077E-04	3.5075E-04	-0.0059%
	8	3.2199E-04	3.2168E-04	-0.0963%
From +1cm to +0cm bottom of the fuel	1	2.2888E-04	2.2887E-04	-0.0045%
	2	2.2888E-04	2.2887E-04	-0.0045%
	3	2.2888E-04	2.2887E-04	-0.0045%
	4	2.2888E-04	2.2887E-04	-0.0045%
	5	2.2888E-04	2.2887E-04	-0.0045%
	6	2.2888E-04	2.2887E-04	-0.0045%
	7	2.2888E-04	2.2887E-04	-0.0045%
	8	2.2888E-04	2.2887E-04	-0.0045%

Table 4.2.2.6 – ^{10}B distribution in the LEU IFE and variation between ANL / *leu2011*

	radial region #	*leu2011* ^{235}U atomic density after homogenization (at/barn.cm)	ANL ^{235}U atomic density after homogenization (at/barn.cm)	variation ANL/*leu2011* (%)
From top to +3cm above bottom of the fuel	1	2.8971E-05	2.9013E-05	0.1450%
	2	2.4728E-05	2.4782E-05	0.2195%
	3	1.7946E-05	1.7983E-05	0.2047%
	4	1.4355E-05	1.4382E-05	0.188%
	5	1.4355E-05	1.4382E-05	0.188%
	6	1.8927E-05	1.8966E-05	0.2096%
	7	2.3928E-05	2.3982E-05	0.2260%
	8	2.4406E-05	2.3189E-05	-4.9877%
From +3cm to +2cm above bottom of the fuel	1	3.1369E-05	2.8970E-05	-7.6460%
	2	2.6915E-05	2.4729E-05	-8.1202%
	3	1.9409E-05	1.9358E-05	-0.2644%
	4	1.4447E-05	1.8275E-05	26.496%
	5	1.4447E-05	1.8268E-05	26.447%
	6	2.1433E-05	2.0786E-05	-3.0193%
	7	2.6031E-05	2.5320E-05	-2.7310%
	8	2.5998E-05	2.5815E-05	-0.7035%
From +2cm to +1cm above bottom of the fuel	1	3.1498E-05	2.9064E-05	-7.7284%
	2	2.6793E-05	2.6732E-05	-0.2273%
	3	2.6164E-05	2.6102E-05	-0.2341%
	4	2.4075E-05	2.6105E-05	8.432%
	5	2.4075E-05	2.6102E-05	8.421%
	6	2.6412E-05	2.6353E-05	-0.2223%
	7	2.8202E-05	2.8138E-05	-0.2267%
	8	2.9920E-05	2.8591E-05	-4.4412%
From +1cm to +0cm bottom of the fuel	1	3.0058E-05	3.0022E-05	-0.1190%
	2	3.0082E-05	3.0022E-05	-0.1974%
	3	3.0082E-05	3.0022E-05	-0.1974%
	4	3.0082E-05	3.0022E-05	-0.1974%
	5	3.0082E-05	3.0022E-05	-0.1974%
	6	3.0082E-05	3.0022E-05	-0.1974%
	7	3.0082E-05	3.0022E-05	-0.1977%
	8	2.9587E-05	3.0022E-05	1.4710%

4.2.3 Region III – Outer Fuel Element (OFE)

The OFE consists of 369 involute-shaped fuel plates. The ORNL MCNP inputs do not model explicitly the plates. As for the IFE, the fuel element is modeled by homogenizing the fuel, cladding and water between the plates. To take into account the radial (and axial, if any) grading of the fuel, the homogenized fuel element is subdivided into radial/axial regions in which the composition of the homogenized fuel changes. A top view of the *HFV4.0* and *leu2011* OFE is provided in Figure 4.2.3.1. In both *HFV4.0* and *leu2011,* the OFE is divided into 9 radial regions. As for the IFE, the radial mesh size, given in Table 4.2.3.1, is different between the two models. The fuel axial divisions used (see Table 4.2.2.2) are identical to the IFE one.

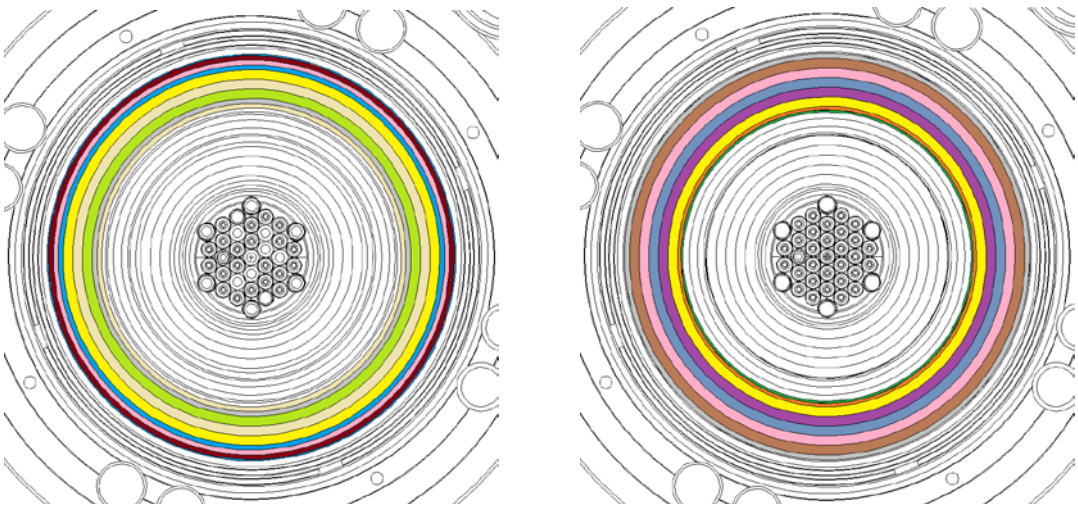

Figure 4.2.3.1 – MCNP screenshots of the OFE. The pictures on the left and right show a top view of the OFE as it is in *HFV4.0* and *leu2011*, respectively. The different colored rings represent the different fuel plate radial regions.

Table 4.2.3.1 – OFE Radial mesh in the MCNP models *HFV4.0* and *leu2011*

	outer radius (cm)		delta radius (cm)	
radial region #	***HFV4.0***	***leu2011***	***HFV4.0***	***leu2011***
1	15.5	15.16	0.37	0.01
2	16.0	15.5	0.50	0.34
3	16.5	16.5	0.50	1.00
4	17.5	17.5	1.00	1.00
5	18.5	18.5	1.00	1.00
6	19.5	19.5	1.00	1.00
7	20.0	20.5	0.50	1.00
8	20.5	20.99	0.50	0.49
9	20.978	21.0	0.478	0.01

As for region II (IFE), cross-checking of Region III involves analyzing whether the materials are correctly homogenized. The few inconsistencies that have been detected in the material compositions in this region and in both inputs are described below.

- As for Region II, three materials are used to model the coolant-clad whether they are above, at the same level or below the fuel (Materials m72, m200, m73). The conditions of pressure and temperature of the coolant are given in Table 4.2.2. As for the IFE, the oxygen and hydrogen densities used in MCNP are, respectively, 0.76% and 1.28% higher than expected.
- In *HFV4.0*, the fuel distribution has been compared to the one that can be extracted from the technical drawing of the outer fuel element [Ref. 22]. Variations in fuel distribution are shown in Table 4.2.3.2. As one can see, the variations are relatively small and do not exceed a few percent. Surprisingly, the greatest differences occur in the first radial regions. The origin of these discrepancies is not understood.
- In *leu2011*, the fuel distribution in the OFE has been compared to the one that can be extracted from the information on the reference LEU design provided in [Ref. 4]. As in Section 4.2.2, due to the axial grading of the fuel, 4 different regions have to be considered: The first one goes from the top of the fuel to 3cm above the bottom of the fuel. The second and third ones go from 3cm above the bottom of the fuel to 1cm above the bottom of the fuel. This is the region where the fuel is axially and radially graded. This 2cm long region is split into two parts equally spaced. The last region goes from 1cm above the bottom of the fuel to the bottom of the fuel (no radial or axial grading). Variations in the ^{235}U distribution between ANL calculations and *leu2011* for these 4 axial regions are shown in Table 4.2.3.3. As one can see, the variations are very small (<0.2%) for most of the fuel materials with the notable exception of the materials in the Radial Region 4, 5 and 6 where the fuel is graded axially and radially (from +3 to +1cm above the bottom of the fuel). The origin of these discrepancies is not understood.
- As for Region II, in *leu2011*, the cladding composition used to homogenize the fuel and coolant is different than the one used for the coolant-clad materials. However, the composition used for the coolant-clad materials in *leu2011* is the same as the one used in *HFV4.0*. If it has been judged necessary to change the cladding composition from *HFV4.0* to *leu2011,* it has not been explained and propagated everywhere.

Table 4.2.3.2 – ^{235}U distribution in the HEU OFE and variation between ANL / *HFV4.0*

radial region #	*HFV4.0* ^{235}U atomic density after homogenization (at/barn.cm)	ANL ^{235}U atomic density after homogenization (at/barn.cm)	variation ANL/*HFV4.0* (%)
1	4.2200E-04	4.2810E-04	1.4444%
2	5.0530E-04	5.1527E-04	1.9729%
3	5.9410E-04	6.0364E-04	1.6065%
4	6.7470E-04	6.7349E-04	-0.1792%
5	6.5000E-04	6.4743E-04	-0.3957%
6	5.2920E-04	5.2543E-04	-0.7122%
7	4.1450E-04	4.1251E-04	-0.4810%
8	3.3870E-04	3.3682E-04	-0.5554%
9	2.6980E-04	2.6868E-04	-0.4165%

Table 4.2.3.3 – ^{235}U distribution in the LEU OFE and variation between ANL / *leu2011*

	radial region #	*leu2011* ^{235}U atomic density after homogenization (at/barn.cm)	*leu2011* ^{235}U atomic density after homogenization (at/barn.cm)	variation ANL/*leu2011* (%)
From top to +3cm above bottom of the fuel	1	6.6309E-04	6.6311E-04	0.0025%
	2	8.0350E-04	8.0331E-04	-0.0232%
	3	1.3587E-03	1.3578E-03	-0.0667%
	4	1.7775E-03	1.7760E-03	-0.083%
	5	1.7775E-03	1.7760E-03	-0.083%
	6	1.7775E-03	1.7760E-03	-0.0827%
	7	1.3510E-03	1.3501E-03	-0.0695%
	8	7.0784E-04	7.0759E-04	-0.0347%
	9	4.8660E-04	4.9557E-04	1.8428%
From +3cm to +2cm above bottom of the fuel	1	5.5553E-04	5.8293E-04	4.9325%
	2	6.9593E-04	6.9562E-04	-0.0441%
	3	1.1889E-03	1.1886E-03	-0.0293%
	4	1.5620E-03	1.3886E-03	-11.099%
	5	1.5620E-03	1.3896E-03	-11.038%
	6	1.5620E-03	1.3886E-03	-11.0994%
	7	1.2057E-03	1.2051E-03	-0.0466%
	8	6.4452E-04	6.4468E-04	0.0254%
	9	4.2329E-04	4.2226E-04	-0.2430%
From +2cm to +1cm above bottom of the fuel	1	3.4998E-04	3.4038E-04	-2.7438%
	2	4.5654E-04	4.5661E-04	0.0151%
	3	6.0818E-04	6.0834E-04	0.0267%
	4	6.1548E-04	6.7324E-04	9.385%
	5	6.1580E-04	6.7324E-04	9.328%
	6	6.1548E-04	6.7324E-04	9.3853%
	7	6.1316E-04	6.1341E-04	0.0402%
	8	4.6652E-04	4.6647E-04	-0.0111%
	9	2.9628E-04	2.9663E-04	0.1174%
From +1cm to +0cm bottom of the fuel	1	2.2886E-04	2.2887E-04	0.0043%
	2	2.2887E-04	2.2887E-04	-0.0001%
	3	2.2887E-04	2.2887E-04	-0.0001%
	4	2.2887E-04	2.2887E-04	-0.0001%
	5	2.2887E-04	2.2887E-04	-0.0001%
	6	2.2887E-04	2.2887E-04	-0.0001%
	7	2.2887E-04	2.2887E-04	-0.0001%
	8	2.2887E-04	2.2887E-04	-0.0001%
	9	2.2886E-04	2.2887E-04	0.0043%

4.2.4 Region IV – Inner Control Element (ICE) & Outer Control Element (OCE)

The control elements (CEs) consist of two concentric cylinders located in the gap between the outer side wall of the outer fuel element and the removable reflector. Light water flows in this gap in order to cool the CEs. To compensate the fuel burnup throughout the life of the core, the CEs are gradually vertically and symmetrically withdrawn. The inner cylinder is moved downward and the outer cylinder, made of four plates that can be moved independently to SCRAM the reactor, is moved upward. These elements are modeled in MCNP and are represented in Figure 4.2.4.1. Their geometry is identical in *HFV4.0* and *leu2011*. To reduce axial variations in the power distributions, the control elements are divided into three axial sections. Each of them is made of a different material that has different neutron absorbing characteristics. The so-called white material (lower section of the OCE, upper section of the ICE) is made of aluminum and has a low neutron absorbing power. The so-called gray material, present in the central section, is made of tantalum dispersed in aluminum and has a moderate neutron absorbing power. The so-called black material (upper section of the OCE, lower section of the ICE) is made of Eu_2O_3 dispersed in aluminum and is highly neutron absorbing. In *HFV4.0,* the absorbing materials are fresh whereas in *leu2011* they are depleted.

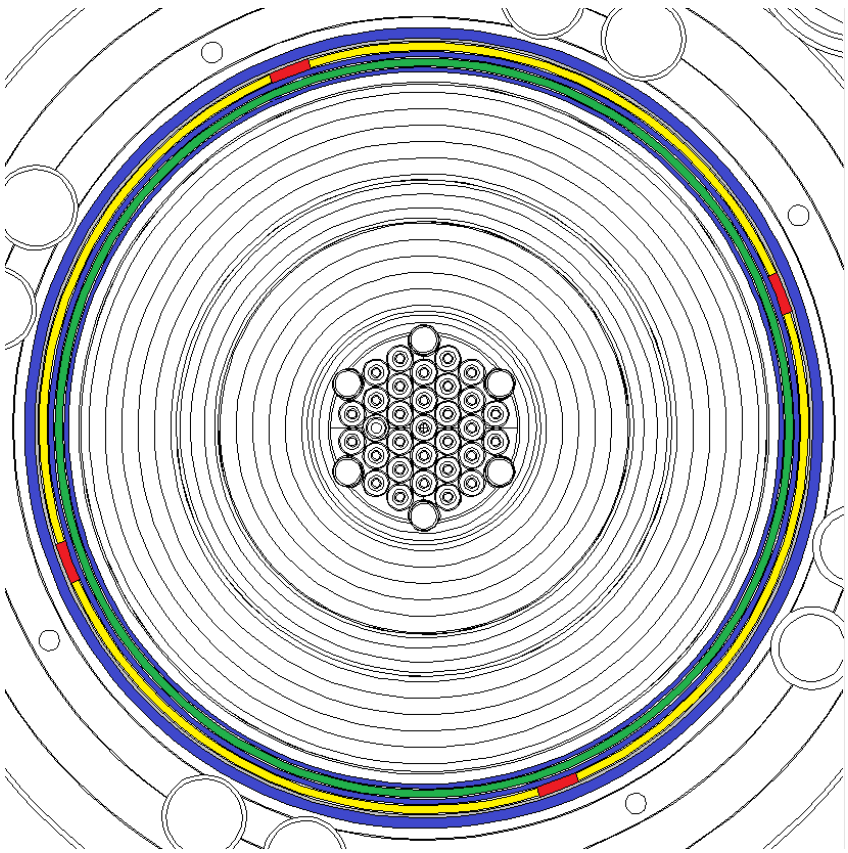

Figure 4.2.4.1 – MCNP screenshot of the control elements (top view). The light water is represented in blue, the inner control element is shown in green and the outer control element (4 plates) is represented in yellow.

The following inconsistencies have been detected.

- From the available documentation regarding the geometry of the CEs, it appears that some dimensions used in the MCNP inputs are slightly off. After internal discussions, the ORNL staff has communicated a new set of reference values. The original dimensions and the updated ones are provided in Table 4.2.4.1.

Table 4.2.4.1 – CE dimensions updated in both MCNP inputs

parameter	value used in MCNP *HFV4.0* and *leu2011* (cm)	new reference value (cm)	reference (drawing numbers)
outer radius of the OFE side plate	21.7475	21.76653	E-42126 rev M
inner radius of the OCE inner clad	22.987000	23.09114	E-M-55623 rev.J
outer radius of the OCE inner clad	23.066375	23.17052	E-M-55623 rev.J
inner radius of the OCE outer clad	23.542625	23.64677	E-M-55623 rev.J
outer radius of the OCE outer clad	23.622000	23.72614	E-49820 rev W
inner radius of the Aluminum liner	23.81250	23.96109	M-11506-OH-200 rev 6

- The mass of the different absorbing materials is provided in [Ref. 23]. In *HFV4.0,* the CE materials are fresh. Their masses are not given directly but can be calculated easily. From these calculations, it appears that the masses used in the MCNP input, included in Table 4.2.4.2, are slightly off.

Table 4.2.4.2 – Reference absorbing materials masses and comparison with *HFV4.0* values

materials	from [Ref. 23], reference mass (g)	mass in *HFV4.0* (g)	difference with reference value (%)
ICE - gray	1292	1242	-3.87%
ICE - black	1912	1847	-3.40%
OCE - gray	1922	1934	0.62%
OCE - black	1297	1301	0.31%

- In *leu2011,* the control element materials are depleted. As stated previously, the masses of the fresh materials are slightly off. Consequently, the depleted compositions, coming from the fresh ones, are slightly off too. The tantalum section (gray material) of the CEs is holed to reduce the potential for mechanical instability allowing water to enter the holes. In both MCNP inputs, the holes are not modeled explicitly. Water normally present in the holes is homogenized in the tantalum composition. The atomic density of water is expected to be the same in both inputs but is actually 15% lower in *leu2011* than in *HFV4.0*. The ratio of hydrogen over oxygen is also greater than two in the gray material of the ICE in *leu2011*. The ratio is two in *HFV4.0*.
- The same materials as in Region I are used to model the light water above, in and below the CEs (Materials m1, m2, m3). The conditions of pressure and temperature of the coolant are included in Table 4.2.1. As a result, it appears that the densities used in MCNP are systematically 0.76% higher than expected.

4.2.5 Region V – Irradiation Facilities & Removable Beryllium Reflector (RB)

The fuel elements are radially reflected by a ~30cm-thick beryllium reflector. The inner ~10cm-thick portion is replaced more often than the rest of the reflector due to embrittlement induced by radiation. This inner part is made of four concentric cylinders axially separated by a thin gap to enable water cooling. The three first cylinders are replaced every ~40 cycles and constitute the Removable Beryllium reflector (RB). The outermost one is replaced every ~80 cycles and is called the Semi-permanent Beryllium reflector (SB). Twenty vertical experiment facilities are located in the RB and SB: Four 0.635cm-radius and eight 2.54cm-radius facilities are located in the RB, the eight others (0.635cm-radius) are located in the SB. Visualization of the RB and SB as modeled in MCNP is shown in Figure 4.2.5.1.

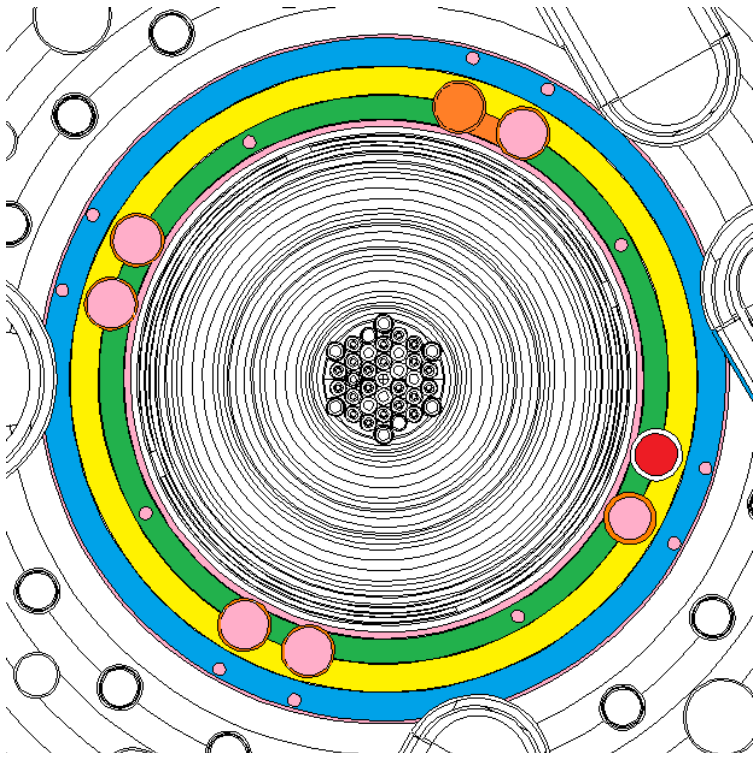

Figure 4.2.5.1 - MCNP screenshot of the removable and semi-permanent reflector (top view). The four annuli of the reflector are colored in pink, green, yellow and blue. The twenty cylindrical experimental facilities are colored in pink, orange and red.

Several inconsistencies have been detected in the MCNP inputs:

- The materials used to model the water above, in and below the core are Materials m4, m5 and m6. As in Region I, the density of these materials used in the MCNP inputs are 0.76% higher than the expected ones (see Section 4.2.1).
- There is a difference of ~10% between the density used in the material cards of the europium liner (m38 and m39) and the cell cards.
- In *leu2011*, the isotope, ^{151}Eu, is used 2 times in the composition of Material m38.
- In *leu2011*, the isotope, ^{153}Eu, is absent from the composition of Material m39.

4.2.6 Region VI – Beam tubes & Permanent Beryllium Reflector (PB)

Region VI in MCNP includes the outermost section of the reflector (called the permanent reflector), the four beam tubes, the light water pool located beyond the reflector and the concrete wall. The permanent reflector extends 20cm beyond the semi-permanent reflector. Sixteen vertical 2cm-radius and 6 vertical 3.6cm-radius experiment facilities are located in the permanent reflector. Visualization of this region is provided in Figure 4.2.6.1.

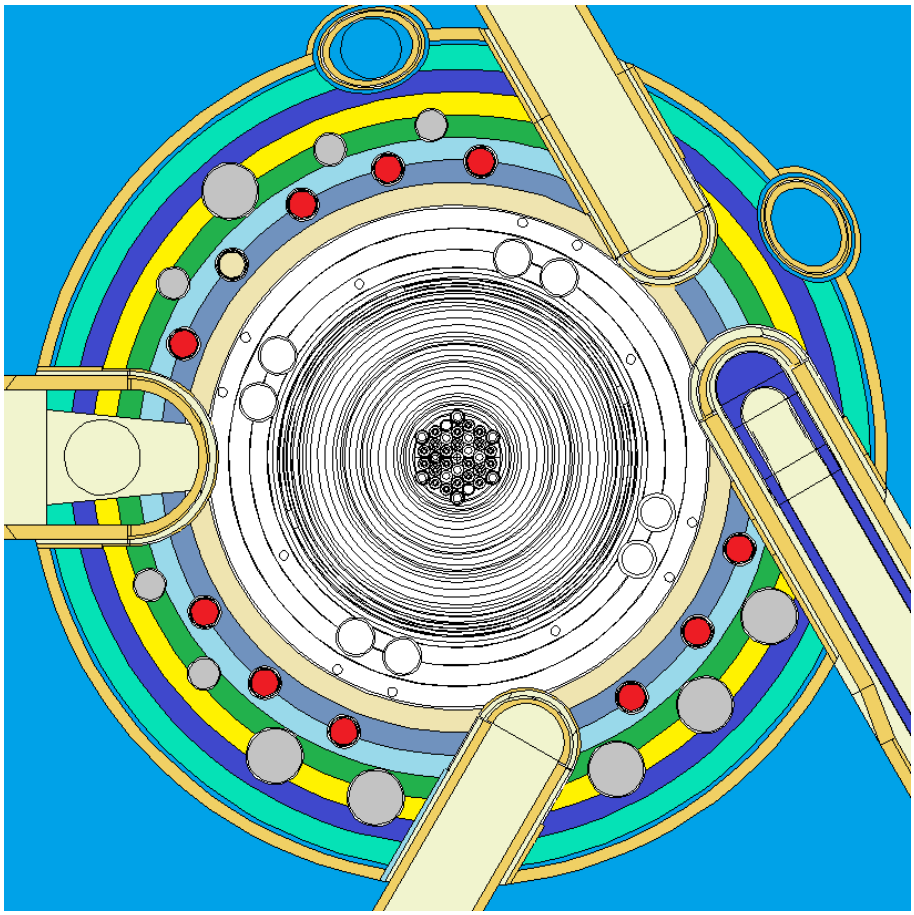

Figure 4.2.6.1 – MCNP screenshot of region VI (top view). This region appears in color on the picture.

Several inconsistencies have been detected in the MCNP inputs:

- The materials used to model the water above, in and below the core are Materials m7, m8 and m9. As in Region I, the density of these materials used in the MCNP inputs are 0.76% higher than the expected ones (see Section 4.2.1).

4.3 Review of the ORNL RRD Neutronic Calculations

This section describes all of the methodologies, calculations and results obtained with the ANL reference inputs generated for the review.

4.3.1 Reference Model Preparation

As explained in Section 4.2, two reference MCNP inputs were provided by ORNL to perform the review: One with a HEU core, called *HFV4.0,* and one with a LEU core, called *leu2011*. The cross-checking of these two inputs has revealed several inconsistencies.

In addition, the configuration of the reactor is different (not the same experimental loadings, not the same control element compositions…) which prevent their use for a direct comparison (see Section 4.2, Table 4.2.1). Recall that in *leu2011*, the flux trap is filled with 31 curium targets whereas only dummy targets are used in *HFV4.0*.

For the review it has thus been decided to produce new reference inputs. The goal was to make an as fair as possible comparison between the HEU and LEU cores. Because the experimental loading is different in *HFV4.0* and *leu2011* and because it has been considered interesting to analyze its impact on the matrix of performance, two series of two reference inputs have been generated. The Series *c400* is composed of two inputs, one HEU and one LEU, with the same experimental configuration found in *HFV4.0*. The Series *l11* is based on the same principle. Two inputs have been generated, one HEU and one LEU, but the experimental configuration is the same as that found in *leu2011*.

4.3.1.1 Explicit Modeling of the Involute

In the ANL reference inputs, the homogenized description of the fuel elements has been replaced by an explicit one. As explained in Section 3.5, MCNP cannot model the involute. To get around this difficulty, ANL has developed a methodology based on the discretization of the involute: The real shape of the object (cladding, fuel, filler…) is split into many small pieces that are modeled by a six-faced polyhedron. The full object is then modeled by juxtaposition of these small polyhedrons. Because this modeling is an approximation, a systemic bias is introduced. However, the bias is directly correlated to the degree of discretization: The finer the discretization, the lower is the bias. Due to the strong symmetry of the core, it is not considered necessary to model all the plates individually. Instead, one plate is explicitly modeled and is then duplicated as many times as necessary to generate the complete fuel element. The space between the plates is then filled up with the coolant and the modeling of the element is complete. More details on the methodology are given in Appendix B. Results of the explicit modeling of the fuel elements compared to the homogenized description is shown in Figure 4.3.1.1.1. Because the HEU and LEU plates have the same dimensions, the same discretization of the cladding has been used in both cores. Twenty-five cells (polyhedrons) per plate have been created to model the inner and outer cladding plate. The result of the cladding modeling is shown in Figure 4.3.1.1.2. The HEU inner fuel, inner filler and outer fuel have been modeled using 22 cells each. Because the filler of the outer plate is made of aluminum, as is the cladding, it has not been explicitly modeled.

The LEU inner fuel, inner filler, outer fuel and zirconium layers surrounding the fuel are explicitly modeled. Except for the fuel region that is axially and radially graded, 22 cells have been used to model each part. The region where the fuel is graded radially and axially required many more cells. Due to the complexity of the shape of the fuel in a curved space, it was not possible to use polyhedrons with a rectangular base. Instead, a triangular base was needed increasing by a factor of about four the number of cells. Three-dimensional views of the LEU fuel as modeled and details on the bottom (where the fuel is doubly graded) are shown in Figure 4.3.1.1.3.

For depletion and power distribution calculations, it is important to capture the gradient of fission and, therefore, of power. The fuel meat has to be "sliced" into several pieces. To avoid introducing a bias in the calculation, the discretization of the fuel is identical for both the depletion and power distribution calculations. The axial and radial slicing of the fuel meat chosen for the ANL reference inputs is slightly different from the ORNL one. Inner fuel, inner filler and outer fuel are discretized in 7 radial x 23 axial divisions. The "mesh" is identical in both HEU and LEU configurations. Depending upon the regions, ORNL has one or two extra very thin radial layers (Δr=0.01cm). These layers have not been considered because in an explicit geometry, the corresponding volume would be very small and very high precision calculations would have been required to obtain well converged results. Conversely, the size and number of the ORNL axial divisions has been judged too coarse to capture the gradient of power in the "peak" area (centerline of the fuel). Consequently, the number of axial divisions has been increased in the ANL reference inputs. The details of the radial and axial ANL mesh are given in Tables 4.3.1.1.1 and 4.3.1.1.2, respectively.

Table 4.3.1.1.1 – ANL reference radial mesh for depletion & power calculations

radial division #	inner element		outer element	
	outer radius, cm	radial increment, cm	outer radius, cm	radial increment, cm
1	7.5	0.36	15.75	0.6
2	8.5	1	16.5	0.75
3	9.5	1	17.5	1
4	10.5	1	18.5	1
5	11.5	1	19.5	1
6	12.2	0.7	20.5	1
7	12.6	0.4	21	0.5

Table 4.3.1.1.2 – ANL reference axial mesh for depletion & power calculations

axial division #	top edge location from bottom of the fuel (cm)	axial increment, cm
1	50.80	0.50
2	50.30	0.50
3	49.80	1.40
4	48.40	3.00
5	45.40	3.00
6	42.40	3.00
7	39.40	3.00
8	36.40	3.00
9	33.40	3.00
10	30.40	2.00
11	28.40	2.00
12	26.40	2.00
13	24.40	2.00
14	22.40	2.00
15	20.40	3.00
16	17.40	3.00
17	14.40	3.00
18	11.40	3.00
19	8.40	3.00
20	5.40	2.40
21	3.00	2.00
22	1.00	0.50
23	0.50	0.50

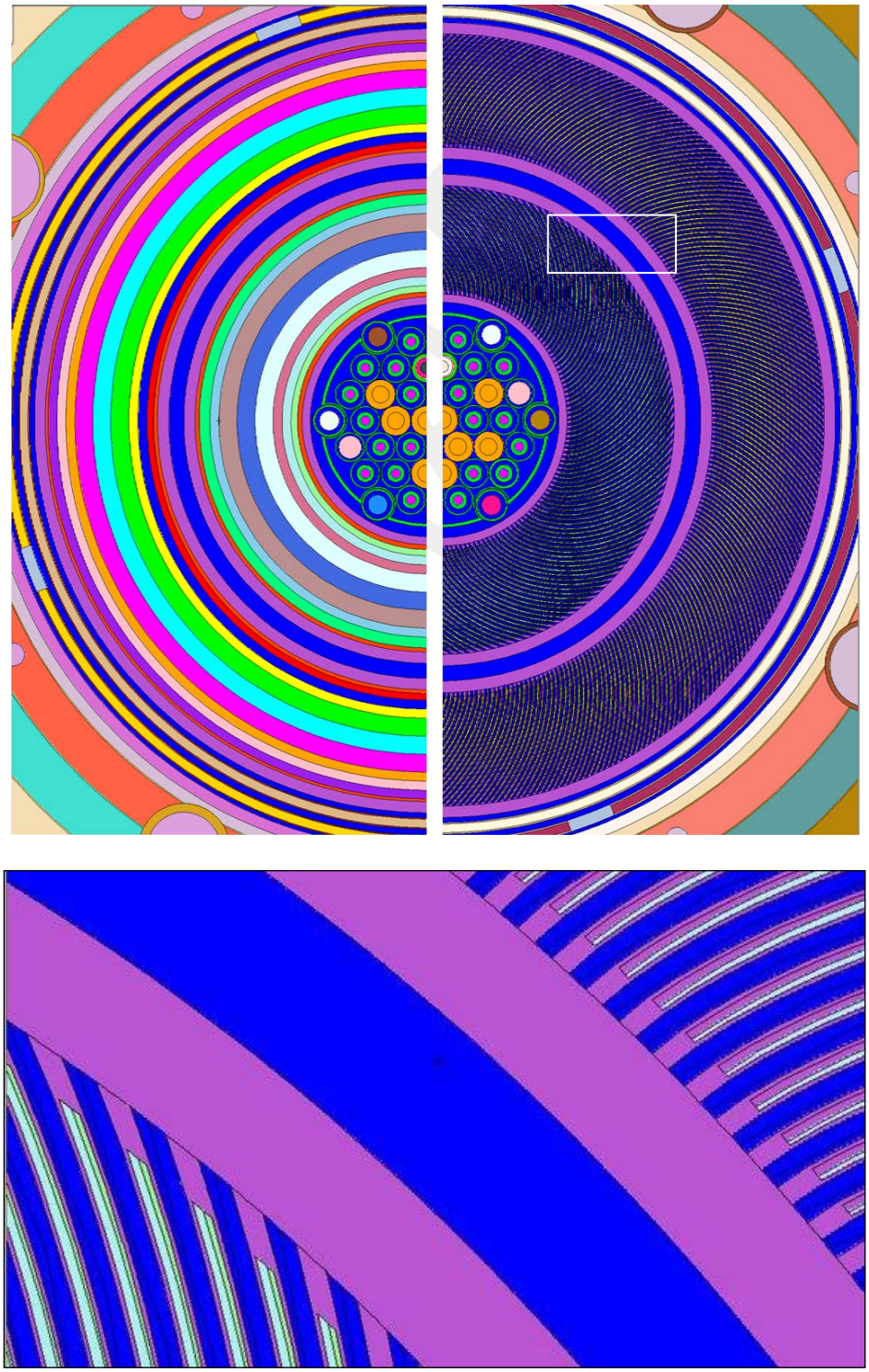

Figure 4.3.1.1.1 – MCNP screenshots of the HFIR fuel elements (half top view). The picture on the top left has been obtained with the ORNL homogenized model. The picture on the top right has been obtained for the ANL explicit model. The bottom picture is an enlargement of the area represented by the white rectangle on the top right picture. Cladding and side plates appear in pink, fuel and filler are colored in light green and yellow, respectively.

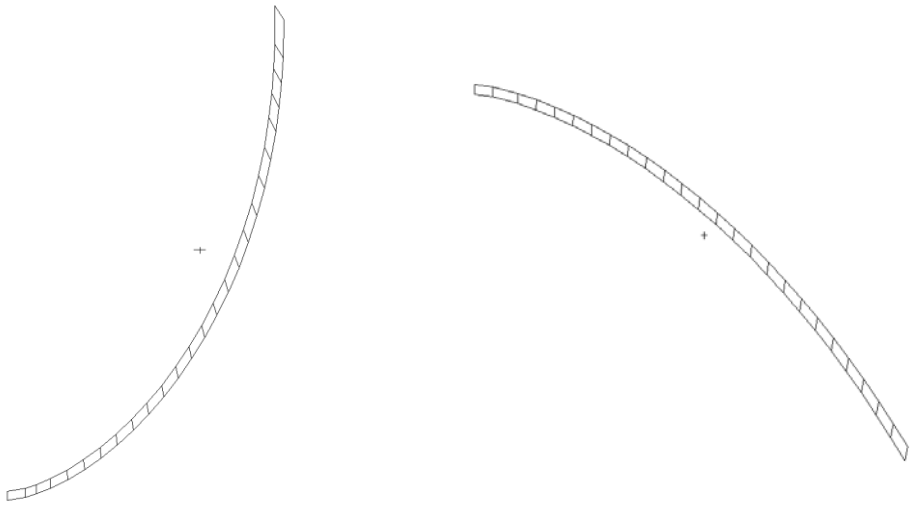

Figure 4.3.1.1.2 – MCNP screenshots of the inner (left) and outer (right) cladding as modeled in both HEU and LEU ANL reference inputs (25 cells each).

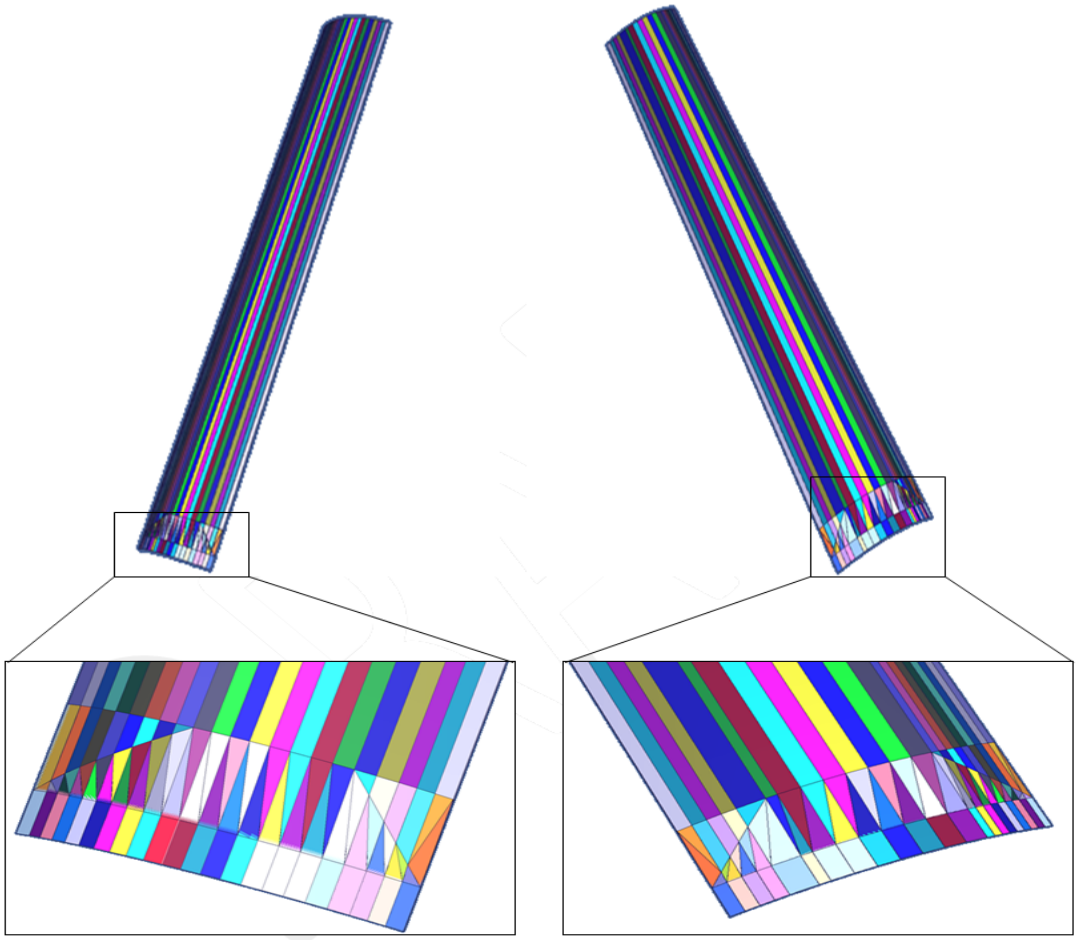

Figure 4.3.1.1.3 – 3D view of the inner (left) and outer (right) LEU fuel and details of the bottom as modeled in the LEU reference inputs. The triangular base of the polyhedrons used to model the region doubly graded is clearly visible on the details pictures.

4.3.1.2 Input Cleaning

HFV4.0 and *leu2011* have been used as a base to produce the series of inputs, *c400* and *l11*, respectively. The main differences from the ORNL inputs are:

- Some inconsistencies have been corrected.
- Homogeneous description of the elements has been replaced by the explicit one.
- All materials are fresh (non-irradiated) at BOL including control materials.
- One set of nuclear data is used (ENDF/B7).

In order to understand the impact of the different changes on the reactivity of the core, the changes have been implemented gradually. Table 4.3.1.2.1 summarizes the effects of the modifications on the reactor reactivity at BOL. All presented results are given at one standard deviation (noted 1-σ in the report).

As one can see, the switch to the explicit description of the fuel elements has little impact on the reactivity. One could think that this is an indication that the homogeneous and explicit descriptions are equivalent. Unfortunately, the reality is more complex as explained in Section 4.3.2 and Appendix C.

The coolant density corrections from the original values to the reference ones (Table 4.2.2) do not affect *HFV4.0* and *leu2011* in the same way: The difference in reactivity is a lot more important in *HFV4.0*. This is easily explained by the fact that the coolant density circulating between the fuel elements was wrong in *HFV4.0* but correct in *leu2011*.

Despite the number of material density corrections made in both inputs (especially in the *HFV4.0* flux trap, see Table 4.2.1.1), the effect on the core reactivity is relatively small (less than 70pcm).

In *HFV4.0*, the cross-sections used were from different libraries. They have been replaced by a unique set of data consistent with *leu2011*: ENDF/B7. The effect of the changes is very small (+37pcm).

The correction for the control element geometry is interesting because the same correction has been applied to both inputs but did not lead to the same effect on the reactivity (-33pcm in *HFV4.0* and +184pcm in *leu2011*). The geometric corrections have resulted in a slight increase in the volume of water between the outer control element and the removable reflector. The LEU core is apparently more sensitive to the presence of water in this area than the HEU core. It is probably due to the fact that the neutron spectrum of the LEU core is more epithermal and additional water can help improve the neutron thermalization which results in a neutron population more likely to create new fissions, increasing the reactor reactivity.

In order to simplify the analyses, the inputs have been prepared with fresh (non-irradiated) materials at BOL. The differences between the two series of reference inputs are only found in the experimental loading. The variation of reactivity due to the change to fresh materials is dramatically different in *HFV4.0* (-87pcm) and *leu2011* (+875pcm). This is due to the fact that in *HFV4.0* only the permanent reflector has been changed whereas, in *leu2011*, the control elements have been replaced by fresh ones in addition to the permanent reflector. The variation

is strong because the efficiency of the black region tends to increase during irradiation due to the buildup of the daughter isotopes of the Europium.

After completing all of the modifications, the overall variation in reactivity between the original and the new reference inputs is significant (-523pcm for *HFV4.0* and +1197pcm for *leu2011*). The second input of each series is obtained by replacing the current fuel elements (HEU or LEU) by the other one (LEU or HEU). A criticality calculation has been carried out at BOL with the two inputs of each series. Results are compiled in Table 4.3.1.2.2. The control element positions were the same in the four inputs. It is then possible to analyze in a consistent way the differences between the two series and between the two cores. It appears that the nature of the experimental loading tends to impact more the LEU cores (749pcm between the two series) than the HEU cores (310pcm). This is also an indication of the difference in spectra between the two fuels (the ratio of thermal/non-thermal neutrons is lower in the LEU fuel region). The variation of reactivity between the HEU and the LEU core can then increase significantly (from 1084pcm in the series *c400* to 1522pcm in the series *l11*).

Table 4.3.1.2.1 – Summary of the different input modifications leading to the ANL reference inputs and their effects on the reactivity. Uncertainty < 12pcm at 1-σ.

Modifications	Variation of reactivity vs. base model (pcm)	
	base model *HFV4.0* (HEU core)	base model *leu2011* (LEU core)
switch to explicit elements	-108	+161
correction coolant density	-314	+44
correction other materials density	-19	-63
switch to ENDF/B7 library	+37	-
correction control elements geometry	-33	+184
fresh materials everywhere (reflector, CEs…)	-87	+875
variation of reactivity from base to reference model (after all above modifications)	-523	+1197

Table 4.3.1.2.2 – Results of the criticality calculations carried out with the 4 ANL reference inputs (control element position 45.72cm withdrawn). Uncertainty < 12pcm at 1-σ.

	series *c400*	series *l11*	variation of reactivity *c400* vs. *l11* (pcm)
Fuel geometry	Explicit	Explicit	-
FTT composition	Dummy targets	Curium targets	-
ICE & OCE materials	Fresh, updated geometry	Fresh, updated geometry	-
RB experiment facilities	Beryllium plugs	Dummy targets	-
Coolant density	3 zones using NIST data	3 zones using NIST data	-
HEU core - k-effective	**1.00353**	**1.00042**	**+310**
LEU core - k-effective	**0.99273**	**0.98541**	**+749**
variation of reactivity HEU vs. LEU (pcm)	**+1084**	**+1522**	

4.3.2 Cycle Length Prediction

The cycle length is one of the metrics of performance of the reactor. It is thus crucial to predict it accurately. To maintain criticality, the control elements are gradually withdrawn during the cycle to compensate for fuel consumption and fission product buildup. The cycle is over when the control elements are fully withdrawn (68.58cm or 27inch from the fully inserted position).

As explained in Section 3.5, the ANL methodology used to predict the cycle length is based on a critical search algorithm. This method provides the critical position of the control element at each time step and the length of the cycle is deduced by determining when the control elements have reached the fully withdrawn position. A model can then be validated by comparing the calculated control element positions with the experimental ones.

The difficulty is that there is no benchmark available for HFIR with a LEU core. Consequently, one has to first study the HEU core and based on engineering judgment, decide if the models and methods can be applied to a LEU core. As seen later in this section, and despite very good agreement for the HEU core, the cycle length predicted by ANL for the LEU core is dramatically different than the ORNL one.

The following section is organized as follow. As a first step, discussion is focused on the HEU core. The comparison between the explicit and the homogenized descriptions of the fuel elements is presented, followed by a benchmark against experiment of an ANL reference input. Then, the LEU core is studied. The non-equivalence between the explicit and homogenized models is revealed and discussed. Finally, using the ANL reference inputs, the results obtained for the evaluation of the matrix of performance are presented.

4.3.2.1 Depletion of the HEU Core

The impact of the explicit description has been studied with the HEU core. To do so, the ORNL input, *HFV4.0,* has been depleted and the results have been compared to the same model but with the homogenized description of the fuel elements replaced by the explicit one. This explicit model is different from the reference one described in Section 4.3.1.3 and will later be called *HFV4.0-explicit*.

Both models have been depleted at 85MW during 27days with a critical search. The results (critical control rod position) are presented in Figure 4.3.2.1.1. The blue line represents the evolution of the control element position obtained with *HFV4.0* (homogeneous) and the red one has been obtained with the explicit model. As one can see, there is excellent agreement between the two curves and thus between the two models. Both models taken in the same conditions lead to the same results.

When using critical search no intrinsic model bias was considered, and so a k-effective value of unity was the target. Also, the modeled k-effective associated with the critical positions is not perfectly 1.00000 but something close associated with a calculation error. The k-effective values and associated error bars (1-σ) obtained for this calculation are shown in Figure 4.3.2.1.2. As one can see, at one standard deviation, the maximum error does not exceed 100pcm which is

considered small enough for this type of calculation. These k-effective values are typical of all critical search calculations carried out for this review and will not be presented again.

An attempt at benchmarking has been carried out. In several ORNL publications (such as [Ref. 4] or [Ref. 24]) reactor physics calculations are benchmarked against experimental data coming from Cycle 400. The control element positions for each day of operation, the length of the cycle and the average power are known [Ref. 24]. This cycle has naturally been selected for the benchmark. The reference HEU input of the Series *c400* has been modified to reflect the configuration of the reactor at BOL of Cycle 400. The modifications include: the material composition of the control elements (from fresh to depleted) and the permanent reflector composition (from fresh to depleted). The depleted composition of the permanent reflector has been found in *HFV4.0* and the depleted control element compositions have been found in *leu2011*. However, it has to be acknowledged that introducing the CEs depleted compositions in this model is somehow inconsistent because geometric modifications have been made in the reference inputs and it has been shown (see Table 4.2.4.2) that the masses of fresh materials (used as a base for the depleted ones) are slightly off. Even more important, the depleted compositions of the CEs are supposed to represent the composition at BOC 400 but the irradiation history of the ICE is incomplete and, consequently, has been approximated for the ICE depleted composition calculation [Ref. 25]. The magnitude of the bias created by these approximations is unknown.

Two calculations have been carried out. In the first one, the experimental critical control element positions have been implemented (no critical search). In this case, the output considered is the k-effective and its deviation from criticality (k-effective=1.00000). The results are shown in Figure 4.3.2.1.3. In the second calculation, the critical search has been used. The deviation between the calculated and experimental control element position is the output of interest. The results are shown in Figure 4.3.2.1.4.

From the first calculation, one can see that the deviation from criticality is strongly negative (~-700pcm) at BOC but for the same period, in the second calculation, the deviation from the experimental CEs position is small (~+0.7cm or ~+0.3inch). This apparent opposite behavior between the two calculations can be explained by the relative worth of the CEs with their positions: The worth is maximal when the CEs are 45cm withdrawn (18inch) but decreases gradually afterwards when they are moved to the fully withdrawn position (68.58cm or 27inch). At BOC, the critical CEs position is~45cm withdrawn where their worth is maximal which means that even a small variation of position can induce a strong difference of reactivity.

Most of the other points seem to follow an inverse behavior: the deviation from criticality is relatively small (+100 to -200pcm) but the deviation from the experimental position is important (up to 2.3cm or 0.9inch). Again, this behavior is explained by the relative worth of the CEs which decreases strongly when the CEs are more and more withdrawn.

From the first calculation and except for the first two points, all of the calculated k-effective deviations are in a range of ±300 pcm at 1-σ. From the second calculation, the calculated critical position deviations are in a range of ±0 to ±0.9inch at 1-σ. Considering the number of unknowns for this benchmark (especially the composition of the ICE) and the unknown magnitude of the associated bias, these two series of calculations seem to agree relatively well with the experimental data.

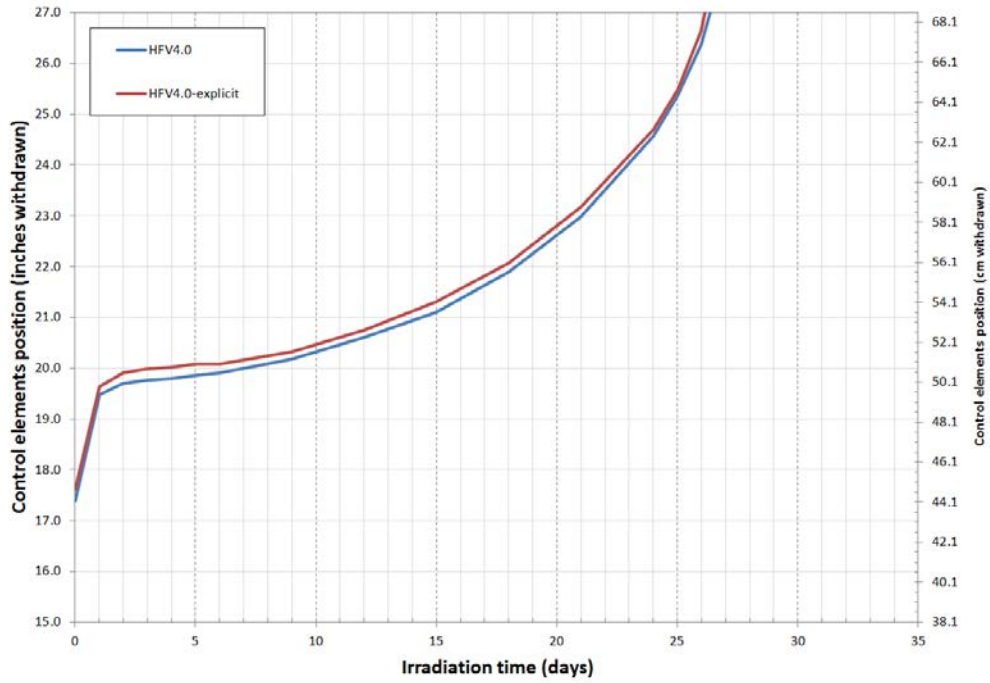

Figure 4.3.2.1.1 – Critical control elements positions obtained with *HFV4.0* and *HFV4.0-explicit* (at 85MW). Uncertainty max. < 100pcm/steady state calculation at 1-σ.

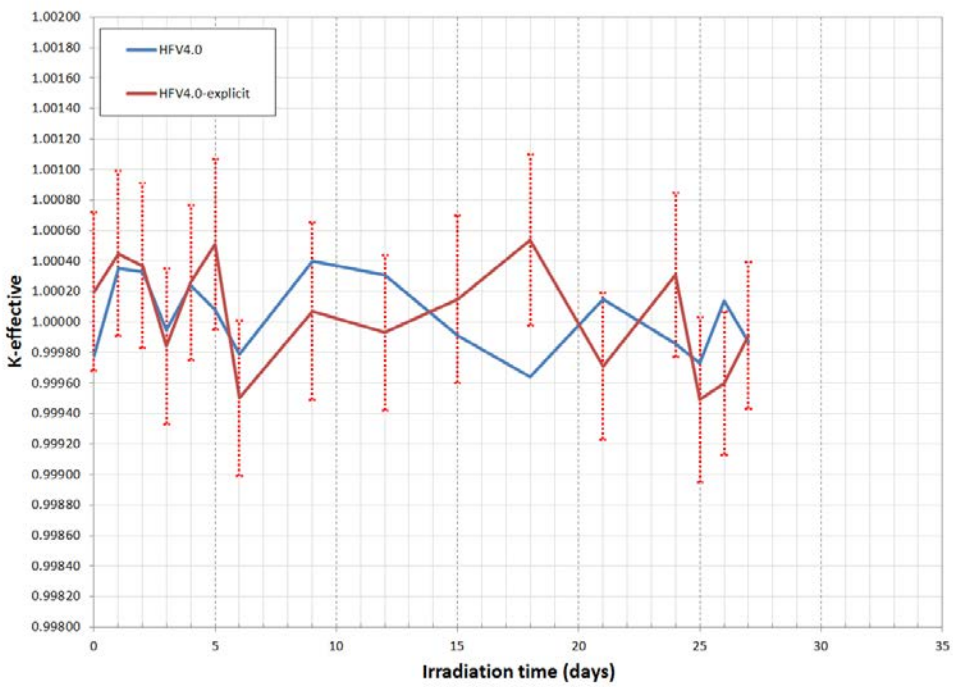

Figure 4.3.2.1.2 – k-effective values associated with the critical control element positions obtained with *HFV4.0* and *HFV4.0-explicit*. To make the figure easy to read, only the error bars of *HFV4.0-explicit* are shown.

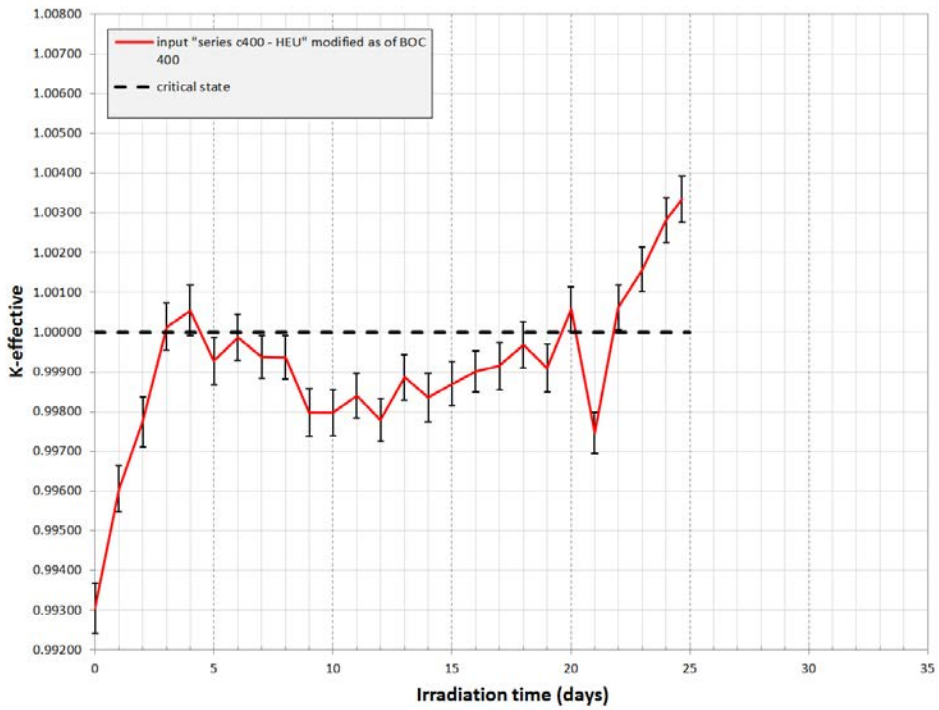

Figure 4.3.2.1.3 – k-effective evolution obtained with ANL explicit model "Series *c400* – HEU" using the experimental critical position modified to reflect the conditions of the reactor at BOC 400.

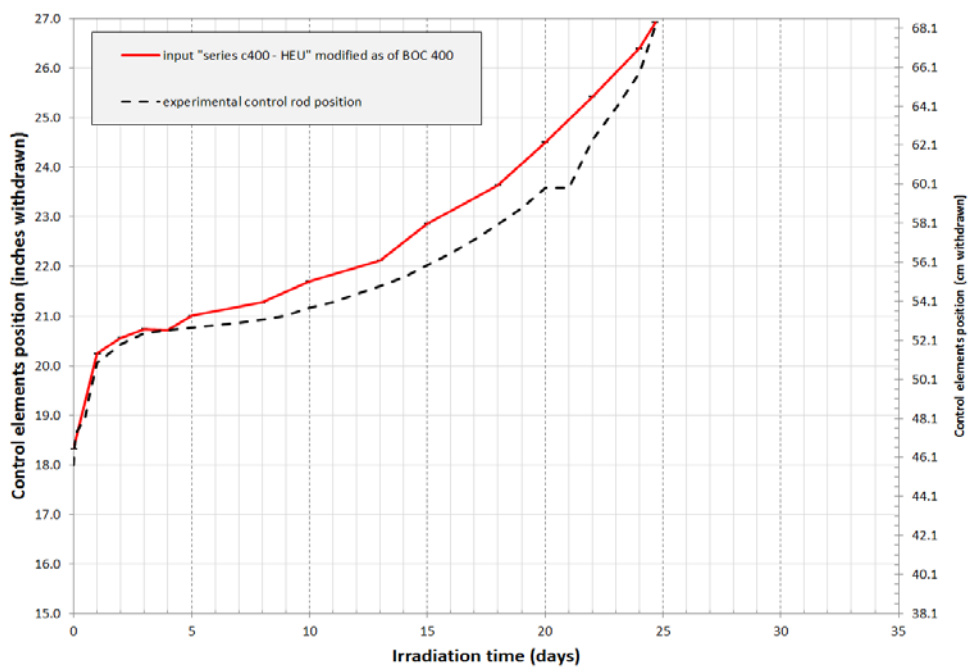

Figure 4.3.2.1.4 – Critical control element positions obtained with ANL explicit model "Series *c400* – HEU" modified to reflect the conditions of the reactor at BOC 400 and comparison with experimental positions. Uncertainty max. < 100pcm/steady state calculation at 1-σ.

4.3.2.2 Depletion of the LEU Core

The same approach used for the HEU core has been used with the LEU core: A comparison of depletion calculations has first been carried out between the original ORNL LEU input, *leu2011* (with homogenized description of the fuel elements), and the one in which the explicit description of the fuel elements is used. This explicit model is different from the reference one described in Section 4.3.1.3 and will referred to as *leu2011-explicit*.

Both models have been depleted at 100MW during 30days with critical search. The results are presented in Figure 4.3.2.2.1. The blue line represents the evolution of the control element positions obtained with *leu2011* and the red one has been obtained with the *leu2011-explicit* model. This time a significant discrepancy appears between the two models. Despite good agreement at BOC, the two curves diverge quickly and increasingly over time. At the end, the discrepancy is so important that the predicted cycle length between the two models is different: a little bit less than 25days is obtained for *leu2011* whereas 29days is obtained for *leu2011-explicit* (a variation of about 16%).

As for the benchmark of the HEU core and Cycle 400 (see previous Section 4.3.2.1), the increase of the discrepancy (not the discrepancy itself) over time has to be related to the decreasing worth of the CEs since blade worth is reduced as the cycle progresses.. To better understand the effect, a second calculation has been carried out using *leu2011-explicit* but without a critical search. The critical positions obtained with *leu2011* have been implemented instead.

Because *leu2011* and *leu2011-explicit* are identical except for the fuel element descriptions and assuming that the control element positions do not affect the fuel burnup distribution, the variation of reactivity between this new hybrid calculation and *leu2011* gives a good estimate of the evolution of the variation of reactivity between the explicit and the homogenized LEU cores.

The results obtained are presented in Figure 4.3.2.2.2. The blue line shows the evolution of the variation of reactivity between *leu2011-explicit* and *leu2011*. This variation is very small at BOC (~+100pcm), but increases quickly in the first week and then remains in the range of 350 to 600 pcm throughout the remainder of the cycle.

Also shown on this figure is the variation of control element positions between the two models (green curve with scale axis on the right). It appears clearly that the variation of reactivity and positions do not follow the same pace which highlights the effect of the relative worth of the CEs with their positions.

Since the models are identical except for the fuel elements description, the non-matching reactivity, or variation of reactivity, is clearly related to the modeling of the fuel regions which then impacts control element position and consequently cycle length.

Since no significant errors have been found in the inputs, an investigation has been carried out to describe the underlying phenomenon that governs the discrepancy between the two models. This investigation was aimed to answer two questions: Why is there a discrepancy between the explicit and homogenized models and why does it occur only with the LEU core. The complete study is presented in Appendix C (physical phenomenon description). Only the most important results and conclusions are provided in this section.

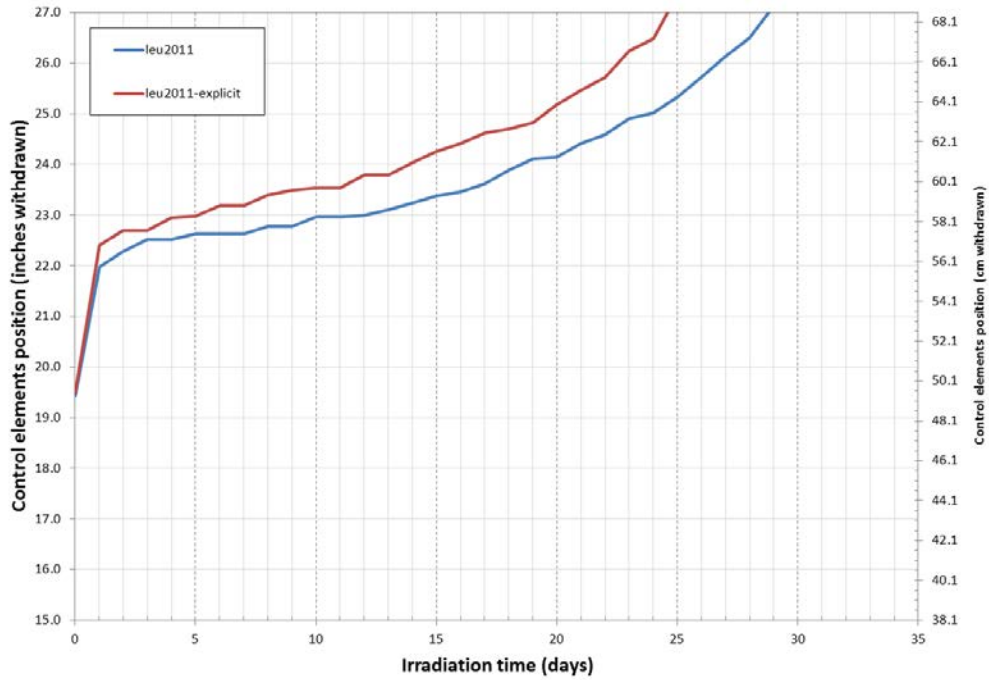

Figure 4.3.2.2.1 - Critical control element positions obtained with *leu2011* and *leu2011-explicit* (at 100MW). Uncertainty < 100pcm/steady state calculation at 1-σ.

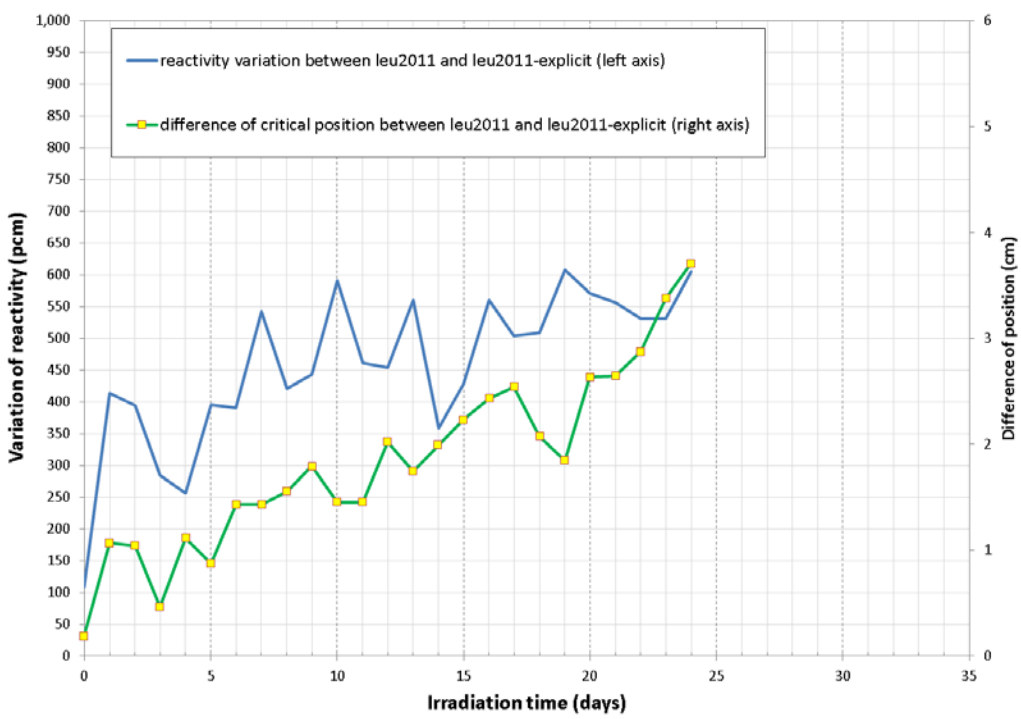

Figure 4.3.2.2.2 – Evolution of the variation of reactivity between *leu2011*-explict and *leu2011* (blue curve). The corresponding discrepancy in control element positions is shown in green (scale on the right vertical axis). Uncertainty < 100pcm/steady state calculation at 1-σ.

In a thermal system, once fission has occurred, the newly created fast neutrons have to slow down and reach thermal energy in order to create new fissions. However, the slowing down process can be stopped at intermediate energy by a parasitic neutron capture in the resonance of the heavy metals absorption cross section (especially the ^{238}U ones). As illustrated in Figure 4.3.2.2.3, in a heterogeneous system, an important fraction of neutrons enter in the moderator in which they can slow down at "no risk" since the moderator is free of heavy metals. Once they are thermalized, they may return into the fuel to create new fissions. This process is not the same in a homogeneous system because slowing neutrons can more easily be captured in a resonance since the probability to "meet" heavy nuclei is higher.

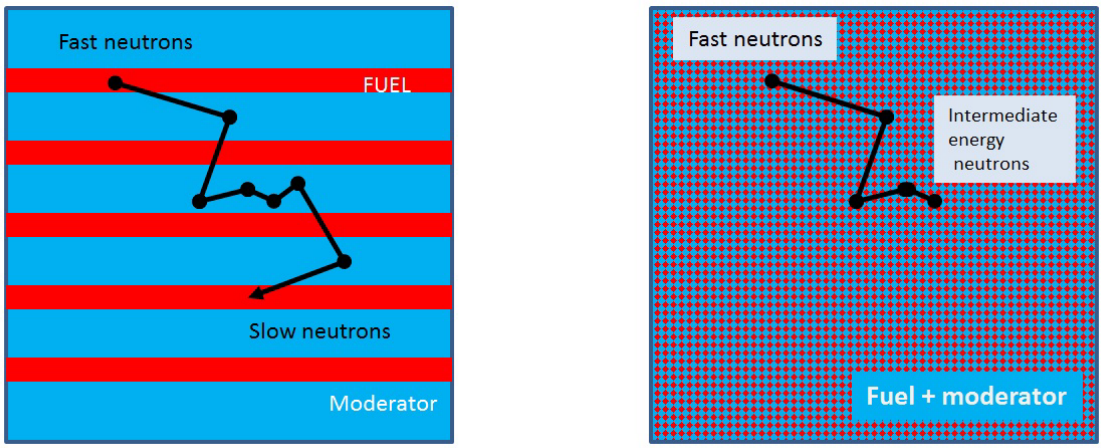

Figure 4.3.2.2.3 – Illustration of the difference between a heterogeneous (left) and homogeneous (right) system. The probability of being captured at intermediate energy is higher in a homogeneous system because the probability to meet heavy nuclei is higher.

Basically, the main difference between a homogeneous and heterogeneous system is the probability for a neutron to escape resonance capture at intermediate energies. If one wants to model a heterogeneous system with a homogeneous description, special care must be taken regarding the bias created by the change made in the physics of the system. Different methods have been developed over the years (Wigner and Bell-Wigner approximations, ABH method, SPH method…) and are generally well explained in the field of reactor physics ([Ref. 26], [Ref. 27], [Ref. 28] for instance).

As a result of the investigation carried out for HFIR (detailed in Appendix C) the following conclusions have been drawn:

- The homogenization of the core affects the reactor physics of both the HEU and LEU core in the same way and at almost the same magnitude (see Appendix C): Differences in neutron spectrum and scalar flux have been clearly identified between the HEU homogeneous/heterogeneous and the LEU homogeneous/heterogeneous models.

- These fundamental differences lead to variations in the evolution of some isotopes (^{135}Xe, ^{149}Sm, Plutonium isotopes…) which can be seen not only by the evolution of their masses but also by their reaction rates and consequently by their worth on core reactivity.

- Despite the number of isotopes impacted by the homogenization, only one has enough worth to create the significant discrepancy observed in the LEU models: The ^{238}U. As it is shown in Table 4.3.2.2.1, the variation of absorption rates between the HEU homogeneous / heterogeneous and the LEU homogeneous / heterogeneous models is the same magnitude (even a little bit more important for the HEU): the ^{238}U absorption rate is clearly higher in the homogenized models but it only impacts the LEU core reactivity because the mass of ^{238}U is 200 times more important in the LEU core than in the HEU one.

- Inversely, the absorption rate of the ^{10}B in the inner filler is more important in the heterogeneous models than in the homogeneous ones. Again, the effect is clearly visible in both the HEU and LEU configurations. This will tend to balance the ^{238}U effect but not for long because the ^{10}B, which in the heterogeneous model separates fuel from moderator, is rapidly depleted and its effect on the core reactivity will decrease rapidly. The boron effect can explain why the agreement between the LEU homogeneous and heterogeneous models is better at BOC than for the rest of the cycle.

Table 4.3.2.2.1 – Absorption rate of ^{238}U (expressed in 10^{12} absorption/s) obtained with the HEU and LEU homogeneous (RZ) and heterogeneous (explicit) models by locations and time in the cycle. Error < 1% at 1-σ.

period	location	HEU			LEU		
		explicit	RZ	variation	explicit	RZ	variation
BOC	IFE	2.18	2.36	**-7.63%**	99.4	108	**-7.96%**
	OFE	2.23	2.42	**-7.85%**	64.9	70.1	**-7.42%**
day24	IFE	2.1	2.26	**-7.08%**	99.2	106	**-6.42%**
	OFE	2.26	2.49	**-9.24%**	67	72.3	**-7.33%**

Of course, one cannot be totally certain of the reliability of the cycle length prediction of the heterogeneous or homogeneous models without a benchmark against experiment. Nonetheless, basic physics arguments can explain why homogeneous representation of a heterogeneous system introduces systemic bias in the reactor physics (neutron escape probability in the resonances at intermediate energies is biased). This bias has to be corrected for if not eliminated through an explicit heterogeneous geometry description. It has been shown that the two geometric representations of the HFIR core, homogeneous and heterogeneous, predict different neutron spectra and fluxes (more details in Apendix C). These differences are independent of the type of fuel considered. However, depending on the nature of the fuel, the differences may or may not impact the overall behavior of the core. As a conclusion of this investigation, ANL would not recommend the use of LEU homogeneous models for HFIR analyses. It is not believed that the explicit models are perfect but the advantage is that the magnitude of the bias introduced by the geometric approximations has been reduced to a minimal level.

4.3.2.3 Cycle length for ANL Reference Inputs

This section presents the cycle length predicted with the ANL reference inputs described in Section 4.3.1 which will be used as inputs of the matrix of performance. Recall that two series of two inputs are considered. The fundamental difference between the two series is the experimental loading in the flux trap (31 curium targets in Series *l11* and only dummy targets in Series *c400*). Each series is made of two inputs, HEU and LEU. The HEU models are depleted at 85MW and the LEU ones at 100MW, always using the critical search capability.

The critical control element positions obtained for the 4 cases are shown in Figure 4.3.2.3.1. The blue and red solid lines represent the results obtained with the Series *c400,* HEU and LEU cores, respectively. The blue and red dashed lines are for the Series *l11,* HEU and LEU cores, respectively. The calculated cycle lengths are compiled in Table 4.3.2.3.1.

From these results, one can draw the following conclusions:

- The difference of experimental loading between l11 and c400 has a limited effect on the cycle length (variation of 2 and 3% for the HEU and LEU cores, respectively).

- The different modifications made in the ORNL original HEU input (*HFV4.0*) to get the model used for the benchmark of Cycle 400 (including the insertion of depleted CEs) or the two ANL reference models did not produce a significant change in the calculated cycle length (*HFV4.0-explicit* = 26days, Cycle 400 input = 24.5days, HEU Series *c400* and *l11* =25.5 and 25days, respectively).

- This is not the case for the LEU cores. Recall that the variation of reactivity between the original *leu2011* and the reference input, *l11* LEU, are about 1200 pcm, mainly due to the switch from depleted to fresh CE compositions (see Section 4.3.1.2, Table 4.3.1.2.1) and induced a variation of 3days in the cycle length. The ageing of the control elements has apparently a very different effect on the HEU and LEU cores. The CEs worth evolution impacts a the LEU elements much more.

- Finally, no matter what series of inputs is considered, the ANL explicit model, the LEU cores are predicted to operate nearly 30% longer than the HEU cores. This extended core operation is noteworthy since it is very favorable for conversion analyses. Whereas the ORNL results predict a cycle length of the LEU core similar to the HEU one (~26days) [Ref. 4], the explicit model presented herein provides a significantly longer predicted operating cycle.

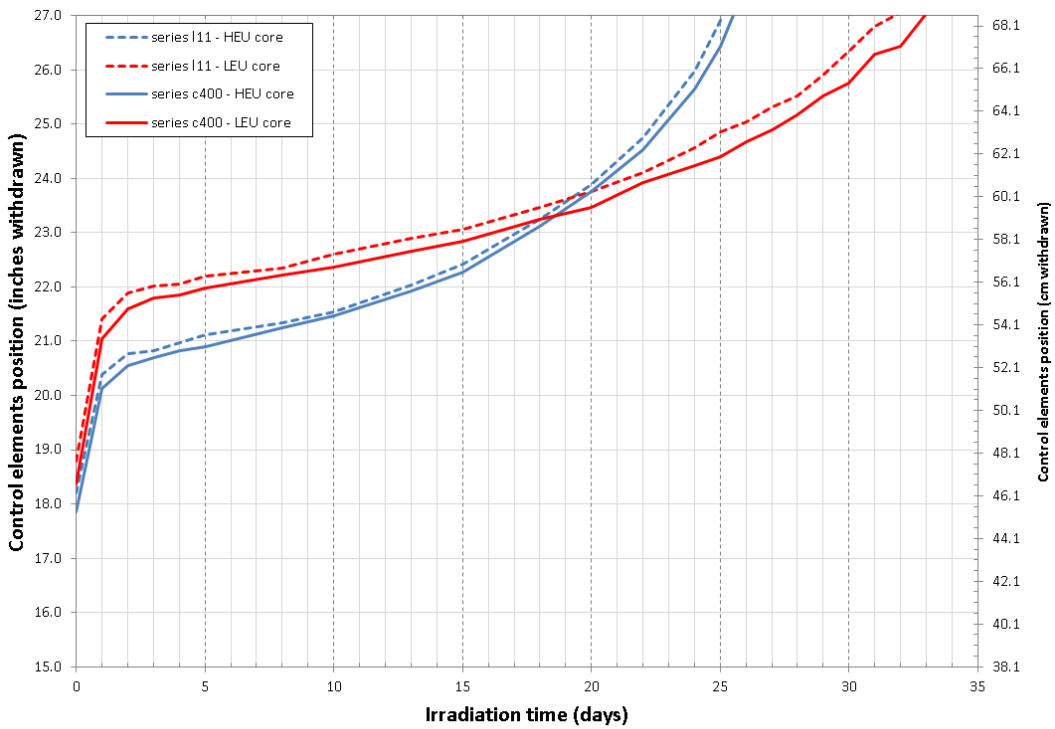

Figure 4.3.2.3.1 – Critical control element positions for the 4 ANL reference inputs. Uncertainty < 100pcm/steady state calculation at 1-σ.

Table 4.3.2.3.1 – Calculated cycle length for ANL reference inputs.

	cycle length (days)		variation *c400* / *l11* (%)
	series *c400*	series *l11*	
HEU	25.5	25	2.0%
LEU	33	32	3.1%
Increase in LEU cycle length vs. HEU (%)	29.5%	28.0%	

4.3.3 Power Distribution

Even though the magnitude and the distribution of power are not direct parameters of the matrix of performance, their accurate estimation is crucial to determine if the reactor can operate safely or not. This section presents the methodologies and results obtained with the two series of reference inputs described in the previous section.

4.3.3.1 Methodology

MCNP does not model all phenomena which contribute to the power and does not calculate the magnitude of the power, only the distribution. One has to introduce some hypotheses and to normalize the calculational results to obtain the parameters of interest. The different contributions considered relevant to the evaluation of the total power are summarized in Table 4.3.3.1.1. All of the calculated contributions are based on the MCNP heating tally, "F6". The beta decay energy is assumed to be deposited only in the fuel, worth 6.5MeV/fission of ^{235}U and its distribution is assumed to be the same as the fission one (obtained using "F6 mode n" tally). The evaluation of the delayed gamma energy is more complicated. Its magnitude is assumed to be constant and worth 6.33MeV/fission of ^{235}U. Its distribution is not calculated by MCNP and it is assumed that the distribution is the same as the prompt gamma one. The problem is that there is no distinction between the capture and prompt gamma energy using a F6 tally. Fortunately, it is possible to disable the capture reaction in MCNP thanks to the card PIKMT, and thus to obtain the prompt gamma distribution. However, two MCNP calculations, with and without the use of the PIKMT card, are required. The total recoverable energy per fission, *Q,* is the sum of the different contributions described in Table 4.3.3.1.1. The MCNP score of a F6 tally is expressed in MeV/MCNP-neutron-source-particle. One has to multiply this score by the number of neutrons per second, ν (also calculated by MCNP), to obtain the energy per fission. Thus, by tallying the entire core and normalizing the number by ν one can deduce *Q*:

$$Q = Q_1 + Q_2 + Q_3 + Q_4 + Q_5 + Q_6$$

$$s_{MCNP} = (Q_1 + Q_2 + Q_3 + Q_4).\upsilon$$

$$Q = s_{MCNP}.\upsilon + Q_5 + Q_6 = s_{MCNP}.\upsilon + 6.5 + 6.33 = s_{MCNP} \cdot \upsilon + 12.83$$

where

- *Q* (MeV/fission): total recoverable energy per fission.
- Q_1, Q_2, Q_3, Q_4 (MeV/fission): total recoverable energy per fission due to the fission fragments, kinetic energy of the neutrons, gamma capture and prompt gamma, respectively.
- Q_5, Q_6 (MeV/fission): total recoverable energy due to beta decay and delayed gamma, respectively.
- S_{MCNP} (MeV/neutron-source): F6 tally score when applied to the entire reactor.
- ν: number of neutrons created per fission.

Once Q is known, the number of fissions created per second, α, in the reactor is deduced from the total nuclear power, P, via the relation:

$$\alpha = \frac{P}{Q \cdot e}$$

where:

- α (fissions/second): number of fissions created per second in the reactor
- P (MW): total nuclear power
- Q (MeV/fission): total recoverable energy per fission
- e (MeV/MJ): constant, from 1eV = 1.602×10^{-19} J.

One can then deduce the power deposited in a region of the reactor, P_{region}, by tallying the region with the adequate F6 tally, normalizing the results to have the local energy deposited per fission, Q_{region} (MeV/fission), and multiplying the result by the product, α·e:

$$P_{region} = Q_{region} . \alpha \cdot e$$

where:

- α (fissions/second): number of fissions created per second in the reactor
- P_{region} (MW): nuclear power deposited in the region
- Q_{region} (MeV/fission): recoverable energy per fission in the region
- e (MeV/MJ): constant, from 1eV = 1.602×10^{-19}J.

The regions of interest for this study are the two fuel elements. The power has not been evaluated only in the fuel meat but in all parts that can impact the coolant temperature:

- cladding
- side plates
- coolant
- filler (with burnable absorber)
- zirconium layers (LEU core only)

Table 4.3.3.1.1 – Contribution to the power and methods to evaluate them

contribution	evaluation	MCNP tallies or values
kinetic energy of fission fragments	calculated	F6
kinetic energy of fission neutrons	calculated	F6
gamma energy from (n,g) capture	calculated	F6
prompt gamma energy	calculated	F6
beta decay energy	assumed deposited in fuel only and to have fission distribution	Relative fraction of core total 6.5MeV/fission ^{235}U scaled base on the local fission distribution
delayed gamma energy	assumed to have prompt gamma distribution	Relative fraction of core total 6.33MeV/fission ^{235}U scaled base on the prompt gamma distribution (used of the PIKMT card)

4.3.3.2 Distribution of Power in the Whole Reactor

The fraction of power deposited in the fuel elements (meat, cladding, coolant, side plates, filler and zirconium layers) has been evaluated for the 4 reference inputs at different time steps. Results obtained are shown in Figure 4.3.3.2.1. The solid and dashed lines represent the results obtained with Series *c400* and *l11*, respectively. The blue and red lines represent the results obtained with the HEU and LEU cores, respectively.

The evolution of the fraction of power deposited in both the inner and outer elements is shown on the top picture. For both the HEU and LEU cores, this fraction is relatively constant over the irradiation: The magnitude of the variation is about 0.5% with an exception for the Series *c400* HEU at day 1 (+2%). There are also small differences between the two series (around 1%). The fraction of power deposited in the LEU core is around 96% and 93-94% for the HEU. This small variation between HEU and LEU can be explained by the fact that the LEU fuel is more absorbing than the HEU one. The value obtained for the HEU core is slightly below the one specified in the HFIR Safety Analysis Report (SAR) (97.5%) [Ref. 15] and used by ORNL for both the HEU and LEU analyses.

The evolution of the fraction of power deposited in the outer and inner fuel elements is shown on the middle and bottom picture, respectively. The relative constancy of the power deposited in both elements is a result of power redistribution trends occurring in the two elements. Thus, it is observed that the fraction of power in the outer element tends to increase over time (+2% for the LEU cores, +3-4% for the HEU cores) whereas the power in the inner fuel element tends to decrease a similar magnitude. This behavior is attributable to the control elements adjacent to the outer element. It is reasonable to think that most of the neutrons captured by the CEs come from the outer element which tends to reduce the element power (less neutrons come back to create new fissions). This effect is reduced when the CEs are withdrawn and the power is rebalanced.

The details of the different contributions (clad, coolant…) to the IFE and OFE power has also been investigated. Results taken at BOC, day 1 and EOC are compiled in Table 4.3.3.2.1. The following observations can be made:

- The fractions of the different contributions do not change significantly over the time except for the inner filler. That can be explained by the depletion of the boron which reduces the alpha heating over the irradiation. But the effect is not important because the magnitude is very small.

- The fuel is obviously the most important contributor. Its importance is slightly greater in the LEU core than in the HEU core but also in the OFE compared to the IFE.

- After the fuel, the two largest contributions come from the coolant (~2.3%) and the cladding (~0.8-1.5%). For an unexplained reason, the contribution of the cladding and the other aluminum structures in general (side-plates) has decreased by almost a factor of two in the LEU cores even though the mass of aluminum is almost the same.

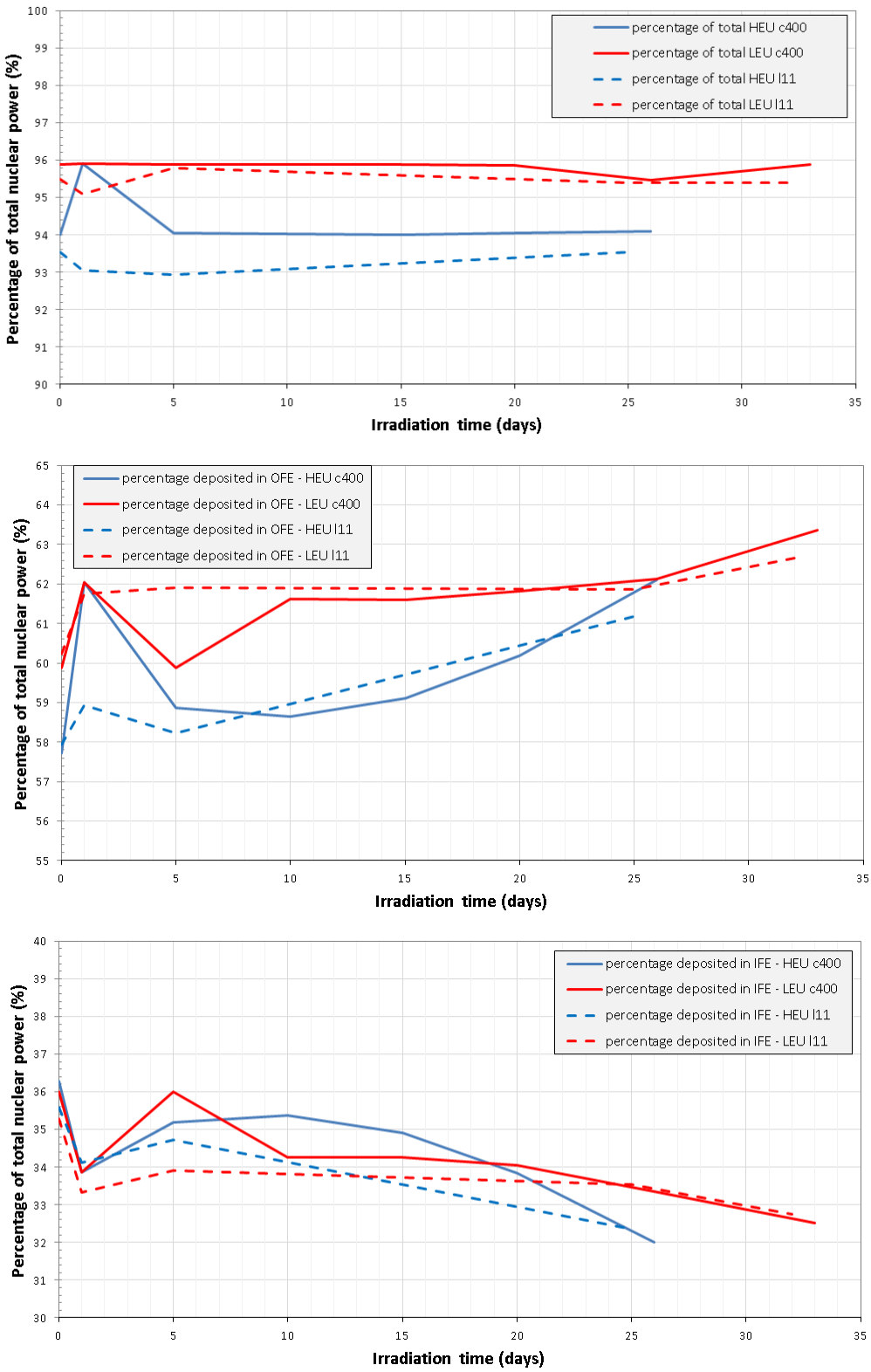

Figure 4.3.3.2.1 – Evolution of the fraction of power deposited in both elements (top), OFE (middle) and IFE (bottom).

Table 4.3.3.2.1 – Detail of the different contributions to the IFE and OFE powers at different periods of time and for the 4 reference inputs. Uncertainty max. < 0.5% of the value at 1-σ

BOC								
Fraction of local power (%) deposited in…	*c400* - HEU		*c400* - LEU		*l11* - HEU		*l11* - LEU	
	IFE	OFE	IFE	OFE	IFE	OFE	IFE	OFE
Fuel meat	94.99%	95.61%	96.10%	97.05%	94.95%	95.62%	96.08%	97.06%
coolant	2.27%	2.15%	1.80%	1.59%	2.29%	2.14%	1.81%	1.58%
cladding	1.25%	1.50%	0.77%	0.82%	1.27%	1.50%	0.78%	0.81%
filler	0.68%	-	0.66%	-	0.68%	-	0.66%	-
inner side-plate	0.22%	0.40%	0.15%	0.23%	0.23%	0.39%	0.15%	0.23%
outer side-plate	0.58%	0.35%	0.35%	0.19%	0.59%	0.35%	0.36%	0.19%
zirconium layer	-	-	0.16%	0.13%	-	-	0.16%	0.13%
Power (MW)	30.83	49.07	35.99	59.89	30.26	49.28	35.28	60.22
day 1								
Fraction of local power (%) deposited in…	*c400* - HEU		*c400* - LEU		*l11* - HEU		*l11* - LEU	
	IFE	OFE	IFE	OFE	IFE	OFE	IFE	OFE
Fuel meat	94.94%	95.69%	96.06%	97.12%	94.91%	95.69%	96.03%	97.12%
coolant	2.31%	2.11%	1.82%	1.55%	2.32%	2.11%	1.83%	1.55%
cladding	1.27%	1.47%	0.79%	0.80%	1.28%	1.47%	0.79%	0.80%
filler	0.66%	-	0.65%	-	0.66%	-	0.66%	-
inner side-plate	0.23%	0.38%	0.15%	0.22%	0.23%	0.38%	0.15%	0.22%
outer side-plate	0.59%	0.35%	0.36%	0.19%	0.60%	0.35%	0.37%	0.19%
zirconium layer	-	-	0.16%	0.12%	-	0.12%	0.16%	0.12%
Power (MW)	29.48	50.48	33.86	62.05	29.00	50.14	33.34	61.74
EOC								
Fraction of local power (%) deposited in…	*c400* - HEU		*c400* - LEU		*l11* - HEU		*l11* - LEU	
	IFE	OFE	IFE	OFE	IFE	OFE	IFE	OFE
Fuel meat	94.83%	95.67%	96.08%	97.08%	94.86%	95.64%	96.09%	97.07%
coolant	2.42%	2.10%	1.88%	1.56%	2.41%	2.11%	1.87%	1.56%
cladding	1.39%	1.51%	0.83%	0.82%	1.38%	1.52%	0.83%	0.83%
filler	0.47%	-	0.51%	-	0.47%	-	0.51%	-
inner side-plate	0.24%	0.36%	0.16%	0.21%	0.24%	0.37%	0.16%	0.21%
outer side-plate	0.64%	0.36%	0.38%	0.20%	0.64%	0.36%	0.37%	0.20%
zirconium layer	-	-	0.17%	0.13%	-	-	0.17%	0.13%
Power (MW)	27.20	52.78	32.52	63.36	27.50	51.97	32.75	62.68

4.3.3.3 Distribution of Power in the Fuel

As explained in Section 4.3.1.1, the fuel and filler in the IFE and fuel in the OFE have been divided in 7 radial x 23 axial regions. Details of the mesh are given in Tables 4.3.1.1.2 and 4.3.1.1.3.

The axial distributions obtained in each radial layer in the IFE and OFE for the HEU cores, *c400* and *l11,* at BOC are presented in Tables 4.3.3.3.1 and 4.3.3.3.2. The distributions at EOC are shown in Tables 4.3.3.3.3 and 4.3.3.3.4. The relative power density is shown there. The radial regions are named Radial 1 to Radial 7 and go from the inner (Radial 1) to the outer (Radial 7) edge of the fuel. On each graph, the blue line and black crosses represent the results obtained with the series, *c400* and *l11*, respectively. The only HEU power distribution found for comparison come from the SAR (black line with yellow dots on the figures). The numbers in the SAR tables come from both calculations and experiment in the sense that critical experiments at zero power have been carried out to evaluate the power distribution but not with the final HFIR configuration. Calculations have been used to extrapolate the data and obtain an estimate of the current HEU design power distribution.

From BOC to EOC, IFE and OFE, the distributions obtained with Series *c400* and *l11* are almost similar. The power distribution in the HEU core can thus be considered independent of the experimental loading in these core configurations. At BOC, the calculated distributions are in very good agreement with the SAR distributions. The effect of the CEs on the power distribution of the outermost radial region of the OFE is clearly visible: The distribution presents a triangular shape more than a cosine shape like in the other regions. Power peaking at the top and bottom of the fuel is also clearly visible. It seems to have the same magnitude at the top and bottom.

At EOC, the comparison with the SAR distributions is also very good except at the edges of the fuel. In the IFE and OFE, the power distribution in the inner (IFE and OFE) and outer edges (OFE) is predicted to be flat and have a low magnitude but in the SAR, the distributions have a more pronounced cosine shape. Recall that the SAR distributions are obtained from calculations and critical experiment data at zero power, meaning that the effect of burnup on the power distribution has been estimated but not measured. From the ANL analyses, the calculated flat profile in the inner edges show that the fuel consumption and poisoning due to fission product buildup is so high that the distribution of power has shifted to the center of the plate. The axial distributions obtained in each radial layer in the IFE and OFE for the LEU cores, *c400* and *l11,* at BOC are given in Tables 4.3.3.3.5 and 4.3.3.3.6. The distributions at EOC are provided in Tables 4.3.3.3.7 and 4.3.3.3.8. The comparison with the ORNL data ([Ref. 4], Tables 5 & 6) is also presented. The corresponding ANL tables for configuration l11 are provided in appendix D (only l11 is presented due to the similarity with the other series). Except for the inner edge of the IFE at EOC, the ANL power distributions are always in good agreement with the ORNL ones. Some variations may exist but it is believed that they are related to the fuel discretization. The effect of the fuel axial grading is also clearly visible: No power peaking occurs at the bottom of the fuel.

In both Series *c400* and *l11*, the maximum heat flux obtained with the LEU cores occurs at day 1 in the outer edge of the OFE and in the mid-plane and is calculated as 404 and 395 W/cm^2, respectively. These numbers seem to be in good agreement with the ORNL one: 393W/cm^2 at the same location and, same day of irradiation [Ref. 4].

Figure 4.3.3.3.1 – Relative Power density in the HEU IFE fuel at BOC. HEU Series *c400* & *l11* compared with the reference distribution provided in the SAR Table 4.3.1. Uncertainty max. < 0.1 relative power density at 1-σ.

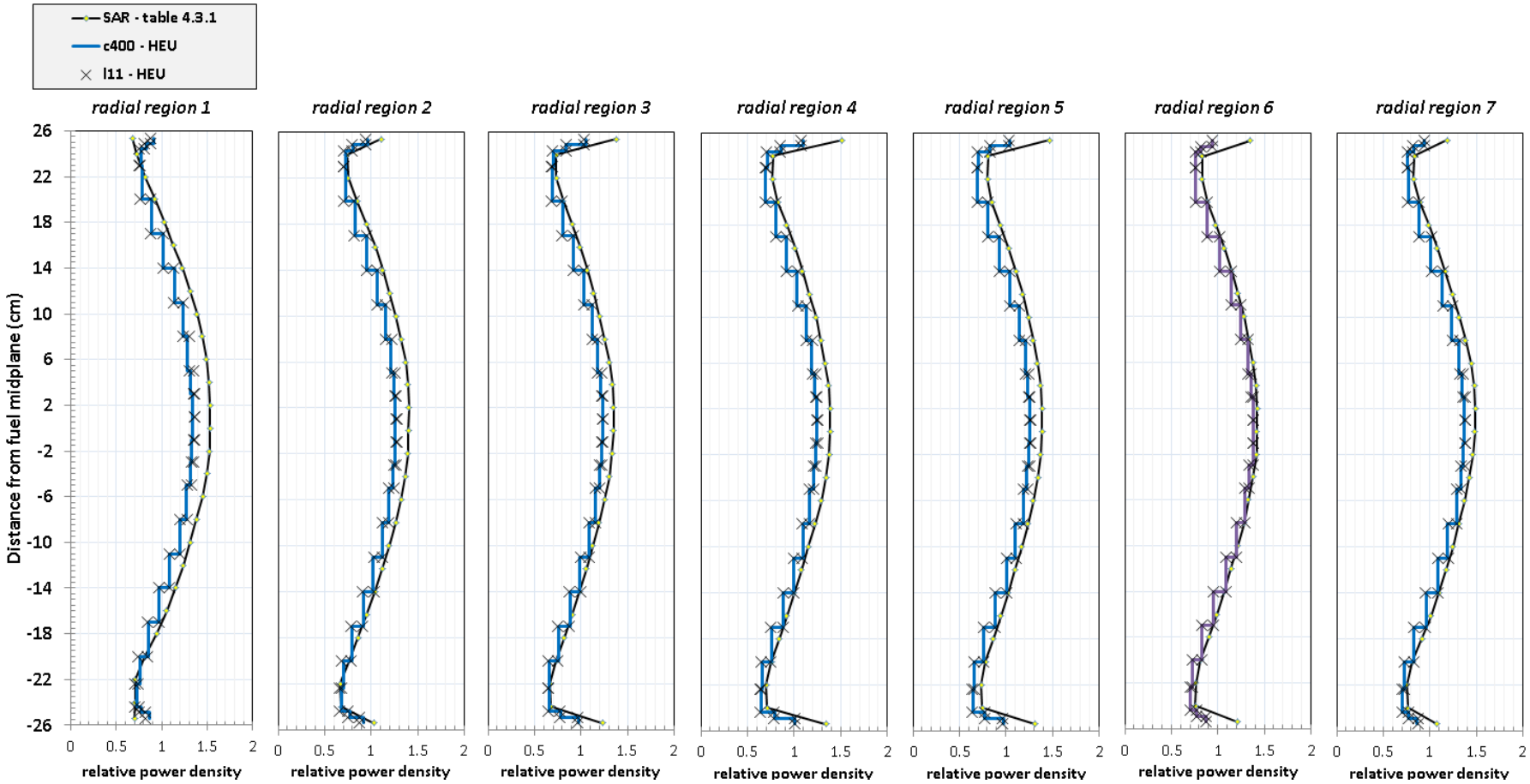

Figure 4.3.3.3.2 – Relative Power density in the HEU OFE fuel at BOC. HEU Series *c400* & *l11* compared with the reference distribution provided in the SAR Table 4.3.1. Uncertainty max. < 0.1 relative power density at 1-σ.

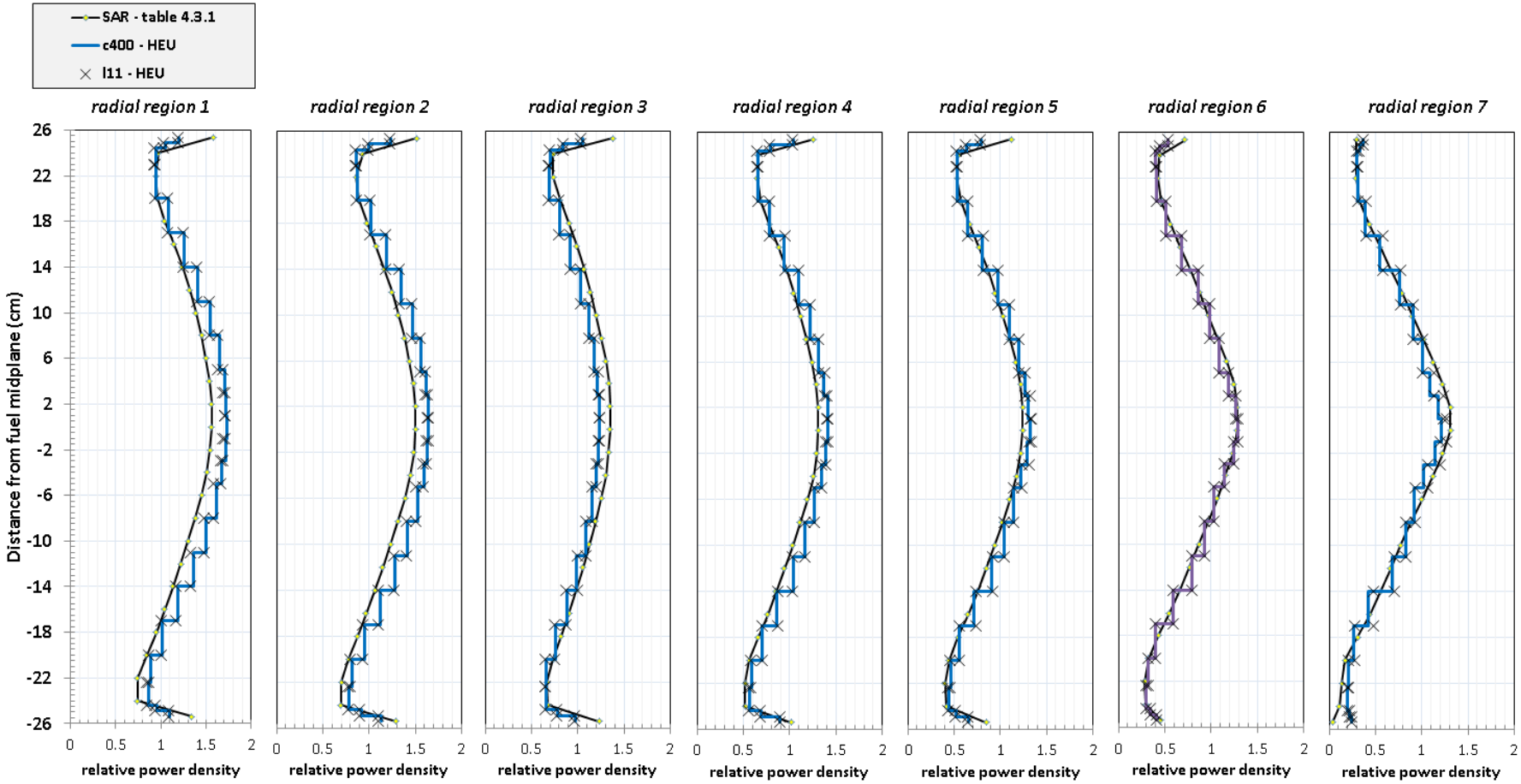

Figure 4.3.3.3.3 – Relative Power density in the HEU IFE fuel at EOC. HEU Series *c400* & *l11* compared with the reference distribution provided in the SAR Table 4.3.1. Uncertainty max. < 0.1 relative power density at 1-σ.

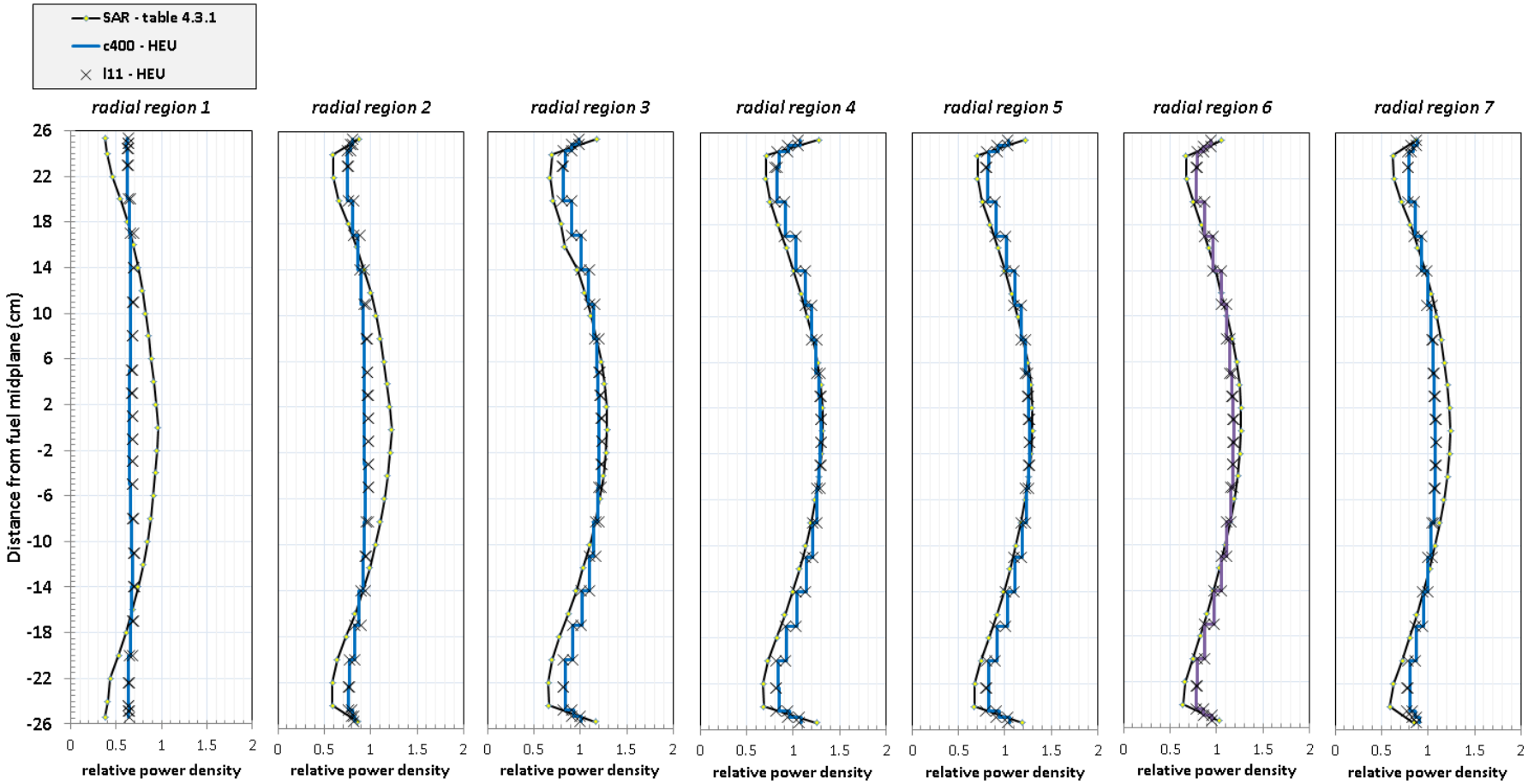

Figure 4.3.3.3.4 – Relative Power density in the HEU OFE fuel at EOC. HEU Series *c400* & *l11* compared with the reference distribution provided in the SAR Table 4.3.1. Uncertainty max. < 0.1 relative power density at 1-σ.

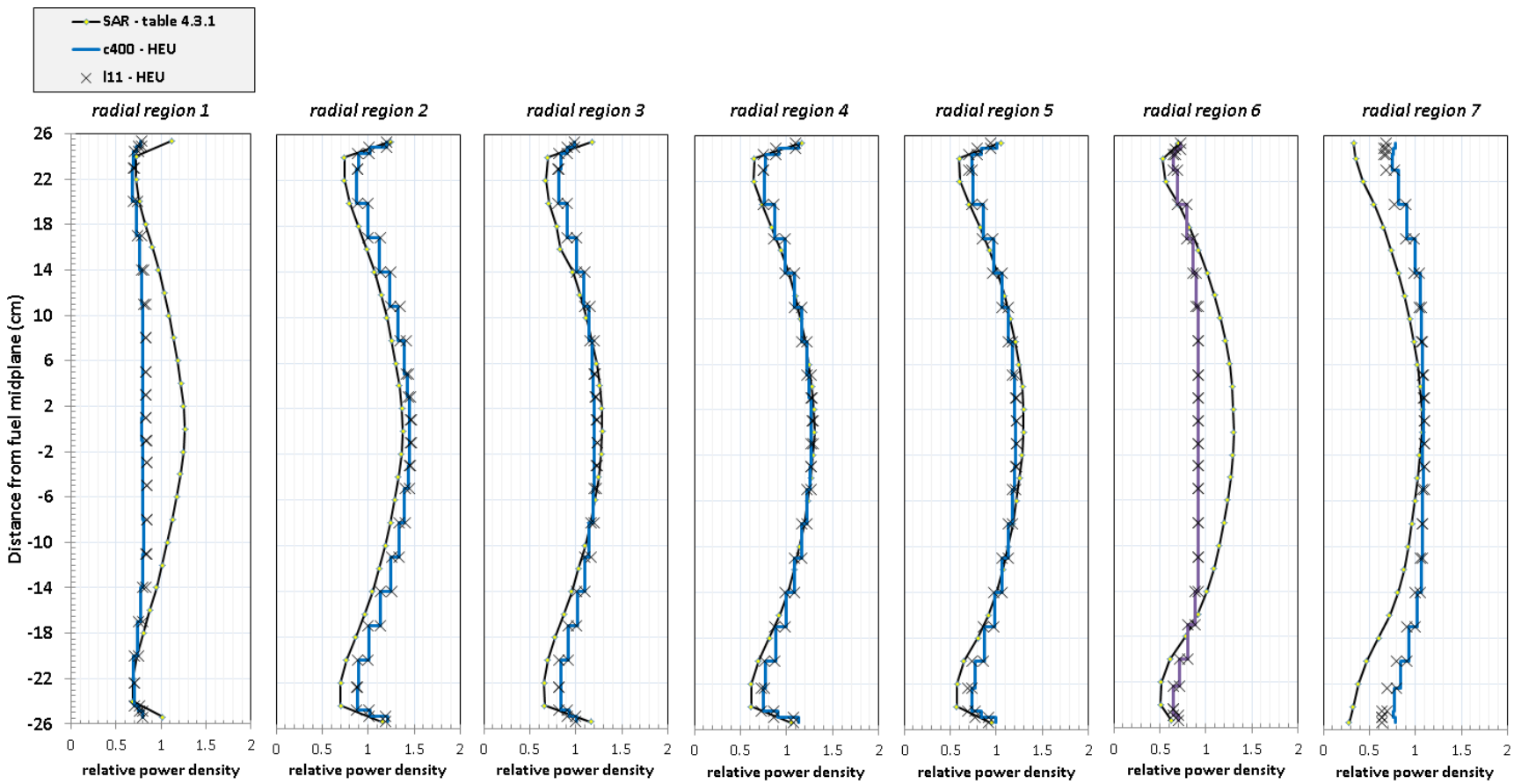

Figure 4.3.3.3.5 – Relative Power density in the LEU IFE fuel at BOC. LEU Series *c400* & *l11* compared with the reference distribution provided in ORNL [Ref. 4], Table 5. Uncertainty max. < 0.1 relative power density at 1-σ.

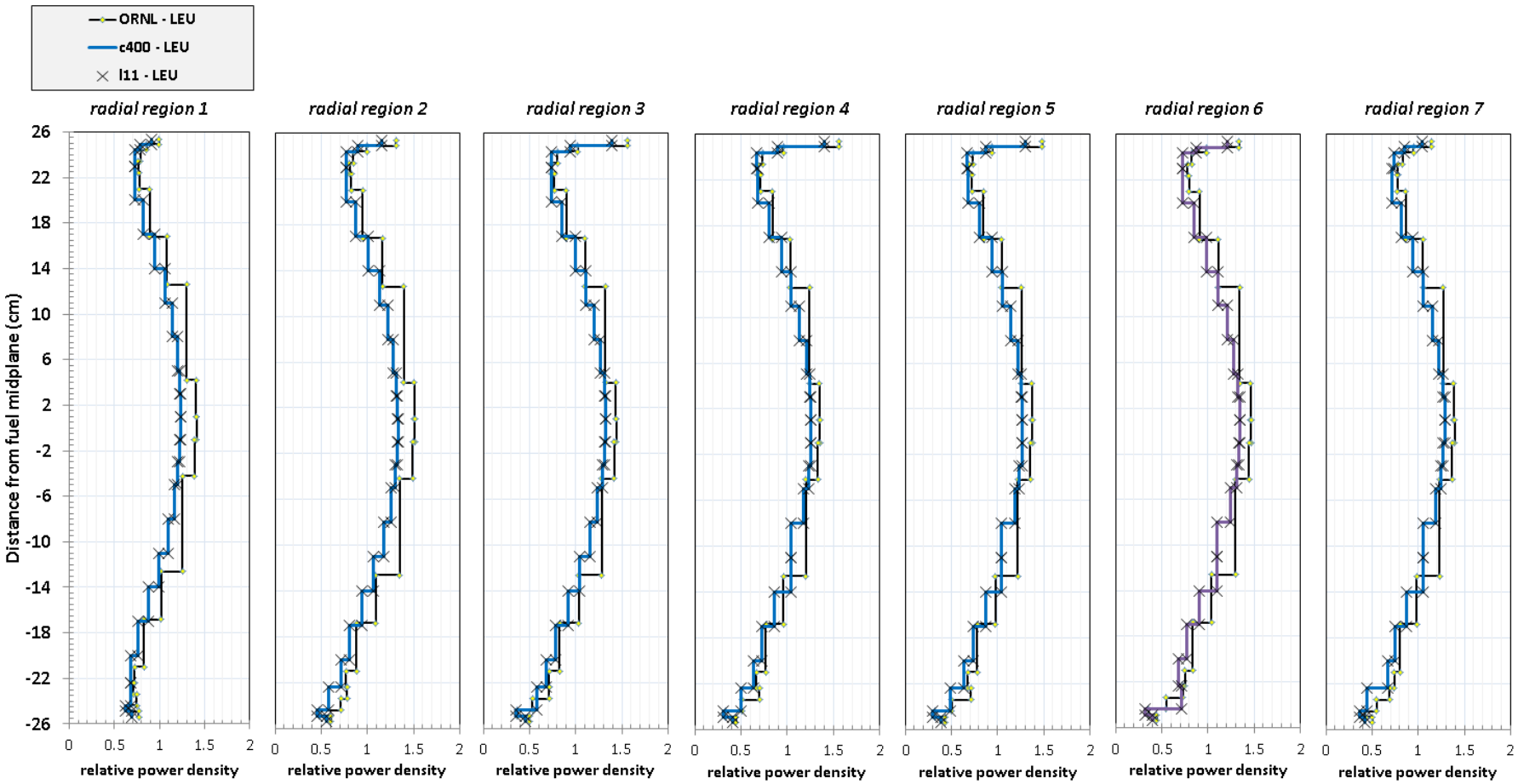

Figure 4.3.3.3.6 – Relative Power density in the LEU OFE fuel at BOC. LEU Series *c400* & *l11* compared with the reference distribution provided in ORNL [Ref. 4], Table 5. Uncertainty max. < 0.1 relative power density at 1-σ.

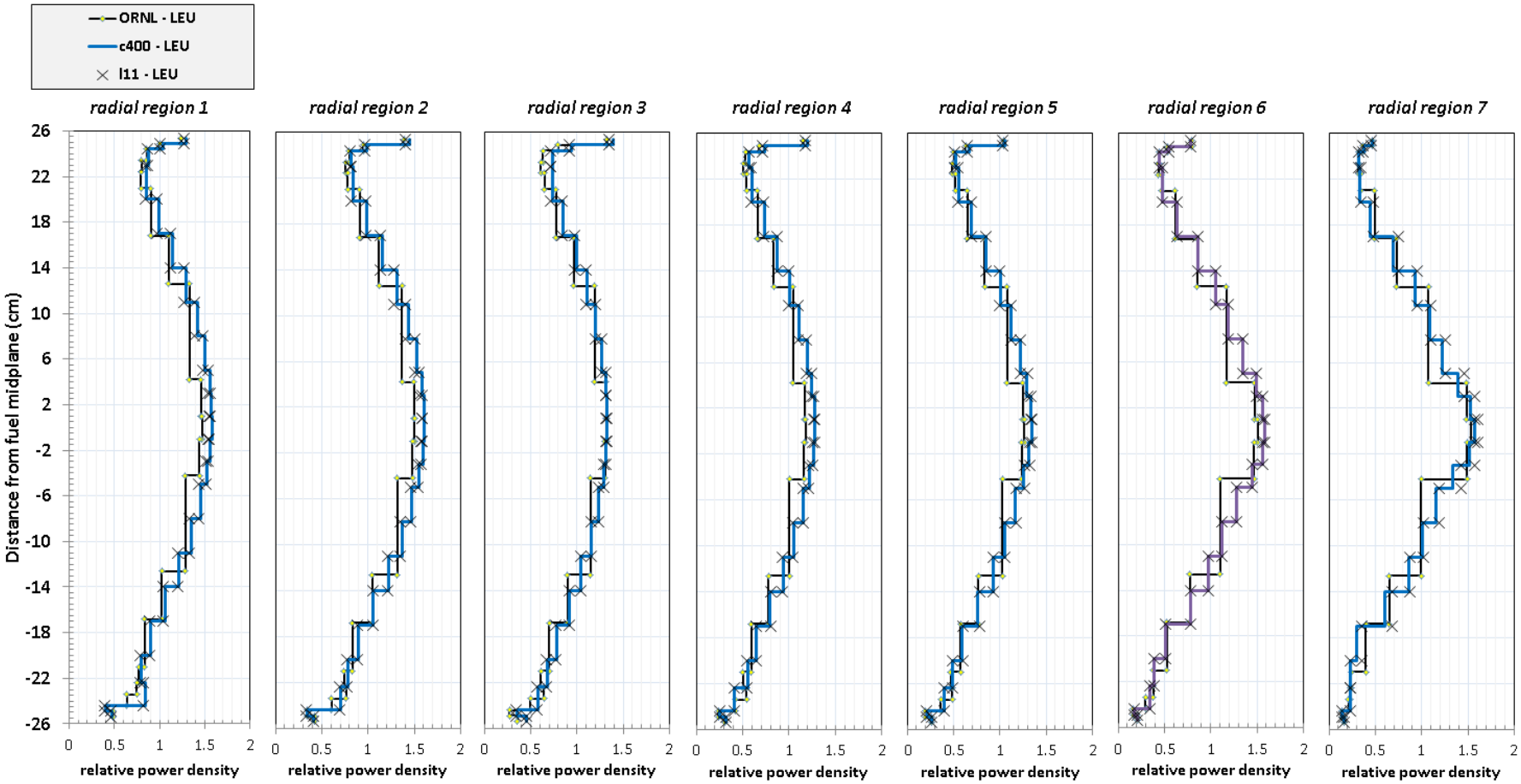

Figure 4.3.3.3.7 – Relative Power density in the LEU IFE fuel at EOC. LEU Series *c400* & *l11* compared with the reference distribution provided in ORNL [Ref. 4], Table 6. Uncertainty max. < 0.1 relative power density at 1-σ.

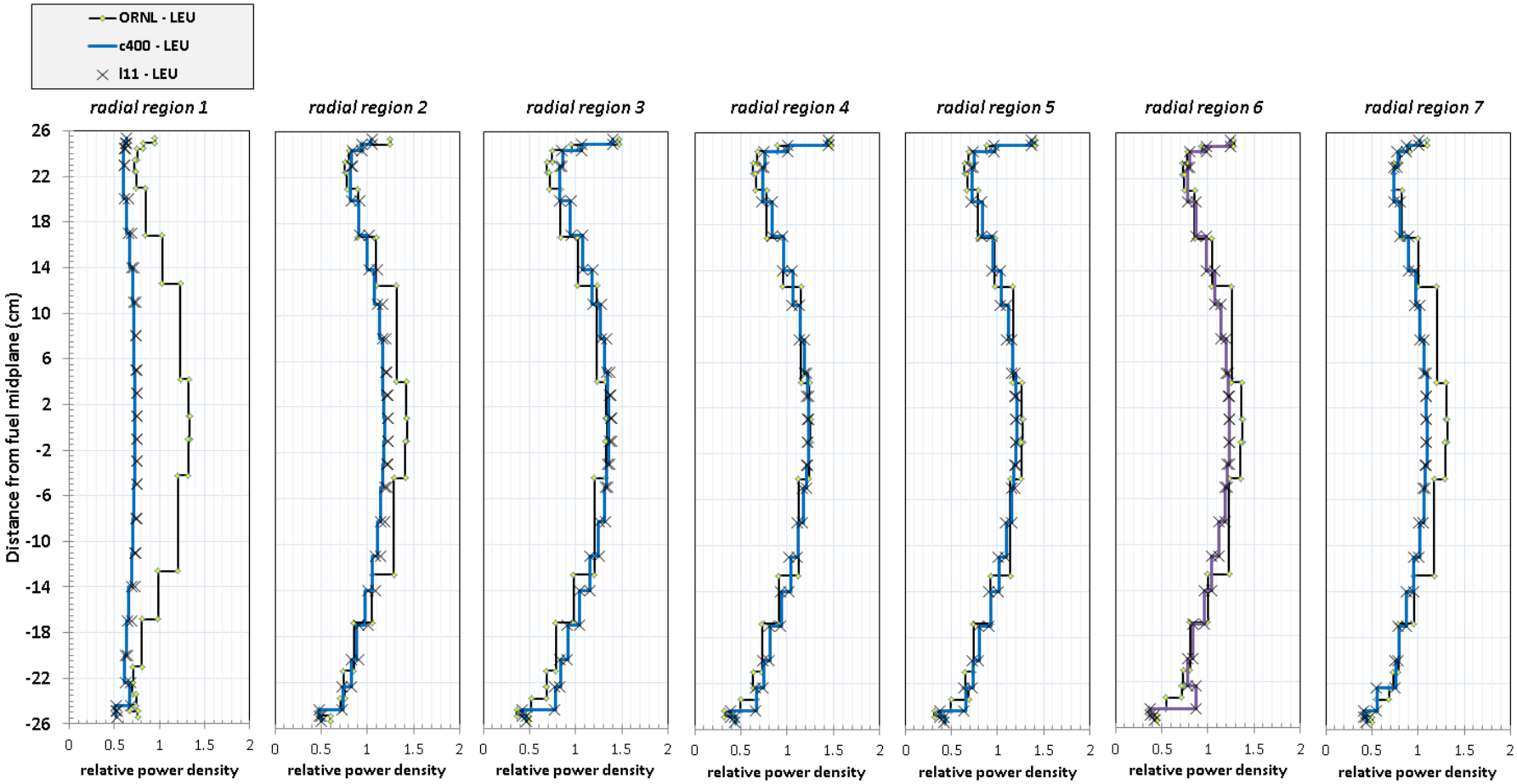

Figure 4.3.3.3.8 – Relative Power density in the LEU OFE fuel at EOC. LEU Series *c400* & *l11* compared with the reference distribution provided in ORNL [Ref. 4], Table 6. Uncertainty max. < 0.1 relative power density at 1-σ.

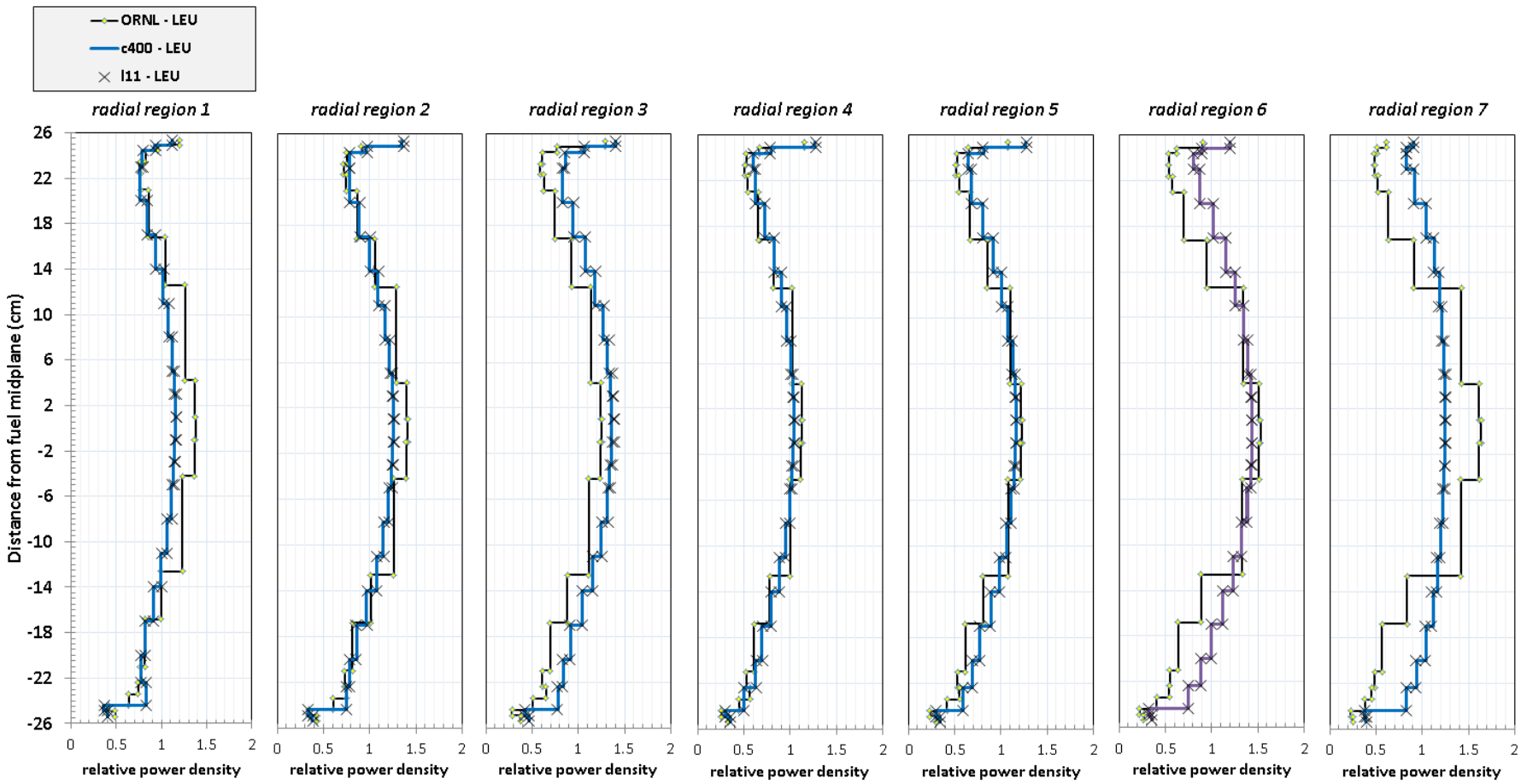

4.3.4 Neutron Flux

The neutron flux together with the cycle length is the key parameter that allows the evaluation of the matrix of performance of the reactor. The methodology to calculate the flux is first described, followed by a comparison of the ANL and ORNL results. Finally, the evaluation of the matrix of performance of the HEU and LEU cores calculated by ANL is presented and discussed.

4.3.4.1 Methodology

The flux has been calculated at different locations, different periods and with the 4 ANL reference inputs with the MCNP "tally" F4, which provides the neutron flux averaged over a cell. It is expressed per neutron-source. The result has to be normalized to obtain a physical unit; it has to be multiplied by the number of neutrons in the reactor, τ. The relation between the total nuclear power in the reactor P (85MW for HEU and 100MW for LEU) and the number of neutrons, τ, is given by the following equation:

$$\tau = \alpha \cdot \upsilon = \frac{P}{Q \cdot e} \cdot \upsilon$$

With:

- α (fissions/second): number of fissions created per second in the reactor
- P (MW): total nuclear power
- Q (MeV/fission): total recoverable energy per fission
- e (MeV/MJ): constant, from 1eV = $1.602e^{-19}$J
- ν: number of neutrons created per fission.
- τ (neutrons/second): number of neutrons created per second in the reactor.

As for the evaluation of the power, the total recoverable energy per fission is required. The methodology to extract this number has already been explained in Section 4.3.3.1. The values of τ obtained with the 4 ANL reference inputs at the different periods considered are shown in Table 4.3.4.1.1. The comparison with the ORNL values is also provided. The ANL numbers differ slightly from one series to the other. The ORNL and ANL numbers are also very close. The significant variation between the HEU and LEU numbers is due to the difference in power between the cores (HEU 85MW and LEU 100MW). Recall that the cycle length predicted by ORNL for the LEU core is~25days which explains the absence of number at day 33 for ORNL.

Table 4.3.4.1.1 – Number of neutrons created per second, τ, in the reactor. Uncertainty max. < 0.5% at 1-σ.

Time	ORNL		ANL series *l11*		ANL series *c400*	
	HEU	LEU	HEU	LEU	HEU	LEU
day 0 (BOC)	6.47E+18	7.66E+18	6.46E+18	7.63E+18	6.46E+18	7.63E+18
day 25 (~EOC for HEU)	6.47E+18	7.66E+18	6.44E+18	7.59E+18	6.45E+18	7.64E+18
day 33 (~EOC for LEU)	-	-	-	7.60E+18	-	7.67E+18

4.3.4.2 Neutron flux distribution

To have a general idea of the distribution and evolution of the neutron flux for both the HEU and LEU cores, the flux has been calculated along the radial direction and averaged axially from +30 to -30cm from the core mid-height (almost the total height of the fuel plates and in-core irradiation positions). Only the ANL reference inputs have been used.

The distributions obtained at BOC and EOC with the Series *l11* (HEU and LEU core) are shown in Figures 4.3.4.2.1 and 4.3.4.2.2, respectively. Only the Series *l11* results are presented because of the strong similarity with the other series. The variation of the flux for LEU and HEU at BOC and EOC is shown in Figures 4.3.4.2.3 and 4.3.4.2.4, respectively. Each figure is made of three plots, one for each energy range: thermal (<0.625eV), epithermal (0.625eV to 100 keV) and fast (100keV to 20MeV). Due to the complexity of the flux distribution, each figure is accompanied with a half-reactor picture making the localization of the flux extremums easier to relate to the HFIR configuration. In the figures, 5 regions are highlighted: Region 1 is the flux trap; Regions 2 and 3 are the IFE and OFE; Regions 4 and 5 are the removable and permanent reflector, respectively. Recall that the HEU and LEU core power is 85 and 100MW, respectively.

For the three energy ranges, at BOC as for EOC, the flux distribution of the HEU and LEU cores follows the same trend. The distribution is complicated but can be easily explained with basic arguments. The fast flux presents a maximum in the fuel elements (more pronounced in the IFE). The maximum occurs in these locations because this is where the fast neutrons are created. The fast neutrons then move into the flux trap, between the fuel elements, or into the reflector where they start to slow down due to collisions with the moderator. In these locations, and as observed in the figures, the fast neutron population is decreasing and the thermal one is increasing. Due to the annular geometry of the core, the thermal flux is maximal in the center of the flux trap where the fast flux distribution presents a local minimum. A local thermal neutron maximum, occurring for the same reason, is also observed in the reflector at approximately 30cm from the center of the core. Inversely, the fuel regions are highly thermal neutron absorbing and create a strong depression of the thermal flux in the fuel where a local minimum is observed. The absorbed thermal neutrons will create new fissions and new fast neutrons.

The difference between the HEU and LEU cores is not found in the shape of the flux distribution but in the magnitude. Due to the significant mass and proportion of ^{238}U, the LEU fuel is significantly more absorbing than the HEU fuel. However, this increase of absorption rate in the LEU fuel is a drawback because most of the additional absorptions do not lead to new fissions and new neutrons. It is perfectly illustrated on the figures where a stronger depression of thermal flux is observed in the LEU core fuel regions. However, the increase of power in the LEU core seems to be high enough to compensate for the losses and maintain, at least at BOC, the magnitude of the thermal flux in the flux trap. The increase in power also increases the epithermal and fast fluxes. When they have escaped far enough from the core, those populations of neutrons slow down and are able to increase the thermal neutron populations enough that the thermal flux is predicted to become locally higher in the LEU core than in the HEU core (occurring for BOC and EOC at a distance of 25cm and 40cm from the core mid-height, respectively). This difference between BOC and EOC is due to the fact that the thermal flux increases over time to compensate the effects of fission product poisoning but apparently not at the same pace for the HEU and LEU. The thermal flux is predicted to increase faster for the HEU than the LEU.

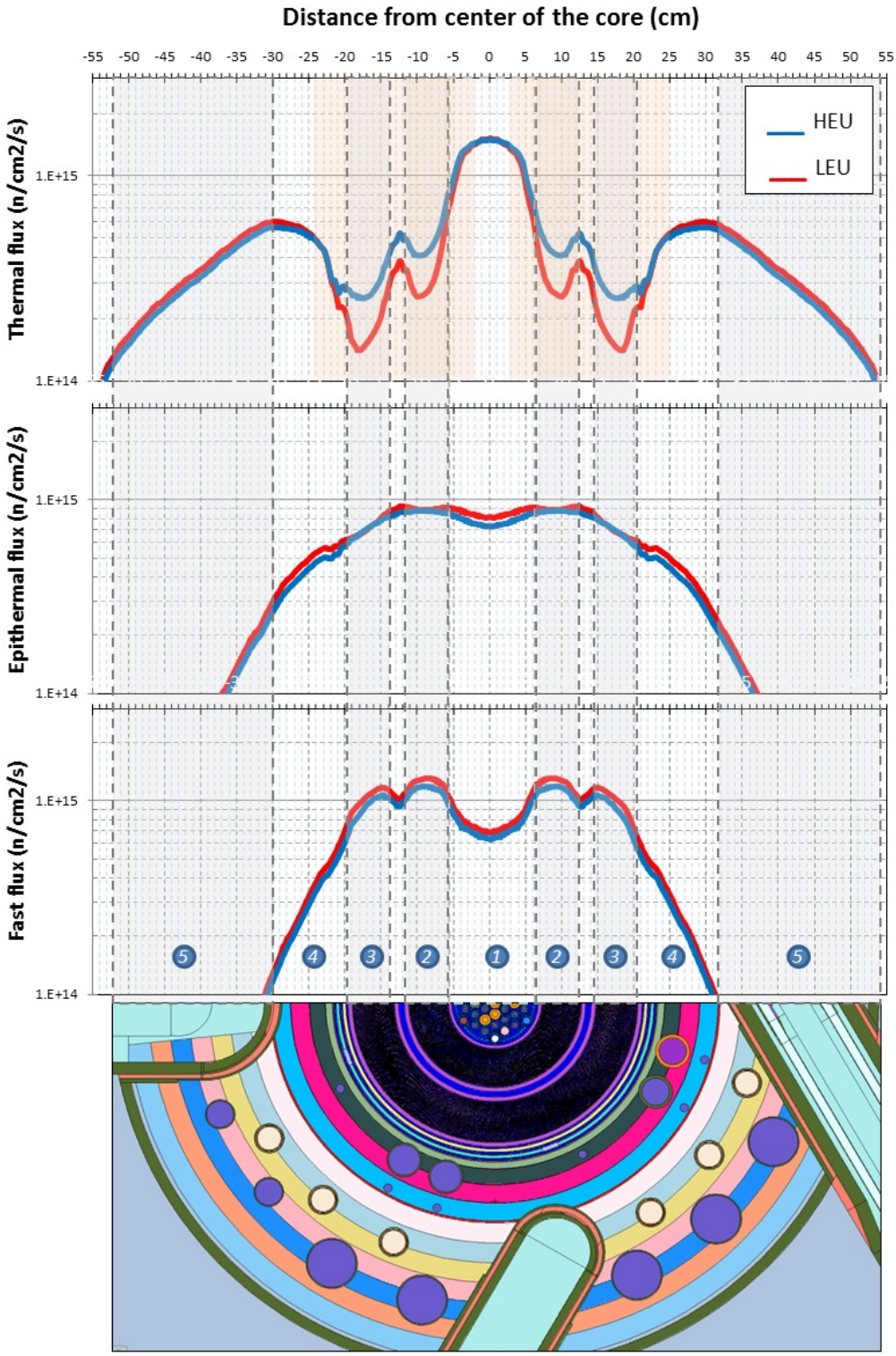

Figure 4.3.4.2.1 – Radial flux distribution at BOC calculated with the Series *l11* HEU and LEU cores. Top, middle and bottom graphs represent the thermal, epithermal and fast flux. A half-core view of the core is added to help the comprehension. Five regions are highlighted: Region 1 is the flux trap; Regions 2 and 3 are the IFE and OFE; Regions 4 and 5 are the removable and permanent reflector, respectively. Uncertainty max. < 1% at 1-σ.

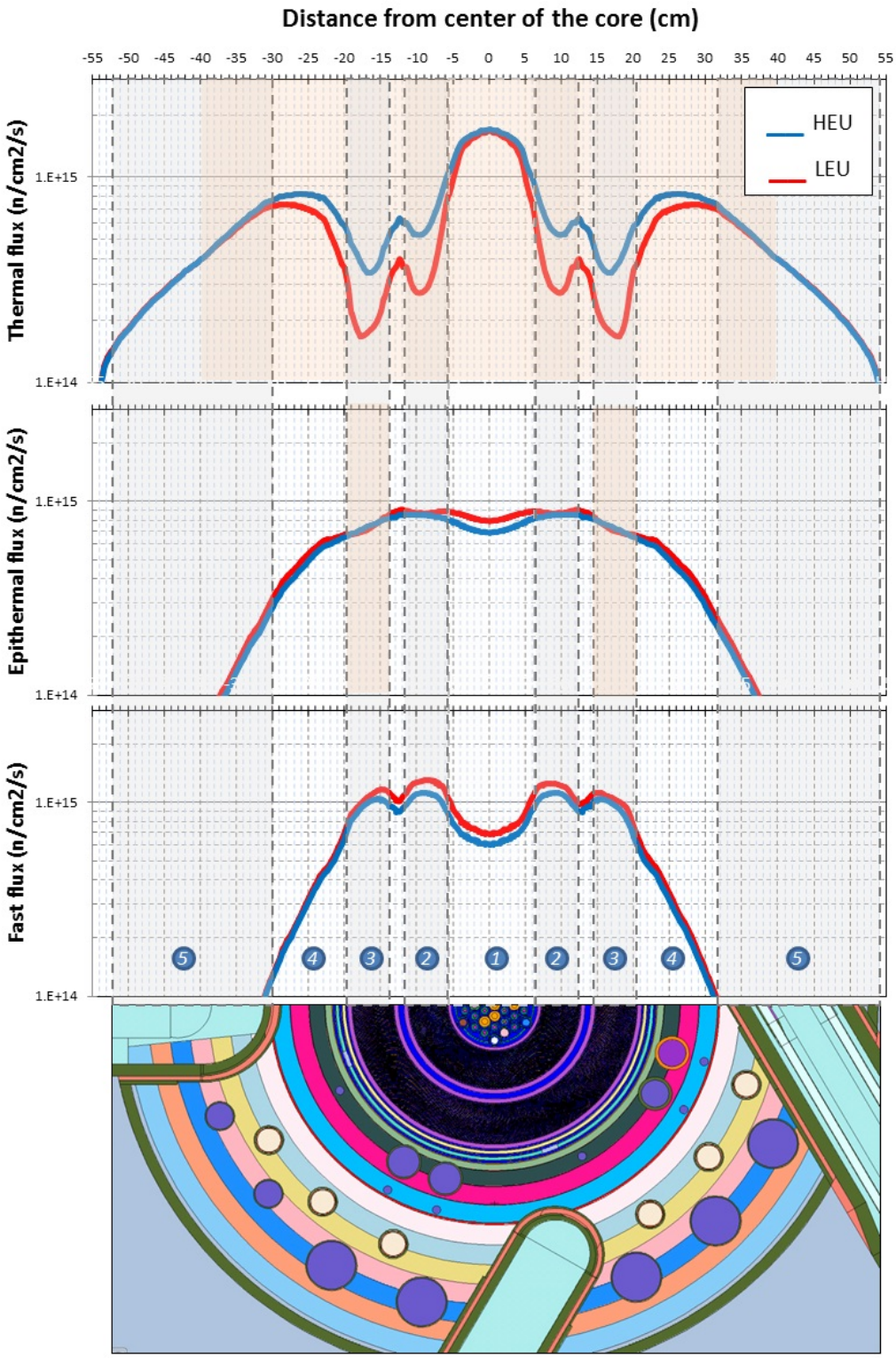

Figure 4.3.4.2.2 – Radial flux distribution at day25 (EOC of the HEU core) calculated with the Series *l11* HEU and LEU cores. Top, middle and bottom graphs represent the thermal, epithermal and fast flux. A half-core view of the core is added to help the comprehension. Five regions are highlighted: Region 1 is the flux trap; Regions 2 and 3 are the IFE and OFE; Regions 4 and 5 are the removable and permanent reflector, respectively. Uncertainty max. < 1% at 1-σ.

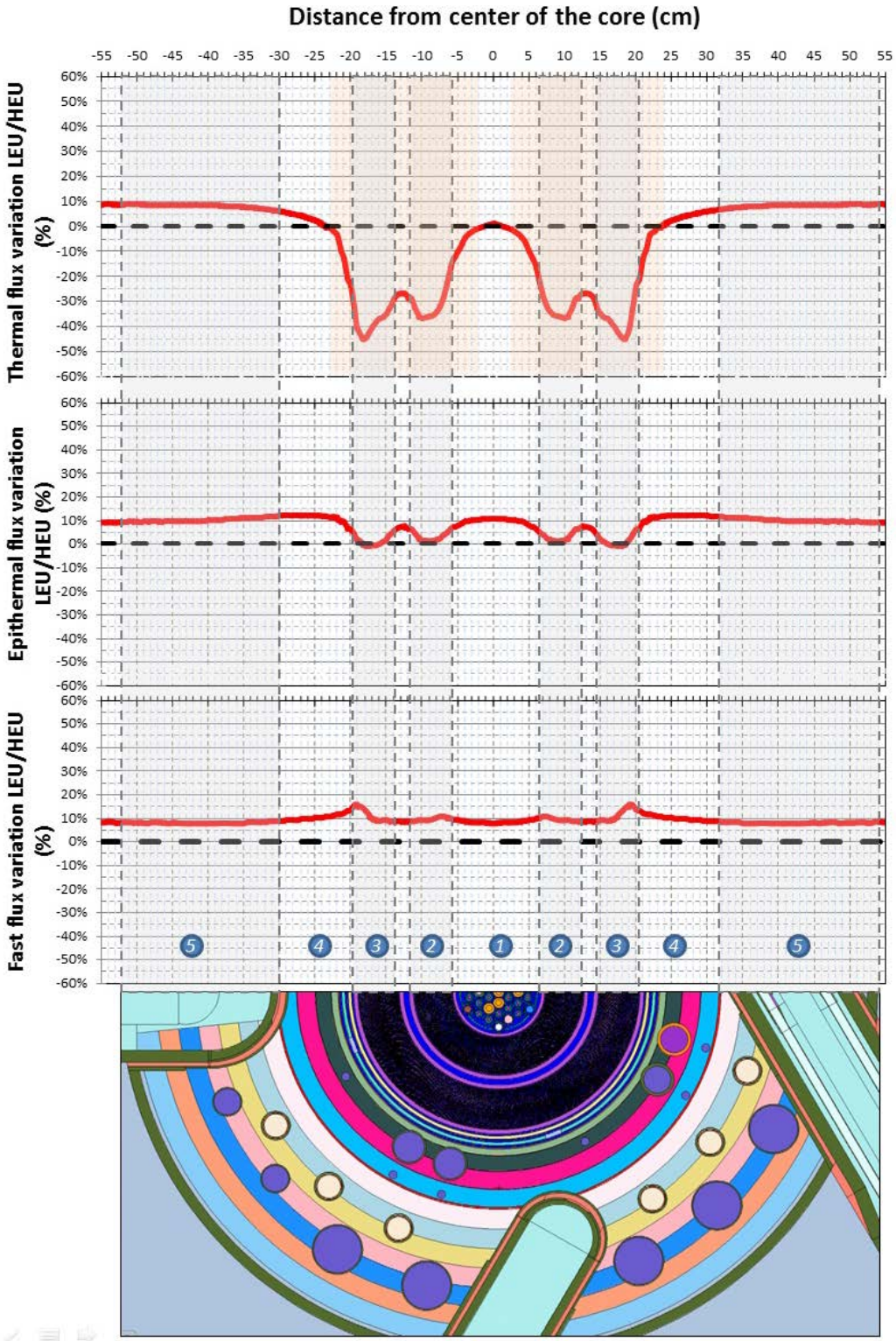

Figure 4.3.4.2.3 – Variation of flux between the LEU and HEU cores at BOC (series *l11*). Top, middle and bottom graphs represent the thermal, epithermal and fast flux. A half-core view of the core is added to help the comprehension. Five regions are highlighted: Region 1 is the flux trap; Regions 2 and 3 are the IFE and OFE; Regions 4 and 5 are the removable and permanent reflector, respectively. Uncertainty max. < 2% at 1-σ.

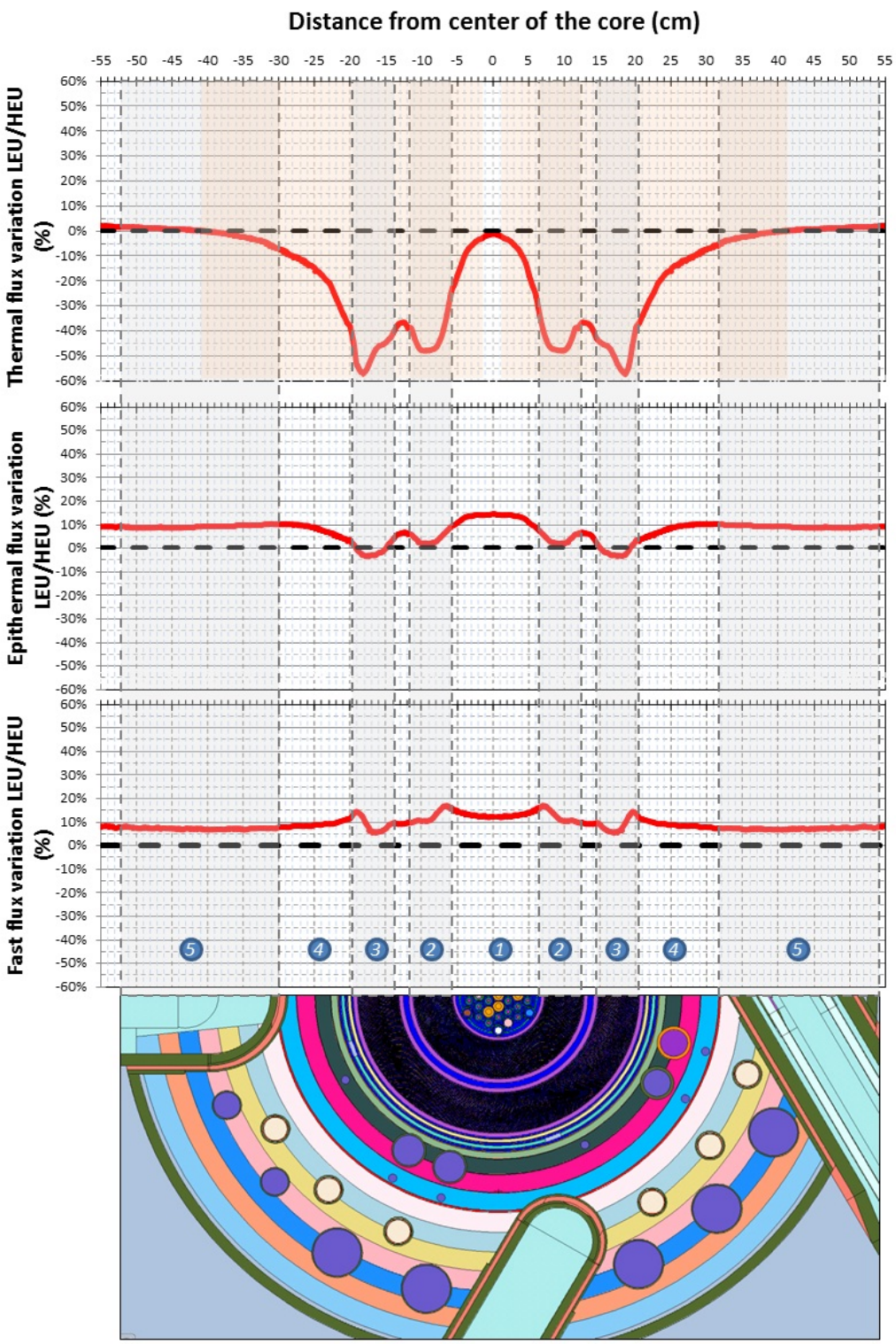

Figure 4.3.4.2.4 – Variation of flux between the LEU and HEU core at day25 (EOC for HEU core). Top, middle and bottom graphs represent the thermal, epithermal and fast flux. A half-core view of the core is added to help the comprehension. Five regions are highlighted: Region 1 is the flux trap; Regions 2 and 3 are the IFE and OFE; Regions 4 and 5 are the removable and permanent reflector, respectively. Uncertainty max. < 2% at 1-σ.

The thermal flux in the beam tubes has also been studied. Recall that only the thermal flux is considered important for this type of experimental equipment. The HEU and LEU thermal flux distribution in the beam tubes is shown at BOC and EOC in Figure 4.3.4.2.5. The variation of thermal flux for LEU and HEU is shown in Figure 4.3.4.2.6. Again, due to the high similarity between the two series, only the results obtained with the Series *l11* inputs are presented. The thermal flux in HB-1, HB-2, HB-3 and HB-4, is shown in red, blue, green and black, respectively, on the figures. The solid and dashed lines represent the LEU and HEU results, respectively. As one can see, the LEU and HEU fluxes follow a similar path. The magnitude decreases strongly with the distance (~2 orders of magnitude / meter). The LEU flux is predicted to be around 10% higher at BOC but 2-3% higher at EOC. As explained before, the variation changes because the HEU and LEU thermal fluxes do not change at the same pace. In Figure 4.3.4.2.6, the spread of the points increases with distance. This is due to the increasing uncertainty in the values with the distance. Calculations were performed at a single level of precision for all distances, and so the uncertainty in Figures 4.3.4.2.5-6 naturally increases in regions further from the beam tube inlet as the flux decreases. The conclusion from these figures is that the flux variation follows a relatively flat trend with distance, and so the reference magnitude is selected at the closest position to the beam tube entrances, where the uncertainty is minimal. Results at the beam tube entrances are presented in section 4.3.4.4 with higher precision calculations.

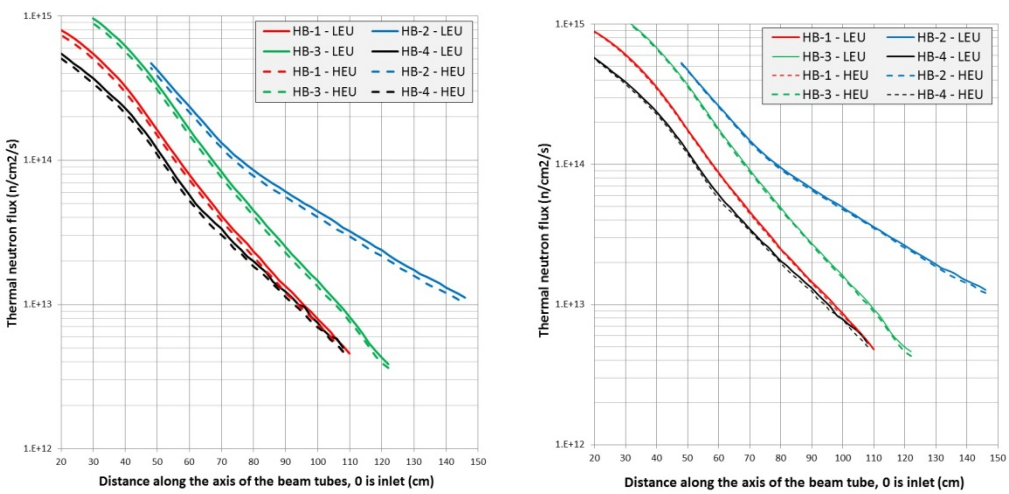

Figure 4.3.4.2.5 – Thermal flux in the beam tubes at BOC (left) and EOC (right) obtained with Series *l11*. Uncertainty max. < 5% at 1-σ.

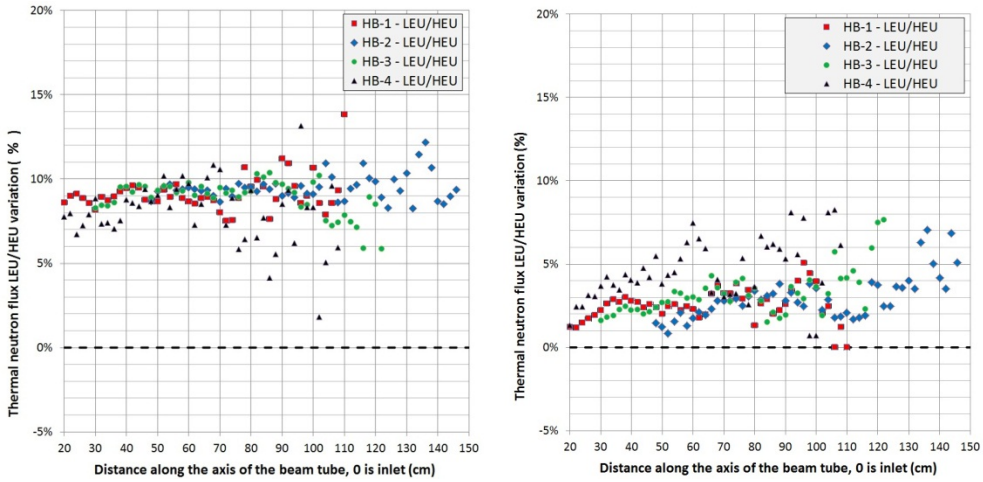

Figure 4.3.4.2.6 – Variation of thermal flux for LEU and HEU in the beam tubes at BOC (left) and EOC (right) obtained with Series *l11*. Uncertainty max < 9% at 1-σ.

4.3.4.3 Comparison with ORNL Neutron Flux

ORNL has evaluated, as shown in section 5.1.4 of [Ref. 4], the neutron flux at three locations: Maximum value in central target (r=0cm from center of the core), beryllium reflector (r=27cm from center of the core) and edge of the cold source (r=35cm from center of the core). Three different ranges of energy have been considered: thermal (<0.625eV), epithermal (0.625eV to 100 keV) and fast (100keV to 20MeV).
ANL has calculated the flux for the same conditions.

The variation of flux ORNL / ANL is presented in Table 4.3.4.3.1. The Series *l11* has been selected for the comparison because the configuration of the reactor is closer to the ORNL one and because very little differences exist between the two ANL series. A more complete presentation at BOC and day 25 (which is the EOC for the HEU core and the ORNL LEU core) of the results is provided in Tables 4.3.4.3.2 and 4.3.4.3.3, respectively.

Table 4.3.4.3.1 – Neutron flux comparison ORNL / ANL. ANL uncertainty max < 0.5% at 1-σ

Variation of flux ORNL/ANL (%)		BOC			EOC		
fuel	energy range	central target (r=0cm)	reflector (r=27cm)	cold source edge (r=35cm)	central target (r=0cm)	reflector (r=27cm)	cold source edge (r=35cm)
HEU	thermal	-2.2	-39.1	3.2	-11.3	-30.3	8.0
	epithermal	9.2	-4.5	26.3	3.8	0.0	26.3
	fast	5.8	13.9	32.9	1.1	17.1	34.3
LEU	thermal	0.0	-33.7	10.3	-0.8	-23.6	-5.3
	epithermal	-3.0	1.3	27.3	-6.3	-2.7	22.7
	fast	5.3	104.9	37.5	-0.9	15.0	25.0

From these results, the following observations can be made:

- The ORNL and ANL fluxes calculated in the central target are in relatively good agreement (whatever the fuel type, period or energy) where the range of the variations is within approximately 10%.

- The agreement of the ORNL and ANL fluxes calculated in the reflector seems to depend on the energy range considered (but not fuel or time): The epithermal flux is in good agreement (in the range -4.5 to 1.3%) at BOC and EOC. The thermal flux is considerably lower in the ANL calculations (-23.6 to -39.1%). It is perhaps due to the positions (or material and geometrical definition) of the CEs which is different between the ORNL and ANL models and very close to the position where the flux was calculated. The variation of fast flux is in the range of +13.9 to +104.9%. This last extreme value comes from the comparison of the ORNL/ANL LEU fast flux at BOC. A typographical error is suspected here, because the ORNL flux value is more than two times higher than the other values calculated in this area. If this value is excluded, the variation of fast flux is in the range of +13.9 to +17.1%.

- The agreement of the ORNL and ANL fluxes calculated at the cold source edge seems to also depend on the energy range considered. The thermal flux is in good agreement (-5.3 to +10.3%) but the variation of epithermal and fast flux varies from +22.7 to 32.9%. There is perhaps a relation between the magnitude of these numbers and the magnitude of the variation of thermal flux found in the reflector (-23.6 to -39.1%). Again, an explanation could be that the variation of the CEs has changed the shape of the flux in the entire reflector since these regions are seen to be sensitive to the CEs as shown by Figure 4.3.4.2.1 vs. Figure 4.3.2.2.2.

Regarding the change in HEU and LEU flux from BOC to EOC, the following observations can be made:

- The magnitude of the thermal flux, calculated by ORNL and ANL, increases everywhere from BOC to EOC other than relatively stable values in the central target. This is expected because the absorption of the fuel tends to increase over the time due to the creation of fission products and the number of fissions, created by thermal neutrons, needs to increase to compensate and keep the power of the reactor constant.

- Inversely, the magnitude of the epithermal and fast flux remain about the same or decrease slightly from BOC to EOC. This is predicted by both the ORNL and ANL calculations with the exception of the reflector fast flux reported by ORNL which decreased by a factor of two (and is possibly in error as noted previously).

- It is noteworthy that in all cases both the ORNL and the ANL calculated LEU flux nearly match (within approximately 10%) or exceeds the HEU flux for both BOC and EOC in the central target, reflector and at the cold source edge.

It is also observed that, except in the central target, Series *c400* and *l11* provide similar results. The differences in the central target are easily explained by the fact that the loading of the flux trap has in terms of reactor physics an opposite effect in that for Series *c400* the trap is filled up

with materials "transparent" to neutrons (dummy targets), whereas in Series *l11* the trap is filled up with highly absorbing materials (curium targets).

Table 4.3.4.3.2 – Neutron flux comparison HEU/LEU at BOC. ANL uncertainty max. < 0.5% at 1-σ

thermal flux ($x10^{14n}/cm^2/s$)		ORNL	ANL series *l11*	ANL series *c400*	variation ORNL/ ANL *l11* (%)
central target (r=0cm)	HEU	22	22.5	22.2	-2.2%
	LEU	23	23.0	22.1	0.0%
	variation LEU/HEU (%)	4.5%	2.2%	-0.5%	
Reflector (r=27cm)	HEU	5.6	9.2	9.2	-39.1%
	LEU	6.3	9.5	9.5	-33.7%
	variation LEU/HEU (%)	12.5%	3.3%	3.3%	
Cold source edge (r=35cm)	HEU	6.5	6.3	6.3	3.2%
	LEU	7.5	6.8	6.8	10.3%
	variation LEU/HEU (%)	15.4%	7.9%	7.9%	
epithermal flux ($x10^{14}n/cm^2/s$)		**ORNL**	**ANL series *l11***	**ANL series *c400***	**variation ORNL/ ANL *l11* (%)**
central target (r=0cm)	HEU	13	11.9	13.2	9.2%
	LEU	13	13.4	14.9	-3.0%
	variation LEU/HEU (%)	0.0%	12.6%	12.9%	
Reflector (r=27cm)	HEU	6.3	6.6	6.5	-4.5%
	LEU	7.6	7.5	7.5	1.3%
	variation LEU/HEU (%)	20.6%	13.6%	15.4%	
Cold source edge (r=35cm)	HEU	2.4	1.9	1.9	26.3%
	LEU	2.8	2.2	2.2	27.3%
	variation LEU/HEU (%)	16.7%	15.8%	15.8%	
fast flux ($x10^{14}n/cm^2/s$)		**ORNL**	**ANL series *l11***	**ANL series *c400***	**variation ORNL/ ANL *l11* (%)**
central target (r=0cm)	HEU	11	10.4	11.0	5.8%
	LEU	12	11.4	12.1	5.3%
	variation LEU/HEU (%)	9.1%	9.6%	10.0%	
Reflector (r=27cm)	HEU	4.1	3.6	3.5	13.9%
	LEU	8.4	4.1	4.0	104.9%
	variation LEU/HEU (%)	104.9%	13.9%	14.3%	
Cold source edge (r=35cm)	HEU	0.93	0.70	0.70	32.9%
	LEU	1.1	0.80	0.80	37.5%
	variation LEU/HEU (%)	18.3%	14.3%	14.3%	

Table 4.3.4.3.3 – Neutron flux comparison HEU/LEU at EOC. ANL uncertainty max. < 0.5% at 1-σ

thermal flux ($x10^{14n}/cm^2/s$)		ORNL	ANL series *l11*	ANL series *c400*	variation ORNL/ ANL *l11* (%)
central target (r=0cm)	HEU	22	24.8	21.9	-11.3%
	LEU	25	25.2	21.5	-0.8%
	variation LEU/HEU (%)	13.6%	1.6%	-1.8%	
Reflector (r=27cm)	HEU	8.3	11.9	12.4	-30.3%
	LEU	8.4	11	11.6	-23.6%
	variation LEU/HEU (%)	1.2%	-7.6%	-6.5%	
Cold source edge (r=35cm)	HEU	8.1	7.5	7.7	8.0%
	LEU	7.2	7.6	7.8	-5.3%
	variation LEU/HEU (%)	-11.1%	1.3%	1.3%	
epithermal flux ($x10^{14}n/cm^2/s$)		**ORNL**	**ANL series *l11***	**ANL series *c400***	**variation ORNL/ ANL *l11* (%)**
central target (r=0cm)	HEU	11	10.6	11.3	3.8%
	LEU	12	12.8	13.7	-6.3%
	variation LEU/HEU (%)	9.1%	20.8%	21.2%	
Reflector (r=27cm)	HEU	6.5	6.5	6.5	0.0%
	LEU	7.3	7.5	7.7	-2.7%
	variation LEU/HEU (%)	12.3%	15.4%	18.5%	
Cold source edge (r=35cm)	HEU	2.4	1.9	1.9	26.3%
	LEU	2.7	2.2	2.2	22.7%
	variation LEU/HEU (%)	12.5%	15.8%	15.8%	
fast flux ($x10^{14}n/cm^2/s$)		**ORNL**	**ANL series *l11***	**ANL series *c400***	**variation ORNL/ ANL *l11* (%)**
central target (r=0cm)	HEU	9.5	9.4	9.2	1.1%
	LEU	11	11.1	11.1	-0.9%
	variation LEU/HEU (%)	15.8%	18.1%	20.7%	
Reflector (r=27cm)	HEU	4.1	3.5	3.4	17.1%
	LEU	4.6	4.0	4.0	15.0%
	variation LEU/HEU (%)	12.2%	14.3%	17.6%	
Cold source edge (r=35cm)	HEU	0.94	0.70	0.70	34.3%
	LEU	1.0	0.80	0.80	25.0%
	variation LEU/HEU (%)	6.4%	14.3%	14.3%	

4.3.4.4 ANL Metrics of Performance of HFIR

The matrix of performance presented here is slightly more varied than the ORNL one, presented in the previous section (magnitude of the flux at distance r=0, 27 and 35cm from core centerline at BOC and EOC and for three different ranges of energy). The additional spatial detail in the approach followed here is justified by the observation of the LEU/HEU flux variation presented in Section 4.3.4.2. It was shown that the flux variation can be positive or negative depending on the energy range, time and distance considered. Considering the wide distributions of the experimental facilities in the reactor, it is thought that the evaluation of the flux in three locations might be too restrictive to capture all of the changes implied by the conversion to LEU fuel. Of the four main types of experiments carried out at HFIR, as discussed in Section 2.4, only two are evaluated. The neutron activation is not calculated because the conversion will certainly not affect the performance (low flux and short period of irradiation are sufficient). The gamma irradiation is obviously not evaluated because the gamma irradiation chamber is not located in the reactor. The matrix is thus reduced to the evaluation of performance in the beam tubes and the in-core irradiation positions. The average of the BOC and EOC thermal flux is considered to be the relevant parameter for the beam tubes whereas the thermal, epithermal and fast fluence, as calculated from the average of the BOC and EOC flux are considered as the pertinent parameters for the in-core irradiation positions. The 73 positions are divided into 11 "rings" in which the fluence is evaluated. More details are provided in Section 2.4 and Table 2.4.1. In evaluating these 11 rings, the value given is the average of the multiple positions listed. Axially, the fluence was averaged over the entire irradiation position (from z=-30 to z=+30cm). This is in contrast to sections 4.3.4.2-4 where the methodology used by ORNL was maintained in this study to evaluate the flux in an axial midplane (from z=-1 to z=+1cm). Fluence over the entire axial average was chosen as a metric of performance to evaluate performance of potential LEU cores. The matrix of performance obtained with the Series *c400* HEU and LEU cores is presented in Table 4.3.4.4.1. The one obtained with the Series *l11* is presented in Table 4.3.4.4.2. The numbers obtained with the two series are relatively close which seems to show that the experimental loading in the flux trap has a limited effect on the overall performance of the reactor. In each table the HEU and LEU results are shown. However, one must exercise caution when comparing these numbers since the cycle length predicted for the LEU core is significantly longer than the corresponding HEU core (28-30%). If this increase can be interpreted as a positive feature for reactor performance, it also impacts other key parameters of the reactor which may prevent such cycle extension. Here are few features that would probably be impacted by a cycle length extension (certainly not an exhaustive list):

- Manpower management and cost
- Scientific experiment management
- Maintenance operation management
- Lifetime of the pressure vessel
- More frequent replacement of the CEs and reflector
- Oxide layer growth on the fuel plates
- …

Because an assessment of the impact of cycle length extension has not been carried out, ANL cannot confirm that HFIR should or could operate at 100MW to maintain its current performance. As explained in the following paragraph, the only thing that can be currently considered are different scenarios and their impact on performance.

Table 4.3.4.4.1 – Matrix of performance for Series *c400* HEU & LEU cores. Uncertainty max. < 1% at 1-σ

Series *c400* - Neutron scattering			
beam tubes	distance from tubes entrance (cm)	Cycle average thermal flux ($x10^{15}n/cm^2/s$)	
		HEU	LEU
HB-1	14	0.94	0.99
HB-2	48	0.49	0.52
HB-3	30	0.97	1.02
HB-4	16	0.63	0.67
days of operation / cycle		**25.5**	**33**

Series *c400* - In-core irradiation position								
ring	position	Distance from core center, cm	thermal fluence ($x10^{21}n/cm^2$)		epithermal fluence ($x10^{21}n/cm^2$)		fast fluence ($x10^{21}n/cm^2$)	
			HEU	LEU	HEU	LEU	HEU	LEU
0	D4	0	4.05	4.99	2.22	3.19	1.87	2.66
1	C4, D5, E5, E4, D3, C3	1.5	3.96	4.87	2.19	3.15	1.85	2.64
2	C5, D6, E6, F6, F5, F4, E3, D2, C2, B2, B3, B4	3	3.68	4.48	2.11	3.03	1.82	2.59
3	B5, C6, E7, F7, G6, G5, F3, E2, C1, B1, A2, A3	4.5	3.01	2.58	1.97	2.81	1.75	2.50
4	A1, A4, D7, G7, G4, D1	5.5	2.16	2.46	1.58	2.24	1.47	2.10
5	RB-2, 4, 6, 8	26.3	1.89	2.29	1.24	1.79	0.76	1.08
6	RB-1A, 1B, 3A, 3B, 5A, 5B, 7A, 7B	27.2	1.93	2.36	1.43	2.05	0.89	1.26
7	CR-1, 2, 3, 4, 5, 6, 7, 8	32	1.65	2.14	0.71	1.02	0.30	0.42
8	VXF-1, 3, 5, 7, 9, 11, 13, 15, 18, 20, 22	38.6	0.97	1.32	0.17	0.24	0.06	0.08
9	VXF-2, 4, 8, 10, 12	44.2	0.71	0.96	0.10	0.14	0.03	0.04
10	VXF-6, 14, 16, 17, 19, 21	45.1	0.66	0.89	0.08	0.11	0.02	0.03

Table 4.3.4.4.2 – Matrix of performance for series *I11*, HEU & LEU core. Uncertainty max. < 1% at 1-σ

Series *I11* - Neutron scattering			
beam tubes	distance from tubes entrance (cm)	Cycle average thermal flux ($x10^{15}n/cm^2/s$)	
		HEU	LEU
HB-1	14	0.94	0.98
HB-2	48	0.48	0.51
HB-3	30	0.97	1.02
HB-4	16	0.62	0.65
days of operation / cycle		**25**	**32**

Series *I11* - In-core irradiation position								
ring	position	Distance from core center, cm	thermal fluence ($x10^{21}n/cm^2$)		epithermal fluence ($x10^{21}n/cm^2$)		fast fluence ($x10^{21}n/cm^2$)	
			HEU	LEU	HEU	LEU	HEU	LEU
0	D4	0	4.09	5.33	1.95	2.82	1.86	2.62
1	C4, D5, E5, E4, D3, C3	1.5	3.91	5.06	1.92	2.77	1.84	2.59
2	C5, D6, E6, F6, F5, F4, E3, D2, C2, B2, B3, B4	3	3.72	4.73	1.95	2.81	1.89	2.67
3	B5, C6, E7, F7, G6, G5, F3, E2, C1, B1, A2, A3	4.5	3.03	3.72	1.76	2.53	1.74	2.47
4	A1, A4, D7, G7, G4, D1	5.5	1.95	2.30	1.26	1..80	1.17	1.67
5	RB-2, 4, 6, 8	26.3	1.72	2.11	1.14	1.65	0.70	0.99
6	RB-1A, 1B, 3A, 3B, 5A, 5B, 7A, 7B	27.2	1.79	2.21	1.40	2.00	0.92	1.31
7	CR-1, 2, 3, 4, 5, 6, 7, 8	32	1.56	2.03	0.73	1.05	0.32	0.45
8	VXF-1, 3, 5, 7, 9, 11, 13, 15, 18, 20, 22	38.6	0.93	1.26	0.17	0.24	0.55	0.77
9	VXF-2, 4, 8, 10, 12	44.2	0.68	0.92	0.09	0.13	0.28	0.37
10	VXF-6, 14, 16, 17, 19, 21	45.1	0.63	0.86	0.08	0.11	0.21	0.30

Three scenarios have been studied. In the first one, it is assumed that the cycle length cannot be increased. The reactor is voluntarily shutdown after 25 days to match the current HEU cycle length despite the ability to operate the LEU core for 32 days. The comparison of performance for HEU/LEU is provided in the top graphs of Figure 4.3.4.4.1 for the Series *c400* and Figure 4.3.4.4.2 for the Series *l11*. In this case, the average thermal flux in the beam tubes is calculated to be around 5% higher than in the HEU core. The epithermal and fast fluences are predicted to be around 10% higher everywhere. However, the thermal fluence is expected to decrease slightly (between -2% and -10%) in the Ring 0 to 6 for Series *c400* and Rings 2 to 6 for Series *l11*. The decrease in LEU vs. HEU flux is in both series larger when closer to the fuel elements (between Rings 4 and 5). It is noteworthy that in all cases 100 MW LEU performance with the current 25 day cycle length nearly matches (within 10%) or exceeds the 85 MW HEU flux, and that on average the LEU performance increases over HEU in the approximate range of 5-10% when considering all the core performance positions modeled.

In the second scenario, the LEU core is burned normally to its last day (32 or 33 days depending of the configuration). The length of the cycle is thus extended. However, 6 cycles per year are scheduled instead of the 7 cycles per year for the HEU core. In this case, the total fluence per year is calculated. The comparison of performance HEU/LEU is provided in the middle graphs of Figure 4.3.4.4.1 for Series *c400* and Figure 4.3.4.4.2 for Series *l11*. Even with 6 cycles per year, the total days of operation would be extended (+19.5 and 17days/year calculated with Series *c400* and *l11*, respectively). The LEU epithermal and fast fluences at this time are around 20% larger. The thermal fluence would be greater than the HEU one everywhere (from a few percent in the flux trap to almost 15% in the reflector). The only exception is found in the Ring 4 in the Series *c400* (-2%). The LEU thermal flux would be 5% higher and in the beam tubes would be available for work for an additional 17 to 20 days per year. Overall, the LEU performance would increase significantly over HEU performance.

The last scenario is the same as the second one except that the same number of HEU elements is burned every year. The comparison of performance for HEU/ LEU is provided in the bottom graphs of Figure 4.3.4.4.1 for Series *c400* and Figure 4.3.4.4.2 for Series *l11*. Because the length of each cycle is extended, the number of days of operation per year is significantly increased (+49 to 52.5 days, depending on the series). As a result, the epithermal and fast fluences increase considerably (around 40%). Because the life of the reflector is tightly linked to the fast fluence, the reflector would probably have to be replaced more frequently. The thermal fluence would increase by 15 to 35%, depending on the in-core position locations. The LEU thermal flux would be 5% higher and in the beam tubes would be available for work for an additional 49 to 52.5 days per year. Overall, the performance would increase significantly

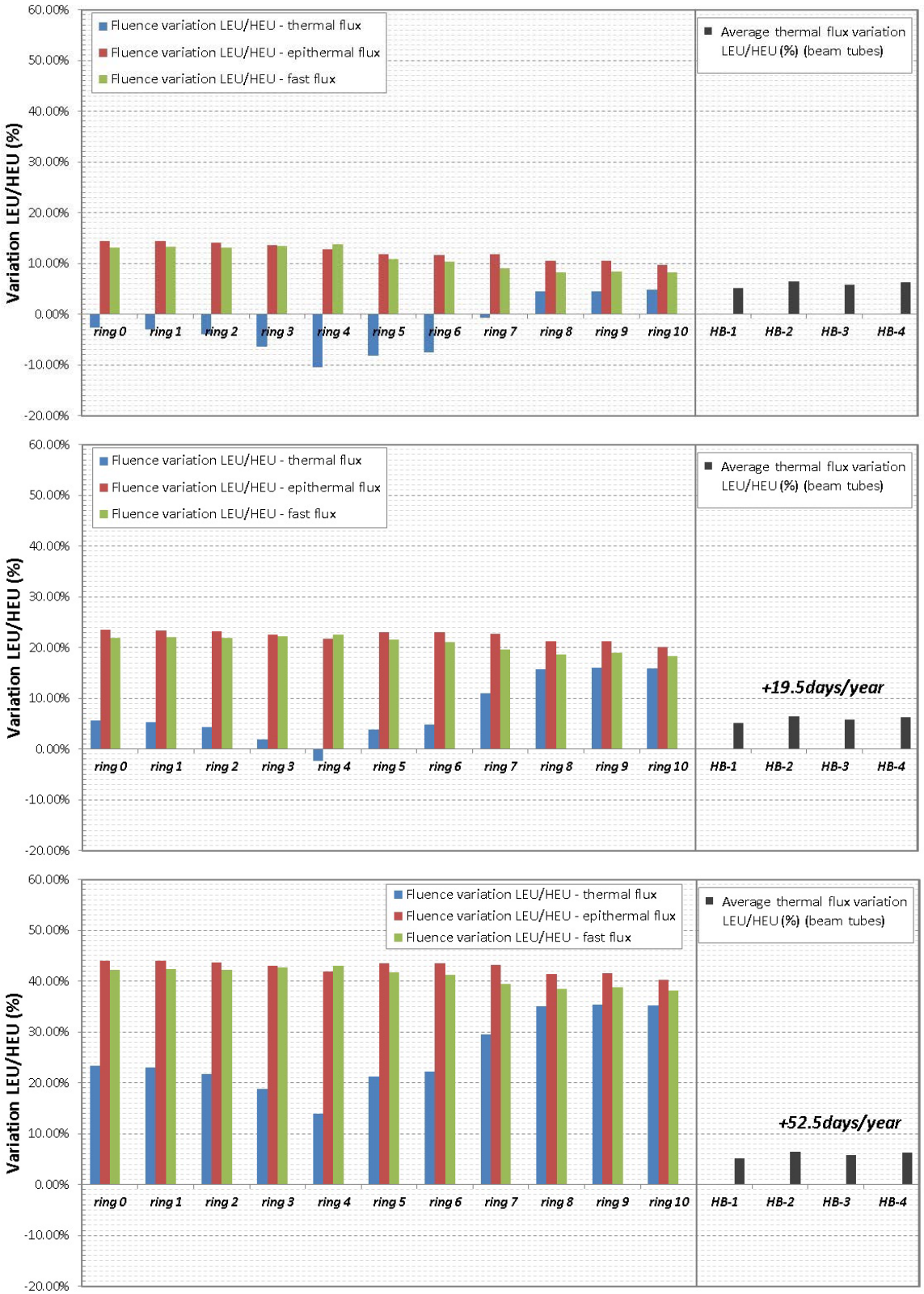

Figure 4.3.4.4.1 – Comparison of performance for LEU/HEU for three different scenarios using the Series *c400* inputs. Uncertainty max. < 2% at 1-σ.

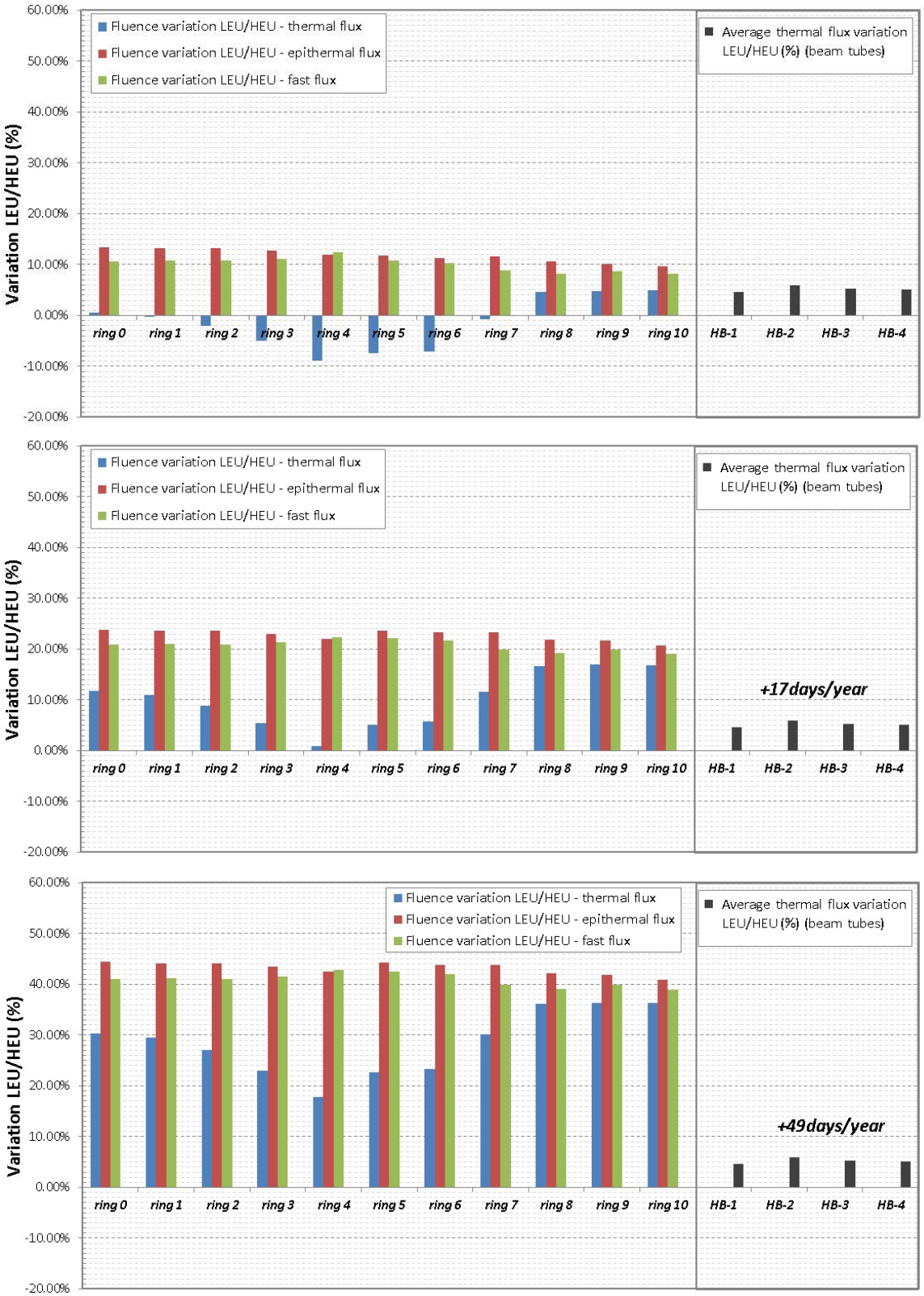

Figure 4.3.4.4.2 – Comparison of performance for LEU/HEU for three different scenarios using the Series *l11* inputs. Uncertainty max. < 2% at 1-σ.

4.3.5 Other Calculations

This section discusses the other calculations presented by ORNL [Ref. 4], [Ref. 16] and that have been reviewed. As before, the two series of ANL reference inputs have been used.

4.3.5.1 Kinetics Parameters

The two kinetics parameters that have been calculated are the beta-effective (β_{eff}) and the neutron lifetime (l). Only the β_{eff} has been evaluated by ORNL. Exceptionally, Version 1.6 of MCNP has been used. The reason is that it is possible to extract these values directly by using the MCNP "kopts" card.

The β_{eff} results obtained with Series *c400* and *l11* are compiled in Table 4.3.5.1.1. The values are a bit lower for Series *l11* than for Series *c400* at BOC and EOC. This is probably explained by the small proportion of fissions created in the curium targets (Series *l11*) from isotopes that have a lower fraction of delayed neutrons (Plutonium…). The increasing fraction of isotopes created by other isotopes than ^{235}U during irradiation also explains the drop observed for both fuel types and for both series from BOC to EOC. As expected, the decrease is more pronounced for the LEU fuel because more plutonium is created with this type of fuel. Nonetheless, the LEU β_{eff} from BOC to EOC remains relatively high. These numbers are also in good agreement with the ORNL ones (HEU: 736pcm at BOC, 740pcm at EOC. LEU: 756pcm at BOC and 707pcm at EOC).

The calculated neutron lifetime obtained with Series *c400* and *l11* are compiled in Table 4.3.5.1.2. The neutron lifetime is inversely proportional to the product of the macroscopic cross section of absorption and the neutron velocity (which is proportional to its energy):

$$l = \frac{1}{v \cdot \Sigma_a} = \frac{1}{\sqrt{\frac{2E}{m}} \cdot \Sigma_a}$$

where:

- l (s): neutron lifetime
- v (m/s): neutron velocity
- E (J = $kg.m^2.s^{-2}$): neutron energy
- m (kg): neutron mass
- Σ_a (cm^{-1}): macroscopic cross section of absorption.

The neutron lifetimes obtained with Series *c400* and *l11* are quite similar which means that the experimental loading has little impact on this parameter. As expected, *l* is considerably lower for the LEU core. This is explained by the fact that the LEU fuel macroscopic cross section of absorption is more important than for the HEU fuel (mainly due to the significant increase of ^{238}U). It is also observed that the neutron lifetime increases considerably over the time of irradiation (by roughly +77 to 87% for HEU fuel and by 64-71% for the LEU fuel).

This sharp increase means that the product $v \cdot \Sigma_a$ has decreased considerably (~50-60%) from BOC to EOC. Because the absorption rate increases over the time (due to absorbing fission product buildup), the decrease of the product $v \cdot \Sigma_a$ is due to the decrease of the neutron velocity and, consequently, the neutron energy (more thermal neutrons). As seen in Section 4.3.4.2, the

thermal neutron population has to increase to maintain the power at a constant level and compensate for the increasing rate of absorption.

It is also noteworthy that the neutron lifetime value obtained for the HEU core at BOC and EOC (~39 and 73µs) is very consistent with the measured and calculated values at BOC (33 and 38µs, respectively) presented in [Ref. 9], and at BOC and EOC (35 and 70µs, respectively), adopted in the SAR [Ref. 15].

Table 4.3.5.1.1 – Beta-effective values obtained with ANL reference inputs. Uncertainty max. < 7pcm at 1-σ

B-eff (pcm)			
series *c400*	**HEU**	**LEU**	**variation HEU/LEU (%)**
BOC	748	749	-0.1%
EOC	720	699	3.0%
variation EOC/BOC (%)	-3.7%	-6.7%	
series *l11*	**HEU**	**LEU**	**variation HEU/LEU (%)**
BOC	731	740	-1.2%
EOC	719	683	5.3%
variation EOC/BOC (%)	-1.6%	-7.7%	

Table 4.3.5.1.2 – Beta-effective values obtained with ANL reference inputs. Uncertainty max. < 0.12×10^{-6}s at 1-σ

neutron life time (10-6s)			
series *c400*	**HEU**	**LEU**	**variation HEU/LEU (%)**
BOC	39.0	28.0	39.2%
EOC	73.2	47.8	53.0%
variation EOC/BOC (%)	88%	70.8%	
series *l11*	**HEU**	**LEU**	**variation HEU/LEU (%)**
BOC	39.9	29.0	37.3%
EOC	70.5	47.5	48.4%
variation EOC/BOC (%)	76.9%	63.7%	

The evolution of a neutron population, n(t), due to an insertion of positive or negative reactivity, ρ, during a time, t, is given by the following equation:

$$n(t) = n(t=0) \cdot e^{\frac{\rho - \beta_{eff}}{l} t} = n(t=0) \cdot e^{\omega(\rho) t}$$

Thus, the evolution of the neutron population is strongly dependent upon ω. The evolution of ω versus the reactivity at BOC and EOC is shown in Figure 4.3.5.1.1 for Series *c400* and Figure 4.3.5.1.2 for Series *l11*. The slope of the LEU curves is always higher than the corresponding HEU ones meaning that the LEU core would be more sensitive to a reactivity insertion (more important increase/decrease of the neutron population for a given insertion of positive/negative

reactivity). It is also observed that the slope of the EOC curves is significantly lower than the BOC ones (for both the HEU and LEU cores).

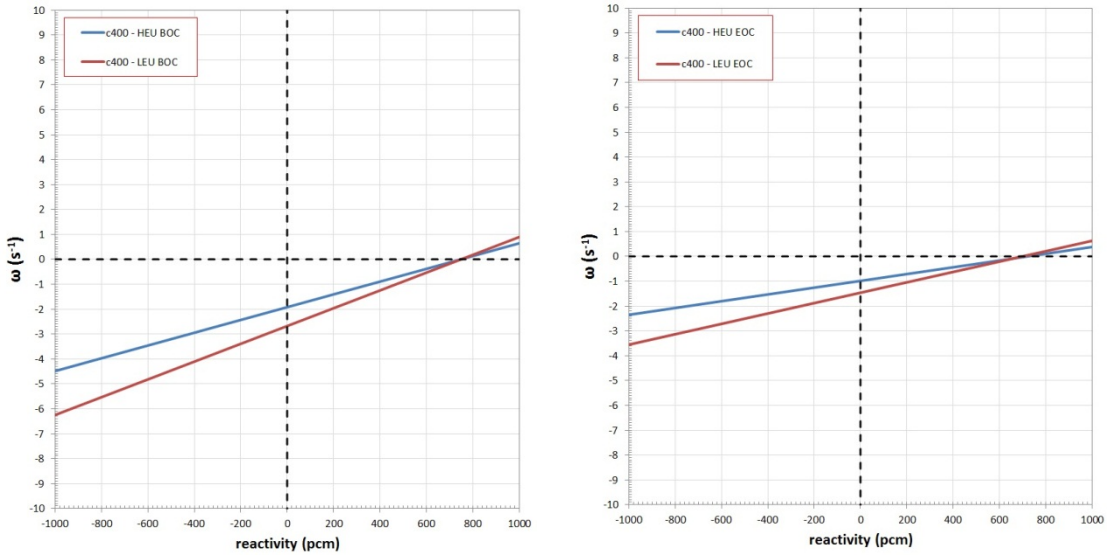

Figure 4.3.5.1.1 – ω versus reactivity for Series *c400* HEU and LEU core at BOC (left) and EOC (right).

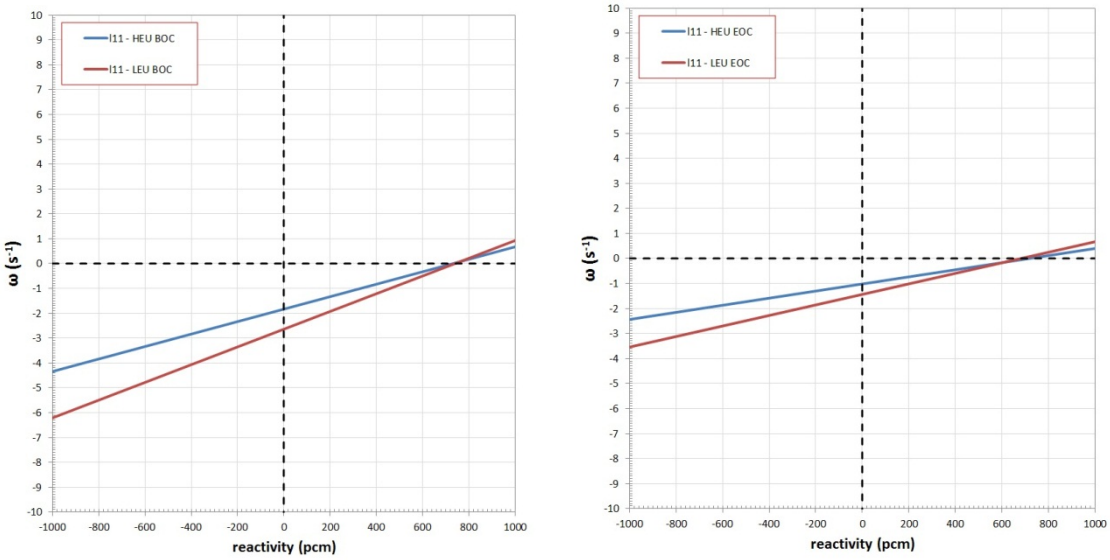

Figure 4.3.5.1.2 – ω versus reactivity for series *l11* HEU and LEU core at BOC (left) and EOC (right).

To illustrate the kinetics differences between the HEU and LEU cores, a simple test case has been studied. At t=0, the reactor is critical and a positive reactivity of 1000pcm is inserted. At t=0.3s, a SCRAM is initiated. Only the safety plates (OCE) are supposed to move; the ICE remains at the same position. The OCE plates move at a speed of 2.75m/s (27”/0.25s). The worth of the OCE safety plates changes with their position. The results obtained in Section 4.3.5.2 have been used to simulate the changing worth of the plates. The results obtained for the Series *c400* HEU and LEU cores, at BOC and EOC, are shown in Figure 4.3.5.1.3. As expected, the insertion of reactivity has a greater impact on the LEU core. Just before the SCRAM (t=0.3s), at BOC, the

neutron population is 30% and 20% greater than that initially present for the LEU and HEU cores, respectively. The same values taken at EOC are less important (20% and 12% for the LEU and HEU core, respectively). This is expected since the neutron lifetime has increased considerably at EOC for both cores. Inversely, once the SCRAM is initiated, the response of the LEU cores is better (drop of reactivity is faster).

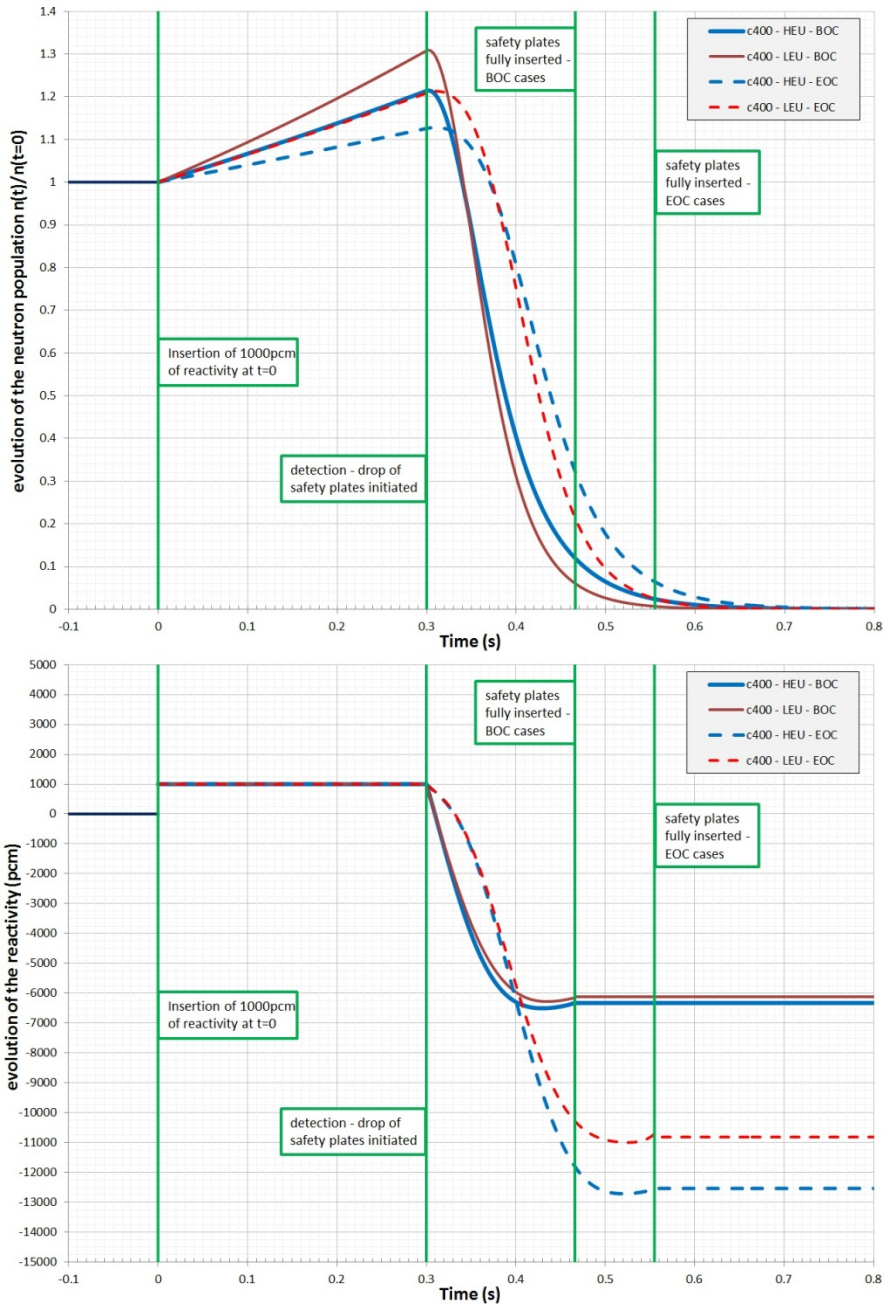

Figure 4.3.5.1.3 – Simulation of the response of the Series *c400* HEU and LEU cores to an insertion of reactivity of 1000pcm and SCRAM initiated 0.3s later. The top figure represents the evolution of the neutron population. The bottom figure represents the evolution of the reactivity.

4.3.5.2 Differential Control Rod Worth

The worth of the ICE, OCE and both ICE and OCE combined has been evaluated for both the HEU and LEU cores. The differential worth, ΔW, at state, I, corresponding to a position, p_i, is given by the following equation:

$$\Delta W(i) = \frac{\rho(i)}{\Delta p_i} = \frac{(k_i - k_{i,p})}{(k_i \cdot k_{i,p})\Delta p_i}$$

where:

- $\rho(i)$ (cents): Reactivity change between state i and a perturbed state p
- k_i : k-effective at state i
- $k_{i,p}$: k-effective in the perturbed state
- Δp_i (inch): Difference of position between state I and the perturbed state p.

This equation is slightly different than the one used by ORNL [Ref. 4]:

$$\Delta W(i) = \frac{|k_i - k_{i,p}|}{|\Delta p_i|}$$

The ANL equation seems more appropriate because ORNL presents their results in cents/inch. To use this unit, one has to use the beta effective which implies the use of the reactivity. Nonetheless, the bias introduced by this different approach does not lead to significant differences in the results (checked but not shown). The beta-effectives obtained in the previous section (4.3.5.1) have been used to express the reactivity in cents. Only the results obtained with Series *c400* are shown in this section because of the similarity of the results obtained with the other series.

The differential worths of the ICE and OCE, presented in the top and middle graphs of Figure 4.3.5.2.1 are shown for the case at BOC only, because they can be compared to the ORNL results. The ANL and ORNL results follow the same trend. The worth is maximal around 18" withdrawn (for both the ICE and OCE). The worth is also predicted to be slightly lower for the LEU core. Nonetheless, as seen in the previous section, the kinetics parameters make the CEs more "efficient" with a LEU core despite their lower worth. Despite the differences in methodology, the ORNL and ANL results match relatively well.

The worth of the ICE and OCE moved together (bottom graph on Figure 4.3.5.2.1) is not equal to the sum of the individual worth of the ICE and OCE but lower. Despite the fact that it is almost the case at 18" withdrawn, the combined worth of the CEs is almost identical or even lower than for the other positions. No ORNL results are available for comparison.

The same type of calculation has been carried out at EOC (only for Series *c400*). The results are shown in Figure 4.3.5.2.2. As expected, the worth of the CEs has increased. This is due to the fact that the fuel has lost a lot of its initial reactivity. The worth is predicted to increase by almost a factor of 10. Again, the worth of the CEs is predicted to be lower with the LEU core.

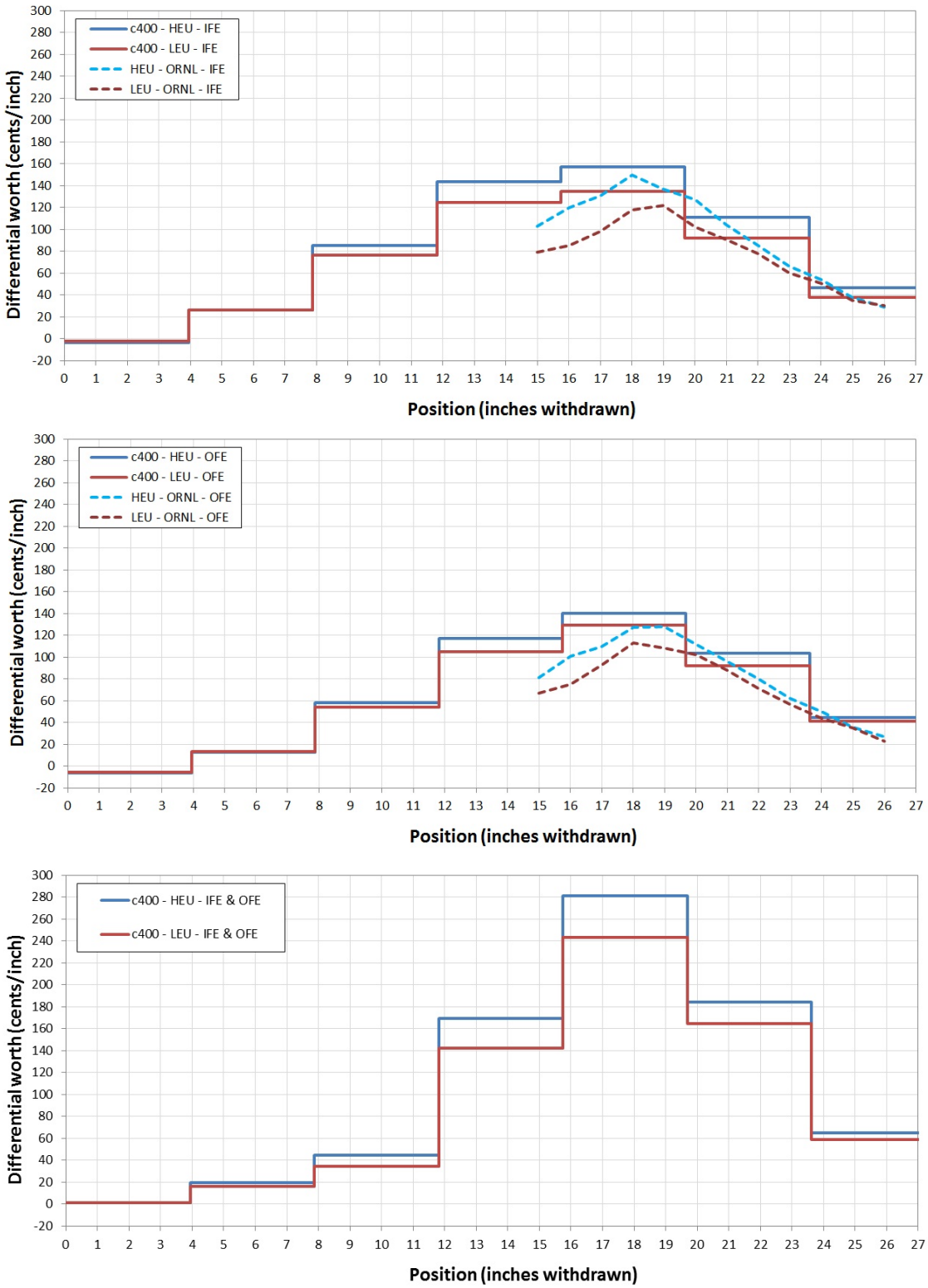

Figure 4.3.5.2.1 – Differential worth of the control elements obtained with Series *c400* at BOC. The top, middle and bottom figure presents the results obtained for the ICE, OCE and ICE and OCE combined, respectively. Uncertainty max. < 5cents/inch at 1-σ.

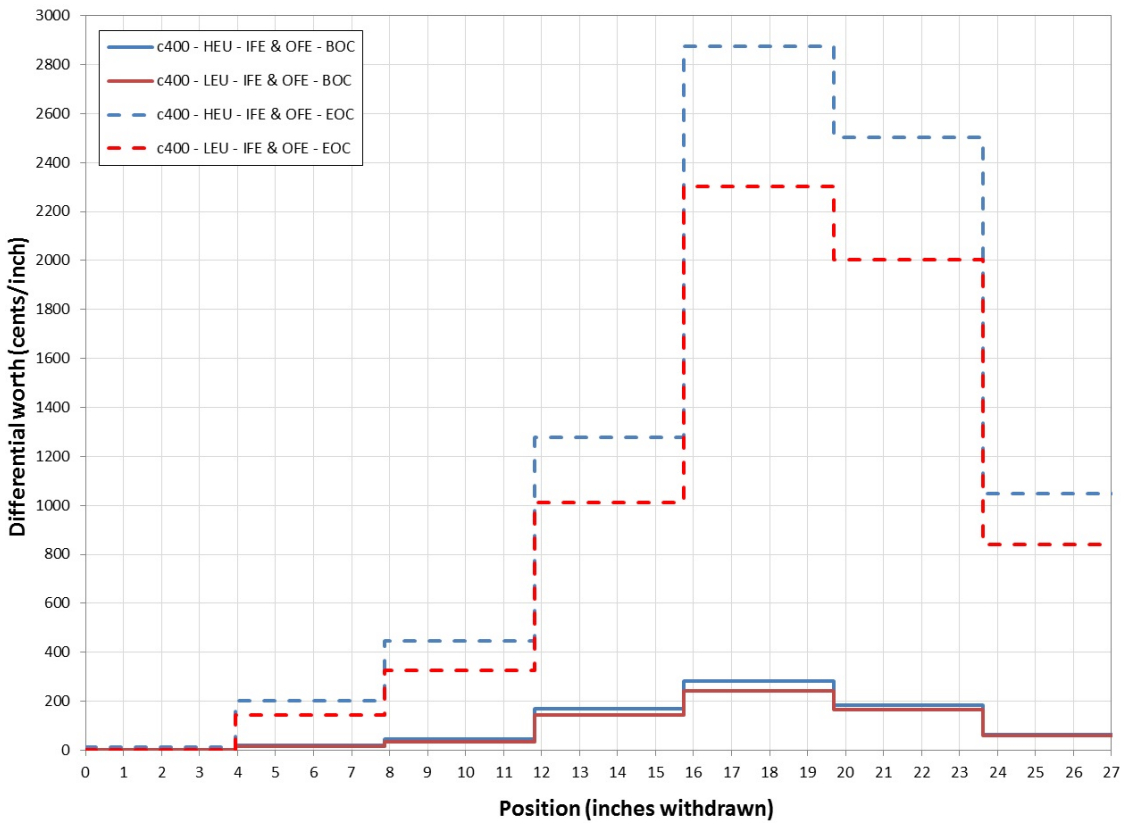

Figure 4.3.5.2.2 – Differential worth of the control elements (ICE and OCE combined) obtained with Series *c400* at BOC and EOC. Uncertainty max. < 5cents/inch at 1-σ.

4.3.5.3 Flux Trap Void Coefficient

The flux trap void coefficient has been studied exactly as was done by ORNL.- Decrease gradually the water density and evaluate the variation of k-effective between the perturbed case and the initial case (0% void). The results obtained at BOC with Series *c400* and *l11* are shown in the top graph of Figure 4.3.5.3.1. The results obtained at EOC are shown in the bottom graph of the same figure. Between the two series, two times and two fuels, the shape of the distribution is always the same. The variation of k-effective increases gradually with the increase of void, reaches a maximum around 40 to 60% void, depending on the series, and then decreases afterwards. The nature of the experimental loading has an impact on the magnitude of the k-effective variation. The magnitude is stronger in the Series *l11* (curium targets in the flux trap), especially at BOC. At EOC, the magnitude is still greater for Series *l11* but once the maximum is reached, the k-effective variation starts to decrease more rapidly than observed with Series *c400*. It is also observed that the magnitude of the variation is always stronger with the HEU core.

The ORNL results cover only the BOC case. The magnitude of the k-effective variation is relatively close but the location of the maximum is shifted in the ANL results to 10% lower void.

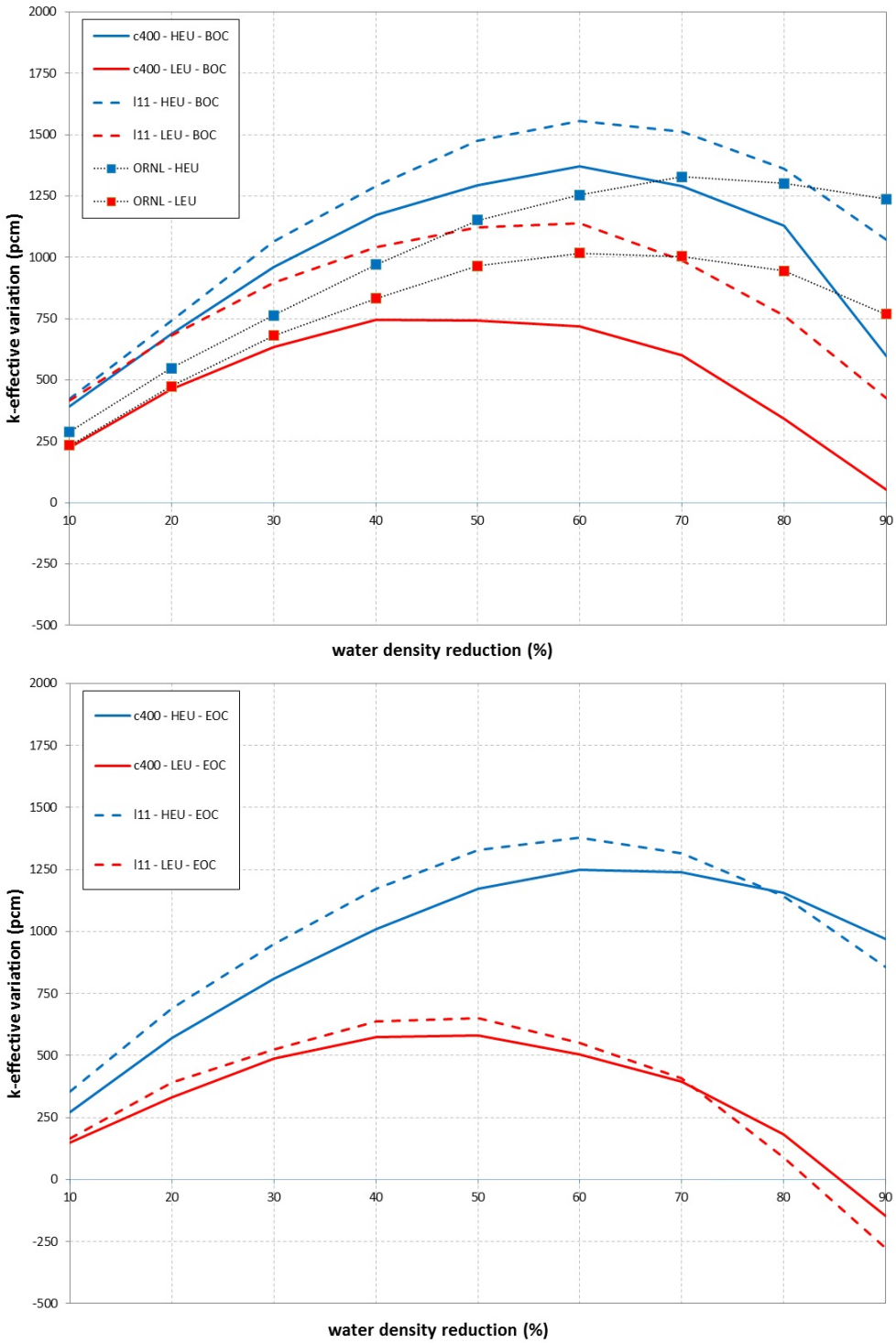

Figure 4.3.5.3.1 – k-effective variation versus the percentage of void introduced in the flux trap. Top and bottom graphs represent the results obtained at BOC and EOC, respectively. Uncertainty max. < 15pcm at 1-σ.

4.3.5.4 Coolant Void Coefficient

The Coolant Void Reactivity coefficient (CVR) is defined by ORNL in [Ref. 4] as:

$$CVR = \frac{(k_1 - k_2)}{(k_1 \cdot k_2) \cdot v_f}$$

where:

- CVR (pcm/%-void)
- k_1, k_2: k-effective of the initial and perturbed states
- v_f(%): fraction of void.

ORNL has evaluated the CVR for an amount of coolant void in the IFE and OFE of 10%. The ORNL and ANL results for this case are shown in Table 4.3.5.4.1. Only the results obtained with Series *c400* are shown because of the high similarity of the results obtained with the other series.

The ANL results obtained with the HEU core are in good agreement with the ORNL ones at BOC as well as at EOC (-1.9 to 3.5%). The results obtained with the LEU models are in less good agreement (10 to 19%) but remain reasonably close. Both HEU and LEU results remained negative.

Table 4.3.5.4.1 – ORNL and ANL Series *c400* CVR values for a coolant void fraction of 10%. Uncertainty max. < 2pcm/%-void at 1-σ

state	region	CVR – HEU (pcm/%-void x10^{-5})			LEU (pcm/%-void x10^{-5})		
		ORNL	ANL	variation ANL/ORNL (%)	ORNL	ANL	variation ANL/ORNL (%)
BOC	**IFE**	-0.102	-0.100	-1.9%	-0.082	-0.090	10.0%
	OFE	-0.218	-0.223	2.4%	-0.153	-0.173	12.9%
	IFE & OFE	-	-0.388		-	-0.275	
EOC	**IFE**	-0.069	-0.071	2.9%	-0.064	-0.075	17.1%
	OFE	-0.146	-0.151	3.5%	-0.108	-0.129	19.0%
	IFE & OFE	-	-0.224		-	-0.135	

5 Conclusions

The goal of this report was to describe the ANL review of the ORNL neutronic calculations supporting conversion of HFIR to the use of the proposed reference LEU fuel. The independent ANL calculations cover the evaluation of the matrix of performance of the reactor, power distribution, kinetics parameters and reactivity coefficients. Two ORNL MCNP inputs were provided to perform the work; one with a HEU core and the other one with the ORNL reference LEU core (described in [Ref. 4]). All calculations carried out with the HEU core assume a total nuclear power of 85MW whereas the reference power of the LEU core was 100MW.

The ORNL reference inputs have been modified to include some corrections related to the discovery of several inconsistencies in the ORNL inputs, and to also replace the homogeneous description of the fuel elements in the ORNL calculations by a heterogeneous one in the ANL calculations. The main motivation for an explicit description of the elements is to reduce the bias in the reactor physics results introduced by homogenizing the geometry. In particular, a simple physics argument can explain how a homogeneous description of a heterogeneous system affects the calculation of the probability for a neutron to escape the resonance captures at intermediate energy which may impact other parameters of the system. Comparison of results calculated for the HFIR explicit and homogeneous models reveals that the calculated neutron spectrum, flux, and reaction rates are slightly different. The magnitude of these differences in results calculated with the two models is relatively similar for both the HEU and LEU fuel types. It was found that those differences do not significantly affect the overall behavior calculated for the HEU core. However, they create significant differences in the behavior calculated for the reference LEU core. Most notably, the cycle length, which is a key parameter of the performance metric, is calculated to be significantly lengthened from 25 to 33 days (almost 30% longer) when the analyses are carried out using the heterogeneous model. This result makes the comparison between the HEU and LEU cores somewhat difficult to assess because extending the length of a cycle may involve other considerations, some of which are beyond the scope of this report. To better understand some of the impacts of a greater cycle length, several scenarios have been studied.

It has been shown that if the LEU core cycle length maintained identical to the HEU one (~25days), the LEU thermal fluence in the in-core irradiation positions nearly matches (within 10%) or exceeds the 85 MW HEU flux. On average the LEU performance increases over HEU in the approximate range of 5-10% when considering all the core performance positions modeled. This first scenario is considered to match current HEU cycle length despite the predicted ability to operate the LEU core for 32+ days. However, if the LEU core is burned to completion for 32-33days, then the overall performance would increase significantly, even when the number of cycles per year is reduced to six from the seven cycles typical of the current HEU cores. The other calculated parameters are generally in good agreement with those calculated by ORNL.

As general conclusions, ANL recommends the use of an explicit description of HFIR LEU cores as well as an assessment of the feasibility and impacts of extension of the cycle length. These evaluations would be useful in consideration of this reference fuel design with two-dimensional fuel grading, as well as future designs which may provide simplifications for improved fuel element fabricability.

References

[Ref. 1] RERTR website, http://www.rertr.anl.gov

[Ref. 2] C. Landers, *"Furthering HEU Minimization through Conversions"*, Reduced Enrichment for Research and Test Reactors (RERTR) Conference, Lisbon, October 2010.

[Ref. 3] ORNL website, http://neutrons.ornl.gov/facilities/HFIR/

[Ref. 4] G. Ilas, R.T. Primm III, *"Low Enriched Uranium Fuel Design with Two-Dimensional Grading for the High Flux Isotope Reactor"*, ORNL/TM-2010/318, March 2011.

[Ref. 5] D.M. Wachs, "RERTR Fuel Development and Qualification Plan", INL/EXT-05-01017 Rev. 4, 8/27/2009.

[Ref. 6] "MCNP - A General Monte Carlo N-Particle Transport Code, Version 5". Los Alamos National Laboratory. Volume I LA-UR-03-1987 & Volume II LA-CP-03-0245. 2003 revised 2005

[Ref. 7] A. G. Croff, " ORIGEN-2 – A revised abd Updated Version of the Oak Ridge Isotope Generation and Depletion Code", ORNL-5621, 1980

[Ref. 8] W. Haeck, "VESTA User's Manual Version 2.0.0". Institut de Radioprotection et de Surete Nucleaire. DSU/SEC/T/2008-331 - Indice A. 2009

[Ref. 9] R.D. Cheverton, T.M. Sims, *"HFIR Core Nuclear Design",* ORNL-4621, July 1971.

[Ref. 10] J. A. Lane et al., "*Ultra High Flux Research Reactors",* ORNL CF-58-7-117, July 1958.

[Ref. 11] J. A. Lane et al., "*High Flux Isotope Reactor Preliminary Design Study",* ORNL CF-59-2-65, March 1959.

[Ref. 12] R.D. Cheverton, *"HFIR Preliminary Physics Report",* ORNL-3006, October 1960.

[Ref. 13] R. D. Cheverton, *"Preliminary Report on Experimental Power and Flux Distribution in HFCE-2"*, ORNL-TM-90, January 1962.

[Ref. 14] "*High Flux Isotope Reactor*", Wikipedia webpage, http://en.wikipedia.org/wiki/High_Flux_Isotope_Reactor, last modified July 10 2012.

[Ref. 15] HFIR Safety Analytic Report, ORNL/HFIR/USAR/2344/Rev. 6, approved 8/2006.

[Ref. 16] G. Ilas, R.T. Primm III, *"Supporting documentation for LEU conversion, neutronic calculations in ORNL/TM-2010/318"*, C-HFIR-2011-11, March 2011.

[Ref. 17] Y. Calzavara et al., "Evaluation of Measurements Performed on the French High Flux Reactor (RHF)", OECD Benchmark, NEA/NSC/DOC(2006)1, revision 3, 2012.

[Ref. 18] W. Haeck, "*An Optimum Approach to Monte Carlo Burnup*", Nuclear Science and Design, Vol. 156, pp. 180-196, 2007.

[Ref. 19] NIST database website, http://www.nist.gov/pml/data/comp.cfm

[Ref. 20] R.T. Primm III et al., *"Design Study for a Low-Enriched Uranium Core for the High Flux Reactor, Annual Report for FY 2008"*, ORNL/TM-2009/87, 2009.

[Ref. 21] Technical drawings IFE fuel distribution, D-42114 rev. J

[Ref. 22] Technical drawings OFE fuel distribution, D-42122, rev. J

[Ref. 23] R.T. Primm III, *"Reactor Physics Studies of Reduced-Tantalum-Content Control and Safety Elements for the High Flux Isotope Reactor"*, ORNL/TM-2003/65, 2003.

[Ref. 24] N. Xoubi, R.T. Primm III, "Modeling of the High Flux Isotope Reactor Cycle 400", ORNL/TM-2004/251, August 2005.

[Ref. 25] G. Ilas, R.T. Primm III, "Methodology for Simulating the Irradiation of the Control Elements in HFIR", ANS Winter Meeting conference, Las Vegas, NV, November 9, 2010.

[Ref. 26] P. Reuss, Neutron Physics, EDP Sciences, 2008.

[Ref. 27] J. Duderstadt et al., Nuclear Reactor Analysis, Wiley-Interscience, 1976.

[Ref. 28] R. Barjon, Physique des Réacteurs Nucléaires, Instituts des Sciences Nucléaires, 1993.

Appendices

Table of Contents

Appendix A – Circle Involute 119

Appendix B – Methodology to Model Step-by-Step the Involute Shape with MCNP 121

B-1 Methodology…….. 121

B-2 Generate a Mesh……. 121

B-3 Generate a plate…….. 123

B-4 Duplicate the plate……. 124

B – References…… 124

Appendix C – Investigation on the Differences between Explicit and Homogenized Models 125

C-1 Introduction……. 125

C-2 Homogeneous vs. Heterogeneous…….. 125

C-3 Predicted Cycle Length…… 127

C-4 Isotope Mass Evolution……. 130

C-5 Scalar Neutron Flux…… 132

C-6 Average Neutron Energy…… 134

C-7 Isotope Anti-reactivity……. 137

C-8 Pseudo k-effective…….. 145

C-9 Conclusion…… 148

C- References…….. 149

Appendix D – HEU and LEU Power Distributions of configuration l11 at BOC, day 1 and EOC 150

Appendix A – Circle Involute

This short appendix is intended to compile the different formulas related to the involute of a circle that have been used for the review. In Cartesian coordinates, the involute of a circle has the following parametric equation:

$$x = k(\cos(\alpha) + \alpha\ \sin(\alpha))$$ Equation A1

$$y = k(\sin(\alpha) - \alpha\ \cos(\alpha))$$

where k represents the radius of the circle generating the involute and α is an angle parameter expressed in radian. This angle is formed between the X axis, the center of the circle and a given point of the involute.

An illustration of involute is provided in Figure A1. The involute is represented in red and starts at the intersection of the blue circle of radius k and the X axis.

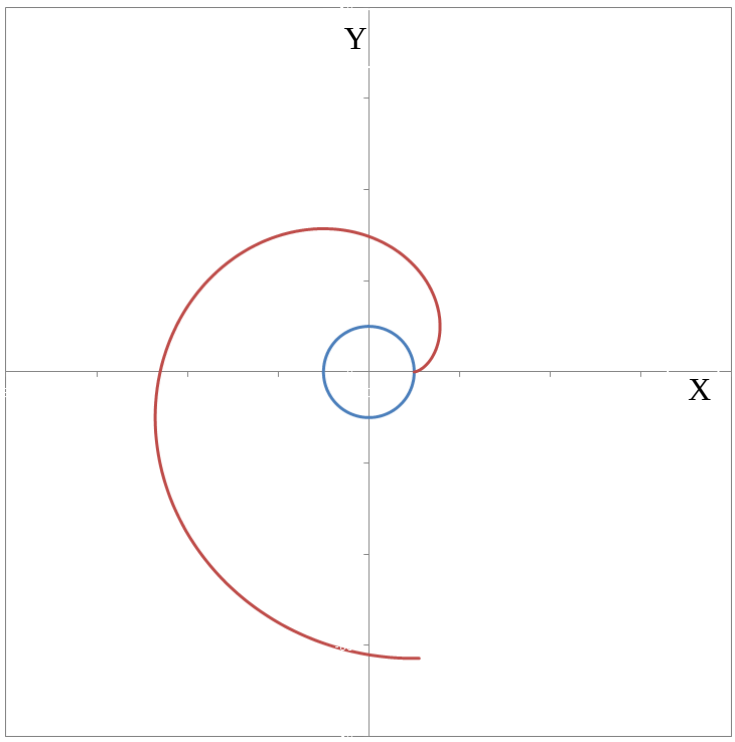

Figure A1 – Representation of a circle involute (red) generated around the blue circle of radius k.

From Equation A1, the distance R between the center and a point of the involute (which depends only on α) is given by:

$$R = \sqrt{x^2 + y^2} = k\sqrt{(1 + \alpha^2)}$$ Equation A2

Equation A2 can be inverted to obtain the relation between the angle α, and the distance to the center, R:

$$\alpha = \sqrt{\frac{R^2}{k^2} - 1}$$ Equation A3

The arc length S is given by:

$$S = \frac{1}{2} k\alpha^2$$ Equation A4

From equation A2 and A3:

$$S = \frac{1}{2}\left(\frac{R^2}{k} - k\right)$$ Equation A5

The coordinates (x',y') of the involute rotated by an angle β in the plane of the involute are given by Equation A6:

$$x' = x\ \cos(\beta) - y \sin(\beta)$$ Equation A6
$$y' = x\ \sin(\beta) + y\ \cos(\beta)$$

where (x,y) the coordinates of the involute given by Equation A1

If the fuel plate thickness, λ_f, coolant channel thickness, λ_c, and number of plates, *n,* of an involute shaped plate element are known, one can deduce the radius of the circle generating the involute:

$$k = \frac{(\lambda f + \lambda c)n}{2\pi}$$ Equation A7

Appendix B – Methodology to Model Step-by-Step the Involute Shape with MCNP

This appendix describes the methodology used at ANL to model the involute shape with the computer code MCNP [Ref. B1]. Equations presented in Appendix A are used several times.

B-1 Methodology

The methodology is based on discretization of the involute. The real shape of the object is taken as a reference and split into several small pieces juxtaposed to produce an approximation of the reference object. Because of the high symmetry of the involute plate cores, there is no need to model each plate individually. One is enough. The others plates are obtained by duplication of the first one. Using MCNP, this implies creating a "mesh" made of as many cells as there are plates and filling up these cells with the plate cells. The process of production can thus be divided in three different steps:

- Produce a "mesh"
- Model one plate
- Duplicate the plate and fill up the mesh

Each step is described in the following subsections.

B-2 Generate a Mesh

The mesh is made of "empty spaces" that are filled up with a duplicate of the fuel plate. There are as many cells in the mesh that there are plates. To have a fast running model, it is recommended to design the mesh as simply as possible. One solution is to define a cylinder (radius and position) designed to be included between two successive fuel plates without any contact as illustrated in Figure B.1. On this figure are represented two successive involute plates (light blue) fastened between two side plates (gray). A portion of cylinder represented by a black dashed line is visible between the two plates. If such cylinders can be defined, one just needs to duplicate it as many times as necessary (one per plate). Then, one cell of the mesh will be defined as the space created by two successive cylinders and the two side plates.

To duplicate the plates, the generation of MCNP "transformation" cards is necessary. The cylinders can use the same transformation card as the plate. Assuming the geometry defined in the plane, (x,y), the transformation cards (12 entries) are generated by:

$$TRx \quad 0\,0\,0 \quad \cos(a(n)) \quad \cos\left(\frac{\pi}{2} - a(n)\right) \quad 0 \quad \cos\left(\frac{\pi}{2} + a(n)\right) \quad \cos(a(n)) \quad 0 \quad 0 \quad 0 \quad 1$$

where:

- TRx transformation number x
- a(n) (rad): angle between the first plate (n=0) and plate n.

The angle a(n) is given by:

$$a(n) = \frac{2\pi}{N} n \qquad \text{Equation B1}$$

where:

- N: total number of plates.

The mesh used for the explicit model of HFIR is represented in Figure B2. The mesh of the outer element has been made with cylinders. The inner element mesh has been made with cylinders and planes.

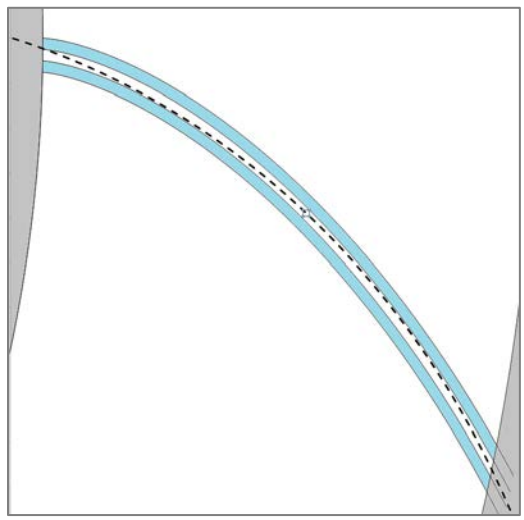

Figure B1 – Portion of cylinder (black dashed line) included between two involute plates (light blue) that can be used to generate a mesh.

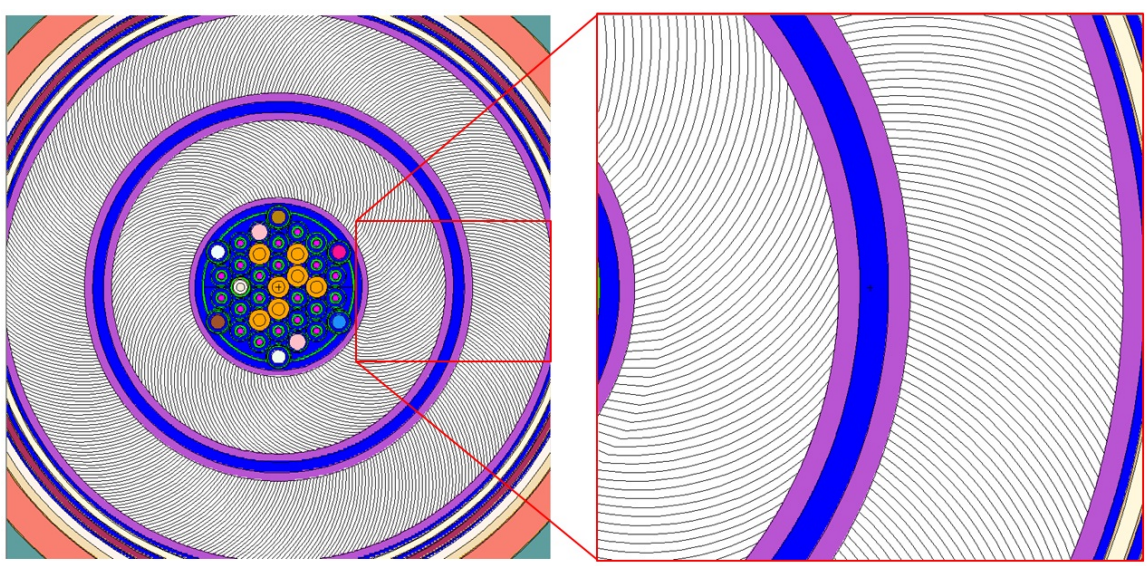

Figure B2 – Mesh generated used for HFIR explicit models. The picture on the right is an enlargement of the left picture.

B-3 Generate a Plate

To generate a plate one has to decide in how many pieces the plate will be split. The error made on the volumes will decrease with the increasing number of pieces. The individual pieces can be modeled in different ways. One easy and economical (number of surfaces reduced at the maximum) way is to use the MCNP card ARB which creates 4 to up to 6-faced polyhedrons. The ARB card requires eight triplets of entries (24 entries) followed by 6 entries. The first eight triplets are used to provide the coordinates of the eight potential corners of the polyhedrons. The last remaining 6 entries are used to determine how to combine the corners. Depending on personal preferences, the number and size of the pieces can always be expressed as a function of the rotation angle of the involute. For instance, one can split the plates into pieces that have the same arc length or have the same radial increment. The relation between the arc length or the "radial" distance from the center can be expressed as a function of the involute rotation angle by using Equation A.3 or A.4. When there is no axial grading, the pieces to model (fuel, cladding…) can be modeled using 6-faced polyhedrons. If we consider that the piece starts at a rotation angle α and stops at α+Δα and is defined axially between the positions, Z1 and Z2, the ARB card number, X, can be written as follows:

$$
\begin{array}{l}
X \quad ARB \ \big(k(\cos(\alpha)+\alpha.\sin(\alpha))\big).\cos(\beta 1)-\big(k(\sin(\alpha)-\alpha.\cos(\alpha))\big).\sin(\beta 1) \\
\quad \big(k(\cos(\alpha)+\alpha.\sin(\alpha))\big).\sin(\beta 1)+\big(k(\sin(\alpha)-\alpha.\cos(\alpha))\big).\cos(\beta 1) \\
\quad \mathrm{Z1} \\
\quad \big(k(\cos(\alpha+\Delta\alpha)+(\alpha+\Delta\alpha).\sin(\alpha+\Delta\alpha))\big).\cos(\beta 1)-\big(k(\sin(\alpha+\Delta\alpha)-(\alpha+\Delta\alpha).\cos(\alpha+\Delta\alpha))\big).\sin(\beta 1) \\
\quad \big(k(\cos(\alpha+\Delta\alpha)+(\alpha+\Delta\alpha).\sin(\alpha+\Delta\alpha))\big).\sin(\beta 1)+\big(k(\sin(\alpha+\Delta\alpha)-(\alpha+\Delta\alpha).\cos(\alpha+\Delta\alpha))\big).\cos(\beta 1) \\
\quad \mathrm{Z1} \\
\quad \big(k(\cos(\alpha)+\alpha.\sin(\alpha))\big).\cos(\beta 1)-\big(k(\sin(\alpha)-\alpha.\cos(\alpha))\big).\sin(\beta 1) \\
\quad \big(k(\cos(\alpha)+\alpha.\sin(\alpha))\big).\sin(\beta 1)+\big(k(\sin(\alpha)-\alpha.\cos(\alpha))\big).\cos(\beta 1) \\
\quad \mathrm{Z2} \\
\quad \big(k(\cos(\alpha+\Delta\alpha)+(\alpha+\Delta\alpha).\sin(\alpha+\Delta\alpha))\big).\cos(\beta 1)-\big(k(\sin(\alpha+\Delta\alpha)-(\alpha+\Delta\alpha).\cos(\alpha+\Delta\alpha))\big).\sin(\beta 1) \\
\quad \big(k(\cos(\alpha+\Delta\alpha)+(\alpha+\Delta\alpha).\sin(\alpha+\Delta\alpha))\big).\sin(\beta 1)+\big(k(\sin(\alpha+\Delta\alpha)-(\alpha+\Delta\alpha).\cos(\alpha+\Delta\alpha))\big).\cos(\beta 1) \\
\quad \mathrm{Z2} \\
\quad \big(k(\cos(\alpha)+\alpha.\sin(\alpha))\big).\cos(\beta 2)-\big(k(\sin(\alpha)-\alpha.\cos(\alpha))\big).\sin(\beta 2) \\
\quad \big(k(\cos(\alpha)+\alpha.\sin(\alpha))\big).\sin(\beta 2)+\big(k(\sin(\alpha)-\alpha.\cos(\alpha))\big).\cos(\beta 2) \\
\quad \mathrm{Z1} \\
\quad \big(k(\cos(\alpha+\Delta\alpha)+(\alpha+\Delta\alpha).\sin(\alpha+\Delta\alpha))\big).\cos(\beta 2)-\big(k(\sin(\alpha+\Delta\alpha)-(\alpha+\Delta\alpha).\cos(\alpha+\Delta\alpha))\big).\sin(\beta 2) \\
\quad \big(k(\cos(\alpha+\Delta\alpha)+(\alpha+\Delta\alpha).\sin(\alpha+\Delta\alpha))\big).\sin(\beta 2)+\big(k(\sin(\alpha+\Delta\alpha)-(\alpha+\Delta\alpha).\cos(\alpha+\Delta\alpha))\big).\cos(\beta 2) \\
\quad \mathrm{Z1} \\
\quad \big(k(\cos(\alpha)+\alpha.\sin(\alpha))\big).\cos(\beta 2)-\big(k(\sin(\alpha)-\alpha.\cos(\alpha))\big).\sin(\beta 2) \\
\quad \big(k(\cos(\alpha)+\alpha.\sin(\alpha))\big).\sin(\beta 2)+\big(k(\sin(\alpha)-\alpha.\cos(\alpha))\big).\cos(\beta 2) \\
\quad \mathrm{Z2} \\
\quad \big(k(\cos(\alpha+\Delta\alpha)+(\alpha+\Delta\alpha).\sin(\alpha+\Delta\alpha))\big).\cos(\beta 2)-\big(k(\sin(\alpha+\Delta\alpha)-(\alpha+\Delta\alpha).\cos(\alpha+\Delta\alpha))\big).\sin(\beta 2) \\
\quad \big(k(\cos(\alpha+\Delta\alpha)+(\alpha+\Delta\alpha).\sin(\alpha+\Delta\alpha))\big).\sin(\beta 2)+\big(k(\sin(\alpha+\Delta\alpha)-(\alpha+\Delta\alpha).\cos(\alpha+\Delta\alpha))\big).\cos(\beta 2) \\
\quad \mathrm{Z2} \\
\quad \mathrm{1234\ 5678\ 1256\ 3478\ 1375\ 2486}
\end{array}
$$

In this example, the x, y and z coordinates of each corner (8) are given on the first through 24th lines. The last line (6 entries) combines the corners to form the 6-faced polyhedrons. The coordinates, x and y, of each corner are expressed as in Equation A6 which makes x and y dependent on the rotation angle α and also on the angle β (rotation of the involute itself in the plane).

The value of β depends on the thickness of the object to model and also on what edge (or which involute) has been taken as a reference. For instance, if the first involute is taken as a reference is an edge of the plate and the object to model is the plate of thickness, λ, the values of β are:

$$\beta 1 = 0$$
$$\beta 2 = \mathrm{atan}(\frac{\lambda}{k})$$

where:

- λ: plate thickness
- k: radius of the circle generating the involute.

In the case of radial grading, the parameter, λ, changes with the rotation angle, α. For instance, in the case of HFIR, one edge of the fuel remains at a constant distance (thickness), λ1, of the inner edge of the cladding whereas the other one, λ2(α), varies along the rotation angle α.

In this case, the values of β are:

$$\beta 1 = \mathrm{atan}(\frac{\lambda 1}{k})$$

$$\beta 2 = \mathrm{atan}(\frac{\lambda 2(\alpha)}{k})$$

In the HFIR explicit models produced by ANL, the fuel, IFE filler, zirconium layers (if any) have been explicitly modeled. The cladding faces have not been explicitly modeled. Instead the object "plate" has been created (from the inner to the outer edge of the plate) from which has been "subtracted" in the cell definition the objects (fuel, filler…) present within.

Based on the same principle, the object "plate" is also included in a larger volume. This larger volume, called the "box", is filled up with the coolant from which is subtracted the object "plate". It has to be larger than the cell "mesh". Again, to have an efficient model (fast running), it is recommended to divide this large volume into smaller ones in such a way that not the entire object "plate" will be subtracted but only a few pieces. This process will reduce the number of surfaces "called" per cell which will accelerate the calculations.

B-4 Duplicate the Plate

To duplicate the plate in the entire mesh, all of the cells of the mesh have to include the MCNP card, FILL, followed by the index of the transformation (different for each cell of the mesh). All the objects that have to be duplicated (box, fuel…) have to include the MCNP card, U.

B - References

[Ref. B1] "MCNP - A General Monte Carlo N-Particle Transport Code, Version 5". Los Alamos National Laboratory. Volume I LA-UR-03-1987 & Volume II LA-CP-03-0245. 2003 revised 2005

Appendix C – Investigation of the Differences between Explicit and Homogenized Models

C-1 Introduction

A new methodology has been developed in late 2010 at Argonne National Laboratory (ANL) to model with reasonable precision the geometry of the involute shape with the code MCNP. This methodology has been applied to model the RHF reactor without homogenization of materials. This new "explicit" RHF model has been benchmarked against a series of criticality measurements at beginning of life (BOL) with satisfactory results [Ref. C1]. In addition, it has been possible to predict very well the cycle length of several RHF cycles by using this explicit model with the depletion code VESTA [Ref. C2, C3] coupled with a critical search algorithm. Criticality calculations carried out for BOL configurations have shown very good agreement between the explicit and homogenized models for both HEU and LEU configurations. Depletion calculations have been carried out using VESTA and the critical search algorithm. The predicted cycle length for both HEU explicit and homogenized calculations is extremely close (less than a day of difference) whereas a significant difference in cycle length has been obtained between the LEU explicit and homogenized models. Since no errors have been found in the inputs (or at least not large enough to explain the discrepancy), an investigation has been carried out to determine the reason for the difference. Looking in more detail at the neutronic parameters and their evolution, it has been possible to provide an explanation for the difference.

C-2 Homogeneous vs. Heterogeneous

To describe all the phenomena occurring in a complex reactor such as HFIR is quite difficult. This is why it is preferred to use tools which allow a full 3D description of the reactor. However, since the purpose of this investigation is to understand the non-equivalence of the homogeneous and heterogeneous models, it can be useful to begin by recalling the expected variations between both descriptions.

In a thermal system, once fission had occurred, the new created fast neutrons have to slow down and reach the thermal energy in order to create new fissions. However, the slowing down process can be stopped at intermediate energy by parasitic neutron capture in the resonances of the heavy metal absorption cross sections (especially the ^{238}U ones). As illustrated in Figure C1, in a heterogeneous system, the neutrons usually go into the moderator in which they can slow down at "no risk," since the moderator is free of heavy metals. Once they are thermalized, some chances exist that they could return into the fuel to create new fissions. This is not the same situation as in a homogeneous system where slowing down neutrons can more easily be captured in a resonance since the probability to "meet" a heavy nuclei is higher.

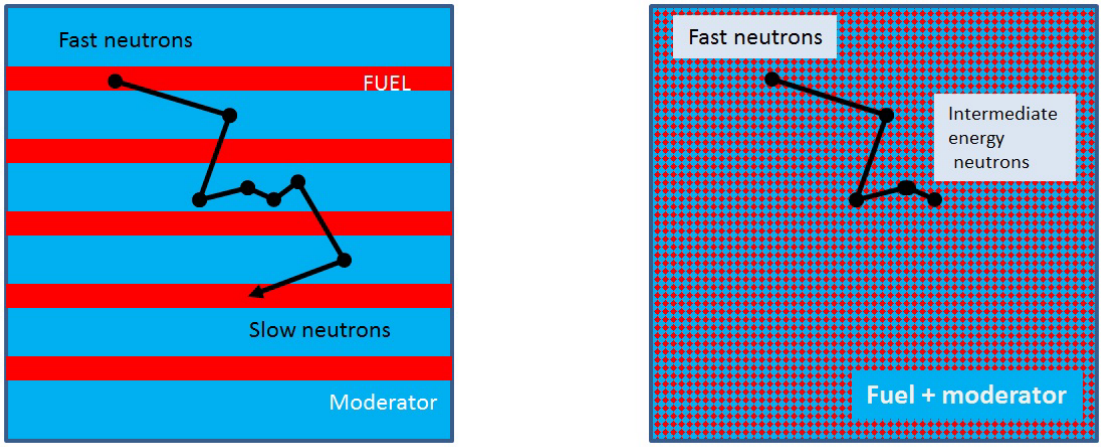

Figure C1 – Illustration of the difference between a heterogeneous (left) and homogeneous (right) system. The probability of being captured at intermediate energy is higher in a homogeneous system because the probability to meet heavy nuclei is higher.

Another important effect that can only be seen in a heterogeneous description is the so-called spatial self-shielding effect: Slowing neutrons which are at intermediate energy that go back into the highly absorbing fuel will tend to be absorbed in the outer layer of the flux creating a flux depression in the fuel at those energies. A higher fuel macroscopic cross section of absorption yields a more pronounced effect.

Basically, the most important difference between a homogeneous and heterogeneous thermal system is the probability for a neutron to escape the resonances at intermediate energy. This probability is considerably higher in the heterogeneous system. That will help the production of thermal neutrons but at the same time that will create a depression of the flux in the fuel due to the spatial self-shielding effect. These two effects will more or less impact the different reaction rates and consequently the reactivity of the fuel (depending on the nature of the fuel and the geometry considered). While It is difficult to predict the magnitude of the effects on a reactor such as HFIR without detailed calculations, the following remarks can be made:

- In a HEU system, the most abundant heavy nucleus is ^{235}U. The fission cross section is considerably higher than the other absorption cross sections. Consequently, the neutrons captured in the resonances at intermediate energy have a strong chance to create new fissions. Since this probability is higher in a homogeneous system, the effect may keep the magnitude of the neutron flux and the fuel reactivity (balance between neutron production over absorption) at a high level.

- In a LEU system, the most abundant heavy nucleus is the ^{238}U. The gamma cross section is higher than the other absorption cross sections. Consequently, the neutrons captured in the resonances at intermediate energy tend to reduce the fuel reactivity (ratio of neutron production over absorption decreases). Since this probability is higher in a homogeneous system, the effect may negatively impact the magnitude of the neutron flux and the fuel reactivity.

Many methodologies are described in the literature to model a heterogeneous system with a homogeneous description [Ref. C7, C8, C9]. For criticality calculations, it is often recommended

to match the averaged reaction rates of the object considered which implies generating correction factors to the cross sections.

C-3 Predicted Cycle Length

Depletion calculations for the MCNP models of HFIR have been coupled with the use of a critical search algorithm. For every time step, criticality is achieved by moving the positions of the control elements. The cycle is over when the control elements have reached the fully withdrawn position (27 inches withdrawn for HFIR). Figure C2 shows the predicted critical positions of the control elements during irradiation for both the HEU explicit and homogenized models. As one can see, and despite a slight discrepancy at BOC, both curves converge to the same value, a cycle length of approximately 26 days.

The same calculations have been carried out with both the LEU explicit and homogenized models. Results are shown in Figure C3 which plots the critical positions obtained with the LEU explicit model, and the LEU homogenized model. The only point that seems to match between these two curves is obtained at the beginning of irradiation. After that, the discrepancy between them increases over the irradiation. Finally, the predicted cycle length using the LEU homogenized model is about 25 days whereas the one predicted using the explicit model is almost 29 days (a large 16% difference).

The large magnitude of the variation was not expected and the presence of an error has been considered. However, after in-depth checking of both inputs, nothing has been found that could explain such results. The consequence of this fruitless search was to admit that the two models are not equivalent.

Thus, in the absence of any modeling simplification or error, the fact that for a given time step the control elements are more withdrawn in the homogeneous model than in the explicit means that the reactivity of the homogenized model is lower than the explicit model. To determine the variation in reactivity difference between the explicit and homogeneous models, the explicit depletion was repeated using the critical control element positions of the homogeneous model, but otherwise with the same conditions (time step, power…). The reactivity difference $\rho_{ex\text{-}rz}(i)$ is then obtained for each time step, I, using Equation C1.

$$\rho_{ex-rz}(i) = \frac{(k_{ex}(i) - k_{rz}(i))}{k_{ex}(i) * k_{rz}(i)} \qquad \text{Equation C1}$$

where:

$\rho_{ex\text{-}rz}(i)$: Reactivity difference between explicit and homogenized models at time step i.

$k_{ex}(i)$: k-effective of the explicit model at time step i.

$k_{rz}(i)$: k-effective of the homogeneous model at time step i.

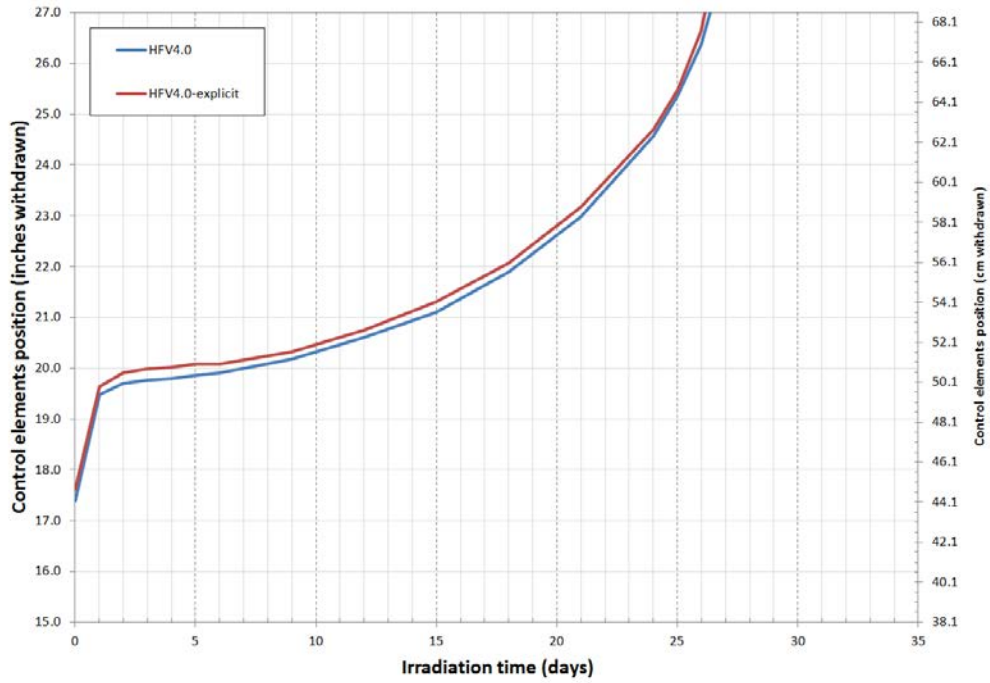

Figure C2 – Predicted control element positions which maintain criticality in the reactor during irradiation at 85MW obtained with HEU explicit and homogenized models.

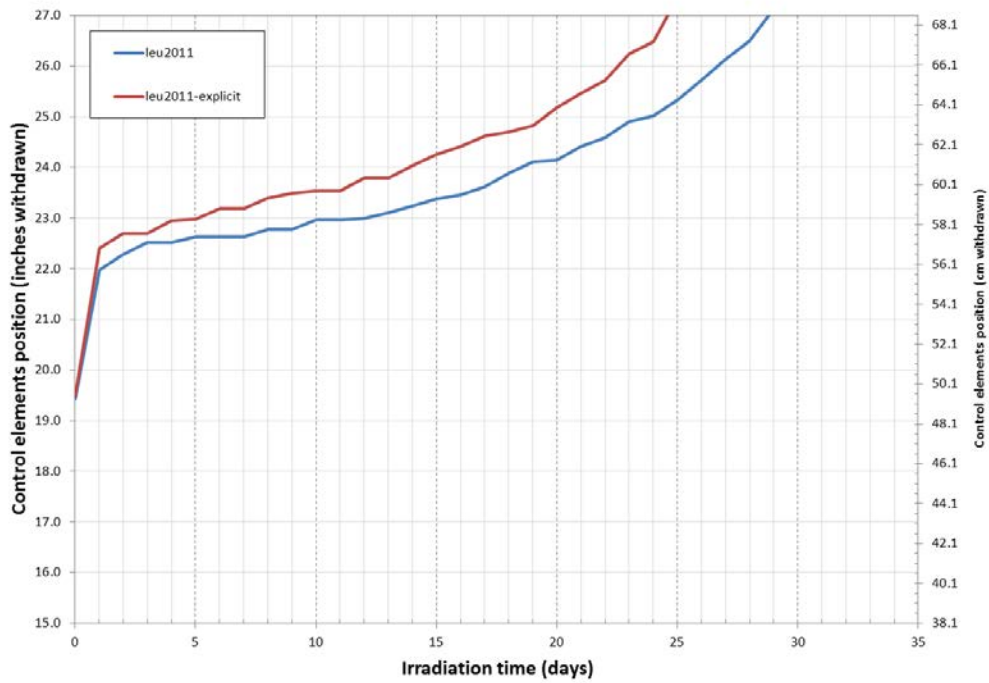

Figure C3 - Predicted control elements positions which maintain criticality in the reactor during irradiation at 100MW obtained with LEU explicit and homogenized models.

The reactivity difference between the LEU r-z homogenized and explicit calculations is shown in Figure C4. As one can see, the reactivity difference is relatively small at the beginning of irradiation, and then increases strongly and rapidly during a few days, and thereafter the trend is a slow increase until the end of irradiation.

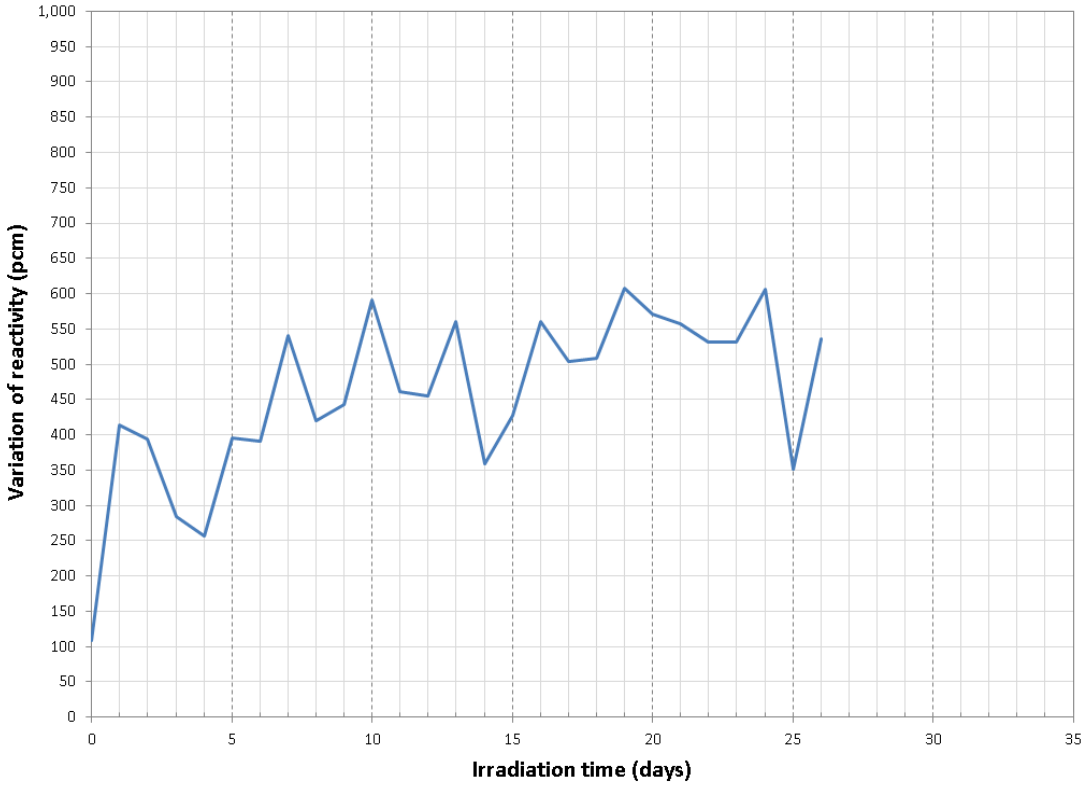

Figure C4 – Evolution of the reactivity difference, where a higher reactivity is modeled with the LEU explicit model vs. the homogeneous model over the course of depletion.

C-4 Isotope Mass Evolution

Comparison of the evolution of various isotopes (^{235}U, ^{238}U, ^{239}Pu, ^{135}Xe, ^{149}Sm and ^{10}B) between the explicit and homogenized models has been carried out for both the HEU and LEU configurations. Results are compiled in Table C1 below. As one can see, isotopic agreement at BOL is very good for both the explicit and homogenized models in the HEU and LEU configurations. However, during the irradiation, some variations are observed, and so as a reference the isotopic masses are listed at 25 days.

For both HEU and LEU configurations, one can make the following remarks:

- The ^{10}B in the IFE filler is predicted to be burned faster in the explicit models than in the homogenized ones.

- There is more ^{239}Pu built up in the homogenized models than in the explicit ones. Since this isotope arises from the depletion of the ^{238}U, it makes sense that the ^{238}U is less depleted in the explicit models.

- The production of Xenon and Samarium is always higher in the homogenized models than in the explicit ones.

The main conclusion that can be drawn at this point is that although more pronounced in magnitude for the LEU, the differences between the explicit and homogenized models are generally of the same nature for both HEU and LEU. Since the evolution of an isotope is flux and cross section dependent, the difference between the explicit and homogenized models has to be explained by a variation of these parameters.

Table C1 – Mass evolution of different isotopes present in the IFE fuel, filler and OFE for HEU and LEU configurations

		Mass BOL explicit models (g)	Mass BOL homogenized model (g)	Variation explicit / homogenized BOL (%)	Mass explicit model at t=25days (g)	Mass homogenized model at t=25days (g)	Variation explicit / homogenized t=25days (%)
IFE filler							
HEU	**^{10}B**	2.79660E+00	2.79746E+00	**-0.03%**	1.84256E-01	1.93121E-01	**-4.59%**
LEU	**^{10}B**	5.39747E+00	5.39726E+00	**0.00%**	1.59142E+00	1.74549E+00	**-8.83%**
IFE fuel							
HEU	**^{235}U**	2.59325E+03	2.59420E+03	**-0.04%**	1.62996E+03	1.62484E+03	**0.31%**
	^{238}U	1.52165E+02	1.52227E+02	**-0.04%**	1.45996E+02	1.45865E+02	**0.09%**
	^{239}Pu	-	-	**-**	3.28770E+00	3.37865E+00	**-2.69%**
	^{135}Xe	-	-	**-**	1.22049E-02	1.22130E-02	**-0.07%**
	^{149}Sm	-	-	**-**	9.02237E-02	9.07389E-02	**-0.57%**
LEU	**^{235}U**	6.37832E+03	6.37835E+03	**0.00%**	5.28494E+03	5.29424E+03	**-0.18%**
	^{238}U	2.55695E+04	2.55695E+04	**0.00%**	2.53721E+04	2.53586E+04	**0.05%**
	^{239}Pu	-	-	**-**	1.17244E+02	1.27199E+02	**-7.83%**
	^{135}Xe	-	-	**-**	5.40264E-02	5.50776E-02	**-1.91%**
	^{149}Sm	-	-	**-**	3.80654E-01	3.88604E-01	**-2.05%**
OFE fuel							
HEU	**^{235}U**	6.79959E+03	6.80366E+03	**-0.06%**	5.12891E+03	5.13702E+03	**-0.16%**
	^{238}U	3.99006E+02	3.99235E+02	**-0.06%**	3.85816E+02	3.85612E+02	**0.05%**
	^{239}Pu	-	-	**-**	7.99934E+00	8.23154E+00	**-2.82%**
	^{135}Xe	-	-	**-**	3.99342E-02	4.02426E-02	**-0.77%**
	^{149}Sm	-	-	**-**	2.80975E-01	2.82460E-01	**-0.53%**
LEU	**^{235}U**	1.88500E+04	1.88519E+04	**-0.01%**	1.69021E+04	1.68347E+04	**0.04%**
	^{238}U	7.55720E+04	7.55736E+04	**0.00%**	7.54433E+04	7.51427E+04	**0.04%**
	^{239}Pu	-	-	**-**	2.57285E+02	2.79016E+02	**-7.79%**
	^{135}Xe	-	-	**-**	1.96191E-01	2.00234E-01	**-2.02%**
	^{149}Sm	-	-	**-**	1.41744E+00	1.44027E+00	**-1.59%**

C-5 Scalar Neutron Flux

The evolution of a given isotope is determined by the product of the neutron flux with cross section. Thus, variation in mass for isotopes is explained by a variation in flux and/or cross section. To analyze the neutron flux evolution, the scalar flux calculated and given in the VESTA outputs (one value per time step and burnup zone) has been used. To simplify the study, it has been chosen to average the flux over a whole region (e.g, a whole region means the whole IFE fuel or filler…) using Equation C2 summed over n regions:

$$\overline{\varphi}_{region} = \frac{\sum_i^n \varphi_i \cdot V_i}{\sum_i^n V_i} \qquad \text{Equation C2}$$

where:

$\overline{\varphi}_{region}$: Average scalar flux over a whole region

φ_i : scalar flux in burnup zone i

V_i : Volume of the burnup zone i.

Evolution of the scalar flux in the IFE and OFE is shown in Figures C5 and C6, respectively. Each figure is made of two plots. One is for HEU, the other is for LEU. On each plot, the scalar flux evolution obtained with the explicit and homogenized models is shown in addition to the variation between them. To ease the comparison between model and configuration, the four plots are at the same scale. The following observations can be made from the plots:

- For each region (IFE fuel, filler, OFE fuel), the flux is always higher in the HEU configuration than in the LEU one. This can be understood since for a given number of fissions, the HEU absorbs less neutrons (more reactivity). This is expected since there are molybdenum isotopes (neutronic poisons) and much more ^{238}U in the LEU fuel.

- The flux in the HEU homogenized regions is always higher than in the corresponding explicit ones (about +4%, from BOL to the end of irradiation). Recalling the expected variation between the homogenous and heterogeneous systems given in the previous section, this effect can be explained by the fact that even if neutrons have a greater chance to be absorbed at intermediate energies (decreasing the flux), these absorptions will in most cases create more fissions and increase the flux. In addition, the spatial self-shielding effect will tend to create a depression in the flux in the explicit model.

- The fact that the ^{10}B in the IFE filler is burned faster in the HEU explicit model indicates that the product of flux with cross section is higher in the explicit model. Since the flux is lower, the only possibility is that the absorption cross section is greater. This is a strong indication of a neutron spectrum variation between the explicit and homogenized HEU model.

- The flux in the LEU homogenized regions is always lower than in the corresponding explicit ones (about -4%, from BOL to the end of irradiation). Again, recalling the expected variation between the homogenous and heterogeneous systems given in the previous section, this result can be explained by the fact that in LEU fuel, more frequent absorptions at intermediate

energies tends to decrease the flux in the homogenized model. This effect is apparently not compensated by the spatial self-shielding effect occuring in the explicit model.

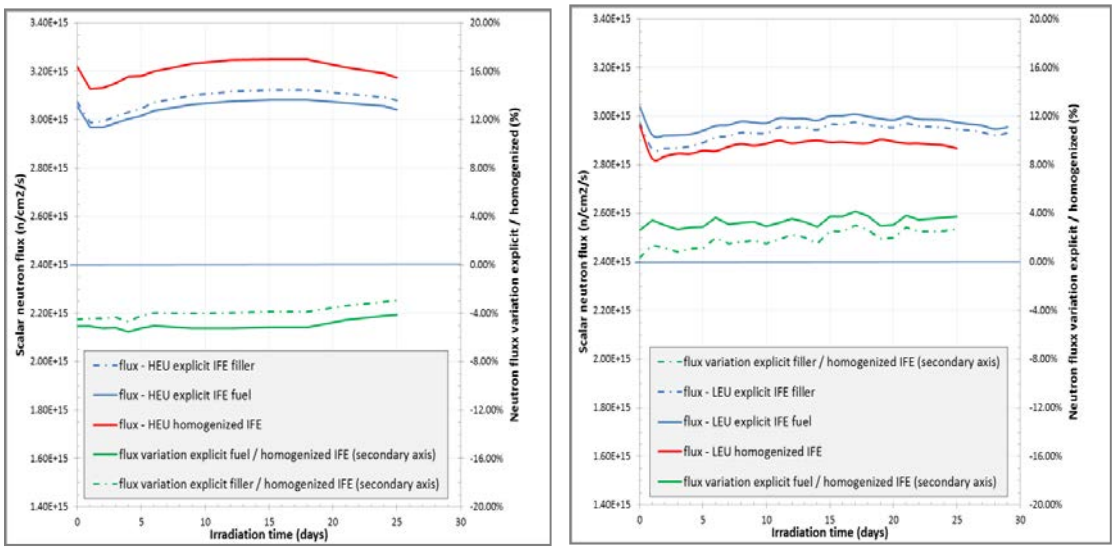

Figure C5 – Neutron scalar flux evolution in the IFE for homogenized and explicit models. Graph on the left is for the HEU configurations. Graph on the right is for the LEU configurations.

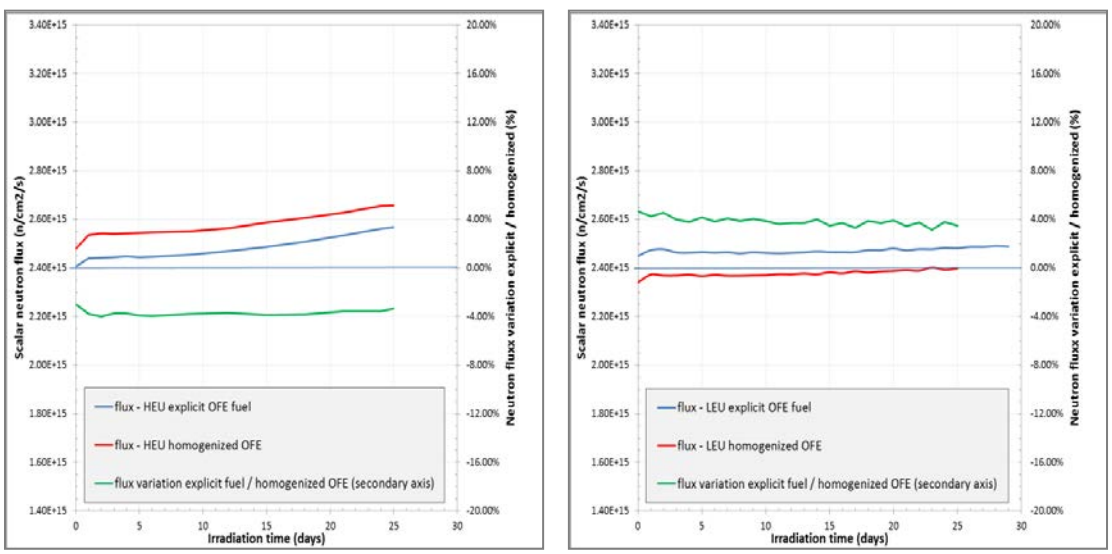

Figure C6 – Neutron scalar flux evolution in the OFE for homogenized and explicit models. Graph on the left is for the HEU configurations. Graph on the right is for the LEU configurations.

C-6 Average Neutron Energy

The analysis of the scalar flux has highlighted the neutron spectrum variation between explicit and homogenized models (for both HEU and LEU configurations). Study of the whole neutron spectrum is a difficult exercise. Instead, a simpler and preferred approach is to extract the average neutron energy of the spectrum in a region and track
its evolution. By this way, only one value per region and per time step has to be tracked. However, such a value is not a direct output of the steady state or depletion calculations.

Most of the Monte Carlo depletion tools calculate reaction rates during the steady state calculation. The idea behind VESTA is to reduce the calculational time by calculating only the neutron flux in the steady state calculation but in a very detailed energy group structure. The parameters needed for the depletion calculation such as the flux and cross sections are then spectrally averaged. Spectrally-averaged reaction rates are then calculated outside of the steady state calculations which can considerably reduce the calculational time. VESTA provides by default all the spectrally averaged cross sections of all nuclides that might be depleted in the simulation, even if they are not present in the steady state calculation. This feature has been used to track the average neutron energy.

Figure C7 shows the (n,α) cross section of ^{10}B in the energy range of 1 to 35 eV. As one can see, this cross section is easy to fit in this particular range of energy. The fit can be inverted to provide the energy as a function of the (n,α) ^{10}B cross section. Since the value of this cross section is known for each burnup zone, the inverted fit (given by Equation C3) can be used to calculate the average neutron energy in each burnup zone. The average neutron energy over a region is then given by Equation 4 which weights the importance of a burnup zone by its flux and its volume,

$$\overline{E} = 3.66028472E + 05 \cdot \sigma_{\alpha}^{-1.99684097E+00} \quad \text{Equation C3}$$

where:

$\overline{E}$: Average neutron energy in a burnup zone(eV)

σ_{α} : ^{10}B (n,α) cross section (barn)

$$\overline{E}_{region} = \frac{\sum_i^n \overline{E}_i \cdot \frac{\varphi_i * V_i}{\sum_i^n V_i}}{\overline{\varphi}_{region}} \quad \text{Equation C4}$$

where:

$\overline{E}_i$: Average neutron energy in burnup zone i (eV)

$\overline{\varphi}_{region}$: Average scalar flux over a whole region (n/cm^2/s)

φ_i : scalar flux in burnup zone i (n/cm^2/s)

V_i : Volume of the burnup zone i (cm^3).

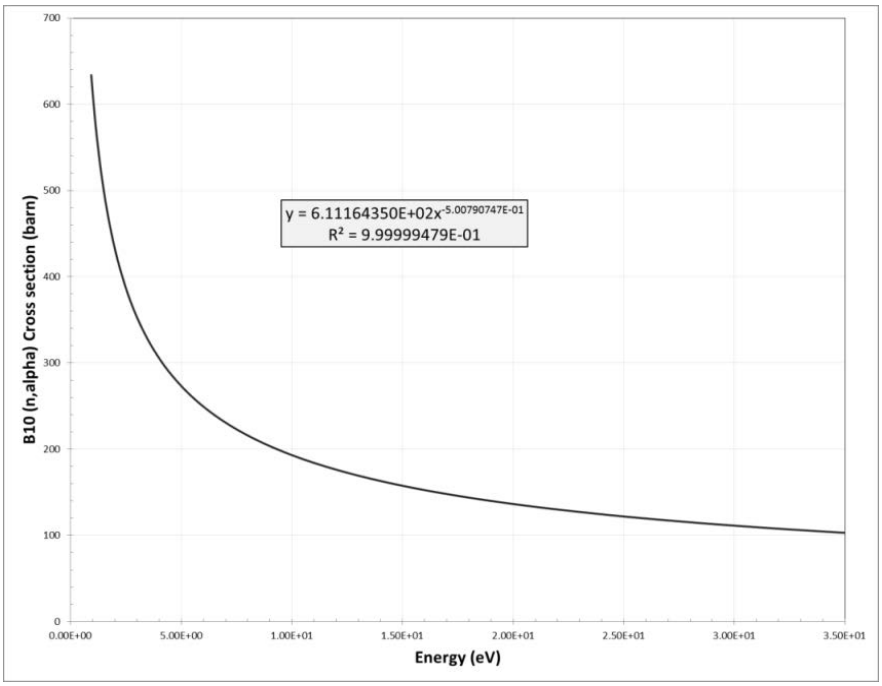

Figure C7 – ^{10}B (n,α) cross section versus energy in the range 1 to 35 eV.

Evolution of the average neutron energy in the IFE and OFE is snhown in Figures C8 and C9, respectively. As for the scalar flux plots, each figure is made of two plots: one for the HEU, one for the LEU. On each plot, the neutron energy obtained with the explicit and homogenized model is shown as well as the variation between them. To ease the comparison between model and the configuration, the four plots are at the same scale. From these plots the following observations can be made:

- In each region, the average neutron energy is considerably lower in the HEU configurations than in the corresponding LEU ones (by a factor of 4 to 6). Thus, fewer neutrons reach the thermal energy since there is more parasitic absorption in the LEU fuel.

- For each region – whatever the configuration – the average neutron energy decreases over time and the spectrum become more thermalized.

- For each region, the average neutron energy calculated in the explicit model is different than the one calculated in the homogenized model.

- For both the HEU and LEU configurations, for both the IFE and OFE, the average neutron energy is always higher in the explicit fuel than the in the homogenized fuel. Due to the complicated shape of most of the fuel isotope cross sections in this range of energy (presence of resonances), it is difficult to assess if the average neutron energy differences increase or decrease the reactivity of the fuel.

- For both HEU and LEU configurations, the average neutron energy in the IFE filler is always lower in the explicit models. The absorption cross section of the ^{10}B is higher in the explicit models. In the case of HEU, this increase more than compensates the fact that the flux is lower.

Consequently, the boron is burned faster in the HEU explicit model. In the LEU case, both flux and absorption cross sections are higher which explains why the ^{10}B is also burned faster in the LEU explicit model.

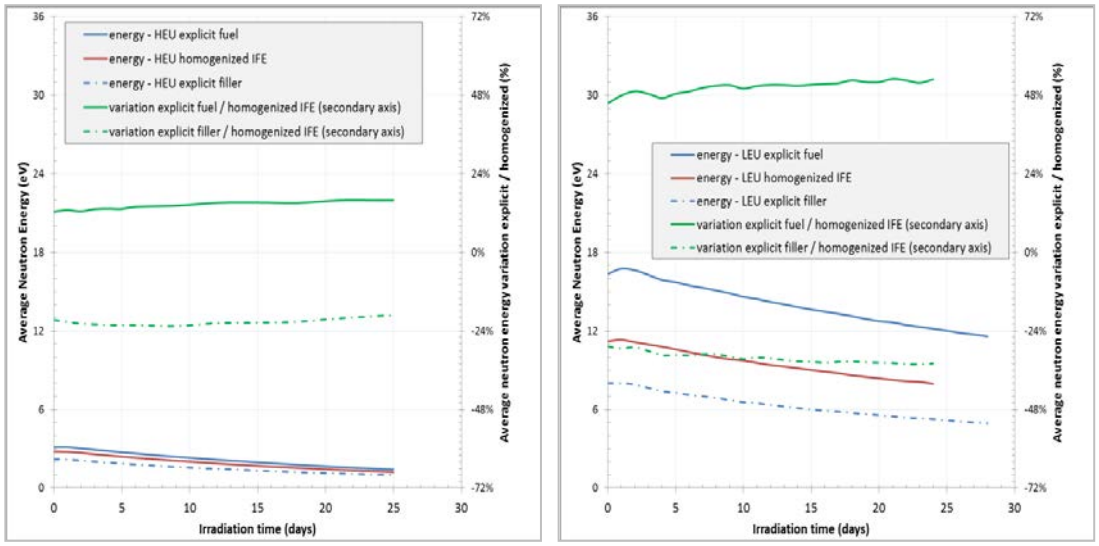

Figure C8 – Average neutron energy evolution in the IFE for homogenized and explicit models. Graph on the left is for the HEU configurations. Graph on the right is for the LEU configurations.

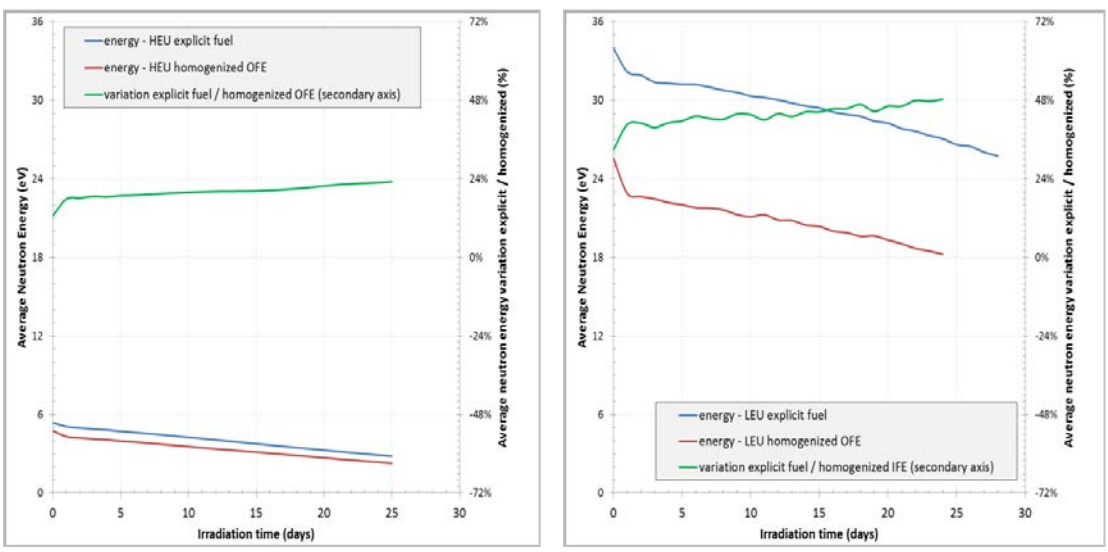

Figure C9 – Average neutron energy evolution in the OFE for homogenized and explicit models. Graph on the left is for the HEU configurations. Graph on the right is for the LEU configurations.

C-7 Isotope Anti-reactivity

At this point of the study, variations in mass, flux and neutron spectrum between the explicit and homogenized models have been highlighted. Between the HEU and LEU configurations, and except for the flux, variation occurs in the same direction and only the magnitude changes. Consequently, and despite the amount of information already extracted, it is still difficult to understand why the variations obtained between the explicit and homogenized models impacts only, and so strongly, the LEU configuration. To gain a better sense of what is happening; it is proposed in this section to study the worth on the fuel reactivity supplied by the most important isotopes. That can be done by calculating the individual anti-reactivity of a given isotope which can be derived from the definition of k_∞ (see Equation C5).

$$k_\infty = \frac{\sum_j^n \nu \Sigma_f}{\sum_i^m \Sigma_{a,i}} \qquad \text{Equation C5}$$

With:

ν : number of neutrons produced per fission.

$\Sigma_{f,j}$: macroscopic cross section of fission of isotope j (cm^{-1}).

$\Sigma_{a,i}$: macroscopic cross section of absorption of isotope i (cm^{-1}).

The k_∞ represents the balance between neutrons production over absorption. The anti-reactivity, ρ_i, supplied by a given isotope, I, is deduced from Equation C5 by the following relation (Equation C6):

$$\rho_i = \frac{\Sigma_{a,i}}{\sum_j^n \nu \Sigma_{f,j}} \qquad \text{Equation C6}$$

Equation 6 represents the contribution of the individual isotope, I, on the total balance of neutron production over absorption. In other words, the anti-reactivity is simply the neutron absorption rate.

Random selection of depleted MCNP materials has shown that, except for ^{135}Xe and ^{149}Sm, the discrepancy in fission product mass between the explicit and homogenized models is relatively small (<1%). Consequently, it is reasonable to assume that they play a minor role in the variation of reactivity difference between explicit and homogenized. However, this is not the case for all of the transuranic elements (neptunium, plutonium). Variation in mass for those isotopes is about~10%.

Taking into account this information, the variation of reactivity between the explicit and homogenized models can likely be understood by analyzing the variation of anti-reactivity supplied by a limited number of isotopes. The ones selected for this study are shown in Table C2. As done previously, the anti-reactivity is averaged over a whole region (Equation C7 below).

A difficulty with this method occurs for the ^{10}B in the IFE filler in the explicit models. Since in this part of the model there is no fissionable material, Equation 6 cannot be applied. The problem can be solved by calculating exactly the ^{10}B macroscopic cross section of absorption in the filler

and the macroscopic cross section of fission in the IFE fuel. The two parameters are normalized by a weight function which depends on the flux and the volume of the two regions (Equation C8 below). This operation is a kind of homogenization of the IFE fuel and filler but using the exact flux and cross section calculated in those regions.

$$\overline{\rho}_{i,region} = \frac{\sum_i^n \rho_i \cdot \frac{\varphi_i \cdot V_i}{\sum_i^n V_i}}{\overline{\varphi}_{region}} \qquad \text{Equation C7}$$

where:

$\overline{\rho}_{i,region}$: Average anti-reactivity supplied by isotope i over the region

$$\overline{\rho}_{10B,IFE} = \frac{\Sigma_{a,10B,filler}}{\sum_j^n \nu \Sigma_{f,j,IFE\ fuel}} \cdot \frac{V_{filler} * \varphi_{filler}}{V_{IFE\ fuel} * \varphi_{IFE\ fuel}} \qquad \text{Equation C8}$$

where:

$\overline{\rho}_{10B,IFE}$: Averaged anti-reactivity supplied by the ^{10}B in the IFE (explicit models only)

$\Sigma_{a,10B,IFE}$: Average ^{10}B (n,α) macroscopic cross section in the IFE (cm^{-1})

$\sum_j^n \nu\, \Sigma_{f,j,IFE}$: Average macroscopic cross section of fission in the IFE (cm^{-1})

$\Sigma_{a,10B,filler}$: Average ^{10}B (n,α) macroscopic cross section in the IFE filler(cm^{-1})

$\sum_j^n \nu\, \Sigma_{f,j,IFE\ fuel}$: Average macroscopic cross section of fission in the IFE fuel (cm^{-1})

V_{filler}: Volume of the IFE filler (cm^3)

$V_{IFE\ fuel}$: Volume of the IFE fuel (cm^3)

φ_{filler}: Average flux in the IFE filler ($n/cm^2/s$)

$\varphi_{IFE\ fuel}$: Average flux in the IFE fuel ($n/cm^2/s$)

Table C2 – Isotopes and reactions selected for the anti-reactivity calculations

isotope	reaction
^{10}B	(n,α)
^{135}Xe	(n,γ)
^{149}Sm	(n,γ)
^{234}U	(n,γ) & (n,f)
^{235}U	(n,γ) & (n,f)
^{236}U	(n,γ) & (n,f)
^{237}U	(n,γ) & (n,f)
^{238}U	(n,γ) & (n,f)
^{237}Np	(n,γ) & (n,f)
^{238}Np	(n,γ) & (n,f)
^{239}Np	(n,γ) & (n,f)
^{238}Pu	(n,γ) & (n,f)
^{239}Pu	(n,γ) & (n,f)
^{240}Pu	(n,γ) & (n,f)
^{241}Pu	(n,γ) & (n,f)
^{242}Pu	(n,γ) & (n,f)

For each configuration (HEU and LEU) and for each model (explicit and homogenized), the anti-reactivity supplied by each isotope shown in Table 3 has been calculated. To ease the understanding, only the variation of anti-reactivity (given by Equation C9) between the homogenized and explicit models of each isotope will be plotted.

$$\Delta\overline{\rho}_i = 10^5 \cdot (\overline{\rho}_{i,homogenized} - \overline{\rho}_{i,explicit}) \quad \text{Equation C9}$$

where:

$\Delta\overline{\rho}_i$: Variation of anti-reactivity of isotope i over a region between the homogenized and explicit models (pcm).

$\overline{\rho}_{i,homogenized}$: Anti-reactivity supplied by isotope i over a region obtained with a homogenized model.

$\overline{\rho}_{i,explicit}$: Anti-reactivity supplied by isotope i over a region obtained with an explicit model.

Figures C10 to C13 show the results obtained in the IFE for both HEU and LEU configurations. Figures C14 to 17 show the same thing but in the OFE. As before, all of these plots are at the same scale.

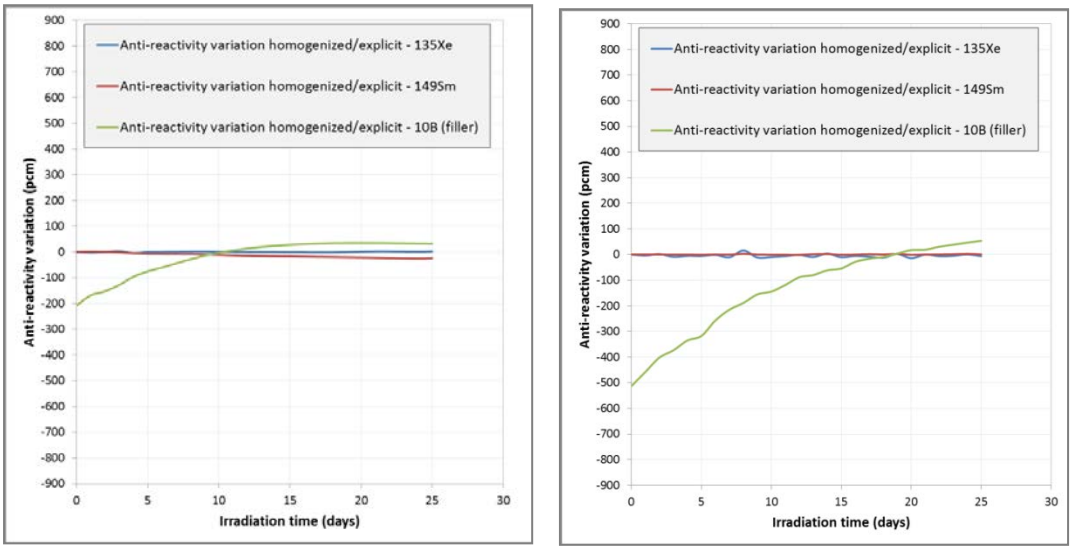

Figure C10 – Variation of anti-reactivity between homogenized and explicit models in the IFE obtained for ^{135}Xe, ^{149}Sm and ^{10}B. Graph on the left is for the HEU configurations. Graph on the right is for the LEU configurations.

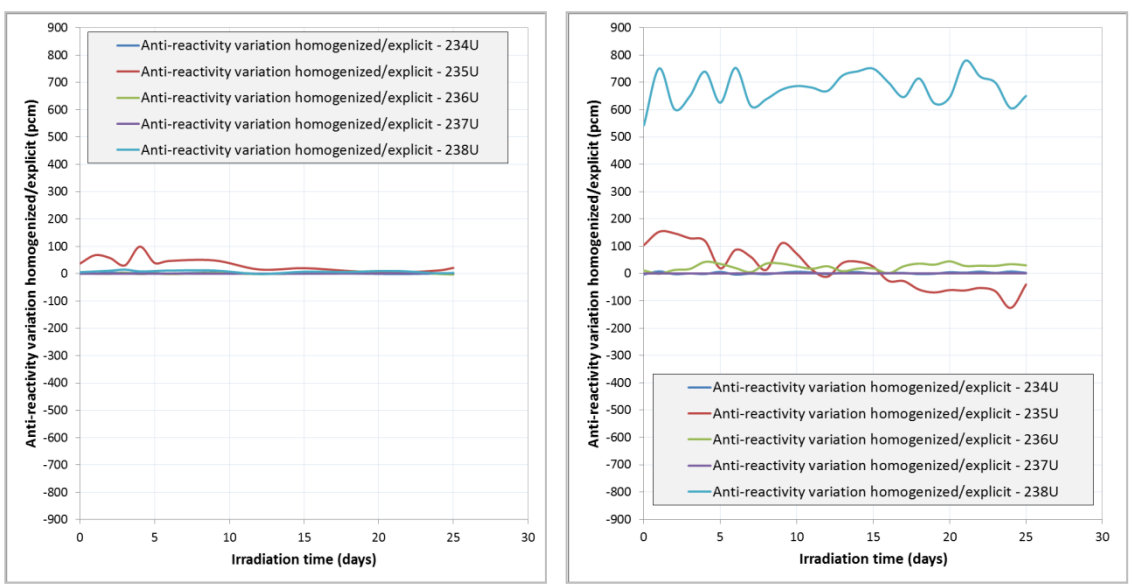

Figure C11 – Variation of anti-reactivity between homogenized and explicit modes in the IFE obtained for ^{234}U, ^{235}U, ^{236}U, ^{237}U and ^{238}U. Graph on the left is for the HEU configurations. Graph on the right is for the LEU configurations.

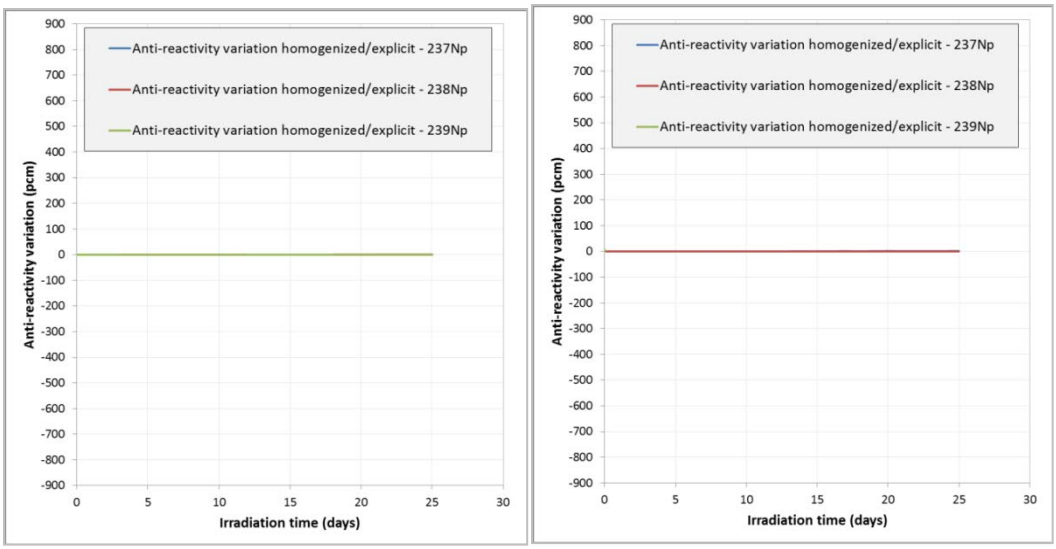

Figure C12 – Variation of anti-reactivity between homogenized and explicit models in the IFE obtained for ^{237}Np, ^{238}Np and ^{239}Np. Graph on the left is for the HEU configurations. Graph on the right is for the LEU configurations.

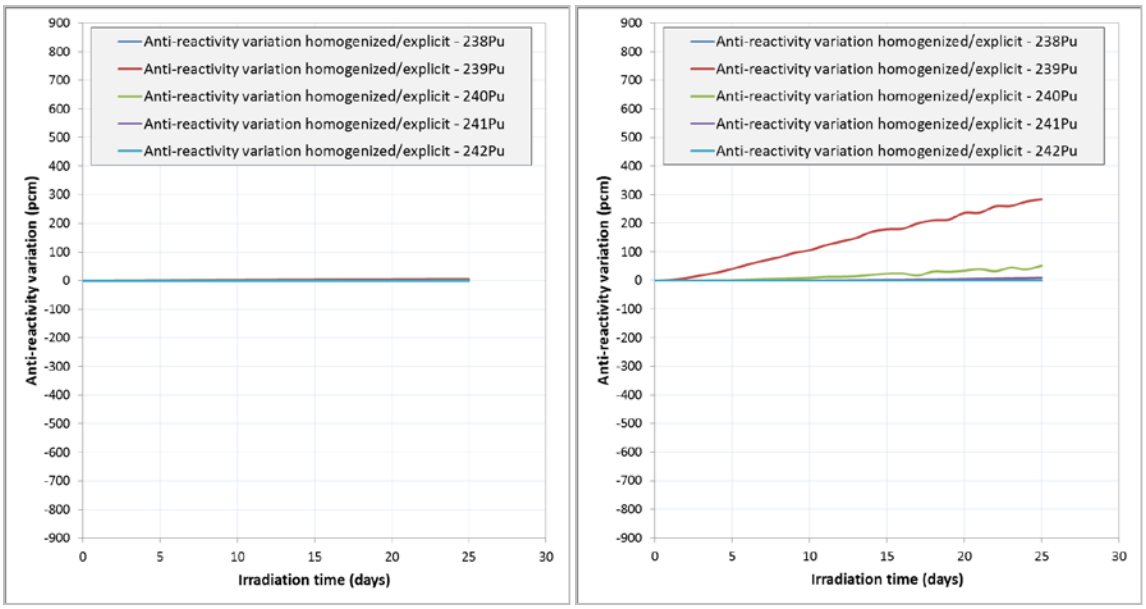

Figure C13 – Variation of anti-reactivity between homogenized and explicit models in the IFE obtained for ^{238}Pu, ^{239}Pu, ^{240}Pu, ^{241}Pu and ^{242}Pu. Graph on the left is for the HEU configurations. Graph on the right is for the LEU configurations.

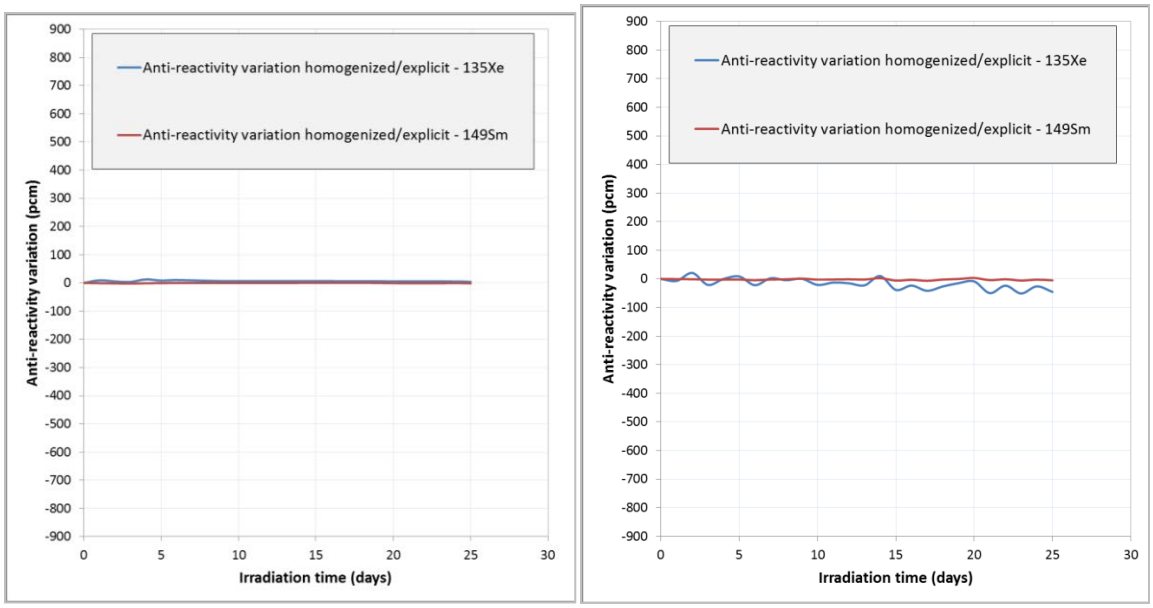

Figure C14 – Variation of anti-reactivity between homogenized and explicit model in the OFE obtained for ^{135}Xe and ^{149}Sm. Graph on the left is for the HEU configurations. Graph on the right is for the LEU configurations.

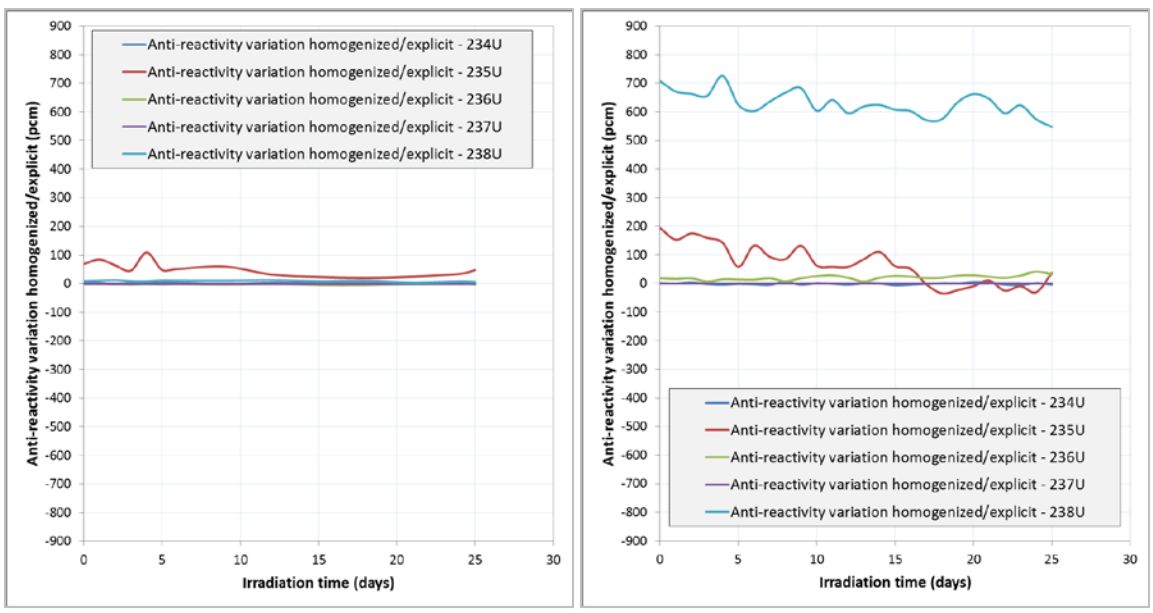

Figure C15 – Variation of anti-reactivity between homogenized and explicit models in the OFE obtained for ^{234}U, ^{235}U, ^{236}U, ^{237}U and ^{238}U. Graph on the left is for the HEU configurations. Graph on the right is for the LEU configurations.

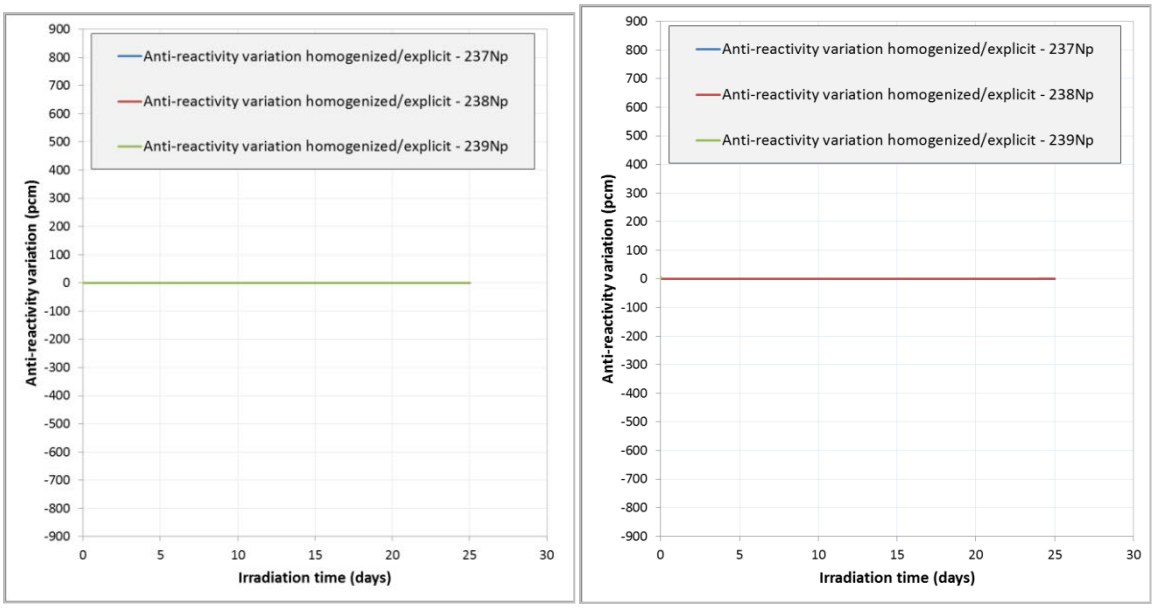

Figure C16 – Variation of anti-reactivity between homogenized and explicit models in the OFE obtained for ^{237}Np, ^{238}Np and ^{239}Np. Graph on the left is for the HEU configurations. Graph on the right is for the LEU configurations.

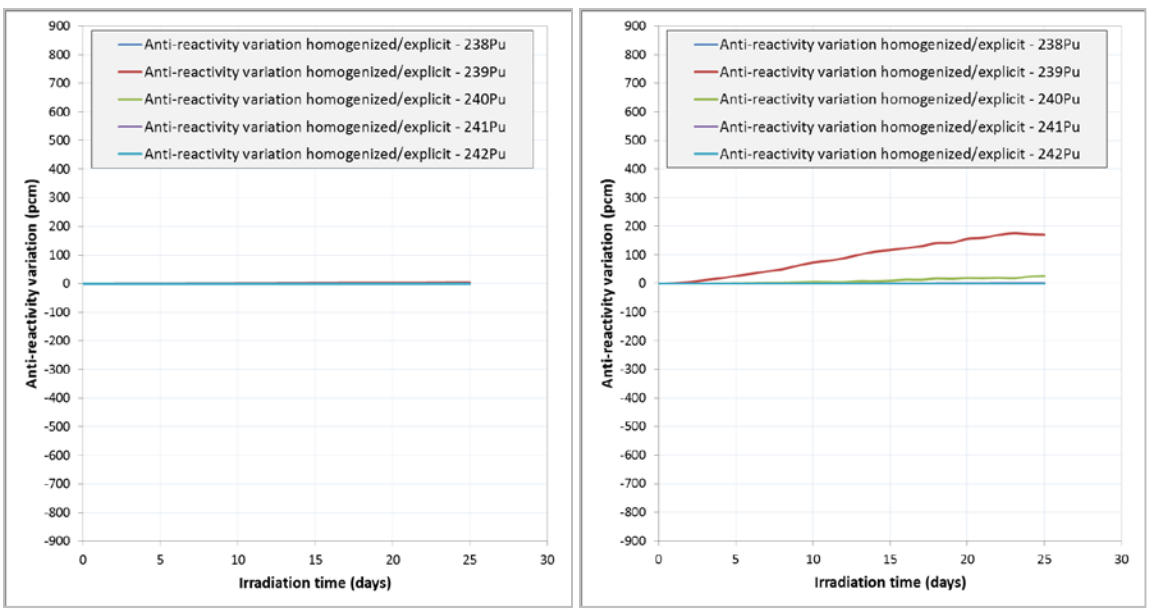

Figure C17 – Variation of anti-reactivity between homogenized and explicit models in the OFE obtained for ^{238}Pu, ^{239}Pu, ^{240}Pu, ^{241}Pu and ^{242}Pu. Graph on the left is for the HEU configurations. Graph on the right is for the LEU configurations.

Despite the variation in mass between the homogenized and explicit models observed for most of the isotopes studied, their impact on the reactivity is predicted to be very similar (variation of anti-reactivity homogenized/explicit is close to zero). However, significant variations exist for the following isotopes: ^{10}B, ^{238}U and ^{239}Pu.

For both HEU and LEU configurations, the anti-reactivity supplied by the ^{10}B is predicted to be greater in the explicit models than in the homogenized ones. However, the difference between the two models tends to disappear over the irradiation because the boron is rapidly depleted.

In the LEU configuration, the ^{238}U anti-reactivity is considerably higher in the homogenized model than in the explicit one (about~700pcm from BOL to the end of irradiation in both the IFE and OFE). The shift in flux and neutron spectrum impacts the absorption rate of this isotope in both HEU and LEU configurations but it is only visible in the LEU one because the mass of ^{238}U is considerably higher (more than 200 times) in the LEU fuel than in the HEU fuel. It is reasonable to assume that the variation of reactivity observed between the explicit and homogenized model is mainly due to this isotope.

Since the ^{238}U absorbs more neutrons in the homogenized model, it produces more transuranic elements, especially ^{239}Pu. Therefore, it is not surprising to observe that the anti-reactivity supplied by this isotope is higher in the homogenized model than in the explicit one.
The magnitude of the anti-reactivity obtained in this section may seem high but it is just because the anti-reactivity here is calculated in the fuel and not in the full reactor in which the neutron leakage would tend to reduce the magnitude as shown in the next section.

C-8 Pseudo k-effective

This last section attempts to link the variation of reactivity obtained between the LEU explicit and homogenized models obtained in Section III with the variation of anti-reactivity calculated in the previous section. The variation of reactivity was plotted in Figure C4 (Section C-3) which is, for convenience, is recalled below.

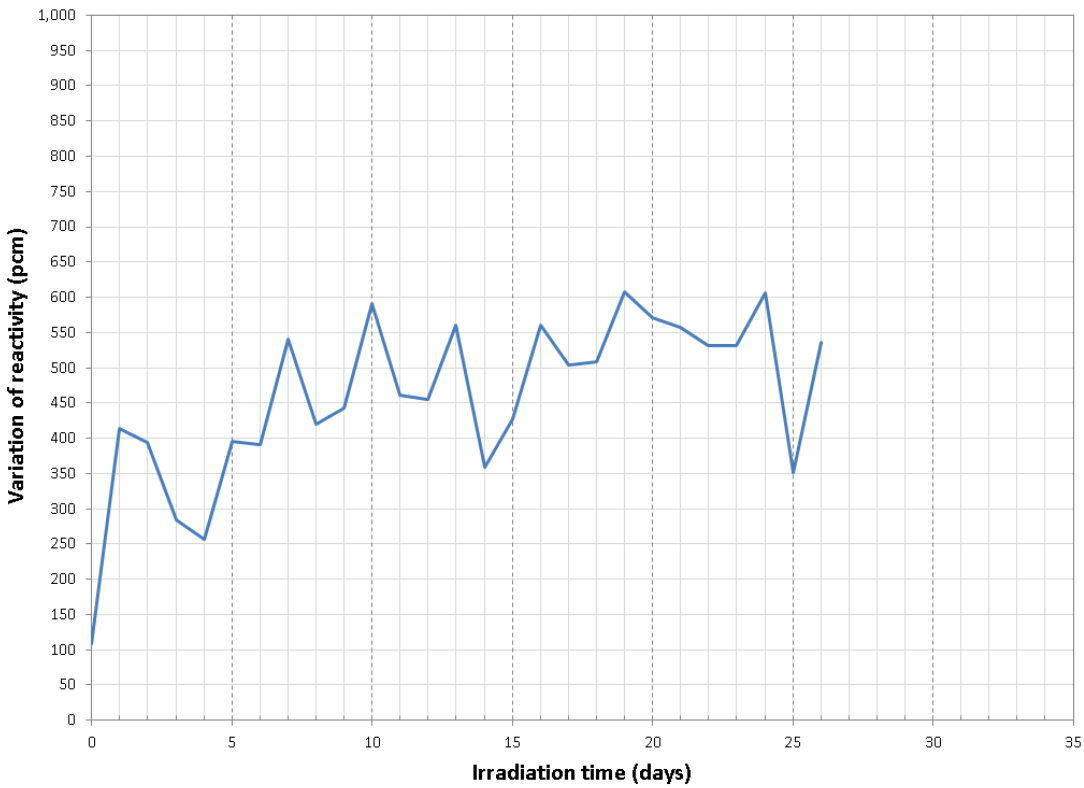

Figure C4 – Evolution of the reactivity difference, where a higher reactivity is modeled with the LEU explicit model vs. the homogeneous model over the course of depletion.

The definition of k-effective can be obtained from the definition of the k_∞ (see Equation C5) by adding a term for neutron leakage in the denominator of Equation C5 (Equation C11):

$$k_{effective} = \frac{\sum_j^n \nu \Sigma_f}{\sum_i^m \Sigma_{a,i} + L} = \frac{\sum_j^n \nu \Sigma_f}{\sum_i^p \Sigma_{a,i} + \sum_{fp} \Sigma_{a,fp} + L} \qquad \text{Equation C11}$$

where:

$\sum_j^n \nu \Sigma_f$: Sum of all macroscopic cross sections of fission (cm-1).
$\sum_i^m \Sigma_{a,i}$: Sum of all macroscopic cross sections of absorption (cm-1).
$\sum_i^p \Sigma_{a,i}$: Sum of the p macroscopic cross sections calculated in the previous section (cm-1).
$\sum_{fp} \Sigma_{a,fp}$: Sum of all the non-calculated absorption macroscopic cross sections (cm^{-1})

L : neutron leakage (lost in the structure or escaping the reactor).
The pseudo k-effective is introduced as (Equation C12):

$$k_{pseudo-eff} = \frac{\sum_j^n \nu\Sigma_f}{\sum_i^p \Sigma_{a\ ,i} + L} \qquad \text{Equation C12}$$

In the previous section, it has been supposed that the variation of anti-reactivity supplied by most of the fission products can be ignored since the variation in mass of these isotopes between the explicit and homogenized model is small. The correctness of this hypothesis is strengthened by the result obtained for the two main fission products studied previously (^{135}Xe and ^{149}Sm): The variation of anti-reactivity between the explicit and homogenized models for those highly absorbing isotopes is close to zero. Using this hypothesis and a few mathematical developments, it can be shown that the variation of reactivity between the explicit and homogenized models (given in Equation 1) can be written as a function of only the corresponding pseudo k-effective (Equation C13).

$$\rho_{ex-rz} = \frac{(k_{ex} - k_{rz})}{k_{ex} * k_{rz}} \approx \frac{(k_{pseudo-eff,ex} - k_{pseudo-eff,rz})}{k_{pseudo-eff,ex} * k_{pseudo-eff,rz}}$$

Equation C13

where:

$k_{pseudo-eff,ex}$: Pseudo k-effective calculated with the explicit model

$k_{pseudo-eff,rz}$: Pseudo k-effective calculated with the homogenized model

The only unknown term in the pseudo k-effective definition is the neutron leakage L. However, it can be roughly estimated by using the k-effective obtained with MCNP at t=0 and supposing that, at t=0, this k-effective is close to the pseudo k-effective. Indeed, at the beginning of irradiation there are no fission products and the term, $\sum_{fp} \Sigma_{a,fp}$ (see E

quation C11), represents only the molybdenum and aluminum (homogenized model only) absorption which is small compared to the other terms.

Using the results obtained previously, the leakage term of the explicit model, L_{ex}, at t=0 is equal to 0.38219 and the homogenized one, $L_{rz,}$ is equal to 0.37670. These two numbers are quite close considering the spectrum and flux variations between the two models. During irradiation, the macroscopic cross section of fission decreases slightly while the absorption one increases considerably. Consequently, the leakage term has to decrease in order to keep the reactor critical. This requirement is achieved by moving the control elements. If it is supposed that the neutron leakage is not fundamentally perturbed by the spectrum and flux variation during irradiation, keeping a constant value for the neutron leakage for the calculation of the pseudo k-effective would be like simulating a depletion of the reactor with no control rod motion. The variation of reactivity between the explicit and homogenized models, ρ_{ex-rz}, should not

depend too much on the control element motions. Consequently, the calculation at every time step of ρ_{ex-rz} by the pseudo k-effective should be close to that obtained in Section III.

The calculations have been performed with the results obtained in the previous section. Results are plotted in Figure C18. For comparison, the variation of the reactivity ratio, explicit / homogenized, obtained in Section III is also shown on this figure. Considering the number of hypotheses introduced, it seems reasonable to conclude that both curves match well.

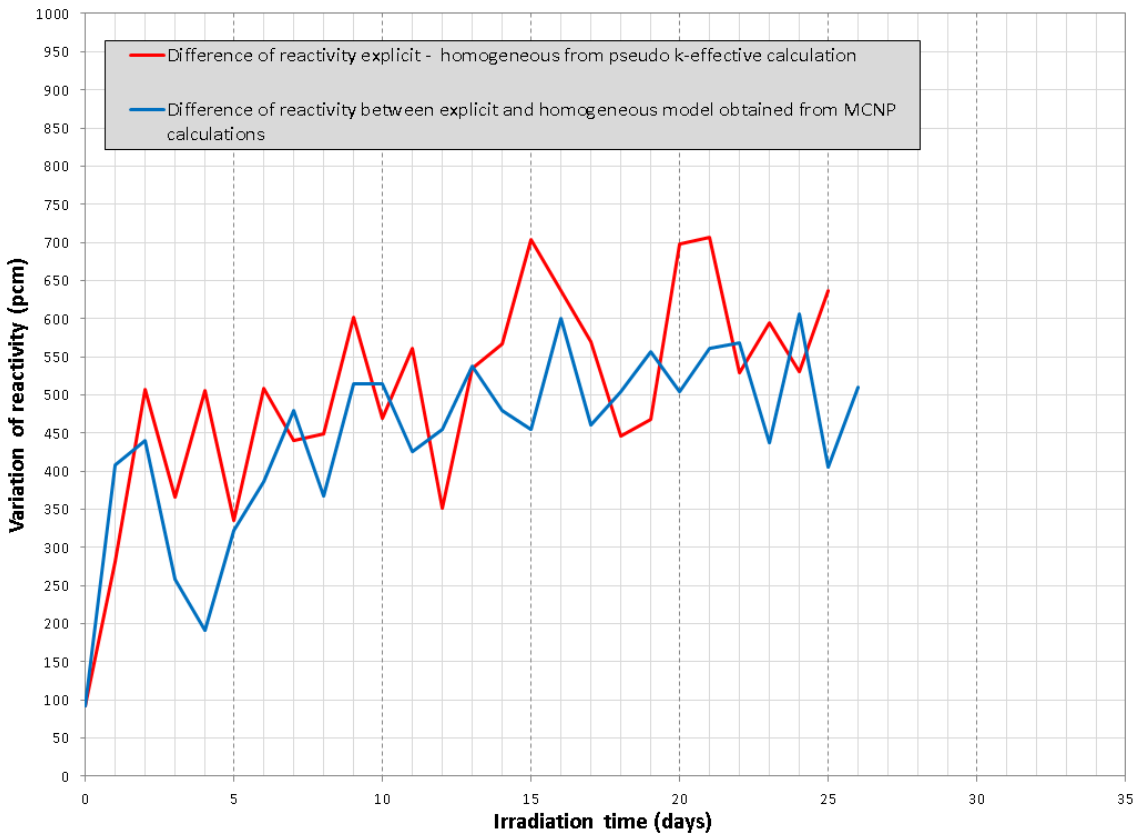

Figure C18 – Evolution of the variation of reactivity between the LEU explicit and homogenized models obtained with MCNP calculations and pseudo k-effective calculations.

C-9 Conclusions

The most significant difference between a homogeneous and heterogeneous system is the probability for a neutron to escape the absorption resonances at intermediate energies during the slowdown process. This probability is higher in the heterogeneous system. Variations in flux and spectrum may then occur and can ultimately impact the fission and absorption rates. It is also anticipated that the higher the fissile enrichment of uranium, the lower the effect will be since less parasitic captures can occur. In order to account for this difference without modeling the heterogenous configuration, it is a typical practice to model a heterogeneous system with a homogeneous description by attempting to match the reaction rates in addition to matching the masses of the two systems. Some methodologies are described in the literature that allow the gneration of correction factors for the cross sections. For the review of the ORNL neutronic calculations supporting the conversion of HFIR, ANL has designed explicit models of the reactor. One of the key parameters which define the matrix of performance of HFIR is the cycle length. At ANL, critical search algorithms have been developed and used with the code, VESTA, to predict the cycle length accurately.

The predicted cycle length obtained with the HEU explicit model is in good agreement with the one obtained with the HEU homogenized model. However, a serious difference has been obtained between the two LEU models. The cycle length is +15% longer for the explicit model. The variation of reactivity between the LEU explicit and homogenized models has been calculated and has shown an increasing trend with irradiation (starting at 100pcm at BOL to finishing around 600pcm). For each model, explicit and homogenized, and for both HEU and LEU configurations, the evolution of the isotopic masses, neutron scalar flux as calculated by VESTA, and average neutron energy have been investigated. It has been shown that for both HEU and LEU configurations, variations exist between the explicit and homogenized models. Anti-reactivity calculations have been carried out and have shown that the main isotope responsible for the LEU cycle length difference is ^{238}U. Despite the fact that variations in reaction rate occur between the HEU explicit and homogenized models, the effect on the core reactivity is only visible in the LEU configuration because the amount of ^{238}U is considerably greater (by more than 200 times). It is noteworthy that the variation in reactivity due to ^{238}U between the explicit and homogenized LEU models is, in some proportion, reduced by the ^{10}B present in the IFE filler since the “absorbing” worth is predicted to be more important in the explicit model.

Variations in neutron flux in the HFIR experimental facilities and the power distribution between the explicit and homogenized models is currently unknown but are subjects for potential future investigation. In light of the results compiled in the present study, use of the explicit description of the HFIR reactor is recommended for LEU fuel in order to more accurately predict the cycle length.

C - References

[Ref. C1] Y. Calzavara et al., "Evaluation of Measurements Performed on the French High Flux Reactor (RHF)", OECD Benchmark, NEA/NSC/DOC(2006)1, revision 3, 2012.

[Ref. C2] W. Haeck, "VESTA User's Manual version 2.0.0", DSU/SEC/T/2008-311 – Index A, 2009.

[Ref. C3] W. Haeck et al., "An Optimum Approach to Monte Carlo Burnup", Nuclear Science and Engineering, Vol. 156, pp. 180-196, 2007.

[Ref. C4] G. Ilas et al., "Low Enriched Uranium Fuel Design with Two-Dimensional Grading for the High Flux Isotope Reactor", ORNL/TM-2010/318, 2011.

[Ref. C5] N. Xoubi et al., "Modeling of the High Flux Isotope Reactor Cycle 400", ORNL/TM-2004/251, 2005.

[Ref. C6] C. Galvez Velit, "Partial Safety Analysis for a Reduced Uranium Enrichment Core for the High Flux Isotope Reactor", ORNL/TM-2007/226, 2009.

[Ref. C7] J. Duderstadt et al., Nuclear Reactor Analysis, Wiley-Interscience, 1976

[Ref. C8] P. Reuss, Neutron physics, EDP Sciences, 2008

[Ref. C9] R. Barjon, Physique des Réacteurs Nucléaires, Instituts des Sciences Nucléaires, 1993.

Appendix D – HEU and LEU Power Distributions of configuration l11 at BOC, day 1 and EOC

On this appendix are listed the power distributions tables obtained with the configuration l11. Relative power density tables for the HEU 85MW IFE and OFE at BOC, day 1, EOC and LEU 100MW IFE and OFE at BOC, day 1, EOC are presented in tables D.1 to D.12. Heat flux tables for the HEU 85MW IFE and OFE at BOC, day 1, EOC and LEU 100MW IFE and OFE at BOC, day 1, EOC are presented in tables D.13 to D.24. The maximum uncertainty is below 0.1 relative power density at 1-σ and the maximum heat flux uncertainty is below 2% at 1-σ.

Table D1 – HEU fuel at 85MW – configuration l11 – BOC – IFE – relative power density

Distance from…	*Core center (cm)*							
Core midplane (cm)	*7.14*	*7.5*	*8.5*	*9.5*	*10.5*	*11.5*	*12.2*	*12.6*
25.40								
24.90		0.88	0.94	1.03	1.07	1.03	0.97	0.94
24.40		0.80	0.80	0.83	0.84	0.83	0.81	0.82
23.00		0.75	0.71	0.70	0.70	0.70	0.72	0.76
20.00		0.76	0.71	0.68	0.69	0.69	0.72	0.76
17.00		0.88	0.82	0.80	0.80	0.81	0.83	0.88
14.00		1.01	0.95	0.92	0.92	0.93	0.96	1.02
11.00		1.13	1.06	1.03	1.03	1.04	1.08	1.14
8.00		1.24	1.16	1.12	1.13	1.14	1.18	1.24
5.00		1.30	1.22	1.18	1.19	1.21	1.25	1.32
3.00		1.34	1.26	1.22	1.23	1.25	1.28	1.36
1.00		1.36	1.27	1.23	1.24	1.26	1.30	1.38
-1.00		1.36	1.28	1.24	1.25	1.27	1.31	1.39
-3.00		1.35	1.27	1.22	1.23	1.26	1.30	1.38
-5.00		1.33	1.25	1.20	1.21	1.23	1.27	1.34
-8.00		1.28	1.19	1.15	1.16	1.19	1.22	1.29
-11.00		1.20	1.12	1.08	1.09	1.11	1.14	1.21
-14.00		1.09	1.03	0.99	0.99	1.01	1.03	1.09
-17.00		0.97	0.90	0.87	0.88	0.89	0.91	0.96
-20.00		0.84	0.79	0.75	0.75	0.76	0.78	0.83
-22.40		0.74	0.68	0.65	0.65	0.66	0.68	0.72
-24.40		0.70	0.66	0.64	0.64	0.64	0.65	0.70
-24.90		0.75	0.75	0.77	0.79	0.77	0.75	0.78
-25.40		0.82	0.88	0.96	1.00	0.96	0.89	0.87

Table D2 – HEU fuel at 85MW – configuration l11 – BOC – OFE – relative power density

Distance from…	Core center (cm)							
Core midplane (cm)	15.13	15.75	16.5	17.5	18.5	19.5	20.5	20.978
25.40								
24.90		1.19	1.23	1.18	1.03	0.79	0.53	0.37
24.40		1.02	0.98	0.90	0.78	0.62	0.45	0.32
23.00		0.92	0.85	0.76	0.64	0.53	0.40	0.30
20.00		0.93	0.86	0.76	0.65	0.53	0.41	0.31
17.00		1.07	1.01	0.91	0.78	0.65	0.51	0.40
14.00		1.24	1.17	1.07	0.95	0.82	0.68	0.58
11.00		1.40	1.33	1.22	1.09	0.97	0.86	0.78
8.00		1.53	1.46	1.35	1.22	1.10	0.99	0.90
5.00		1.63	1.55	1.44	1.31	1.20	1.09	1.01
3.00		1.68	1.60	1.50	1.38	1.27	1.19	1.13
1.00		1.71	1.63	1.52	1.41	1.32	1.27	1.23
-1.00		1.70	1.64	1.52	1.41	1.34	1.29	1.27
-3.00		1.69	1.62	1.51	1.39	1.31	1.24	1.20
-5.00		1.66	1.59	1.47	1.34	1.24	1.14	1.06
-8.00		1.58	1.51	1.40	1.27	1.15	1.03	0.93
-11.00		1.47	1.40	1.29	1.16	1.04	0.93	0.83
-14.00		1.33	1.27	1.15	1.03	0.91	0.80	0.70
-17.00		1.17	1.10	1.00	0.87	0.73	0.59	0.48
-20.00		1.00	0.94	0.83	0.71	0.56	0.40	0.27
-22.40		0.87	0.80	0.70	0.58	0.45	0.32	0.21
-24.40		0.84	0.77	0.67	0.56	0.43	0.30	0.20
-24.90		0.94	0.89	0.81	0.68	0.52	0.34	0.22
-25.40		1.09	1.10	1.06	0.89	0.65	0.41	0.25

Table D3 – HEU fuel at 85MW – configuration l11 – day 1 – IFE – relative power density

Distance from…	Core center (cm)							
Core midplane (cm)	7.14	7.5	8.5	9.5	10.5	11.5	12.2	12.6
25.40								
24.90		0.87	0.93	1.03	1.07	1.03	0.96	0.93
24.40		0.80	0.79	0.82	0.84	0.82	0.80	0.82
23.00		0.73	0.70	0.68	0.69	0.69	0.71	0.76
20.00		0.75	0.70	0.67	0.67	0.68	0.71	0.76
17.00		0.87	0.81	0.78	0.78	0.79	0.82	0.87
14.00		1.01	0.94	0.91	0.90	0.92	0.95	1.01
11.00		1.13	1.06	1.02	1.02	1.03	1.07	1.13
8.00		1.22	1.16	1.11	1.11	1.13	1.16	1.24
5.00		1.30	1.23	1.18	1.18	1.20	1.25	1.33
3.00		1.33	1.27	1.22	1.22	1.24	1.29	1.37
1.00		1.36	1.28	1.24	1.24	1.26	1.31	1.39
-1.00		1.36	1.29	1.25	1.25	1.27	1.31	1.39
-3.00		1.35	1.28	1.23	1.24	1.26	1.30	1.39
-5.00		1.33	1.26	1.22	1.21	1.23	1.27	1.35
-8.00		1.28	1.22	1.17	1.17	1.19	1.23	1.30
-11.00		1.20	1.13	1.09	1.09	1.11	1.14	1.21
-14.00		1.10	1.04	1.00	1.00	1.01	1.04	1.11
-17.00		0.99	0.93	0.89	0.88	0.89	0.92	0.97
-20.00		0.85	0.80	0.76	0.76	0.77	0.79	0.84
-22.40		0.75	0.69	0.66	0.65	0.66	0.69	0.73
-24.40		0.71	0.67	0.65	0.64	0.65	0.66	0.71
-24.90		0.76	0.76	0.78	0.80	0.78	0.76	0.79
-25.40		0.84	0.89	0.97	1.01	0.98	0.90	0.89

Table D4 – HEU fuel at 85MW – configuration l11 – day 1 – OFE – relative power density

Distance from…	Core center (cm)							
Core midplane (cm)	15.13	15.75	16.5	17.5	18.5	19.5	20.5	20.978
25.40								
24.90		1.09	1.15	1.11	0.97	0.75	0.52	0.36
24.40		0.95	0.92	0.85	0.73	0.60	0.44	0.33
23.00		0.85	0.79	0.71	0.61	0.51	0.39	0.31
20.00		0.86	0.80	0.72	0.63	0.54	0.45	0.38
17.00		0.99	0.94	0.86	0.76	0.68	0.59	0.53
14.00		1.14	1.09	1.00	0.90	0.82	0.72	0.65
11.00		1.29	1.24	1.15	1.04	0.94	0.85	0.79
8.00		1.42	1.37	1.27	1.16	1.09	1.02	0.98
5.00		1.52	1.47	1.37	1.28	1.24	1.21	1.22
3.00		1.57	1.52	1.43	1.34	1.31	1.32	1.35
1.00		1.60	1.55	1.45	1.37	1.34	1.36	1.39
-1.00		1.60	1.55	1.46	1.38	1.35	1.37	1.41
-3.00		1.59	1.54	1.45	1.37	1.34	1.35	1.39
-5.00		1.56	1.51	1.41	1.34	1.31	1.31	1.35
-8.00		1.50	1.45	1.35	1.26	1.21	1.20	1.21
-11.00		1.39	1.34	1.24	1.14	1.05	0.97	0.91
-14.00		1.26	1.21	1.11	0.99	0.89	0.79	0.71
-17.00		1.11	1.06	0.96	0.86	0.76	0.66	0.59
-20.00		0.95	0.90	0.82	0.72	0.63	0.54	0.47
-22.40		0.82	0.77	0.68	0.59	0.50	0.40	0.32
-24.40		0.80	0.73	0.65	0.54	0.44	0.31	0.22
-24.90		0.90	0.85	0.77	0.66	0.51	0.34	0.22
-25.40		1.03	1.06	1.02	0.86	0.64	0.40	0.25

Table D5 – HEU fuel at 85MW – configuration l11 – day 1 – IFE – relative power density

Distance from…	Core center (cm)							
Core midplane (cm)	7.14	7.5	8.5	9.5	10.5	11.5	12.2	12.6
25.40								
24.90		0.64	0.81	0.99	1.05	1.03	0.94	0.87
24.40		0.63	0.78	0.91	0.94	0.92	0.86	0.82
23.00		0.63	0.75	0.82	0.82	0.81	0.79	0.79
20.00		0.64	0.76	0.81	0.80	0.79	0.78	0.78
17.00		0.66	0.82	0.90	0.91	0.89	0.87	0.85
14.00		0.69	0.88	1.01	1.02	1.00	0.97	0.93
11.00		0.70	0.93	1.09	1.13	1.10	1.05	0.99
8.00		0.69	0.95	1.16	1.20	1.17	1.11	1.04
5.00		0.68	0.96	1.20	1.25	1.22	1.14	1.06
3.00		0.68	0.97	1.22	1.28	1.25	1.17	1.07
1.00		0.68	0.97	1.23	1.30	1.26	1.18	1.08
-1.00		0.68	0.98	1.23	1.30	1.27	1.18	1.08
-3.00		0.68	0.98	1.23	1.30	1.26	1.18	1.08
-5.00		0.68	0.97	1.22	1.29	1.25	1.17	1.08
-8.00		0.69	0.97	1.20	1.26	1.23	1.15	1.07
-11.00		0.70	0.96	1.17	1.21	1.18	1.11	1.04
-14.00		0.70	0.94	1.10	1.13	1.10	1.06	1.00
-17.00		0.70	0.89	1.01	1.03	1.01	0.97	0.94
-20.00		0.68	0.83	0.92	0.91	0.89	0.88	0.86
-22.40		0.65	0.77	0.82	0.81	0.80	0.79	0.79
-24.40		0.64	0.76	0.82	0.81	0.80	0.79	0.78
-24.90		0.64	0.79	0.91	0.94	0.91	0.86	0.83
-25.40		0.65	0.82	1.00	1.06	1.04	0.95	0.88

Table D6 – HEU fuel at 85MW – configuration l11 – day 1 – OFE – relative power density

Distance from…	Core center (cm)							
Core midplane (cm)	15.13	15.75	16.5	17.5	18.5	19.5	20.5	20.978
25.40								
24.90		0.79	1.20	1.17	1.10	0.94	0.73	0.68
24.40		0.75	1.01	0.95	0.88	0.80	0.67	0.66
23.00		0.70	0.89	0.80	0.74	0.71	0.64	0.68
20.00		0.69	0.88	0.79	0.74	0.73	0.70	0.77
17.00		0.74	1.00	0.91	0.86	0.85	0.79	0.89
14.00		0.79	1.13	1.03	0.98	0.97	0.86	0.98
11.00		0.81	1.25	1.14	1.09	1.06	0.90	1.04
8.00		0.83	1.34	1.22	1.16	1.13	0.91	1.07
5.00		0.83	1.41	1.28	1.22	1.18	0.92	1.08
3.00		0.84	1.44	1.31	1.26	1.21	0.92	1.09
1.00		0.84	1.46	1.33	1.27	1.23	0.92	1.10
-1.00		0.83	1.47	1.34	1.28	1.22	0.92	1.10
-3.00		0.84	1.46	1.33	1.27	1.22	0.92	1.10
-5.00		0.84	1.45	1.32	1.26	1.21	0.92	1.09
-8.00		0.84	1.40	1.28	1.22	1.18	0.92	1.08
-11.00		0.84	1.34	1.22	1.17	1.13	0.92	1.07
-14.00		0.83	1.25	1.14	1.09	1.06	0.92	1.06
-17.00		0.80	1.13	1.03	0.99	0.97	0.89	1.00
-20.00		0.75	1.00	0.91	0.87	0.86	0.81	0.91
-22.40		0.71	0.89	0.80	0.75	0.74	0.72	0.79
-24.40		0.71	0.87	0.78	0.72	0.69	0.65	0.69
-24.90		0.76	1.01	0.94	0.86	0.77	0.65	0.64
-25.40		0.80	1.19	1.16	1.07	0.91	0.70	0.64

Table D7 – LEU fuel at 100MW – configuration l11 – BOC – IFE – relative power density

Distance from…	Core center (cm)							
Core midplane (cm)	7.14	7.5	8.5	9.5	10.5	11.5	12.2	12.6
25.40								
24.90		0.88	1.14	1.35	1.36	1.31	1.21	1.03
24.40		0.76	0.88	0.92	0.88	0.85	0.88	0.85
23.00		0.69	0.74	0.72	0.66	0.67	0.73	0.74
20.00		0.70	0.74	0.72	0.67	0.68	0.73	0.72
17.00		0.81	0.86	0.84	0.80	0.81	0.86	0.82
14.00		0.93	1.00	0.98	0.93	0.94	0.99	0.95
11.00		1.05	1.12	1.10	1.04	1.05	1.11	1.06
8.00		1.14	1.22	1.20	1.14	1.15	1.22	1.17
5.00		1.21	1.29	1.27	1.20	1.22	1.30	1.23
3.00		1.25	1.34	1.31	1.25	1.27	1.33	1.27
1.00		1.27	1.34	1.32	1.26	1.28	1.36	1.29
-1.00		1.27	1.35	1.33	1.26	1.28	1.36	1.30
-3.00		1.26	1.34	1.32	1.25	1.27	1.34	1.28
-5.00		1.22	1.31	1.29	1.22	1.24	1.31	1.26
-8.00		1.18	1.26	1.24	1.17	1.19	1.26	1.20
-11.00		1.11	1.18	1.15	1.09	1.10	1.17	1.12
-14.00		1.00	1.07	1.04	0.99	1.00	1.05	1.01
-17.00		0.88	0.93	0.91	0.86	0.87	0.92	0.89
-20.00		0.76	0.80	0.77	0.73	0.74	0.78	0.75
-22.40		0.66	0.70	0.67	0.63	0.63	0.68	0.67
-24.40		0.65	0.57	0.57	0.49	0.49	0.72	0.45
-24.90		0.59	0.44	0.35	0.31	0.30	0.32	0.37
-25.40		0.68	0.54	0.45	0.41	0.39	0.40	0.43

Table D8 – LEU fuel at 100MW – configuration l11 – BOC – OFE – relative power density

Distance from…	Core center (cm)							
Core midplane (cm)	15.15	15.75	16.5	17.5	18.5	19.5	20.5	21
25.40								
24.90		1.27	1.41	1.34	1.17	1.04	0.78	0.46
24.40		1.00	0.97	0.86	0.72	0.65	0.54	0.37
23.00		0.86	0.80	0.68	0.56	0.52	0.45	0.32
20.00		0.84	0.82	0.71	0.59	0.55	0.48	0.34
17.00		0.97	0.97	0.86	0.72	0.69	0.63	0.48
14.00		1.12	1.14	1.02	0.87	0.85	0.87	0.75
11.00		1.26	1.28	1.15	1.00	1.00	1.05	0.95
8.00		1.38	1.41	1.27	1.10	1.12	1.19	1.09
5.00		1.48	1.51	1.36	1.18	1.22	1.35	1.26
3.00		1.53	1.55	1.41	1.24	1.30	1.49	1.46
1.00		1.55	1.58	1.43	1.26	1.34	1.57	1.57
-1.00		1.55	1.58	1.43	1.27	1.35	1.59	1.61
-3.00		1.54	1.57	1.42	1.26	1.32	1.56	1.57
-5.00		1.51	1.54	1.39	1.21	1.27	1.45	1.42
-8.00		1.43	1.46	1.31	1.15	1.18	1.28	1.19
-11.00		1.33	1.35	1.21	1.04	1.06	1.13	1.02
-14.00		1.20	1.21	1.08	0.93	0.93	0.98	0.88
-17.00		1.04	1.05	0.94	0.80	0.78	0.79	0.68
-20.00		0.89	0.89	0.78	0.65	0.60	0.52	0.35
-22.40		0.79	0.77	0.67	0.55	0.49	0.39	0.24
-24.40		0.82	0.69	0.64	0.40	0.40	0.34	0.24
-24.90		0.40	0.34	0.29	0.25	0.21	0.17	0.14
-25.40		0.46	0.41	0.37	0.32	0.27	0.21	0.16

Table D9 – LEU fuel at 100MW – configuration l11 – day 1 – IFE – relative power density

Distance from…	Core center (cm)							
Core midplane (cm)	7.14	7.5	8.5	9.5	10.5	11.5	12.2	12.6
25.40								
24.90		0.89	1.13	1.38	1.38	1.31	1.22	1.06
24.40		0.77	0.88	0.93	0.87	0.85	0.89	0.87
23.00		0.69	0.74	0.71	0.66	0.67	0.73	0.75
20.00		0.70	0.74	0.71	0.67	0.68	0.73	0.72
17.00		0.81	0.86	0.83	0.79	0.80	0.85	0.82
14.00		0.94	1.00	0.97	0.92	0.93	0.99	0.95
11.00		1.04	1.12	1.10	1.03	1.04	1.11	1.07
8.00		1.14	1.22	1.19	1.12	1.13	1.21	1.17
5.00		1.20	1.29	1.26	1.19	1.21	1.29	1.24
3.00		1.24	1.33	1.30	1.23	1.25	1.33	1.28
1.00		1.26	1.34	1.32	1.25	1.27	1.35	1.30
-1.00		1.26	1.35	1.32	1.25	1.28	1.36	1.32
-3.00		1.25	1.34	1.30	1.24	1.26	1.34	1.29
-5.00		1.23	1.32	1.28	1.21	1.23	1.31	1.27
-8.00		1.18	1.26	1.23	1.17	1.19	1.26	1.22
-11.00		1.10	1.18	1.15	1.09	1.10	1.17	1.13
-14.00		1.01	1.07	1.04	0.98	1.00	1.06	1.03
-17.00		0.89	0.95	0.92	0.86	0.88	0.93	0.90
-20.00		0.76	0.81	0.78	0.73	0.74	0.80	0.77
-22.40		0.67	0.70	0.67	0.64	0.65	0.70	0.70
-24.40		0.68	0.58	0.58	0.51	0.51	0.74	0.47
-24.90		0.62	0.46	0.36	0.33	0.32	0.34	0.39
-25.40		0.70	0.57	0.47	0.43	0.41	0.42	0.46

Table D10 – LEU fuel at 100MW – configuration l11 – day 1 – OFE – relative power density

Distance from…	Core center (cm)							
Core midplane (cm)	15.15	15.75	16.5	17.5	18.5	19.5	20.5	21
25.40								
24.90		1.18	1.30	1.27	1.11	1.01	0.80	0.52
24.40		0.94	0.89	0.79	0.68	0.64	0.57	0.44
23.00		0.80	0.74	0.63	0.53	0.52	0.51	0.43
20.00		0.79	0.76	0.67	0.57	0.57	0.59	0.53
17.00		0.90	0.90	0.81	0.70	0.70	0.73	0.66
14.00		1.03	1.05	0.94	0.82	0.83	0.89	0.82
11.00		1.16	1.18	1.07	0.94	0.97	1.08	1.04
8.00		1.28	1.30	1.18	1.04	1.11	1.31	1.35
5.00		1.37	1.39	1.26	1.12	1.21	1.48	1.56
3.00		1.41	1.44	1.31	1.17	1.26	1.56	1.66
1.00		1.43	1.46	1.33	1.19	1.29	1.59	1.70
-1.00		1.43	1.47	1.33	1.19	1.29	1.60	1.70
-3.00		1.42	1.45	1.32	1.18	1.28	1.58	1.69
-5.00		1.39	1.42	1.30	1.16	1.25	1.55	1.65
-8.00		1.34	1.36	1.24	1.10	1.19	1.47	1.55
-11.00		1.24	1.26	1.15	1.01	1.08	1.29	1.34
-14.00		1.12	1.14	1.02	0.90	0.92	1.02	0.96
-17.00		0.98	0.99	0.89	0.77	0.78	0.82	0.74
-20.00		0.84	0.83	0.74	0.64	0.64	0.67	0.61
-22.40		0.76	0.73	0.65	0.55	0.55	0.56	0.49
-24.40		0.80	0.67	0.62	0.40	0.43	0.43	0.39
-24.90		0.39	0.33	0.29	0.25	0.22	0.19	0.17
-25.40		0.45	0.40	0.36	0.32	0.27	0.23	0.18

Table D11 – LEU fuel at 100MW – configuration l11 – EOC – IFE – relative power density

Distance from…	Core center (cm)							
Core midplane (cm)	7.14	7.5	8.5	9.5	10.5	11.5	12.2	12.6
25.40								
24.90		0.64	1.05	1.40	1.44	1.37	1.25	1.01
24.40		0.63	0.94	1.07	1.00	0.97	0.98	0.88
23.00		0.61	0.84	0.85	0.75	0.74	0.80	0.78
20.00		0.61	0.83	0.83	0.73	0.72	0.78	0.74
17.00		0.66	0.92	0.95	0.84	0.83	0.87	0.80
14.00		0.69	1.03	1.08	0.95	0.94	0.98	0.89
11.00		0.72	1.11	1.19	1.05	1.03	1.07	0.97
8.00		0.74	1.16	1.28	1.13	1.10	1.14	1.02
5.00		0.74	1.20	1.34	1.18	1.16	1.20	1.07
3.00		0.75	1.22	1.37	1.21	1.18	1.23	1.08
1.00		0.75	1.23	1.38	1.23	1.20	1.23	1.09
-1.00		0.75	1.22	1.39	1.22	1.20	1.24	1.09
-3.00		0.75	1.22	1.37	1.22	1.20	1.23	1.09
-5.00		0.75	1.21	1.35	1.20	1.19	1.22	1.08
-8.00		0.75	1.19	1.32	1.17	1.15	1.19	1.05
-11.00		0.73	1.15	1.25	1.11	1.08	1.13	1.00
-14.00		0.72	1.08	1.16	1.02	1.01	1.05	0.95
-17.00		0.69	1.00	1.05	0.93	0.91	0.96	0.87
-20.00		0.65	0.90	0.91	0.80	0.80	0.84	0.78
-22.40		0.62	0.83	0.83	0.73	0.73	0.79	0.75
-24.40		0.68	0.73	0.77	0.66	0.64	0.87	0.55
-24.90		0.52	0.48	0.43	0.39	0.38	0.38	0.41
-25.40		0.53	0.50	0.47	0.44	0.43	0.42	0.44

Table D12 – LEU fuel at 100MW – configuration l11 – EOC – OFE – relative power density

Distance from…	Core center (cm)							
Core midplane (cm)	15.15	15.75	16.5	17.5	18.5	19.5	20.5	21
25.40								
24.90		1.12	1.36	1.38	1.28	1.28	1.20	0.91
24.40		0.93	0.97	0.89	0.78	0.81	0.90	0.83
23.00		0.80	0.79	0.68	0.60	0.65	0.80	0.83
20.00		0.77	0.78	0.70	0.62	0.68	0.87	0.91
17.00		0.85	0.90	0.82	0.73	0.80	1.02	1.04
14.00		0.94	1.01	0.92	0.82	0.91	1.15	1.12
11.00		1.02	1.10	1.00	0.90	1.00	1.26	1.18
8.00		1.08	1.17	1.07	0.96	1.08	1.34	1.21
5.00		1.12	1.23	1.12	1.01	1.13	1.40	1.23
3.00		1.15	1.25	1.15	1.03	1.15	1.43	1.25
1.00		1.16	1.26	1.16	1.04	1.16	1.44	1.25
-1.00		1.16	1.27	1.16	1.05	1.17	1.44	1.25
-3.00		1.16	1.26	1.15	1.04	1.16	1.44	1.25
-5.00		1.14	1.25	1.14	1.02	1.15	1.43	1.25
-8.00		1.12	1.21	1.11	1.00	1.11	1.39	1.22
-11.00		1.07	1.15	1.06	0.95	1.06	1.32	1.19
-14.00		1.00	1.08	0.98	0.88	0.99	1.23	1.16
-17.00		0.92	0.97	0.89	0.80	0.89	1.12	1.10
-20.00		0.82	0.86	0.78	0.70	0.77	0.99	1.03
-22.40		0.77	0.79	0.71	0.63	0.69	0.88	0.93
-24.40		0.83	0.75	0.74	0.50	0.59	0.75	0.83
-24.90		0.37	0.33	0.31	0.30	0.30	0.32	0.38
-25.40		0.40	0.39	0.37	0.35	0.35	0.36	0.40

Table D13 – HEU fuel at 85MW – configuration l11 – BOC – IFE – heat flux (W/cm^2)

Distance from…	Core center (cm)							
Core midplane (cm)	7.14	7.5	8.5	9.5	10.5	11.5	12.2	12.6
25.40								
24.90		195	209	229	238	229	216	208
24.40		178	177	185	187	184	179	182
23.00		166	157	155	155	154	159	169
20.00		169	157	152	152	154	159	170
17.00		195	182	177	177	179	184	196
14.00		225	210	204	205	207	213	227
11.00		251	235	228	230	232	239	253
8.00		274	256	249	250	253	261	275
5.00		289	271	262	265	269	277	293
3.00		298	279	271	273	277	284	302
1.00		301	282	273	276	280	288	306
-1.00		303	284	275	278	282	291	308
-3.00		300	282	272	274	279	287	306
-5.00		295	277	266	269	273	281	298
-8.00		284	265	256	258	263	271	287
-11.00		266	249	240	242	246	253	268
-14.00		242	228	220	220	223	229	242
-17.00		215	200	194	195	198	202	213
-20.00		187	174	167	167	169	174	184
-22.40		163	152	145	144	146	150	161
-24.40		156	147	143	142	142	145	156
-24.90		166	166	172	174	170	166	172
-25.40		183	195	214	222	213	198	194

Table D14 – HEU fuel at 85MW – configuration l11 – BOC – OFE – heat flux (W/cm^2)

Distance from…	Core center (cm)							
Core midplane (cm)	15.13	15.75	16.5	17.5	18.5	19.5	20.5	20.978
25.40								
24.90		221	228	219	191	146	99	68
24.40		190	183	168	144	115	83	60
23.00		171	157	141	119	98	73	55
20.00		173	159	142	121	99	76	58
17.00		200	187	168	146	121	94	74
14.00		230	218	198	176	152	127	108
11.00		260	246	226	203	181	160	144
8.00		284	271	250	226	204	184	168
5.00		302	289	268	244	223	203	188
3.00		312	298	278	255	237	221	209
1.00		317	302	283	261	246	235	228
-1.00		317	304	283	263	248	240	235
-3.00		313	301	281	259	243	231	224
-5.00		309	295	273	250	230	212	197
-8.00		294	281	260	235	213	191	173
-11.00		273	260	239	215	194	172	154
-14.00		247	235	214	191	170	148	131
-17.00		217	205	185	161	136	110	89
-20.00		187	174	155	131	104	74	51
-22.40		161	148	130	108	84	59	39
-24.40		156	143	125	104	80	55	37
-24.90		174	166	151	125	96	63	40
-25.40		202	204	196	165	120	75	46

Table D15 – HEU fuel at 85MW – configuration l11 – day 1 – IFE – heat flux (W/cm^2)

Distance from…	Core center (cm)							
Core midplane (cm)	7.14	7.5	8.5	9.5	10.5	11.5	12.2	12.6
25.40								
24.90		185	198	218	227	218	204	197
24.40		169	168	174	179	175	170	175
23.00		156	150	145	146	147	150	161
20.00		159	149	143	143	145	151	161
17.00		185	173	166	166	168	174	185
14.00		214	201	193	192	195	202	214
11.00		240	225	216	217	219	227	241
8.00		260	246	236	237	240	248	264
5.00		276	261	251	252	256	265	282
3.00		284	270	260	260	264	274	291
1.00		289	273	264	264	268	278	297
-1.00		290	275	265	266	270	279	296
-3.00		288	273	262	263	269	277	295
-5.00		283	268	258	258	262	271	288
-8.00		273	259	249	249	252	261	277
-11.00		256	241	232	233	235	243	258
-14.00		235	221	212	212	214	221	235
-17.00		210	197	188	187	189	195	207
-20.00		181	170	162	161	163	168	178
-22.40		159	147	140	138	140	146	156
-24.40		152	143	138	137	137	141	151
-24.90		162	163	166	169	166	161	168
-25.40		178	190	207	216	208	192	189

Table D16 – HEU fuel at 85MW – configuration l11 – day 1 – OFE – heat flux (W/cm^2)

Distance from…	Core center (cm)							
Core midplane (cm)	15.13	15.75	16.5	17.5	18.5	19.5	20.5	20.978
25.40								
24.90		206	217	210	183	142	98	69
24.40		180	175	161	139	113	83	62
23.00		161	149	134	115	96	75	59
20.00		163	152	135	118	102	86	72
17.00		187	178	162	144	128	112	100
14.00		216	206	190	171	154	136	124
11.00		244	234	217	196	178	161	148
8.00		268	259	240	220	205	193	185
5.00		287	278	259	242	233	229	231
3.00		298	288	270	253	248	249	254
1.00		303	294	274	259	253	256	263
-1.00		303	293	276	261	256	259	266
-3.00		300	292	273	259	254	256	263
-5.00		295	285	267	253	247	248	254
-8.00		283	274	255	238	229	226	228
-11.00		262	252	234	215	199	184	172
-14.00		238	228	209	188	169	149	134
-17.00		210	200	181	162	144	125	111
-20.00		180	170	154	136	119	102	89
-22.40		156	145	129	111	94	75	60
-24.40		151	139	122	103	82	59	42
-24.90		170	161	146	124	96	65	42
-25.40		194	200	193	163	121	76	47

Table D17 – HEU fuel at 85MW – configuration l11 – EOC – IFE – heat flux (W/cm^2)

Distance from…	Core center (cm)							
Core midplane (cm)	7.14	7.5	8.5	9.5	10.5	11.5	12.2	12.6
25.40								
24.90		128	164	199	213	209	191	176
24.40		127	158	183	190	185	174	166
23.00		126	151	166	166	163	160	159
20.00		128	153	164	163	160	159	158
17.00		134	166	183	184	180	176	171
14.00		139	179	204	207	203	196	188
11.00		141	187	221	228	223	213	200
8.00		139	192	234	242	237	224	210
5.00		137	195	242	253	246	231	214
3.00		136	195	246	259	252	236	216
1.00		138	197	248	262	254	238	218
-1.00		137	198	249	263	256	239	219
-3.00		137	197	249	262	255	239	219
-5.00		138	197	247	260	253	237	218
-8.00		139	196	243	254	248	233	216
-11.00		141	193	236	244	238	225	210
-14.00		142	189	222	228	223	214	202
-17.00		141	181	205	208	204	197	190
-20.00		137	168	185	185	181	178	173
-22.40		131	156	166	165	162	161	159
-24.40		129	153	165	164	161	159	157
-24.90		130	160	184	191	184	175	167
-25.40		131	166	203	215	209	192	177

Table D18 – HEU fuel at 85MW – configuration l11 – EOC – OFE – heat flux (W/cm^2)

Distance from…	Core center (cm)							
Core midplane (cm)	15.13	15.75	16.5	17.5	18.5	19.5	20.5	20.978
25.40								
24.90		154	234	230	215	184	143	134
24.40		147	198	185	173	156	131	130
23.00		138	174	157	146	139	126	134
20.00		136	172	155	146	144	136	151
17.00		146	196	178	169	167	155	174
14.00		154	222	202	193	189	169	193
11.00		159	245	223	213	208	177	204
8.00		162	263	239	228	222	179	209
5.00		163	276	251	240	231	180	211
3.00		164	282	256	247	237	180	214
1.00		164	286	260	249	240	181	215
-1.00		163	287	262	251	240	181	215
-3.00		165	286	261	249	239	181	215
-5.00		165	283	258	247	237	181	214
-8.00		164	275	250	239	231	180	212
-11.00		164	263	239	229	221	181	210
-14.00		162	246	224	213	208	180	207
-17.00		156	222	203	193	190	174	196
-20.00		148	196	179	170	168	158	178
-22.40		138	174	157	148	146	140	155
-24.40		139	171	154	142	135	127	135
-24.90		148	197	184	169	152	127	125
-25.40		156	233	227	210	179	137	126

Table D19 – LEU fuel at 100MW – configuration l11 – BOC – IFE – heat flux (W/cm^2)

Distance from…	Core center (cm)							
Core midplane (cm)	7.14	7.5	8.5	9.5	10.5	11.5	12.2	12.6
25.40								
24.90		227	294	350	353	340	313	267
24.40		197	227	238	227	220	227	221
23.00		180	192	187	171	172	190	191
20.00		181	191	186	174	176	190	186
17.00		210	223	218	206	210	221	213
14.00		241	258	253	240	243	256	245
11.00		272	290	284	270	272	288	275
8.00		295	315	309	294	298	314	302
5.00		313	334	328	311	316	335	319
3.00		323	346	340	322	328	344	330
1.00		329	348	341	326	331	352	334
-1.00		328	349	344	327	332	351	335
-3.00		325	346	340	324	328	347	331
-5.00		317	338	334	316	321	340	325
-8.00		305	325	321	303	309	325	311
-11.00		286	304	298	282	285	302	290
-14.00		259	276	270	256	258	272	261
-17.00		227	242	236	223	224	238	229
-20.00		196	207	200	188	192	203	194
-22.40		171	180	173	162	164	176	174
-24.40		169	146	147	128	127	186	117
-24.90		153	114	90	81	78	83	95
-25.40		175	140	117	106	100	102	110

Table D20 – LEU fuel at 100MW – configuration l11 – BOC – OFE – heat flux (W/cm^2)

Distance from…	Core center (cm)							
Core midplane (cm)	15.15	15.75	16.5	17.5	18.5	19.5	20.5	21
25.40								
24.90		287	319	305	266	235	177	104
24.40		226	220	195	163	148	123	84
23.00		195	182	154	128	117	102	73
20.00		190	186	161	134	125	109	77
17.00		219	221	195	164	157	144	109
14.00		254	258	231	197	194	197	171
11.00		286	291	260	225	226	238	215
8.00		313	319	288	249	253	271	248
5.00		335	342	308	268	277	305	286
3.00		347	352	319	281	295	337	330
1.00		352	358	324	286	303	355	356
-1.00		351	359	325	288	305	360	364
-3.00		348	356	322	285	300	353	357
-5.00		341	349	315	275	288	329	323
-8.00		324	331	298	260	267	291	269
-11.00		301	306	275	237	239	255	231
-14.00		271	274	245	211	211	221	199
-17.00		236	238	212	181	177	179	155
-20.00		201	201	176	147	136	117	80
-22.40		179	174	151	124	111	88	53
-24.40		186	156	145	92	91	77	53
-24.90		90	76	67	57	48	38	31
-25.40		105	93	83	72	60	47	36

Table D21 – LEU fuel at 100MW – configuration l11 – day 1 – IFE – heat flux (W/cm^2)

Distance from…	Core center (cm)							
Core midplane (cm)	7.14	7.5	8.5	9.5	10.5	11.5	12.2	12.6
25.40								
24.90		218	277	336	336	320	299	259
24.40		188	216	227	214	209	218	212
23.00		169	181	174	161	163	179	183
20.00		172	181	173	163	165	179	176
17.00		199	211	204	193	195	208	201
14.00		229	244	238	225	228	241	233
11.00		255	274	268	252	255	271	262
8.00		279	297	290	273	277	297	286
5.00		294	315	308	290	295	315	304
3.00		304	325	317	301	306	325	314
1.00		308	329	322	305	311	329	318
-1.00		308	331	322	305	312	332	322
-3.00		306	328	319	304	309	327	316
-5.00		300	322	314	297	302	321	310
-8.00		288	308	301	285	291	309	297
-11.00		270	289	281	266	269	286	277
-14.00		246	262	255	240	244	260	251
-17.00		218	232	225	211	215	228	220
-20.00		187	198	190	179	181	195	189
-22.40		163	172	165	156	158	171	171
-24.40		166	143	141	124	124	182	115
-24.90		152	113	88	79	78	83	95
-25.40		171	139	115	105	101	102	112

Table D22 – LEU fuel at 100MW – configuration l11 – day 1 – OFE – heat flux (W/cm^2)

Distance from…	Core center (cm)							
Core midplane (cm)	15.15	15.75	16.5	17.5	18.5	19.5	20.5	21
25.40								
24.90		275	303	294	258	234	186	120
24.40		219	208	184	157	149	133	102
23.00		185	172	147	124	120	118	101
20.00		183	177	156	133	133	137	122
17.00		208	209	187	162	162	171	154
14.00		240	243	218	190	194	207	190
11.00		271	275	248	218	226	252	241
8.00		298	301	273	242	258	305	313
5.00		318	322	293	261	282	343	362
3.00		327	334	304	272	293	361	385
1.00		333	339	308	276	299	370	394
-1.00		333	340	309	277	301	371	395
-3.00		329	336	306	274	298	368	393
-5.00		323	330	303	269	291	359	382
-8.00		311	316	287	256	277	341	360
-11.00		289	293	266	236	251	299	311
-14.00		260	264	238	209	214	237	224
-17.00		228	230	207	179	181	191	171
-20.00		196	194	173	149	150	156	141
-22.40		176	170	150	129	127	129	114
-24.40		186	155	145	94	99	101	90
-24.90		90	76	67	59	51	44	39
-25.40		105	93	84	74	63	52	43

Table D23 – LEU fuel at 100MW – configuration l11 – EOC – IFE – heat flux (W/cm^2)

Distance from…	Core center (cm)							
Core midplane (cm)	7.14	7.5	8.5	9.5	10.5	11.5	12.2	12.6
25.40								
24.90		154	253	337	347	329	300	244
24.40		151	226	257	241	233	236	211
23.00		147	201	205	180	178	193	187
20.00		148	200	199	175	173	188	177
17.00		158	222	228	202	200	210	194
14.00		167	247	260	230	227	237	215
11.00		173	266	287	253	249	258	233
8.00		177	280	307	272	265	274	245
5.00		179	288	322	284	278	289	257
3.00		180	293	329	292	285	295	261
1.00		179	295	333	295	288	296	262
-1.00		181	294	334	294	288	298	263
-3.00		180	294	331	294	288	296	261
-5.00		180	291	325	289	285	293	260
-8.00		180	286	318	281	277	286	253
-11.00		177	276	301	267	261	271	242
-14.00		174	261	279	246	243	252	229
-17.00		166	242	251	223	219	231	209
-20.00		156	218	219	194	192	203	188
-22.40		149	199	200	177	176	190	179
-24.40		163	175	185	158	154	210	133
-24.90		124	115	102	94	91	92	98
-25.40		128	121	113	105	102	102	105

Table D24 – LEU fuel at 100MW – configuration l11 – EOC – OFE – heat flux (W/cm^2)

Distance from…	Core center (cm)							
Core midplane (cm)	15.15	15.75	16.5	17.5	18.5	19.5	20.5	21
25.40								
24.90		265	322	326	301	301	282	214
24.40		220	229	209	185	191	212	196
23.00		189	186	161	142	152	189	195
20.00		182	184	164	146	161	206	215
17.00		200	211	192	172	189	241	245
14.00		222	237	218	194	216	272	265
11.00		241	258	237	213	237	298	277
8.00		255	276	253	227	254	317	286
5.00		265	289	265	238	265	329	291
3.00		270	295	271	243	272	337	296
1.00		274	297	273	246	274	339	295
-1.00		274	299	275	247	275	340	296
-3.00		273	297	272	245	274	339	294
-5.00		270	295	270	241	270	337	294
-8.00		264	286	262	236	263	327	288
-11.00		251	272	249	224	250	312	281
-14.00		236	254	232	208	232	290	273
-17.00		216	230	210	188	210	265	261
-20.00		193	202	184	165	182	235	242
-22.40		182	186	166	149	162	208	220
-24.40		196	176	175	117	139	177	195
-24.90		87	79	74	71	70	76	89
-25.40		95	91	87	83	82	85	93

Nuclear Engineering Division
Argonne National Laboratory
9700 South Cass Avenue, Bldg. 208
Argonne, IL 60439-4842

www.anl.gov

Argonne National Laboratory is a U.S. Department of Energy
laboratory managed by UChicago Argonne, LLC